

VŠB – TECHNICAL UNIVERSITY OF OSTRAVA

17. listopadu 15, 708 33 Ostrava – Poruba, Czech Republic

FACULTY OF MINING AND GEOLOGY

INSTITUTE OF GEOINFORMATICS

Monitoring of Terrain Relief Changes using Synthetic Aperture Radar Interferometry

Application of SAR Interferometry Techniques in a
Specific Undermined Ostrava-Karviná District

Dissertation Thesis

Ostrava, 2011

Ing. Milan Lazecký

Supervisor:	doc. Ing. Petr Rapant, CSc.
Study platform:	Geodesy and cartography
Study domain:	Geoinformatics

Abstract

The main objective of this PhD thesis is to investigate an applicability of satellite synthetic aperture radar interferometry (InSAR) methods to perform a monitoring of terrain deformations in the region of Ostrava-Karviná district in Czech Republic. Cities in the region are affected by an intensive mining of a black coal for over 200 years. Character of the area, a velocity and spatial scale of the subsidence, are challenging the limits of InSAR. These limits were investigated, several optimizing scenarios were found to increase the performance of differential InSAR and multitemporal InSAR using C-band and L-band data to detect and estimate deformations due to subsidence and landslides in the region. While extents of subsidence troughs are often possible to delimitate, the deformation rates are usually underestimated. This was compared also to existing data from levelling. A strong potential can be seen in monitoring of slow deformations such as decay subsidence after a closure of mines. In Ostrava city, some subsidence of several mm/year was detected even 15 years after the closures in 1990s. For monitoring of a landslide in Doubrava, corner reflectors were designed but probably due to inappropriate installation on site their contribution couldn't be evaluated. In a conclusion, InSAR techniques were evaluated as appropriate for a systematic monitoring of a subsidence in the region. It can be used as a complementary technique to levelling measurements.

Key words: InSAR, subsidence, landslide, coal mining, undermining, ERS, Envisat, Alos, corner reflector.

Abstrakt

Hlavním cílem disertační práce je ověření použitelnosti metod družicové radarové interferometrie (InSAR) pro monitorování terénních deformací na území Ostravsko-karvinského revíru. Města tohoto kraje jsou ovlivněna intenzivním dobýváním černého uhlí, které zde probíhá již po více než 200 let. Charakter zasažených oblastí, rozsáhlost a rychlost poklesů způsobují problematické nasazení této metody. Byla prozkoumána omezení metody InSAR a bylo navrženo několik způsobů, jak umožnit použití diferenční i mnohosnímkové techniky InSAR nad daty radiového pásma C a L pro správnou detekci a odhad míry poklesů a sesuvů v regionu. Zatímco rozlohu poklesových kotlin je často možné pomocí InSAR ohraničit, rychlost deformací je velmi často podhodnocena. To bylo zjištěno srovnáním s naměřenými hodnotami z nivelací. Metoda InSAR má vysoký potenciál v monitorování pomalých deformací, jako jsou doznívajcí poklesy po ukončení těžby. V Ostravě byly zjištěny poklesy o míře několika mm/rok až 15 let po ukončení těžby, které proběhlo v 90. letech 20. století. Pro pokus o sledování sesuvu v Doubravě byly navrženy koutové odražeče; pravděpodobně však nebyly správně instalovány a jejich použití se tak nezdařilo. Techniky InSAR byly závěrečně vyhodnoceny jako vhodné techniky pro soustavné sledování poklesů v kraji. Mohou být použity jako doplňkové metody k nivelačním měřením.

Klíčová slova: InSAR, pokles, sesuv, uhelné hornictví, poddolování, ERS, Envisat, Alos, koutový odražeč.

Prohlašuji, že jsem celou disertační práci vypracoval samostatně, podle pokynů školitele, s použitím uvedené literatury, v souladu se směrnicí děkana č. 1/2010 disertační práce a autoreferát a v souladu se Studijním a zkušebním řádem pro studium v doktorských studijních programech Vysoké školy báňské – Technické univerzity Ostrava.

V souladu s §47a zákona č. 111/1998 Sb. o vysokých školách a o změně a doplnění dalších zákonů souhlasím s publikováním textu své práce na webové stránce HGF VŠB-TU Ostrava.

Ve Vila Real 7. června 2011

Ing. Milan Lazecký

Motivation

The region of Ostrava-Karviná district where I live is largely affected by terrain changes caused by a longtime black coal mining. It is not practically possible to perform levelling missions or other demanding measurements on every subsiding site to properly achieve a knowledge about a real subsidence in these areas. A relatively new method of combining radar acquisitions from satellites to detect even very small terrain changes looked very promising to provide accurate information about subsidence development in the whole affected area. There was a need to investigate a suitability of InSAR for a continuous monitoring of terrain deformations in this undermined region.

As a person living in the undermined region, knowing about regional problems, feeling the shaking of a twelve-floor building after an explosion of methane, I was highly motivated to run through all of the obstacles to learn a way to prevent some disaster that may happen to people living in this place. I have achieved a unique observation tool which I try to describe within this thesis.

Objectives

The main objective of the thesis is to investigate possibilities and limitations of Synthetic Aperture Radar Interferometry (InSAR) methods in their application for a continuous monitoring of subsidence in the undermined parts of the Moravian-Silesian Region, in Ostrava-Karviná district.

Both differential InSAR and multitemporal InSAR techniques are to be used.

Results will be compared with available levelling measurements.

Additionally an experiment using corner reflectors of radar signal to overcome problems in less suitable localities will be performed and evaluated. These corner reflectors will be used to investigate InSAR suitability to monitor landslides.

A methodology for the continuous monitoring of terrain changes in the Moravian-Silesian Region will be an output of the thesis.

Acknowledgements

The way to finish this PhD thesis was a way to find my own self, to set the proper life values, to learn about the world itself. I am still surprised by the opportunity that I got. I am really grateful to my supervisor, Petr Rapant and to Jiří Horák that they didn't close the door in front of "phantom of Poezie". I believe they were considering my stay and I really appreciate their trust in me. I hope I didn't disappoint you and that I neither will in the future. Thank you for such great support during the whole years of my study.

The project about monitoring subsidence using the satellite radar interferometry was already in an active stage (even that the stage was quite early). Markéta Hanzlová has made a great piece of work preparing a ground and already planting the first seeds for me to take care of.

A cooperation with Eva Jiráňková, Michal Kačmařík with his father and factual prompts by Pavel Bláha and Petr Rapant helped me to search for the right questions in the broad branch of InSAR. I have learned a lot about the subsidence in the region from conversations with Arnošt Grmela and by travelling by bus together with Martin Mucha. I want to thank to Lena Halounová that allowed me a short stay in CTU Prague where I managed to acquire my best processing result of Alos Palsar (after a long time struggling with alternative ways).

My thanks to kind support of all these colleagues that worked or are still working in the field of InSAR, for their understanding and helpfulness that you showed during all my study years. Thank you, Zbigniew, Miguel, Mahmut, Shizhuo, Andy, Petar, Sami, Maryam, Freek, Bára, Ivana, Pooja, Batuhan, Giovanni, Mr. Deledalle, Prof. Pottier, thank you for all your help. I tried not to distract you much by my beginner questions. But I have remembered and used every precious advice you have given to me. I want to thank especially to Ramon Hanssen that gave me the possibility to stay at TU Delft and guided me through the far-flung corners of InSAR. It was my pleasure - and my honour. I want to acknowledge a work of Andrew Hooper, his StaMPS. Dear Andy, I pay my respect for your masterpiece as a set of original ideas that you have put fully available for the scientific and student community.

I was really desperate in certain times during my study, due to various reasons. So my very special thanks go to my friends. My best friends that supported me by forming so much joy and let me participate in writing their own books of life. I know they will pardon me to leave them for such a long time. But they know that we are to experience more adventure together yet!

I have decided to spent my last semester in Portugal. Here, surrounded by mountains and vineyards, in Vila Real, I have written the whole thesis. You have saved my sanity and optimism, so much needed to write, João! Thank you so much.

Yes, I have quite travelled during the work on my thesis. At every stop I learned something new for my work - but also for life, from all these great people I met, or their heritage I got acquainted with. I hope that once I will be able to exist as a good example for others - as you were to me, even that sometimes your examples were very deterrent.

To my family that supported me patiently all my life, no matter what was happening. And to the one which life should be beautiful.

Data Sources

Data used within the thesis were acquired from various sources:

- All SAR data were achieved from ESA, within a Category-1 project ID C1P.4578: "Surveillance of man-induced terrain changes using earth observation data",
- Background ortophotomaps were used from Google EarthTM. Copyright 2009 Google Inc.,
- Aerial photographs on Fig. 4.7.7 from 2006 were provided by GEODIS BRNO, Ltd.,
- Data of ZABAGED for the thesis processing were lend by Zeměměřický úřad (COSMC),
- ASTER GDEM is a product of METI and NASA,
- orbit solutions for ERS-2 were produced in the framework of the REAPER (REprocessing of Altimeter Products for ERS) project, funded by the European Space Agency (ESA),
- Situational photographs in Fig. 3.1.1 and Fig. 4.1.1 were achieved from doc. Ing. Arnošt Grmela, CSc. (VŠB-TU Ostrava) and RNDr. Pavel Bláha, CSc. (GEOtest, Corp.),
- Levelling and other essential data were provided by VŠB-TU Ostrava,
- Data about mining activities in Northern Moravia were collected by Ing. Radovan Kukutsch PhD, a maintainer of project "Zdař Bůh.cz".

Financial Support

During my work on the thesis, I have achieved several grants providing a financial support. These were grants of:

- IGS 2009 (by VŠB-TUO),
- SGS SP/2010149 (by MŠMT),
- Erasmus/LLP (by EU),
- Student Mobility project (by Moravian-Silesian Region),
- project B/CZ0046/3/0010 (by EEA/Norway Grants),
- project CV 5489911 (by MŠMT, no. 19/18),
- project CV 5460011 (by MŠMT),
- HS 548 703,
- financial support from Czech Space Office and ESA.

Contents

Abstract	3
Motivation	8
Objectives	9
Acknowledgements	10
Data Sources	11
Financial Support	11
List of Figures	16
List of Tables	16
Nomenclature	17
List of Symbols	17
List of Abbreviations	18
1 Introduction	21
1.1 Structure of the Thesis	21
1.2 State of the Art: SAR Interferometry	22
2 Synthetic Aperture Radar Interferometry	27
2.1 Introduction	27
2.1.1 Historical Fly-by	28
2.2 Synthetic Aperture Radar	29
2.2.1 Application in Remote Sensing	29
2.2.2 SAR Acquisition Principles	30
2.3 Satellite Missions capable of InSAR	35
2.3.1 Characteristics of Acquisitions	35
2.3.2 Available Satellites	38
2.3.3 Constellation Missions	39
2.3.4 Practical notes	40
2.4 Interferometry	41
2.4.1 Differential InSAR Processing	42
2.4.2 Coherence	46
2.5 Limits of SAR Interferometry	47
2.5.1 Orbit Errors	48
2.5.2 DEM Errors	48
2.5.3 Processing Errors	50

2.5.4	Decorrelation	51
2.5.5	Atmospheric Effects	54
2.6	Multitemporal SAR Interferometry	57
2.6.1	Introduction	57
2.6.2	Methods of Multitemporal InSAR	58
2.6.3	StaMPS Processing Techniques	61
2.7	Summary	63
3	Monitoring of Subsidence in Northern Moravia	65
3.1	Area of Interest	66
3.1.1	Exploitation of Black Coal in OKR	66
3.1.2	Effects of Undermining in OKR	67
3.1.3	Formation of Subsidence Trough	69
3.2	Available Datasets	70
3.2.1	SAR datasets	70
3.2.2	Levelling Datasets	74
3.3	InSAR Processing Issues	75
3.3.1	Differential InSAR Processing	75
3.3.2	General Notes for MT-InSAR Processing	82
3.3.3	Actual StaMPS Processing Approaches	85
3.3.4	Comparison with Levelling Data	93
3.3.5	Discussion	95
3.4	Final InSAR Overview of Regional Subsidence	96
3.4.1	Overview of OKR Subsidence Basin	96
3.4.2	Overview of Selected Sites	99
3.5	Summary	107
4	Detection of Landslide in Doubrava	109
4.1	Introduction	109
4.2	Area of Interest	110
4.3	InSAR for Landslide Monitoring	111
4.3.1	Needs for Corner Reflectors	112
4.4	Design of Corner Reflector	113
4.4.1	Radar Cross Section	113
4.4.2	Final Corner Reflector Design	117
4.5	Orientation of Corner Reflector	119
4.5.1	Comparison of Methods	121
4.5.2	Applied Computations for Current Experiment	121
4.6	Corner Reflectors Experiment	122
4.6.1	Corner Reflectors Deployment	122
4.6.2	Evaluation of Experiment	123
4.6.3	Summary	126
4.7	Results of InSAR Processing	127
4.7.1	Differential InSAR Processing	127
4.7.2	MT-InSAR Processing	136
4.8	Summary	138

5	Final Summary	139
5.1	Discussion	139
5.1.1	General Limitations	139
5.1.2	Can MT-InSAR fully Replace Levelling?	140
5.2	Results and Findings	141
5.2.1	Comparison with other works	142
5.2.2	Suitability of InSAR for Subsidence Monitoring	143
5.3	A Proposal for a Systematic Monitoring of Terrain Changes in Moravian-Silesian Region using InSAR	144
5.4	Ideas for a Future Work	146
5.5	Final Words	147
	Vyhodnocení	149
	Bibliography	152
	Website References	160
	About the Author	161
	List of Relevant Publications	163
A	Computation Methods to Properly Orientate a Corner Reflector	165
A.1	Computation Methods of Azimuth and Incidence Angle	165
A.1.1	Computation in Local Reference Frame	165
A.1.2	Computation based on Existing Acquisition	169
A.1.3	Azimuth Computation using Satellite Inclination Angle	170
A.1.4	Azimuth Computation using Image Footprints	172
A.1.5	Incidence Angle Computation using Image Footprints	173
A.2	Correction of Azimuth for a Squint Angle	174

List of Figures

2.2.1	Distribution of different radiation frequencies through the atmosphere . . .	29
2.2.2	Principle of SAR acquisition	31
2.2.3	Effect of layover, foreshortening and shadow in SAR observation	34
2.3.1	Activity of SAR satellites offering data for InSAR processing in central Europe	35
2.4.1	Interferometrical geometry	41
2.5.1	Relation between height ambiguity and a perpendicular baseline	50
2.5.2	Decorrelating effect of a critical perpendicular baseline	52
2.5.3	Decorrelating effect of Doppler centroid frequency differences	53
3.1.1	Effects of mine subsidence - tramline to Karviná and damaged housing . .	67
3.1.2	Formation of subsidence trough over undermined area	69
3.2.1	Descending ERS-1 and ERS-2 (track 494) acquisitions before 2001	71
3.2.2	Ascending ERS-2 acquisitions (track 415)	71
3.2.3	Descending ERS-2 acquisitions (track 494) after January 2001	72
3.2.4	Descending Envisat acquisitions (track 494)	73
3.2.5	Ascending Envisat acquisitions (track 415)	73
3.2.6	Ascending Alos acquisitions	73
3.2.7	Profile plots of levelling results of (a) Lazy Mine area and (b) Holkovice	75
3.3.1	Gray colour scale used for wrapped interferograms	76
3.3.2	Decorrelating effect of temporal baseline in ERS and Envisat	77
3.3.3	Decorrelating effect of perpendicular baseline in ERS and Envisat	77
3.3.4	ERS/Envisat interferogram coherence with regards to the seasons of the year	78
3.3.5	Example of phase filtering of subsiding area	78
3.3.6	Removal of atmospheric phase screen from differential interferogram . . .	79
3.3.7	Topography removal by chosen DEM models	81
3.3.8	Small baseline configurations of StaMPS processing approaches	86
3.3.9	Atmospheric phase screen of StaMPS processing master image	88
3.3.10	Incremental deformation estimations - ERS descending	89
3.3.11	Comparison of mean LOS velocity results	90
3.3.12	Observed relation between B_{perp} and weather conditions	91
3.3.13	Mean LOS deformation velocities in Doubrava area from ERS (1995-2000)	92
3.3.14	Selected results from levelling comparison	94
3.4.1	Subsidence basin of Karviná district detected using DInSAR	96
3.4.2	Extents of the whole subsidence area of Karviná district	97
3.4.3	OKR investigated by multitemporal InSAR processing of ERS	98
3.4.4	Investigation of Ostrava area by MT-InSAR	99
3.4.5	Subsidence activity nearby Ostrava mines from MT-InSAR analysis	100
3.4.6	DInSAR results of Lazy Mine surroundings	102

3.4.7	MT-InSAR processing attempts using Envisat ascending data	104
3.4.8	DInSAR results around Holkovice area, differences within 10 years	105
3.4.9	DInSAR to observe subsidence progression of levelled Holkovice site	106
3.4.10	MT-InSAR processing of Holkovice area	107
4.1.1	Damages caused by landslide after floods in 2010. Photo by RNDr. Pavel Bláha, CSc., GEOTest Corp.	109
4.3.1	Influence of look direction to the hill slope	111
4.4.1	Retro-reflecting area of basic corner reflectors plate shapes	116
4.4.2	Dependency of angle deviations for computed RCS of a trihedral CR	118
4.4.3	Design of the corner reflector (a) and its deployment in terrain (b)	119
4.5.1	Orientation of a corner reflector to the satellite line of sight	120
4.6.1	Multi-Image reflectivity map of SAR images	126
4.7.1	Viewing directions of SAR satellites during observing Doubrava slope	128
4.7.2	Intensity images of constructed interferograms	129
4.7.3	Selected interferograms showing the landslide activity	130
4.7.4	Expected phase change caused by a landslide	130
4.7.5	Effect of non-local mean filtering for Alos Palsar interferogram	133
4.7.6	Situation map and differential interferograms of landslide in Doubrava	135
4.7.7	Progression in the surroundings of HV-2 location	137
A.1.1	Geometrical relations between corner reflector and satellite position	166
A.1.2	Computation of satellite position	167
A.1.3	Satellite inclination angle	171
A.1.4	Computation of azimuth angle and incidence angle for point HP-3	172
A.2.1	Squint angle	175

List of Tables

2.1	Selected radar bands (0.3-40 GHz)	30
2.2	Overview of selected SAR satellites characteristics	37
2.3	Example of SAR configurations used to validate DInSAR error sources	47
2.4	Phase induced by delays through different atmospheric conditions	54
3.1	General parameters of available DEMs	80
3.2	Performed StaMPS processing approaches of ERS/Envisat data	86
3.3	Changing parameters of StaMPS processing optimizing results for local areas	92
4.1	Boresight Radar cross section of a squared trihedral corner reflector	118
4.2	Results of different methods to obtain azimuth angle θ and incidence angle δ	121
4.3	WGS-84 coordinates of corner reflectors mounting points	122
4.4	Identification of corner reflectors in the SAR reflectivity images	125

Nomenclature

List of Symbols

B	geometrical baseline
B_a	azimuth time bandwidth
B_r	range bandwidth
B_{perp}	perpendicular baseline
B_{temp}	temporal baseline
c	speed of light
Δ_{gr}	ground range resolution
Δ_{slant}	slant range resolution
ε_r	relative permittivity
f_0	SAR carrier frequency
f_{DC}	Doppler centroid frequency
γ	coherence
H_{amb}	height ambiguity
λ	wavelength
μ	boundary angle of influence of exploitation
φ	phase
R	range between a resolution cell and the satellite
σ	standard deviation
σ_0	radar cross section
θ_{inc}	incidence angle
θ_{look}	look angle

List of Abbreviations

AOCS	Attitude and Orbital Control System
AOI	Area of Interest
APS	Atmospheric Phase Screen
ASAR	Advanced Synthetic Aperture Radar
CHMI	Czech Hydro-Meteorological Institute
CR	Corner Reflector
DEM	Digital Elevation Model
DInSAR	Differential InSAR
ESA	European Space Agency
FBS	Fine Beam Single Polarization
GIS	Geographic Information System
GPS	Global Positioning System
HH	Transmitting and Receiving Horizontally Polarized Radiation
IDW	Inverse Distance Weighting
IMS	Image Mode Single-Look Complex
InSAR	Synthetic Aperture Radar Interferometry
JAXA	Japan Aerospace Exploration Agency
LOS	Line of Sight
MIRM	Multi-Image Reflectivity Map
MTI	Multitemporal SAR Interferometry
NL-MEAN	Non-Local Mean Filtering Algorithm
OKD	Ostravsko-karvinské doly, a. s.
OKR	Ostrava-Karviná District
PRF	Pulse Repetition Frequency
PS	Persistent Scatterer Pixel
PSC	Persistent Scatterer Candidate
PSI	Permanent®/Persistent Scatterers Technique

RADAR	Radio Detection and Ranging
RCS	Radar Cross Section
SAR	Synthetic Aperture Radar
SB	Small Baselines
SCLA	Spatially Correlated Look Angle Error
SLC	Single Look Complex
SRTM	Shuttle Radar Topography Mission
StaMPS	Stanford Method for Persistent Scatterers
VV	Transmitting and Receiving Vertically Polarized Radiation
WGS	World Geodetic System
ZWD	Zenith Wet Delay

"Earth! You seem to look for something at my hands.
Say, old top-knot, what do you want?"

WALT WHITMAN, LEAVES OF GRASS

[CITED BY HOWARD FAST, FREEDOM ROAD]

Chapter 1

Introduction

The region of Ostrava-Karviná district in Northern Moravia, Czech Republic is largely affected by terrain changes due to over 200 years history of black coal mining. It is not practically possible to perform levelling missions or other demanding measurements on every subsiding site to properly achieve a knowledge about a real subsidence in these areas. Subsidence is often estimated using some computational model, but also several attempts to use common remote sensing data were performed here.

A relatively new method of combining radar acquisitions from satellites to accurately detect terrain changes looks very promising. In fact one is not capable to observe his own house descended for a couple of millimetres during one year while it is claimed that an instrument watching this house from almost a thousand kilometres from the Earth surface is able to!

Of course the reality is never clearly bright and the path following the radar beam is not straightforward. The practical use of InSAR is often problematical. This thesis investigates an applicability of this technology in this undermined region. If this will be confirmed, the synthetic aperture radar interferometry (InSAR) can be used in the future for a continuous monitoring of subsidence in Ostrava-Karviná district.

1.1 Structure of the Thesis

I have done my best writing every of these chapters almost independently. I have tried to achieve a situation where every chapter would describe different issues and could be read by persons working or planning to work with InSAR itself, persons concerned in subsidence of OKR, eventually in landslides, or persons interested generally in potentials of InSAR. I personally hope you will find some useful information in some of these pages.

Chapter 1 Here, in the Introduction part, you can read also about an actual state of the art of InSAR as I have composed from the fraction of publications I could get in touch with during my work. You may find a progress of InSAR during last 10 years described here, mostly connected with a subsidence monitoring.

Chapter 2 In this part I present the fundamental issues of InSAR. In fact every second PhD thesis about InSAR includes theoretical aspects of this branch. In my approach I tried to describe the general issues as I have understood them, emphasizing issues that are not repeated commonly in similar works and tried to complete them by own graphs and practical information about the InSAR processing itself.

Chapter 3 This chapter is dedicated to the main InSAR processing of Northern Moravia region. All of my available data and instruments are described here, together with brief information about a subsidence activity in Northern Moravia, in Ostrava-Karviná district.

Chapter 4 Investigations of a landslide in Doubrava were taken as a second objective of my work. For these investigations also corner reflectors were designed, built, installed and failed in their purpose. However their correct concepts are presented here. In this chapter you may find some ways to a proper interpretation of differential interferograms.

Chapter 5 This chapter summarizes my work, some ideas and a plan for a systematic monitoring are proposed here.

1.2 State of the Art: SAR Interferometry

The SAR Interferometry has been already applied in the field of subsidence monitoring as well as for monitoring of landslides and the results were presented in many scientific works during around 20 years period of civil SAR satellites activity. Main advantages but also limitations of different processing techniques were described, this is to summarize up-to-date state of the art as achieved from available literature. Only publications relevant to the application of InSAR in my area of interest are selected. Used terminology will be explained further within this thesis.

To mention an important publication that lead to applying the InSAR for Northern Moravia, Dr. Perski (Perski et al., 2003) partially succeeded in detection of subsidence due to black coal mining in Upper Silesia, Poland using C-band SAR data from satellites ERS and Envisat in various configurations. The location is very close to the Northern Moravia region and both regions share very similar conditions. However, in this and similar publications regarding processing of the area, several main problems were discussed. Problems such as temporal decorrelation in the interferograms, impossibility to correctly process phase unwrapping of the images etc. The same main author has applied a PSI technique to this area, using TU Delft Persistent Scatterers Interferometry implementation - DePSI (Perski et al., 2007). In this processing only urban areas could be monitored, no significant

subsidence was detected there. The author also applies DInSAR technique for SAR images with different wavelengths. While popular C-band data from ERS or Envisat satellites need to be obtained with a very short temporal and geometrical baselines to reduce irreversible decorrelation, L-band data (JERS, Alos) is more suitable to detect faster subsidence even within long temporal gaps (Guang et al., 2009). Precise X-band acquisitions of TerraSAR-X with a short temporal baseline of 11 days provide more detailed overview of subsidence area and possibility of more accurate georeferencing (Krawczyk et al., 2008), but a longer temporal difference becomes prone to a decorrelation.

To overcome some of the known and described problems using C-band data, I have investigated modern available possibilities of various filtering. The work of (Li et al., 2006b) was dedicated to correction of errors caused by difference in radar wave propagation delay through the atmosphere. Provided results depict a great achievement for InSAR processing after such a filtering using either data exploited from Envisat MERIS acquisitions or using GPS zenith wet delay computations. Even for multitemporal methods that actually estimate the atmospheric delay variance in the interferograms, the reliability of the multitemporal processing was significantly extended by prefiltering of input interferograms using this atmosphere filtering approach.

Other investigations were aiming to find an appropriate filter for resulting interferograms. It is possible to filter highly decorrelated differential interferograms using an available Goldstein technique after modifications according to (Baran et al., 2003). Formidable enhancements are shown by (Deledalle et al., 2010) using his own algorithm of a non-local mean filtering originally created as a high quality denoising filter of SAR amplitude images.

Because the levelling data describes a relatively fast subsidence in my area of interest that can approach almost 1 m/year in some locations, I searched for published research results of similar conditions that challenge the InSAR limits. In (Yun et al., 2007), a problem of detection of Sierra Negra volcano subsidence of 5.4 metres during 8 days in 2005 was partially resolved. Yun's team challenge existing InSAR processing software capabilities (ROI_PAC, Doris and GAMMA was tested), finding that all of them are limited by algorithms that are used within. Such a large subsidence has shifted physical terrain displacements over several pixels in the acquisitions. Using new flexible „rubber-sheet“ algorithm for coregistration of C-band SAR images together with amplitude processing to estimate pixel movement offsets, even subsidence exceeding current InSAR limits was discovered. This and other attempts proved a necessity of a further development of processing algorithms that can provide more results from SAR data.

The Permanent ScatterersTM (PSI) (Ferretti et al., 2000) and other derived multitemporal methods have several limitations as will be described further. The methods can be used successfully for monitoring even very slow deformations of less than 10 mm/year, such as in the case of subsidence due to oil and gas exploration in Groningen area, Netherlands (Ketelaar, 2009). The precision of year deformation rate was shown to be better than 0.5 mm/year. In case of a higher rate of subsidence the PSI technique usually fails in correct estimation or even in the detection of subsiding areas.

After Fringe 2003 conference, ESA initiated the Persistent Scatterer Interferometry Codes Cross-Comparison And Certification (PSIC4) Project to produce reliable information about the accuracy and dependability of these methodologies (Raucoules et al., 2009). A

coal mining site in Gardanne, France was chosen as an area of interest. The deforming area is mostly non-urbanized with an expected rate of subsidence of up to 25 mm/year. Eight top expert teams with own PSI methods participated anonymously in processing of 109 ERS SAR data of 1992-2004. Because of absence of strong reflecting objects in vegetated areas, significant atmospheric delay variations and not included a priori information about the deformations that could have been used to identify the main deformation trends, as well as other error factors, none of the teams provided absolutely precise estimations. However even that the spatial coverage of identified PS pixels was usually very sparse, the subsidence and stable area were located correctly in almost all the cases. In mainly affected (note that also densely vegetated) areas the techniques underestimated the deformation velocity even for 10 mm/year and the results in general deviated less than 5 mm/year within the whole scene for all the teams. After PSIC4 evaluation, the teams achieved more external data (levelling amongst them) in order to fine tune their results and enhance their algorithms. That was a case also for (Samiei-Esfahany, 2008) that presents better fitting results using adapted algorithms used in DePSI that should be possible to apply also for other similar areas.

In the case of urban areas, the PSI is a very valuable tool for terrain monitoring. Several InSAR studies were performed in monitoring of Mexico City that is undergoing a rapid subsidence due to ground water extraction. Note that Mexico City is a densely urbanized flat area in a very dry environment preserving high correlation between SAR acquisitions. Processing of 23 C-band Envisat ASAR data of Mexico City in period of 2004-2006 by the DePSI technique (Osmanoglu et al., 2011) was aiming to describe seasonal deformation changes searching for signs of aquifer recharging - these weren't found, though. The technique has estimated deformations of maximum mean velocity of around 300 mm/year. These estimations were compared with GPS measurements. Both methods resulted within ± 6.9 mm/year difference matching a very similar trend model.

For usage in natural terrain in occurrence of vegetation cover, the PSI technique is limited. For monitoring of subsidence due to groundwater extraction in rural areas of Tehran, Iran, the differential C-band InSAR fails due to strong temporal decorrelation. Usual PSI techniques that use amplitude dispersion index to choose PS pixels have problems to detect stable scatterers in non-urban areas. Such a technique as implemented in TU Delft (DePSI) was tested by Dehghani et al. (Dehghani et al., 2009b). Processing was performed using 22 descending Envisat ASAR images of 2003-2008 and 19 ascending Envisat ASAR images of 2004-2009. The technique failed in this area also due to errors in phase unwrapping due to a fast subsidence causing phase jumps in large temporal gaps in the SAR data stack. The terrain deformations reach similar values as the before-mentioned case of Mexico City, up to 250 mm/year as measured by levelling, including also horizontal movements of up to 80 mm/year. A method of PSI known as Stanford Method for PS (StaMPS), originally developed to monitor volcanic activities using InSAR (Hooper et al., 2004) succeeded to detect PS pixels in the area, however the results were underestimated. Better fitting estimations were achieved using Small Baseline Subset (SBAS) algorithms implemented in GAMMA software (Dehghani et al., 2009a). For StaMPS processing, using only highly coherent interferograms, the probable main trend of subsidence was modelled and removed from the whole interferogram stack that was then processed to estimate only seasonal deviations from the trend. Also, using both descending and ascending acquisitions, it was

possible to reconstruct amounts of vertical and horizontal components that concurred to expectations.

For monitoring of movements in natural terrain, Lauknes (Lauknes et al., 2008) chose small baselines subset multitemporal InSAR method (SBAS) instead of PSI with a view of better performance in monitoring of rockslides. However results of both methods were very similar. This conclusion was made independently on work of Hooper et al. (Hooper, 2008) that incorporates similar implementations within StaMPS software.

The multitemporal InSAR can be used for detection of a slow horizontal movement or landslides, as was described also for example by Perski et al. (Perski et al., 2009).

Also a method using combinations of diversely polarized radar waves in so-called Polarimetric SAR Interferometry developed into an applicable state. This technique is used mostly in the field of ice and biomass volume changes monitoring where the sensitivity for polarization angles is most significant. For example, because the polarization signatures of the vegetated canopy and the ground differ, it is possible to separate the radar echos from the ground and from a top of the trees. In the field of land deformation monitoring this can be used to identify scatterers that are coherent at different polarizations and to improve the estimations of deformation velocity. Projects such as (Pipia et al., 2009) assure about diverse results of differential InSAR processing of various polarized data. Their combination can improve the final result significantly. Also, a combination with the PSI technique is very effective. By a polarimetric optimization it is possible to dramatically increase the number of proper PS pixel candidates.

Summary

To monitor subsidence and landslides, InSAR was confirmed as a valuable technique. It is used within a Terrafirma project for global monitoring of subsidence and landslides in Europe and it will be used for monitoring and data integration together with insitu data in the future by the Global Monitoring for Environment and Security (GMES) initiative by European Commission and ESA. Within areas of relatively fast subsidence and non-urbanized areas the typical InSAR processing is still limited. Limits can be overcome by advanced processing algorithms or by processing of acquisitions made by a sensor of more suitable characteristics (several different SAR missions are active and new missions are planned to be launched in a near future, they will be described within this thesis).

Note that the art is already in an advanced state. Nowadays several main InSAR processing techniques exist that are still being improved by several expert teams residing in institutions with a proper background of activity in this field of research. The technology is now being commercialized, not all implementations are available for testing purposes. In this recherche I searched mostly for projects with a connection to processing by software packages that are available free of charge as open-source and are used within this thesis, even that they don't include all up-to-date developed algorithms often implemented in commercial software.

"Denkt wel, spreek wel, doet wel."
(Think well, speak well, do well.)

CLAAS NOMEN [TO PETER THE GREAT]

"Говори кратко, проси мало, уходи борзо!"
(Speak briefly, demand little, leave soon!)

PETER THE GREAT

Chapter 2

Synthetic Aperture Radar Interferometry

2.1 Introduction

Spaceborne Synthetic Aperture Radar (SAR) Interferometry, a technique that allows us nowadays to measure even sub-centimetre terrain changes on nearly any part of the world, is not an overnight miracle. It is a result of a longtime human scientific progress managed by observing physical reactions of the Nature used to observe physical reactions of the solid Earth. In this scope the technique allowed us to describe in details effects of earthquakes on the surface, behaviour and activity of volcanos, to precise monitor a motion of glaciers or a creep on geological faults, to detect a danger of land or rock slides, to evaluate surface subsidence, as well as to perform topographical mapping, to detect places affected by floods or by a forest fire or even a growth of vegetation can be monitored using this advanced remote sensing technique (Hanssen, 2001).

The technique in general combines a knowledge of radio detection and ranging (radar) with a theory of interferometry, aerospace technologies and with a help of modern information technologies. The main result is an image of interferogram that is the base for all the terrain evaluations. The interferogram phase image is created as a difference between two measurements of a radar wave phase, i.e. between fractions of a wavelength of a radio wave as was reflected from the surface. If these measurements are taken with some temporal delay (denoted as a temporal baseline between measurements), any terrain deformation during this delay will be detected in a form of these changes of wave phase that the deformation

caused. If there was a subsidence during this time, the radio wave will travel longer through the atmosphere in the second pass causing a different phase.

The radar instrument can be installed onboard a satellite orbiting the Earth upon the ionospheric atmosphere layer. The microwave spectrum of radiation used by the radar can fully penetrate throughout the atmosphere, unlike radiations of different wavelengths – see Fig. 2.2.1. The microwave spectrum is defined as a spectrum of wavelengths in range between 1 mm and 1 m, while the practical range used in spaceborne SAR is between 3-30 cm (disregarding missions not concerned in a solid terrain monitoring). Because only a difference within reflected fractions of wavelength is computed using interferometry, the technique can reach sensitivity for a terrain change in a millimetre scale in optimal conditions. However, natural conditions limit such high sensitivity, as will be discussed.

2.1.1 Historical Fly-by

Even that the SAR Interferometry (InSAR) is very specific, it is currently possible to reconstruct interferogram images of large areas of several (tens) kilometers with a ground resolution up to around 1 meter (in the case of X-band SAR satellites). To achieve such high technology level, it took more than 100 years since the first radar was created. After discoveries in 19th century by Maxwell and later on by Hertz, first radar systems were developed and used for ship tracking already in 1903. Radars were profitable in military and scientifically in the field of radio astronomy since the first radar study of the Moon in 1946. First radar observations from space succeeded in 1972 by lunar topography mapping from Appollo 17, then also Venus was mapped globally. Since early 1960s, a concept of the synthetic aperture radar culminated from Carl Wiley's idea in 1951. This concept would increase radar azimuth resolution of three orders and finally detect and preserve phase information together with amplitude. A true milestone for mass development of SAR applications for Earth remote sensing was a success of the first SAR satellite mission Seasat in 1978. However, the Seasat data were processed using interferometry techniques much later, in 1987 (Li et al., 1987), as the first demonstration of satellite InSAR processing.

After a mostly experimental period of InSAR in the late 1980s demonstrating its effectivity in topography estimations, the first idea of a very accurate deformation monitoring was published in (Gabriel et al., 1989) and demonstrated by mapping of a displacement field of Landers earthquake in 1992 (Massonnet et al., 1993). During the 1990s several SAR satellites were launched to the Earth orbit for systematic collection of data – these missions will be discussed in Section 2.3. Within the availability of a large amount of sensed data, new processing algorithms were developed including a revolutionary Permanent Scatterers technique (Ferretti et al., 2000). Also, after data processing of Shuttle Radar Topography Mission (SRTM) in 2000, created global DEM could be used effectively for topography removal in differential interferograms, thus an even easier deformation monitoring. As a summary of the the Sixth International Symposium on Land Subsidence of UNESCO in 2000, the differential SAR interferometry was found as a very potential method for detection of land subsidence and other ground displacement with a relatively high precision at a low cost (Carbognin, 2003).

Nowadays, the InSAR is already developed into a valuable tool for terrain monitoring applications. During the last ten years, new high quality SAR systems were launched into the space, new algorithms were developed for data processing, new applications of InSAR in the field of remote sensing were found, most of sources of noise were identified and methods for their correction were designed and implemented. Actual state of the art was briefly described in previous chapter.

2.2 Synthetic Aperture Radar

2.2.1 Application in Remote Sensing

The active system of transmitting and receiving radar waves has several main advantages against a passive scanning of higher frequencies radiation (thermal or optical). The radar can work independently on the daylight, the lower frequencies pass through the atmosphere without being absorbed - see Fig. 2.2.1 as a simplified version of Fig. 1.1 from (Richards, 2009), and in general the radar energy scattering behaves differently from optical energy scattering. It is more sensitive to the dielectric characteristics and a geometry of the scattering object.

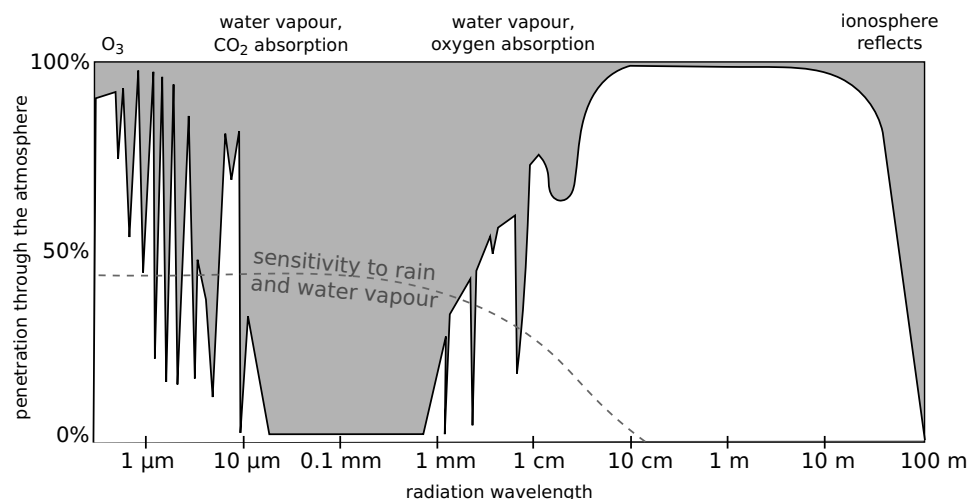


Figure 2.2.1 – Distribution of different radiation frequencies through the atmosphere; adapted from (Richards, 2009)

Besides the interferometry usage (that apply for any terrain change detection or a mapping of topography) the SAR images have their application for example in a ship or oil slick detection, land cover classification, flood monitoring, forestry, oceanography, soil moisture measurements, but also for example in archeology since the radar signals can even penetrate into some materials, as into a dry sand.

The microwave spectrum is usually defined as an electromagnetic energy with a frequency ranging from approximately 1 GHz to 100 GHz; in the past also lower frequencies were included. Most common applications are within the 1 to 40 GHz range. Microwave frequency bands, as defined by the Radio Society of Great Britain [12], plus P-band, are shown in the Tab. 2.1.

Any application depends on the frequency of used radar wave. For example, L-band is much more sensitive for a soil moisture than other bands. Its wavelength is much larger than a typical tree leaf so certain vegetation types are transparent to the L-Band sensor - the SAR receives more echoes from the ground compared to the vegetation. L-band is more susceptible to ionosphere effects than other bands. X-band doesn't need so large antenna as other bands to achieve a high slant range resolution so it can be used for some fine scanning. Also the short wavelength will reflect from very small objects (tree leaves). X-band is more sensitive on the atmospheric phenomenas (heavy rain). Great penetration abilities are ascribed to P-band. No known satellite InSAR capable SAR system using the P-band exists, though.

Table 2.1 – Selected radar bands (0.3-40 GHz)

Band	Frequency (GHz)	Wavelength (cm)	Band	Frequency (GHz)	Wavelength (cm)
P	0.3-1	30 - 100	X	8-12	2.5 - 3.75
L	1-2	15 - 30	Ku	12-18	1.67 - 2.5
S	2-4	7.5 - 15	K	18-26.5	1.13 - 1.67
C	4-8	3.75 - 7.5	Ka	26.5-40	0.75 - 1.13

Another important characteristic is a polarization of the radar wave. Usually the wave is transmitted and received in the same polarization (HH or VV) which ensures a strong response. However, for some cases it is useful to work with a cross-polarized wave, for example by transmitting horizontally polarized wave and receiving vertically polarized wave (HV). This is used for example in detection of objects in a sea, since in this case the backscatter from water surfaces is very small. Or for discrimination of some vegetation types. Comparing HH and VV, these result very similarly. Some slightly higher reflection from buildings as well as a lower reflection from a wet grass was found in the VV case in (Lee et al., 2007).

2.2.2 SAR Acquisition Principles

This section doesn't aim to fully explain the whole bunch of information that form the whole principles of SAR, from acquisition to final processing. I will try only to introduce the basic (and sometimes simplified, hopefully without a loss of correctness) knowledge needed to understand the SAR interferometry issue. Most of the information gathered is properly described in (Cumming et al., 2004) and (Hanssen, 2001). Following paragraphs are according to these books. The section will describe only a monostatic radar principle (using one transmitter/receiver only) in a stripmap mode (the Doppler centroid line aiming in the constant direction) which is a standard principle of SAR satellite systems.

2.2.2.1 Synthetic Aperture Radar

The satellite is beaming the ground in a look angle θ_{look} by electromagnetic pulses that are described as a chirp (usually a linear function that modulates a radar frequency in time) of a specific signal bandwidth with a center radar carrier frequency f_0 . The pulse will expand

in concentric spheres. Each point on the ground will be illuminated by the pulse for the duration T_p . Regarding to the character of the ground scatterers, only some portion of the beam will be reflected back. This reflected signal will be received and sampled into complex numbers. Such a signal can be then (later) reconstructed into a spatial representation. This is a simplified overview of a SAR principle for the range direction processing, i.e. a direction perpendicular to the satellite track. In the SAR image the rows represent the **range** direction. The chirp solution (the frequency bandwidth around a base frequency f_0) allows to achieve such a high range resolution as the modern SAR systems have it today.

The satellite advances along its path, it transmits and then receives these pulses in a frequency denoted as a pulse repetition frequency (PRF). This way it stores the row (range) data in every line, that represents this **azimuth**, the along track direction.

The signal propagates as concentric spheres. This means that after every pulse, the whole ground will be illuminated. Every object will be illuminated by hundreds of pulses from different angles. The strongest reflection will be in the case when the range distance between the target and the satellite will be the smallest. Normally it should be the case when the target is in the perpendicular direction from the satellite. But, because actually the satellite is moving on its track, as well as the Earth rotates, this close range distance will be slightly different. These movements will cause a change in frequency known as a Doppler effect. Therefore, every illumination of the object in each angle can be characterized by different **Doppler frequency**. The target's strongest return will be when the Doppler frequency equals zero. This is really the perpendicular direction to the satellite plus a squint angle, as it can be seen in Fig. A.2.1.

By forming radar images at this point, the azimuth direction resolution can be computed in the order of several kilometers. This is a principle of a *real aperture radar*, the azimuth resolution is dependent mostly on the physical antenna length. Because the SAR systems retrieve also Doppler changes of signal frequency, it is actually possible to synthesize a long radar antenna by a special signal processing. The length of this synthetic antenna depends on the time that a target stays within the radar beams in the azimuth direction. The principle is depicted in Fig. 2.2.2. The resulting azimuth resolution usually reaches the order of meters.

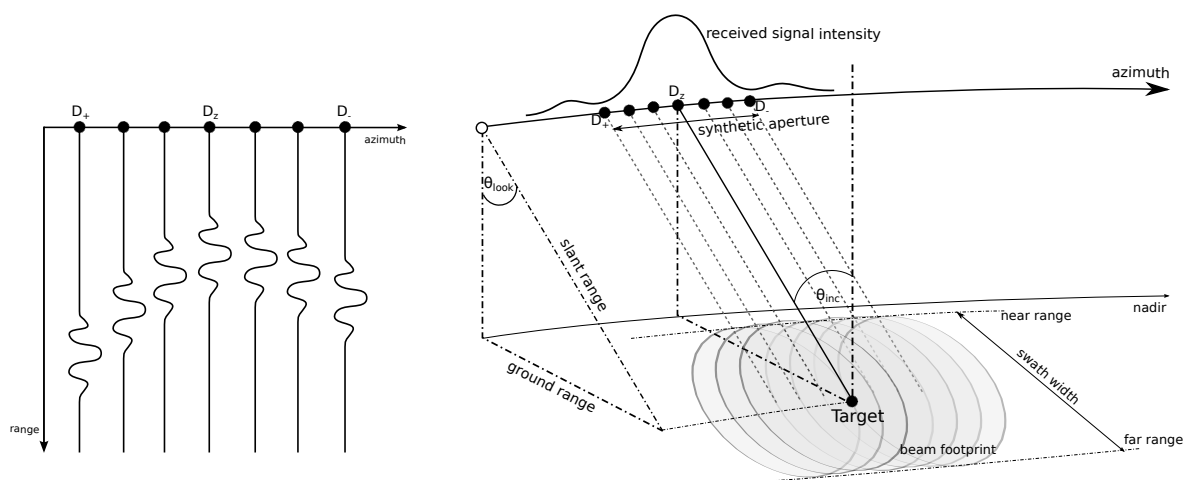


Figure 2.2.2 – Principle of SAR acquisition; adapted from (Cumming et al., 2004)

It should be noted that due to the stated principles, the SAR has more specific properties. Talking about resolution, both range and azimuth direction has a different resolution in terms of a minimum separation of two objects in the radar reference system. Another type of resolution is a ground resolution. A relation between a slant range resolution and the ground resolution is:

$$\Delta_{gr} = \frac{\Delta_{slant}}{\sin \theta_{inc}} \quad (2.2.1)$$

, while the slant range resolution Δ_{slant} is given by the effective pulse length formed in the whole range bandwidth B_r with regards to the chirp modulation¹:

$$\Delta_{slant} = \frac{c}{2B_r} \quad (2.2.2)$$

The relation in Eq. (2.2.1) also means that the ground resolution differs throughout the final SAR image since the incidence angle will be different. Supposing a flat terrain, the smallest incidence angle will be at the near range, while the largest incidence angle (and the highest ground resolution) will be at the far range. The **local incidence angle** is defined as the angle between the normal vector of the backscattering element (i.e. vector perpendicular to the ground surface) and the incoming radiation vector (i.e. vector formed by the satellite position and the backscattering element position). So, the resolution is also highly dependent on the local topography.

2.2.2.2 Focusing to Doppler Centroid

Due to the velocity of the satellite as well as the rotation of the Earth, the acquired radar pulses are affected by a Doppler effect. Each time a target is illuminated, it is affected by a different Doppler frequency shift. The whole set of these shifts of one target is described as a Doppler bandwidth B_{Dop} . Therefore this Doppler bandwidth has a direct relation to the azimuth beamwidth/synthetic aperture size, during which the target is still illuminated and therefore it can determine the azimuth resolution of the focused SAR image:

$$\Delta_{azi} = \frac{v_{sat}}{B_{Dop}} \quad (2.2.3)$$

As it was stated, a target has a peak backscatter in its closest range to the satellite, therefore in the configuration where there is a zero Doppler frequency D_z (see Fig. 2.2.2, left). To enhance the azimuth resolution by synthesizing the aperture, the whole B_{Dop} is used to form an image where every pixel value arises as an average measurement valid for a beam direction in the time when the Doppler frequency was the Doppler centroid f_{DC} , i.e. the average frequency of B_{Dop} . In the ideal situation, the $f_{DC} = D_z = 0\text{Hz}$. In this beam

¹Sometimes a range pixel spacing as a sampled response of the pulse can be used instead of Δ_{slant} . Then, a sampling frequency f_s will be used in the Eq. (2.2.2) instead of B_r .

the target had the strongest response. But in reality there is always some squint angle (see Fig. A.2.1) that deviates direction of the central f_{DC} from the zero Doppler frequency D_z . In modern SAR systems the squint angle caused by Earth rotation (that is almost 4° in the equator) is corrected by yaw and pitch steering of the satellite, so often the $f_{DC} \approx 0$.

In the interferometric praxis it is important to have both SAR images focused on a similar f_{DC} value with some tolerance of usually several hundreds Hz, since the f_{DC} describes also the angle from which the target has been illuminated. However it is not necessary to achieve $f_{DC} = 0$ for InSAR purposes.

The SAR processing is performed differently in the range and azimuth directions. To fully understand the SAR focusing principles, I recommend a book of (Cumming et al., 2004).

Practical Note

It is possible and usually it is recommended also to order already processed SAR data into a focused single look complex format that is ready for interferometry processing. However if needed, ROI_PAC package allows to focus the raw data also. A description of ROI_PAC processing can be found in (Rosen et al., 2004). It is possible to focus on a determined f_{DC} or to deskew the data to $f_{DC} = 0$.

2.2.2.3 Geometrical Distortions in SAR Images

Note that the SAR image is related to the slant range, that is, the scanning is performed in the satellite line of sight that is not perpendicular to the ground/ellipsoid. So, the geometry of topography as we know it will differ in the resulting image - large areas will be **shadowed** by some higher mountain that would be visible in some optical system observing perpendicularly to nadir.

The radar waves cannot be regarded as usual rays of light. They are of 10^5 x lower frequency making their wavelength comparable to incident objects. These objects will also scatter this kind of radiation differently than scattering the light (also a Rayleigh scattering will affect the resulting image). The receiver, supposing of typical monostatic SAR system, is observing the reflected wave from more or less the same direction. Because the radar beam is (generally speaking) propagating in all directions, we can imagine it as a sphere with the antenna in its center. All points that are in the same range distance to the antenna will form a temporally equidistant spheric layer and all of them will be imaged as only one point detected in time t , without their distinguishing. Of course this disadvantage is already managed by the whole principles and techniques of SAR that in the end provide the radar image synthesized as like a set of very narrow rays of a low-frequency radiation. However in some specific cases the observations can get distorted anyway, mostly across the satellite track (range direction) and mostly due to the topography of the beamed area.

Typically if a mountain slope is facing nearly perpendicularly to the satellite line of sight, all the slope area will be equidistant to the satellite. The whole slope will be compressed in a few image pixels of a high intensity, since the backscattering from more objects in the same range distance will be summed. This is called a **foreshortening**.

Another situation occurs in steep mountains or more narrow look angle. A backscatter from the top of the mountain B can be detected sooner than the bottom part A that is geographically nearer to the satellite nadir. In this case the point B will precede point A in the final image causing a **layover** effect - this slope will be reversed in the slant range image.

Effects of shadow, foreshortening and layover are demonstrated on Fig. 2.2.3. A more quantitative explanation regarding the slope angle can be found in Section 4.3 since for the landslide monitoring these effects are particularly important.

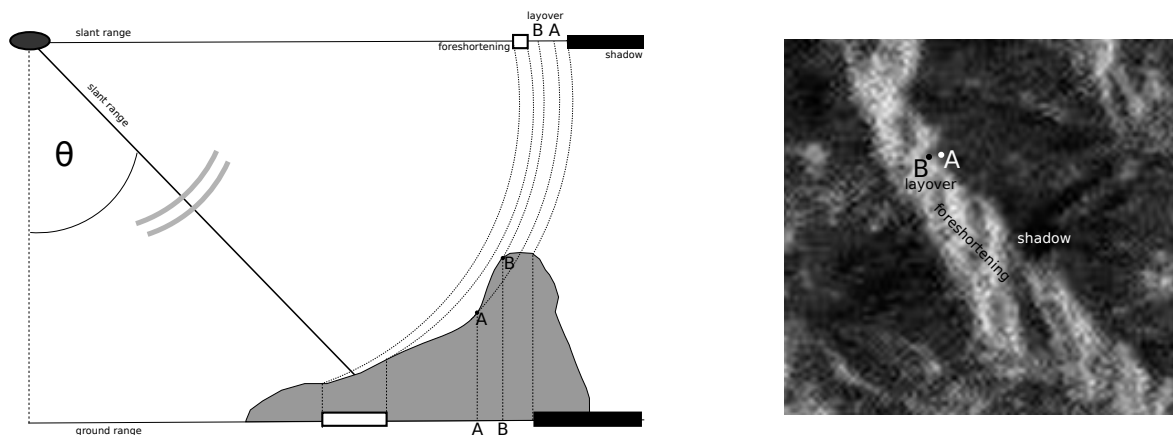


Figure 2.2.3 – Effect of layover, foreshortening and shadow in SAR observation in the presence of a variable topography

2.2.2.4 Storage of SAR Data

There are several different storage formats for the SAR data. For interferometric purposes, SAR data focused on some Doppler centroid are needed, since only data in image space can be combined interferometrically. The data are stored usually in a complex format. From the complex data both intensity and phase information can be derived. The principle is that the real-valued received signal is demodulated by a discrete Fourier transform. The real channel is created by mixing the signal with a cosine wave and filtering of a high frequency component, while the imaginary channel is the same signal multiplied with a sine wave (of the same frequency). This process is called a quadrature demodulation.

After various phases of the SAR data processing, the resulting data can be achieved either in a raw format that needs to be further processed to the single look complex data that are two-dimensional (spatial) complex valued images capable of interferometry.

The raw files can be additionally processed using the complex values in a higher sampling rate to achieve some two times higher resolution in both range and azimuth direction. These images can then be geocoded and used for other remote sensing purposes. However these are images that don't possess any information about a phase as the single look data have. In this thesis, as a SAR image, a single look complex data will be meant, if not specified other way.

2.3 Satellite Missions capable of InSAR

Several SAR satellite missions provide data that can be used for systematic monitoring of terrain deformations since 1991. Fig. 2.3.1 provides a timeline of the satellites activity. More information is provided in Tab. 2.2 as acquired from particular missions handbooks and fact sheets. Before ERS-1, other spaceborne SAR data exist from american Seasat satellite (1978) or SIR-B mission from 1984 or later SIR-C from 1994. These data are also capable of interferometry. For purposes of this thesis, only data that are available for scientific purposes and cover or are potentially able to cover area of interest in Northern Moravia, Czech republic (as defined in Section 3.1), are selected and described. Please note that there are more SAR satellites in the Earth orbit with this potential but they are simply not available for a civil use at the moment. For example, an israel X-band SAR satellite TecSAR is in the orbit since 2008 with a resolution believed to be up to 1 m [17]. Even higher resolution (50 cm) is attributed to satellites in a SAR-Lupe constellation [16].

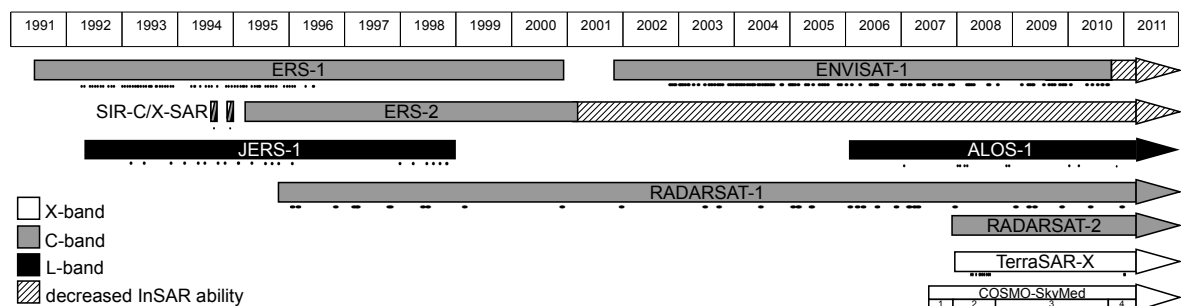


Figure 2.3.1 – Activity of SAR satellites offering data for InSAR processing in central Europe. Available acquisitions of Ostrava-Karviná region in Czech republic are marked by black dots.

2.3.1 Characteristics of Acquisitions

All the SAR satellites fly in a sun-synchronous dawn-dusk orbits that allow them to be permanently illuminated by sun and therefore to be powered almost entirely by its solar panels. The acquisitions are taken in descending and ascending flight direction. Most of the satellite mission sensors are only right side looking, therefore one acquisition can be taken in the morning time only (descending mode) and one in the evening (ascending mode). Because the radar response is sensitive to the geometry of reflecting objects, only acquisitions from the same direction and the same polarization angle can be used for InSAR processing. It is advisable and sometimes even necessary to plan the required acquisitions in advance to achieve appropriate interferometric pairs – also, even that satellites have almost a full global coverage, the areas that are to be acquired and archived need to be selected; data amounts are enormously boosting storage needs, data capacity onboard satellites is limited, as well as the length of simultaneous activity of the instrument.

Past generation of SAR satellites could provide images of only one polarization. The most preferred polarizations are horizontal wave transmit and receive (HH) or vertical wave transmit and receive (VV). The strength of the reflected signal in one of these modes is very similar in the land conditions. For specific purposes (like detection of targets on a

water surface or thematic mapping) also cross-polarization is used with advantage (HV, VH). However the cross-polarization backscatter is generally lower since the cross-polarised return only appears through multiple scattering. Most of the SAR satellites are capable of operating in one polarization mode only at one time, while this polarization mode can be selected for each acquisition in a planning stage (Single mode). Actually, for radar polarimetry and polarimetric InSAR purposes, new SAR instruments are capable of more polarizations at a time. This is obtained by alternating the polarization mode, however at the expense of about two times lower spatial resolution of the final image. In Dual mode the final images are polarised in dual combinations HH+HV or VV+VH (while TerraSAR-X is capable also for HH+VV combination). In the case of QuadPol (quadrature polarization), all four combinations HH, VV, HV, VH of the scene are created.

Acquired scenes from each satellite differ in terms of their azimuth/range resolution and swath width, amongst other properties. Simplifying information from Section 2.2.2, when the central wavelength is decreasing, the radar beam gets more narrow, more details can be recognized then. Therefore X-band satellites can offer a spatial resolution around 1 m.

In modern satellites, several common image acquisition modes are used, depending on the user requirements (see Fig. 2.3.1):

- *Stripmap/Standard mode* – this is a standard mode. The antenna pointing direction is held constant as the radar platform moves. The beam sweeps along the ground at an approximately uniform rate and a contiguous image is formed (Cumming et al., 2004). It is possible to predetermine swaths of various width and resolution based on different antenna looking angles.
- *Wide/ScanSAR mode* – the principle remains similar to the Stripmap mode but the swath width gets extended – the swath is up to 5x wider than in Stripmap mode. By changing of antenna looking angles, several sub-swaths are illuminated for a short period enough to synthesize a radar image, and then combined to obtain a full image coverage. The resolution is much coarser (azimuth resolution depends on the number of scanned swaths).
- *Ping-pong/Alternating polarization/Co-polar mode* – a special form of acquisition mode working in one swath as defined for Stripmap mode. After a short illumination enough to synthesize a radar image in the required range resolution, the instrument switches into a different polarization scanning mode and repeats the operation several times. The resolution is usually two times coarser than in Stripmap mode.
- *Spotlight mode* – an extra precise resolution (even less than 1 m in azimuth direction) is achieved by steering the beam gradually backwards as the sensor passes the scene. The area is illuminated from various angles, a larger aperture is simulated. However, the coverage is not contiguous (only a spot of radius of several km² is imaged). All actual X-band satellites and also Radarsat-2 are able of the Spotlight mode.

More modes are sensor dependent. For example, Radarsat-2 handles with Fine (5.2x7.7 m resolution in range/azimuth) or Ultrafine (1.6/2.8 m resolution range/azimuth) modes which are stripmap modes achieved with a very high sampling rate, in a cost of imaged scene dimensions.

Table 2.2 – Overview of selected SAR satellites characteristics

Mission	Agency	Period of activity	Height (km)	Revisit (days)	θ_{inc}^* (°) min/std/max	Δ_{gr} (m) spot/std/wide	Swath (km) spot/std/wide	Polarization**	f_0 (GHz)	λ (cm)
ERS-1	ESA	1991-2000	790	35	21/23/26	-/26/-	-/100/-	VV	5.3	5.57
ERS-2	ESA	Since 1995	790	35	21/23/26	-/26/-	-/100/-	VV	5.3	5.57
JERS-1	JAXA	1992-1998	568	44	26/35/41	-/18/-	-/75/-	HH	1.275	23.5
Radarsat-1	MDA	Since 1995	792	24	10/34/58	-/8-30/ 50-100	-/45-100/ 300-500	HH	5.3	5.57
Radarsat-2	MDA	Since 2008	798	24	10/34/60	1.6/9/ 40-75	20/100/ 300-500	S, D, Q	5.405	5.54
Envisat	ESA	2002-2010***	800	35	15/23/45	-/25/150	-/100/405	S1, D	5.331	5.56
Alos	JAXA	Since 2006	692	46	8/34/60	-/10/100	-/70/ 250-350	S1, D, Q	1.27	23.6
TerraSAR-X	DLR	Since 2008	515	11	15/32/60	1/3/18	10/30/100	S, D	9.65	3.11
Cosmo-1	ASI	Since 2007	620	16	20/38/60	1/3/ 30-100	10/40/ 100-200	S, D	9.66	3.12
Kompsat-5	KARI	Planned 2011	550	28	20/45/55	1/3/20	30/Unknown	S, (D)	9.66	3.12
Sentinel-1	ESA	Planned 2012	693	12	20/23/45	-/5/ 20-40	-/80/ 250-400	S1, D	5.405	5.54
SIR-C/ X-SAR	NASA/ DLR/ASI	1994	225	174	17/40/63	-/30/-	-/15/-	VV, Q****	1.28/ 5.2/9.7	23.5/ 5.8/3.1

* Incidence angle is ranging from its min to max; "std" is used commonly for most of stripmap scenes or is an average in standard stripmap

** S=single, S1=single one polarization (HH or VV only), D=dual, Q=quad

*** In October 2010 Envisat changed its orbit; only acquisitions from latitude $38 \pm 5^\circ$ (S/N for ascending/descending) can be used for InSAR

**** For X-band radar, only VV polarization is available, all polarizations for L- and C-band radars

2.3.2 Available Satellites

In civil and common scientific field, four main organizations partake in SAR remote sensing from space – European ESA, Japanese JAXA, German DLR and Canadian MDA. While NASA participated in the key moments of spaceborne SAR evolution especially by its SAR space shuttle missions – SRTM and SIR-A/B/C, there are no known plans of NASA for developing its own SAR satellite. For SIR-C/X-SAR joint mission of NASA, DARA and ASI, two expeditions were undertaken – in April 1994 and October 1994. Experience from processing data obtained using beams of three different wavelengths and different polarizations were applied for ongoing satellite missions.

The ESA's C-band ERS satellites were highly successful in the past and even now their unique amount of continuous archived data allows more data mining using multitemporal processing algorithms. Both ERS-1 and ERS-2 exceeded their planned lifetime by far. During 1995-1998 they flew in a tandem constellation with 1 day delay. Since June 1996 the ERS-1 operated only as a back-up for ERS-2 until a hardware failure in March 2000. Even that ERS-2 is still active, its SAR acquisitions are problematical for InSAR usage due to an unstable Doppler centroid frequency deviating for around 4500Hz (ESA, 2008). Because of technical issues of ERS-2 since 17 January 2001 that culminated in a total gyroscope failure, the data are strongly affected by the satellite orbital attitude instability – not every image pair is interferometrically combinable and a possibility of multitemporal InSAR processing is practically excluded. The gap between gyroscope failure of ERS-2 and the ASAR sensor activity of Envisat, that began on March 2002, caused a discontinuity in numerous InSAR terrain deformation monitoring projects.

ESA's Envisat contains more instruments onboard than ERS to collect various remote sensing data – some of them can be used to increase the InSAR effectivity, like atmospheric delay correction using the MERIS spectrometer (Li et al., 2006b). The Advanced Synthetic Aperture Radar (ASAR) provides observations of more polarities and extends observed swath dimensions. Other attributes remain similar to ERS, so it is also possible to process both ERS-2 and Envisat, that fly in a tandem mode with a 30 minutes delay, by a cross-interferometry, using specific algorithms that surpass the slight difference between beam frequencies and other barriers (Arnaud et al., 2003). Since 22 October 2010 Envisat has changed its orbit descending of 17.4 km. There is no inclination drift control anymore, the perpendicular baselines can reach values even 20 km, while the limit for InSAR is around 1 km. Only areas in $38 \pm 5^\circ$ degrees of latitude are covered by InSAR available acquisitions (Miranda, 2010).

JAXA satellites JERS (the Japanese Earth Resource Satellite-1) and ALOS (Advanced Land Observing Satellite) are unique for their L-band usage within their SAR sensors. For InSAR usage, Alos contains a Phased Array type L-band SAR (PALSAR) capable of Fine and ScanSAR mode acquisitions. Because of resource requirements of other sensors that work during the day time acquisitions during descending phase, the high resolution Fine mode of SAR is active only during satellite ascending. The orbit cycle is 46 days, but to systematically acquire images in all available modes, with different off-nadir angles and polarizations, the modes are strictly distributed during the year [1].

C-band SAR satellites from Canadian CSA/MDA, Radarsat-1 and Radarsat-2, fly in an orbit with about 50 minutes separation designed to view any part of Canada within

three days. Satellites possess various acquisition modes. Similarly to ASI Cosmo-SkyMed satellites (see further), the Radarsat-2 is able to change look direction from standard right to left-looking - the revisit time of an area of interest can be greatly decreased and a routine imaging of Antarctic is also supported.

The German Aerospace Center (DLR) is the leader of TerraSAR-X project, the first commercially available radar satellite that offer image products of around 1 m resolution, in Spotlight mode. When such images are used for DInSAR processing, even 1 mm terrain displacements can be reliably measured. Also, the image pixel orthorectification is accurate of up to 1 m thanks to a precise satellite attitude and orbit determination.

2.3.3 Constellation Missions

For ongoing future missions, satellites are planned to work in constellations as the actual constellation missions prove a high effectivity of such approach. A constellation of four X-band SAR satellites known as Cosmo-SkyMed (Constellation of Small Satellites for Mediterranean basin Observation) is providing advantages of a short revisiting time less then 5 days allowing monitoring of fast dynamic terrain phenomems. Even that this mission mainly aims the Mediterranean basin, where any point in this region can be reached by a beam every 7 hours in average (only from different view angles excluding InSAR applicability), the acquisitions are taken globally. Since October 2010 the Cosmo-SkyMed (CSK) constellation is complete. While each satellite performs one Earth cycle in 16 days, within a regularly distributed constellation it is possible to achieve interferometrically combinable SAR acquisitions every 4 days. It is also possible to reconfigure the orbits for tandem interferometry where two satellites reach the same position in 20 seconds or a tandem-like interferometry with a shortest delay of 1 day (Covello et al., 2010).

The mission of TerraSAR-X has been enhanced since June 2010 by a second satellite flying at a nominal distance of a few hundred meters (at an orbital speed of 7.5 km/s this means a temporal distance in the order of tens of miliseconds). Both satellites together form a constellation called TanDEM-X that will generate a global highly accurate DEM model (resolution of 12 m and 10 m absolute, 2 m relative height accuracy). The global DEM is planned to be completed in 2014. The satellites fly in a helix track and have a unique ability to achieve bistatic SAR images – one satellite transmits the radar signal, both satellites receive its reflection. Acquired data is regarded to have a strong impact on the state-of-the-art of satellite SAR science since the bistatic SAR imaging has a *“potential for the retrieval of sea state parameters, the estimation of surface roughness and terrain slope, as well as stereogrammetric, meteorological and atmospheric applications”* (Krieger et al., 2007).

A Canadian RADARSAT Constellation Mission is planned to be fully functional in 2015. This constellation will be composed of three new satellites with C-band SAR instrument with a 12 days repeat cycle per each with a spatial resolution up to 5 m. Korean Kompsat-5 and later on Kompsat-7 are also planned to work in a constellation. Project SMMS of China includes four SAR satellites operating in S-band (Wang et al., 2005).

Finally, the ESA Sentinel-1 mission (Attema et al., 2007) is a constellation of two C-band SAR satellites that will provide monitoring of sea ice, marine environment and land surface

in terms of GMES project requirements. The first satellite will be launched in 2012, the second will follow several years later. Its basic characteristics are summarized in Tab. 2.2.

2.3.4 Practical notes

Data from ESA SAR satellites (ERS-1, ERS-2, Envisat) as well as Alos PALSAR and possibly others in a near future are available to order from archive or to plan their future acquisition, respectively, after a registration of a new project in ESA Earth Observation website [8], using an EOLi-SA tool [5] that provide also advanced functions as a computation of interferometric baselines etc. Archived data from ESA SAR satellites are available free of charge². An archive of TerraSAR-X data is available in [3] with advantaged conditions for scientific use. To achieve data from other SAR satellites, please visit websites of corresponding agencies for more information.

Note that data are stored in various specific formats. Check the read capabilities of your InSAR processing software. The most preferable open-source InSAR processing software, Doris and ROI_PAC, read data from ERS, Envisat, JERS, Alos, Radarsat-1 and TerraSAR-X. A support of data from other SAR satellites, especially for Radarsat-2, are under development. Another processing software, GMTSAR (Sandwell et al., 2010), is capable of reading the same data but due to a simplified processing technique, data from JERS and Radarsat-1 are marked as problematical because of their imprecise orbit information. Other known freely available InSAR processing software is IDIOT [10] and Radar Tools [15]. While IDIOT provides a simple automatical DInSAR processing of Envisat SLC data, InSAR processing using Radar Tools should be applicable also on other SAR data. A former ESA software for SAR data processing called NEST [13] is able to read numerous SAR data formats. It includes an implementation of Doris now, however in an early stage. After this implementation will be fully functional, this software will be able of a direct InSAR processing on perhaps any available SAR data.

Alos Palsar SLC focused images as available from ESA is also problematical to process using one of the freely available processors because of used Actual Doppler (AD) focusing technology – see Section 2.2.2.2. For Alos Palsar processing it is highly recommended to order unfocused (Level 1.0) data and then apply focusing, for example using ROI_PAC or GMTSAR. In my case, I had to process the AD data in GAMMA software.

²Read the Terms and Conditions first, as presented on the website

2.4 Interferometry

The created SAR image allows to identify a range distance to differently scattering objects. The applicability of SAR will improve if two SAR images taken from different positions are combined. This way, using a radar stereometry the topography can be measured. However the radar stereometry is very limited by the range resolution capabilities and a satellite track (orbit) knowledge accuracy. In the end, using an Envisat configuration with a perpendicular baseline length of $B_{\text{perp}} = 100$ m the stereometry processing would yield a height accuracy of only 4 km.

The SAR Interferometry approach will improve the topography measurements significantly. It is based on a complex multiplication of complex values S_M, S_S as achieved after SAR processing, of corresponding points taken from two slightly different satellite positions. The complex values, or phasors, can be decomposed in an amplitude $|A|$ and phase components φ as $S_{M,S} = |A_{M,S}| \exp(j\varphi_{M,S})$. Their complex multiplication will result in a difference of phase measurements, as can be seen from Eq. (2.4.1):

$$I = S_M \cdot S_S^* = |A_M| \cdot |A_S| e^{j(\varphi_M - \varphi_S)} \quad (2.4.1)$$

Every point is then measured under a different angle but, compared to the radar stereometry, with a principle of advantageously taking into account fine phase changes in the backscatter of the objects. A phase φ can be imagined simply as a scattered part $\varphi = (-\pi; +\pi)$ of a radar wavelength λ . In the end, using the same Envisat configuration with a $B_{\text{perp}} = 100$ m the height accuracy is improved into 300 m (Manunta, 2009). The geometry of SAR interferometry combination is described in Fig. 2.4.1.

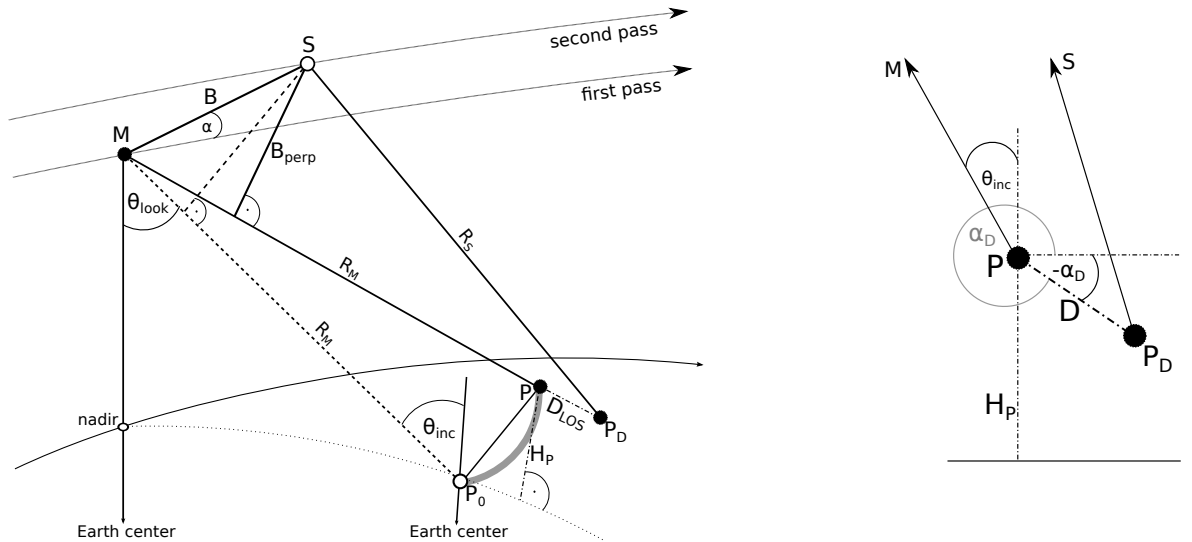


Figure 2.4.1 – Interferometrical geometry. First acquisition is denoted as a master (M), second in time as a slave (S); adapted from (Curlander et al., 1991; Hanssen, 2001; Lauknes et al., 2008)

However the strongest part of the SAR Interferometry is its unique ability of monitoring fine changes of the heights in time. If two SAR acquisitions were taken in some time delay,

the phase difference of the same object will not be caused only by the slightly different observing angle but any change during this time of the object position with regard to the radar will imply a phase change - the wave will propagate a slightly shorter or longer distance to the object. The difference of sensitivity to topography height H_P and to this physical object movement (a deformation) $D_{M,LOS}$ in the satellite line of sight (in master position) to point P is demonstrated in Eq. (2.4.2), simplified from (Hanssen, 2001). If Envisat parameters of Tab. 2.3 are used within an effective baseline $B_{perp} = 100$ m, the phase would change for $H_P = 1$ m only per $\varphi_P = 4.5^\circ$ while for $D_{M,LOS} = 1$ cm the phase difference would be even $\varphi_P = 127^\circ$.

$$\varphi_P = \varphi_{P,ref} - \frac{4\pi}{\lambda} \left(D_{M,LOS} + \frac{B_{perp}}{R_M \cdot \sin \theta_{look}} H_P \right) \quad (2.4.2)$$

$R_{MP_0} \dots$ range from the first (master) satellite pass to the image P_0 on the reference surface (i.e. a location of P if lied on the ellipsoid),

$\varphi_{P,ref} \dots$ phase from a reference surface (usually an ellipsoid WGS-84) derived from the orbit geometry. This can be computed as $\varphi_{P,ref} = -4\pi/\lambda \cdot B \sin(\theta_{look} - \alpha)$.

The Eq. (2.4.2) is a simplified version valid in ideal conditions. The resulting phase will be influenced also by other contributions as an atmospheric delay signal, and affected by various errors, such as orbit data errors. The minus sign of the phase is used to describe the direction w.r.t. satellite. This originated by the Doppler effect, where the velocity towards the sensor (or a decrease in range) results in a positive Doppler frequency f_D . There is a valid relation for a SAR carrier frequency $f_0 = 1/2\pi \cdot \Delta\varphi/\Delta t$ (Hanssen, 2001) that supposes the minus sign of the phase φ .

2.4.1 Differential InSAR Processing

Differential InSAR processing (DInSAR) is a technique to derive only phase changes due to temporal surface movements (deformations). Every phase difference between two corresponding points (the SAR images are coregistered in a sub-pixel level, therefore I rather mention *points* instead of *pixels*) is composed by various phase yielding sources. Schematically it can be written as:

$$\Delta\varphi_{total} = \Delta\varphi_{ref} + \Delta\varphi_{topo} + \Delta\varphi_{defo} + \Delta\varphi_{atmo} + \Delta\varphi_{noise} \quad (2.4.3)$$

To remove a reference phase $\Delta\varphi_{ref}$ caused by the Earth curvature, precise orbits are used that apply some ellipsoid to describe the phase propagation on the surface, relating to the actual satellite position. The phase term caused by a delay of radar wave propagation through the atmosphere $\Delta\varphi_{atmo}$ cannot be distinguished using two SAR images only - see Section 2.5.5. Main noise $\Delta\varphi_{noise}$ is filtered using various techniques.

Theoretically if the effective perpendicular baseline B_{perp} was zero, there would be no phase contribution $\Delta\varphi_{topo}$ from a topography. This is usually not happening. This technique

deals with removing the topography phase term using some digital elevation model (DEM) scaled to the line of sight using the baseline estimations. It is possible to use some external DEM (2-pass DInSAR) or the elevations can be derived from an InSAR pair of a short temporal baseline (to prevent a temporal decorrelation and terrain deformations that might occur). The latter solution can be known as a 3-pass DInSAR method, if the same base SAR image (master) is used in both topography InSAR pair and in final deformation InSAR pair.

The differential phase change of $\varphi = 2\pi$ is associated to a line of sight (LOS) displacement of $\lambda/2$ - since two ways signal propagation is accounted for. This means the upper limit of the proper deformation detection per pixel. A higher deformation than $\lambda/2$ in the line of sight will cause so-called phase jump since the phase can achieve values only from a set of $\varphi \in (-\pi; +\pi)$. On the other hand, this also mean that the phase can unveil a very small change in a rate of a fraction of the radar wavelength.

According to Fig. 2.4.1, the deformation D in a direction α_D will result in a slant range deformation (Franceschetti et al., 1999)

$$D_{M,LOS} = |D| \sin(\theta_{inc} - \alpha_D) \quad (2.4.4)$$

In the case of usual narrow incidence angles, such as around $\theta_{inc} = 23^\circ$ for Envisat, this means much higher sensitivity for vertical deformations than horizontal ones. In the case of $\alpha_D = \theta_{inc} \pm \pi/2$, such a change will not be detected at all, remaining in the same slant range. Please note that in the InSAR, the second acquisition (usually chronologically latter) depicted as a slave image, is reoriented to match the geometry of the first acquisition, master image. Therefore all the geometrical properties of a final interferogram (as a line of sight, slant range or an incidence angle) are related to the master image.

Since the DInSAR technique is used for a spatial dataset, it is possible and valuable also to present the resulting differential interferogram as a raster image. In this raster image the terrain deformation movement is represented by homocentric circles, called fringes. A center of a fringe is a deformation epicenter and every circle contour formed by the whole colour spectrum in the image (usually from red to blue as a direction towards the radar) figures the terrain movement from the epicenter in the length of half wavelength in the satellite line of sight direction.

The phase change values are wrapped as a part of a wave period in radians in the LOS. To get the metric values of land movement, a *phase unwrapping* must be applied. This technique tries to estimate the real terrain deformation from only a phase modulo of the whole distance from satellite to the terrain - it is not possible to reconstruct the whole number of cycles the wave has done on its way between the surface and satellite. For a higher rate of deformations the situation is complicated because of the phase jumps where a phase unwrapping often fails to properly estimate the deformation. Also the phase is affected by a decorrelation, only using well filtered data the process may enumerate correctly the deformation, relatively to some reference height level.

2.4.1.1 Standard DInSAR processing in Doris

Within this thesis, a Doris software (Kampes et al., 2003) has been used to perform differential InSAR processing. This summarizes the basic processing chain of the software that is described in more details in (Kampes et al., 2008):

- *Read images information* - the task of this step is to read relevant parameters of master (base) and slave (that will be adapted to fit the master) images - these parameters identify the scene (location, time of acquisition) and the sensor properties (wavelength, type of satellite, pulse repetition frequency etc.),
- *Precise orbits application* - even that the originally provided image file already contains orbital data (information about satellite position during radar sensing) computed during satellite flight, these orbits could be much more enhanced using precise orbit ephemerides, computed by satellite agencies from later acquired data - erroneous orbits can induce a residual phase trend in resulting interferogram,
- *Crop of data* - the full scene can contain an area too large to process, it is recommended to crop to the area of interest. Note that the slave image should be cropped as a fairly larger area than the master image to ensure their full overlap if the satellite characteristics during the scanning differ too much (looking angle or different line of sight due to satellite position etc.),
- *Oversample* - to avoid aliasing of an interferogram spectrum, it is possible to interpolate new points between every neighboring pixels by this step,
- *Coregistration of images* - to ensure that the images fit to each other in the sub-pixel level (as a requirement for the interferometric processing), their coregistration parameters are computed. First, the images are usually coregistered together coarsely using precise orbits (with accuracy of about 30 pixels), then coarsely using computation of offsets in lines and rows in accuracy of about 1 pixel by computation of correlation between both images in windows distributed in spatial or frequency domain - and final coregistration is done in similar way by sub-pixel "fine" coregistration that leads to computation of offset vectors to align the slave image to the master - another principle of images coregistration is to use a DEM as a reference of positioning master and slave images together (this is very useful if the master and slave images are not well correlated),
- *Azimuth filtering* - this step filters images in azimuth direction for non-overlapping parts of data spectrum due to different Doppler centroid frequency chosen in the SAR focusing technique) - the most effective usage of azimuth filtering is after the coarse coregistration based on correlation and before the so-called fine (sub-pixel) coregistration,
- *Mathematical model of a master and slave alignment* - using coregistration parameters it is possible to describe a 2-D polynomial model of certain degree to fit the behaviour of how the slave image is aligned to the master image,

- *Resample of the slave image* - by using mathematical model, the slave image is resampled to fit (in sub-pixel accuracy) the master image using some of the interpolation methods,
- *Range filtering* - because of slightly different viewing angles of both sensors, the spectrum in range is not overlapping fully - the range filtering is useful mostly for longer spatial baselines (perpendicular baseline) between the positions of satellites,
- *Computation of interferogram* - the interferogram is computed as a complex multiplication of wave amplitude and phase values of both images that includes the required information about the phase difference,
- *Correction for "flat Earth"* - in this step the phase changes trend caused by the reference system surface used for the image coordinates (WGS84) is computed and subtracted from the interferogram, based on precise orbits data,
- *Filtering of topography phase* - in order to acquire only a phase value due to deformation of surface in time, the unneeded phase contribution of topography is filtered out using some digital elevation model,
- *Phase filtering* - to reduce noise in the differential interferogram and/or to sharpen the detected fringes, the phase image is filtered using some kernel-based method, usually applied after fast Fourier transformation,
- *Phase unwrapping* - the most difficult process of radar interferometry is to estimate the full phase value. Because the number of wave cycles between the radar antenna and an object is not measurable but only the part of one wave period could be detected as a wrapped phase φ , various algorithms attempt to recreate the full unwrapped phase,
- *Conversion of phase values in the radar line of sight to an ellipsoid height* - this is done by computation of the heights in the radar coded system from the phase unwrapped in the line of sight and then by geocoding every pixel to some reference ellipsoid (WGS-84).

There are more available methods to better combine both master and slave images - or another types of filtering. Also within the Doris package, a timing error between DEM and a master image could be estimated using a synthetic master amplitude simulated by orbital information and topographic data. After improving the master timing, it can be used then in a coregistration method using DEM or computation of reference phases of interferograms. As an example of an advanced filtering, some atmospheric model can be used to reduce the influence of atmosphere on the phase values.

2.4.2 Coherence

A complex coherence γ as a degree of similarity between two SAR images is defined as

$$\gamma = \frac{E\{S_M \cdot S_S^*\}}{E\{S_M \cdot S_M^*\} \cdot E\{S_S \cdot S_S^*\}} \quad (2.4.5)$$

, where the E operator is the mean value along a predefined spatial window of complex SAR images. For this window the phase value of γ will be a multilooked interferogram phase. More interesting is the magnitude $|\gamma|$ that yields values of $\langle 0;1 \rangle$ describing a level of similarity of the window in the interferometrical time delay. Number 0 would mean absolutely decorrelated pixels that cannot indicate any proper information about the observed terrain. However, practically there are always higher values since this definition of coherence overestimates the cross-correlation between the two images, as stated in (Lauknes et al., 2008).

Changes of geometrical settings (rotation, movement etc.) of reflecting objects with regard to acquiring satellite position or any other change that would cause their different scattering, in the same way as changes in satellite view angle will cause a loss of coherence. The sources of the scattering stability decrease are called decorrelation sources - see Section 2.5.4. Stable scatterers, usually in urban areas, will have a high coherence and they are the most suitable targets for interferometry processing.

2.4.2.1 Sensitivity for Moisture

In (Zhanga et al., 2008), authors inspected the coherence of ERS-1 interferogram between images of dry period and a time close after heavy raining and compared to a model of soil moisture difference between these periods. As a conclusion, it was proven that the coherence is lowering dramatically when the moisture difference is increasing. With a 10 % moisture increase the coherence of the affected pixel drops down to 20% in average. This seems valid for any type of surface (note that urban areas were excluded from the investigations due to impossibility to model moisture in these areas; urban areas remained of high coherence over 45%). This coherence loss can be used with an advantage to detect and monitor flooded areas or wetland activities.

It seems that the soil moisture affects only amplitude of SAR image, the reflectivity changes due to significant difference in dielectric properties between dry soil ($\epsilon_r \sim 6$) and liquid water ($\epsilon_r \sim 80$); this is best observable in L-band that is most sensitive for moisture (Barrett et al., 2009). Within the phase values, the soil moisture is biasing indirectly. According to (Barrett et al., 2009), the increase of soil moisture is causing a slight uplift, observable by the phase difference. This is based on a hypothesis that increases and decreases in water content causes an expansion or contraction of the soil. It is disputable if the uplift caused by soil moisture is a subject of removal by using some kind of soil moisture model or measurements because this is a real elevation change anyway. But these even centimetre order elevation changes can induce a difference of MT-InSAR deformation estimations against levelling measurements that are applied on stable levelling points.

2.5 Limits of SAR Interferometry

It is not a simple task to properly extract an information about a terrain deformation from the InSAR phase difference. The most of the unwanted/noise phase contributions according to Eq. (2.4.3) are removed within DInSAR techniques, leaving hopefully only $\Delta\varphi_{defo}$ together with another unwanted $\Delta\varphi_{atmo}$ contribution which can be subtracted using more sophisticated methods (see Section 2.5.5). In the reality, phase residuals are still a part of the total phase difference. This is to investigate their sources. A detailed investigation was performed in (Hanssen, 2001) – after 10 years, the basic principles and error contributions remain unchanged.

For each error source an example of its influence will be showed, if possible to estimate systematically. In this example, a configuration of Envisat with parameters of Table 2.3 will be used. The angles θ_{look} and θ_{inc} will be commuted for the sake of simplicity as some central value, their real difference however can be around 4° for ERS (Hlaváčová, 2005) in reality, caused mainly by Earth curvature and a land topography. That means that after a correction to the flat Earth using orbit data and removing the topography phase using DEM, the differences will really fuse resulting in $\theta_{inc} = \theta_{look}$.

The computed errors $\Delta\varphi$ are related to the final phase difference. This can be recomputed to a length measurement in the satellite line of sight (LOS) to achieve their error influence on the final deformation estimation. One 2π cycle describes a length λ of a wave that had to travel from the satellite to the terrain and back. A deformation itself will therefore propagate into the phase measurement two times, thus the error $\Delta D = \Delta\varphi / 4\pi \cdot \lambda$.

Table 2.3 – Example of SAR configurations used to validate DInSAR error sources

sensor	f_0 (GHz)	λ (cm)	B_{perp} (m)	R (km)	$\theta_{look} \simeq \theta_{inc}$	B_R (MHz)	B_A (kHz)
ERS/Envisat ASAR	5.3	5.6	100	870	23°	15.5	1.36
Alos PALSAR	1.27	23.6	1000	850	34.3°	28	1.7
TerraSAR-X	9.65	3.1	100	610	32.5°	150	2.2

Talking about theoretical detection limits of a deformation, this can be estimated for a satellite LOS direction using a maximal detectable phase gradient B_R/f_s (Hanssen, 2001), where f_s is a range sampling frequency:

$$\Delta D_{LOS,crit} = \frac{B_R}{f_s} \cdot \frac{\lambda}{\Delta_{slant,s}} = \frac{B_R}{f_s} \cdot \frac{f_s \lambda}{c} = \frac{B_R}{f_0} \quad (2.5.1)$$

This will mean that (with a theoretical coherence of $\gamma = 100\%$) it is possible to enumerate the detection limits of LOS deformation for each satellite in Tab. 2.3 as $\Delta D_{Envisat} = 2.9 \text{ mm/m}$, $\Delta D_{Alos} = 22 \text{ mm/m}$ and $\Delta D_{TSX} = 15.5 \text{ mm/m}$. If the deformation is steeper the phase will decorrelate totally.

2.5.1 Orbit Errors

Orbital satellite ephemerides are satellite state vectors that should precisely describe position and velocity in any time during the satellite flight. They are necessary for InSAR at least to determine the interferometric baselines. Their precision differs by different computation techniques - to fully correct the residual interferometric fringes, their accuracy should be in the order of mm. Usually a precision in the order of several cm is achieved. More detailed information about orbits and their influence on the interferogram quality can be found in (Hlaváčová, 2005).

The residual phase from the (flat-Earth) reference phase $\Delta\varphi_{ref}$ is fully related to the precision of the orbit data. Any imperfection causes an error in estimation of baselines B_v , B_h and B_{perp} which will result in residual fringes (Hlaváčová, 2008):

$$\Delta\varphi_{ref}^{res} \simeq \frac{4\pi}{\lambda} (\Delta B_h \sin \theta_{look} - \Delta B_v \cos \theta_{look}) \simeq \frac{4\pi}{\lambda} B_{perp} \quad (2.5.2)$$

Envisat Example An error of $\Delta B_{perp} = 0.1\text{m}$ will yield a residual of a reference phase of around 22 rad which corresponds to a displacement error of around $10 \text{ cm}/2\pi$. However, orbit errors in flat-Earth correction will propagate in the interferogram image regularly and it is usually possible to estimate and remove them by finding the proper phase changing trend. Typically, with the latest orbit data precision, the baseline determination error achieves such phase error that corresponds to a displacement error in order of tenths of millimetre per neighboring pixels which can be neglected (Ketelaar, 2009).

Similarly, errors caused by the orbit inaccuracy will propagate also into topography subtraction, together with DEM errors - see Eq. (2.5.3). In this case, the error doesn't get so significant as for the flat-Earth removal.

2.5.2 DEM Errors

Effect of a residual topographic signal can be described as modified from (Hlaváčová, 2008; Manunta, 2009):

$$\Delta\varphi_{topo}^{res} \simeq \frac{4\pi}{\lambda} \left(\frac{B_{perp} + \Delta B_{perp}}{R \sin \theta_{inc}} \Delta H_P \right) \quad (2.5.3)$$

Envisat Example An error of $\Delta H_P = 5\text{m}$ will yield an error of 0.3 rad (1.5 mm error in deformation estimation) if $B_{perp} = 100 \text{ m}$ but the error would be 2 rad (i.e. $D_{LOS} = 9 \text{ mm}$) if $B_{perp} = 600 \text{ m}$.

The effect of topography is dependent on the perpendicular baseline of computed interferogram. With a very small perpendicular baseline up to several meters, meaning

the satellite is scanning both images from almost the same spot in some time delay, there will be a very small or negligible stereoscopic effect. This is an optimal configuration for deformation monitoring. The phase contributions by topography can be removed by using a DEM, converted to SAR coordinates as a simulated phase with the same height ambiguity as in the interferogram.

The most popular DEM model for this topography removal is the global SRTM from year 2000 with a resolution of 90 m (in Europe) and vertical accuracy that should be better than 15 m (with some 90% coverage within a tolerance of 5 m). Because the used SAR data are usually of a higher spatial resolution (ESA SAR sensors of approximately 30 m), it seems to be necessary to use a more detailed DEM for topography removal. Another global ASTER GDEM of 30 m resolution may be chosen but because of its technological limits the vertical accuracy is lower, up to around 25 m, with a small confidence over vegetated areas. A more-pass DInSAR method can be applied creating own DEM model directly from SAR images that lead to the same resolution and characteristics as the final deformation map but affected by errors from temporal decorrelation. In areas where the SRTM DEM is updated by radar altimetry data, the ACE2 DEM model can be a more suitable DEM choice than SRTM. In areas without high mountains, SRTM/ACE2 is practically precise enough. Of course a local DEM (e.g. from levelling) achieves much higher accuracy and is often preferred.

Another DEM subtraction is performed during a multitemporal InSAR processing which algorithms are able to estimate the topography residuals quite precisely and remove them as so-called spatially correlated errors.

In case of the maximal B_{perp} for ESA satellites as the Envisat ($B_{perp,crit} \simeq 1200$ m) the height ambiguity (an elevation change that will propagate as one 2π fringe in the interferogram) is computed using Eq. (2.5.4) as $H_{amb} = 8.5$ m, while for commonly used pairs of images of less than $B_{perp} = 500$ m the height ambiguity is higher than 17.5 m. This indicates that it is not necessary to use a very precise DEM for topography removal in shorter B_{perp} configurations, especially in areas with not very high terrain gradients.

$$H_{amb} = \frac{\lambda}{2} \cdot \frac{R \sin \theta_{inc}}{B_{perp}} \quad (2.5.4)$$

The graph plotted in Fig. 2.5.1 shows the distribution of H_{amb} per a pixel with different B_{perp} . It would be possible to estimate a needed precision of DEM used for a proper topography removal for different B_{perp} configurations of the chosen SAR satellites. This kind of estimation, after relating to the same resolutions, would be still coarse, depending on actual terrain geometrical properties.

There is another phase contribution that is in a relation with the topography. The atmospheric phase delay is caused by vertical atmosphere inhomogeneity at low altitudes, this may result in fringes appearing to correspond with the topography (Ge et al., 2001).

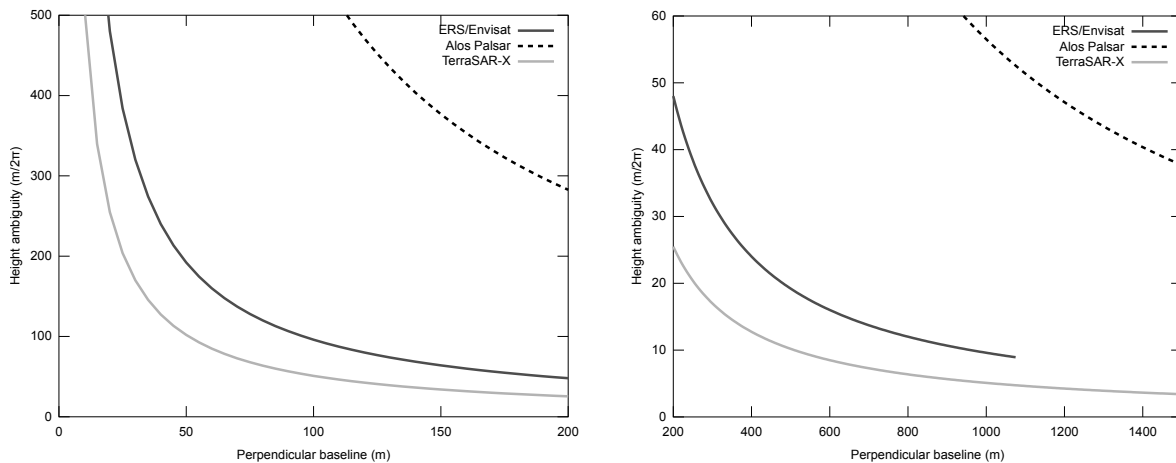


Figure 2.5.1 – Relation between height ambiguity and a perpendicular baseline

2.5.3 Processing Errors

Amongst other processing errors that are mentioned as a processing decorrelation (Section 2.5.4), I want to highlight two processes that still cause significant problems in the actual InSAR processing. These are:

- Phase unwrapping - this procedure is very sensitive for input errors. It depends on the used algorithm. Anyway every incorrect phase unwrapping estimation would yield an error in final deformation estimation of an integer multiply of 2π ,
- Georeferencing - to georeference InSAR results into some global coordinate system, such as the geographic WGS-84, precise orbits can be used. However because of a presence of SAR geometry distortion as introduced in Section 2.2.2.3, errors in ground and height estimation from range direction, orbit inaccuracies and usually a coarse SAR ground resolution of pixels, this task is affected by significant errors.

Practical Notes

Both these techniques yielded too large errors in the result, so in the processing described in Chapter 3 I haven't used phase unwrapping (since the subsidence can be observed even from the wrapped phase) and in many cases the georeferencing had to be performed by a manual ground control points (GCP) matching to achieve an appropriate precision.

2.5.4 Decorrelation

Effect of decorrelation can be described as a noise that cause a loss of coherence. Again, the decorrelation is explained in various works, together with its influence on the phase standard deviation, e.g. in (Hanssen, 2001).

It is possible to distinguish the decorrelation error sources and describe them mathematically. Then the total coherence can be computed as a multiplication of their mathematical representations:

$$\gamma_{total} = \gamma_{therm} \cdot \gamma_{geom} \cdot \gamma_{DC} \cdot \gamma_{vol} \cdot \gamma_{proc} \cdot \gamma_{temp} \quad (2.5.5)$$

2.5.4.1 Thermal Decorrelation

γ_{therm} can be derived as $\gamma_{thermal} = 1/\sqrt{(1 + SNR_M^{-1})(1 + SNR_S^{-1})}$ using a signal-to-noise ratio of a SAR system $SNR = \text{signal power}/\text{power of noise}$ that is mostly SAR sensor dependent.

This noise is induced by the device itself, it is dependent on the device detection limits. The coherence will lower if a normalized radar cross section σ_0 (see Section 4.4.1) of illuminated area is approaching the sensor detection limit. For ERS detecting area with $\sigma_0 = -20\text{dB}$, then $\gamma_{thermal} = 0.85$ (Hanssen, 2001).

2.5.4.2 Geometric Decorrelation

γ_{geom} is caused by large differences in incidence angles θ_{inc} of both master and slave acquisitions. The main factor here is a B_{perp} that will cause too different θ_{inc} . Mathematically it can be computed as

$$\gamma_{geom} = \left| \frac{B_{perp,crit} - B_{perp}}{B_{perp,crit}} \right|, \text{ for } |B_{perp}| \leq B_{perp,crit}$$

$$\gamma_{geom} = 0, \text{ for } |B_{perp}| > B_{perp,crit}$$

A critical $B_{perp,crit}$ causes a spectral shift equal to the signal frequency bandwidth B_R (then the backscattered frequencies don't match and cannot be combined). This is when $B_{perp,crit} \simeq 1200\text{m}$ for ERS/Envisat satellites and a flat terrain. It is possible to compute the critical baseline with regard to the topographic slope α as shown in Fig. 4.3.1: $B_{perp,crit} = \lambda/2 \Delta_{slant} R \tan(\theta_{look} - \alpha)$, from (Franceschetti et al., 1999).

The slope facing away from the satellite should be affected less by B_{perp} while facing towards the satellite will achieve a zero coherence in much smaller B_{perp} , as described in (Hanssen, 2001) and according to the plot in Fig. 2.5.2. The coherence decreases linearly with B_{perp} approaching the $B_{perp,crit}$. Note that with shallower look angles of Alos Palsar and TerraSAR-X together with their other parameters (see Tab. 2.3) the tolerance for critical B_{perp} is much higher. For slope angle $\alpha=0$ (flat terrain) the $B_{perp,crit} = 12.8\text{ km}$ for Alos Palsar in fine mode with single polarisation and $B_{perp,crit} = 6\text{ km}$ for TerraSAR-X in a standard stripmap mode.

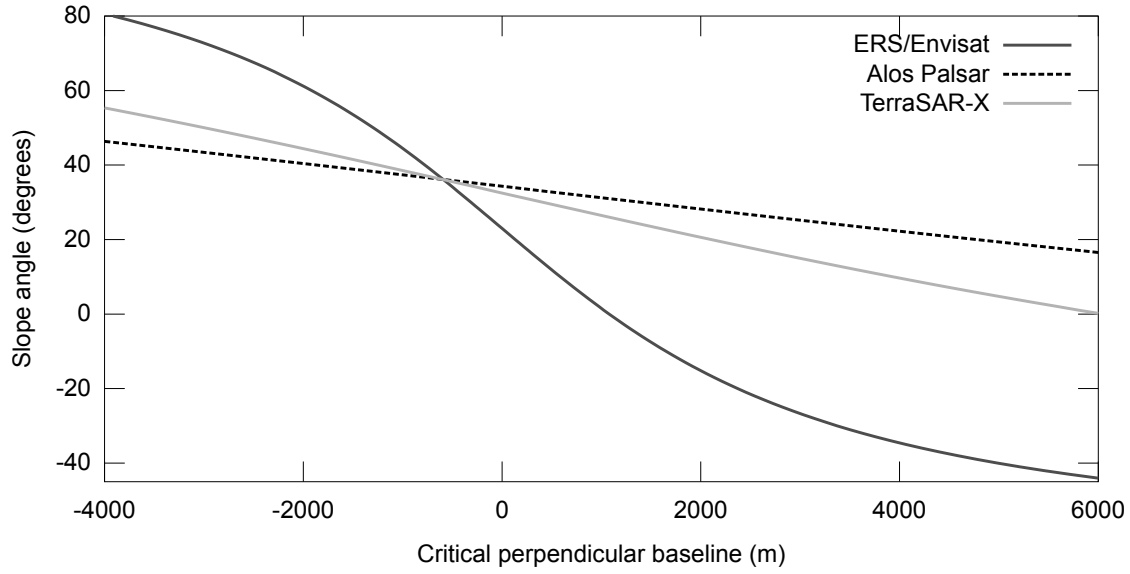


Figure 2.5.2 – Decorrelating effect of a critical perpendicular baseline with relation to the illuminated slope lift.

2.5.4.3 Doppler Centroid Decorrelation

γ_{DC} is an azimuth equivalent to γ_{geom} . It is related to a difference in Doppler centroid frequencies Δf_{DC} :

$$\gamma_{DC} = |1 - \frac{\Delta f_{DC}}{B_A}|, \text{ for } |\Delta f_{DC}| \leq B_A$$

$$\gamma_{DC} = 0, \text{ for } |\Delta f_{DC}| > B_A$$

, where B_A is the azimuth direction bandwidth.

Important is that this will be of concern in large Doppler centroid variations, i.e. in MHz, caused by differences in squint angles (see Fig. A.2.1). This is not the case of yaw steered satellites but it needs to be taken into account e.g. for Radarsat-1 or ERS-2 after its gyroscopes failure in 7 February 2000.

Note that this approach describes only γ_{DC} in the azimuth direction. The Doppler centroid differs also in range, due to differences in incidence angles plus factors as satellite velocity, Earth rotation in the range direction. This is not accounted here but its influence is described e.g. in Section 4.6.3 of (Franceschetti et al., 1999).

2.5.4.4 Volume Decorrelation

γ_{vol} is related to the penetration of the radar waves, it depends on the used radar wavelength and the scattering medium. This is more described in (Hoen et al., 2000).

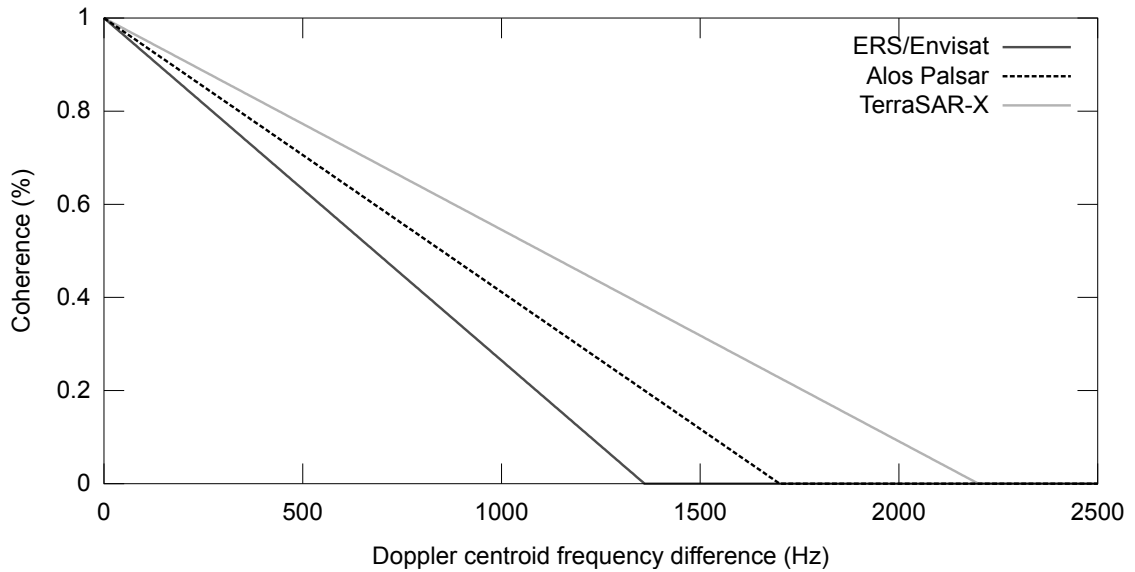


Figure 2.5.3 – Decorrelating effect of Doppler centroid frequency differences

2.5.4.5 Processing Decorrelation

γ_{proc} means errors due to such procedures as an image pre-processing, errors due to misalignments after coregistration, interpolation errors in the resampling phase and similar. According to (Franceschetti et al., 1999), in coregistration procedure, the complete decorrelation is generated when the misalignment equals resolution dimensions, while an error of 1/20th of the resolution cell generates $\gamma_{proc} = 0.996$.

2.5.4.6 Temporal Decorrelation

γ_{temp} is caused by scattering changes of objects in a resolution cell in time - this can be their physical change (movement, rotation of scatterer) or a change in dielectric properties (e.g. increased moisture after a rain, decorrelation due to snow cover). This decorrelation term is especially significant in vegetated areas.

Obviously a shorter temporal baseline between acquisitions will not be affected by γ_{temp} much - or when matching same seasons of the year, as depicted in Fig. 3.3.2. Temporal decorrelation times can be as long as months to years for arid terrain and as short as several hours to several days for rainy and/or forested areas.

2.5.5 Atmospheric Effects

Atmospheric disturbances $\Delta\varphi_{atmo}$ are caused by a time delay of radar echoes caused by a different refraction index of the atmosphere. Microwave signals emitted by satellites passing through the atmosphere are being mainly affected by its two components, troposphere (layer up to ~ 20 km) and ionosphere (higher than ~ 90 km). Other layers of atmosphere also affect microwave signals, but their effects are very small and normally not taken into account.

Phase shifts due to homogenous atmospheric delay produce additional interferometric fringes of a large scale, that are easily distinguishable from other phase contributions. But in case of high variations, mostly caused by temporally variable water vapour in troposphere, these phase shifts can be eventually misinterpreted as a deformation.

In general, the phase delay of radar wave through the troposphere depends on air temperature, pressure and the partial pressure of water vapour. The phase change caused by atmospheric water vapour can be exchanged for terrain deformations and cause large errors in differential interferogram, in order of *decimetres*. Even that SAR images are not so sensitive for precipitation, it still can change the phase significantly. A heavy torrential rain could cause a delay of the signal in the maximum amount of *several cm* in C-band data (Solheim et al., 1999). Table 2.4, adapted from (Li, 2005), summarizes common atmospheric effects on phase measurements.

Table 2.4 – Phase induced by delays through different atmospheric conditions

Delay source	Max. delay (mm/km)	Delay source	Max delay (mm/km)
dry air	290	haze	0.02
high water vapour	140	drizzle	0.2
low water vapour	15	steady rain (<20 mm/h)	2
cloud	8	heavy rain (<200 mm/h)	11 (C-band)
advection fog	0.3	hail	~ 5 (C-band)
volcanic ash	0.01	snow	~ 1 (C-band)
sand	18	aerosols	0.1

Note Tropospheric refraction delays can be induced also by aerosols and volcanic ashes. This fact may be significant in the Northern Moravia region since this region struggles from an excessive air pollution by small particles and dust. On the other hand, the aerosols/ashes can induce a zenith wet delay of some 0.01 mm/km (Solheim et al., 1999) which is too small value. To have a significant impact on the radar delay, the particles should be of a size around 1 mm, as it is for sand that can cause a delay of up to some 18 mm/km.

The radar phase delay depends on the refractivity index N of the atmosphere, for the needs of InSAR it can be computed for a height difference between points P and Q for times of acquisitions in M , S (Hanssen, 2001) as

$$\varphi_{P,Q} = \frac{4\pi}{\lambda \cdot \cos \theta_{inc}} 10^{-6} \int_P^Q (N_M(z) - N_S(z)) dz \quad (2.5.6)$$

The refractivity index N changes in each height component dz where the delay is caused by pressured molecules of the air, this can be named as a hydrostatic (dry) delay, and by passing through the air water vapour with a different pressure, a wet delay. These delays are changing in the vertical direction - they vary most in lower heights, up to some 5 km (Hanssen, 2001). Their total sums in the zenith direction are known as a zenith hydrostatic delay ZHD and zenith wet delay ZWD. We can also maintain a zenith ionospheric delay ZID. Both ZWD and ZHD are induced mainly within the troposphere and their general variations are very seasonal (Doin et al., 2009).

$$\sum N(z) = ZHD + ZWD + ZID \quad (2.5.7)$$

The wet and dry components of index N can be computed mathematically (Delacourt et al., 1998), some model of temporal variations related to the actual place on Earth, such as from (Baby et al., 1988), can be used with a high reliability for dry hydrostatic delay contribution. A precise computation of both ZWD and ZHD on place can be achieved by GPS meteorology, see further.

Apart from the GPS meteorology technique it is possible to mitigate and correct phase changes due to atmospheric water vapour using water vapour measurements or computed models. In (Li et al., 2008), a valuable method using Envisat MERIS and Terra MODIS data is demonstrated improving DInSAR results significantly. In the approach of using interferometric stacks or in permanent scatterers analysis, the phase variation due to atmospheric effects can be isolated from multiple interferograms. In particular, for large numbers of interferograms, the atmospheric effects can be identified as a random process over time and thereby separated from other contributions to the interferometric phase.

2.5.5.1 Stratified Tropospheric Delay Estimation

As shown in Tab. 2.4, the strongest impact on radar wave phase in troposphere is caused by a dry air pressure and a water vapour. While the water vapour is highly variable in space and time, the dry air pressure changes slowly during seasons of the year. It is well known that the air temperature and pressure varies with elevation in a radar scene. This correlation can be modelled.

The term of ZWD is mostly unpredictable and can be approximated only coarsely with regard to a water vapour pressure and temperature, that both change with elevation also. The unpredictable variations of ZWD shouldn't be disregarded, since it causes a trend related to the terrain elevation that is about two times higher than in the ZHD case. A mathematical apparatus of the same basis for this estimation of ZHD and ZWD is presented in (Delacourt et al., 1998; Doin et al., 2009; Puysegur et al., 2007).

Using this apparatus it should be possible to approximate the stratified tropospheric delay that can be relatively precise, in case of no turbulent effects in the atmosphere. The only inputs will be an elevation, a surface temperature, pressure and humidity on place in the time of acquisitions.

2.5.5.2 Tropospheric Delay Estimation using GPS Meteorology

Troposphere is a non-dispersive medium for radio waves at frequencies less than 15 GHz which means that the value of signal delay will be the same for the GPS and InSAR signal. It allows the usage of GPS system derived values of atmospheric delay as a source of atmospheric corrections for InSAR images. The troposphere affects microwave signals in two ways. First, the signal bends in response to gradients in the index of refraction of the atmosphere, travelling a curved path instead of a straight line. Second, the waves travel slower in a region of finite density than they would in vacuum. Sum of those two components is a total delay of the wave.

Zenith total delay (ZTD) is a total delay of the signal caused by the troposphere in the zenith angle above the particular place. Its value is typically about 2.5 m at sea level and standard atmosphere conditions. This total delay can be also separated for described purposes into a large quantity which is caused by the hydrostatic part of the atmosphere ZHD and a smaller (but more variable) quantity caused by the wet part of the atmosphere ZWD.

The hydrostatic part is dependent mainly on the surface pressure and the temperature and the wet part of the water vapour (Bevis et al., 1992). The result of GPS data processing is the ZTD value. The ZHD can be calculated from ZTD if values of atmospheric pressure and temperature are available. Then, $ZWD = ZTD - ZHD$.

For InSAR correction the ZWD is essential because it has huge time and spatial variability, contrary to ZHD. While the change of ZHD between two InSAR images can be negligible at one place, the ZWD can vary significantly and it is what really limits the accuracy. Typical values of ZWD at sea level vary from 1 cm to 45 cm (Solheim et al., 1999).

When standard atmosphere conditions are held, the atmospheric pressure, temperature and amount of water vapour in troposphere decrease with increasing altitude, which also cause decreasing of ZTD. Successful modelling of impacts of the turbulent mixing of water vapour in lower troposphere was demonstrated by (Li et al., 2006a; Song et al., 2008).

2.5.5.3 Effect of Ionosphere

The ionosphere is a dispersive medium for microwave signals so the influence on delay is frequency dependent. The effect of ionosphere is increasing with the increasing wavelength. The signal from C-band will be less influenced than from L-band. Of course the magnitude of ionospheric delay is strongly dependent on the amount of solar radiation which is time and spatial variable (Gray et al., 2000).

Typical minimal value of ionospheric delay for C-band is 1 cm and maximum about 100 cm. The L-band is influenced about 4-16x more, therefore it is beneficial to correct

L-band interferograms by using some kind of ionosphere measurements or model, it is even possible to correct this impact partially by mathematical processing, as shown in (Meyer et al., 2008).

Ionospheric effects are large scaled, they cause phase distortions in distances larger than 100 km, sometimes also around 1 km streaks can be observed in azimuth direction (Gray et al., 2000).

Note The ionosphere variability over the middle part of Europe is very low, therefore no compensation is needed at all neither for L-band processing in this area regarding ionosphere impact.

2.6 Multitemporal SAR Interferometry

2.6.1 Introduction

Since the DInSAR leads to achieve an image of terrain changes between two acquisitions in some time delay, it still copes with such problems as an atmosphere-pass phase induction, errors of external data (orbital data, DEM) or a decorrelation. It is possible to minimize the effect of some error sources by processing more radar images in a stack. For example, to understand the land movement in a large time delay, it is possible to create differential interferograms of a shorter temporal difference, that will not be affected by a decorrelation so much, and then to combine them in time order to achieve a full time scale model of deformations. Because a physical character of observed objects will cause a high variance of phase measurements in time and from various angles, only a subset of pixels representing stable radar wave scattering objects through the whole stack are used in praxis.

In fact, this process is more complicated because of various error sources during processing of each interferogram. Most of them can be filtered using the stack processing. If a sufficiently high number of interferograms is used to combine together, it is possible to denote too distinct values that may be filtered out or to form a trend model of atmosphere induction (that is temporally very variable, in comparison with a continuous deformation trend), so-called atmospheric phase screens (APS). Several methods have been developed to carry out this processing idea. They differ mostly in the way of selecting the proper pixels that will be used for the terrain change investigation. As basic techniques that are used in multitemporal processing, the Persistent Scatterers Interferometry method and methods known as Small Baselines techniques should be mentioned.

In the end, the multitemporal InSAR (MT-InSAR) processing will result in a set of points with estimated movement in a high precision. As was stated in (Komac et al., 2007), for a typical ERS interferogram with $B_{\text{perp}} = 300 \text{ m}$ a deformation can be estimated with a precision of 2.8 mm, but if used in a MT-InSAR stack, this accuracy of deformation estimation will be enhanced to around 0.1 mm/year (depending on quantity of acquisitions and a density of detected points).

2.6.2 Methods of Multitemporal InSAR

2.6.2.1 Persistent Scatterers Interferometry

As a first revolutionary multitemporal InSAR method, the Permanent Scatterers Interferometry (PSI) method has been patented by a Polimi University in Milan in the late 1990s (Ferretti et al., 2000) and nowadays is being improved in many of its original aspects. Some of too different versions have been promoted to a new method (Hooper et al., 2004; Kampes, 2005; Werner et al., 2003), but the basic principle remains almost the same.

In this method, the algorithms search for the pixels that scatter the radar beam with the same (permanent) intensity within all the images in a stack, because these pixels provide the most stable phase information. Physically it can be some rocks, roads, bridges, building corners etc. - therefore it is very valuable for using mainly in urban areas. For ground resolution elements containing such permanent dominant scatterer, the phase is not decorrelated at all even in very disadvantageous InSAR configuration. While if no dominant scatterer is present, the phase of the pixel will be summed of contributions from all smaller (distributed) scatterers that is very sensitive to decorrelating factors. Because the method of PSI selects only highly coherent pixels, it can reconstruct a meaningful deformation series even from interferograms that are highly overall decorrelated and disregarded for an interpretation using DInSAR.

In PSI one radar image with the most optimal configuration, with regard to the whole dataset in the means of time, satellite position and look angle, is selected as a master image. All the other images, denoted as "slaves", are used to form interferograms with this common master image. To achieve reliable results, at least around 25 SAR images should be provided. A computation of all possible differential interferogram combinations resampled to the common master image is performed then.

Combinations may be limited by choosing some maximal applicable temporal or Doppler centroid baseline. Since the permanently scattering objects are usually stable in a high variety of incidence angles as well as in time, also high baselines can be used, exceeding critical limits for DInSAR, for example $B_{\text{perp,max}} \simeq 1500 \text{ m}$ for ERS/Envisat, maximal Doppler centroid can be $B_{\text{Dop,max}} = B_A$ (where for ERS the azimuth bandwidth $B_A = 1380 \text{ Hz}$) and $B_{\text{temp,max}} = 15 \text{ years}$, all according to (Ketelaar, 2009). However still it is recommended to use data of a maximal Doppler centroid frequency difference $B_{\text{Dop,max}} = B_A/2$ and a shorter temporal and perpendicular baselines to increase PS density.

The PSI processing itself is performed using following steps, in general, as used in TU Delft implementation of PSI as a Delft Persistent Scatterers Toolbox software (DePSI). Note that the word *persistent* achieves the same meaning as *permanent*:

- searching for *persistent scatterers candidates* (PSCs) over the scene. The candidates are found as pixels with a value of an amplitude dispersion within all scenes that is smaller than a threshold (this ensures a stability of temporal phase behaviour over the whole data stack). To compare the magnitudes/amplitudes between the scenes, they must be radiometrically corrected first, so the pixel values will be directly related to the radar backscatter of the scene, without any radiometric bias. For a radiometrical correction a mathematical pseudo-calibration was proved to achieve sufficient results

(Ketelaar, 2009). In the initial step, only most stable pixels of a very low amplitude dispersion are selected,

- computation of phase *double-differences* of each PSC point of the initial PSC spatial network. Because of the wrapped phase observations, a meaningful interpretation of the DInSAR stack is achieved only based on both temporal and spatial (double) differences with regards to the common reference time (master scene) and a reference point. To enhance reliability of phase unwrapping and to detect erroneous PS candidates, several local reference points can be used that are connected into a Delaunay triangulated network, instead of relating all the pixel differences to only one reference point (with increasing distance, these differences can be more affected by errors from atmosphere or orbit residuals),
- estimation of *error phase screens*. That means to estimate several unknown parameters that represent an atmospheric delay, DEM error, orbit errors, noise and remove them from the phase information to achieve only a deformation part. This estimation is done iteratively by one of statistical models, e.g. periodogram. After each iteration the data are compensated for the new estimation. If the computed phase is not regarded as reliable enough (it has to follow a supposed trend), the processed PSC will be eliminated,
- *densification of PS network*. More pixels of a higher amplitude dispersion are selected and again tested for reliability. They are chosen relatively to the first order PS network (chosen PSCs). Then the error screens are estimated again.

In the end, a deformation model is created with a result of pixels representing the values of a subsidence rate in the precision of a mm/year. The result is a data file containing points with a rate of subsidence velocity, with every source of noise, if possible, filtered out. One of the dangers of non-reliability of the results are the phase unwrapping errors in situations where the land deformation of an interferogram pixel is higher than a detectable value (a half of radar wavelength per pixel).

2.6.2.2 Methods of Small Baselines

While in PSI the objects of interest are dominant scatterers that don't change its scattering character in time and that scatter similarly when viewed from slightly different angles, other methods exist that increase the amount of detected pixels that may not be as stable as these PS. These methods are based on processing of smaller stack subsets with lower baselines, so they can detect pixels that would be decorrelated if viewed from too different angles (caused by large perpendicular baseline) etc. A general name of these methods can be a Small Baselines (SB) processing.

The main principle of SB methods is that the whole stack of acquisitions is divided in several subsets of small baselines (perpendicular, temporal and Doppler centroid), without any common reference image. Then these subsets should be connected with some algorithm to merge the detected points and estimate a deformation rate for all of them with regard to a common reference in time and space. In comparison with PSI that searches for pixels

containing some dominant scatterer, pixels with phase that decorrelates only little in the whole dataset are the main targets.

The SB techniques are useful especially for areas where there are not many persistent scatterers available, like non-urban areas. By forming interferograms only between images separated by a short time interval and with a small difference in look and squint angle, decorrelation is minimized and for some resolution elements it may be small enough so the underlying signal is still detectable. With a short perpendicular baseline also a DEM error effect is lowered. Decorrelation is further reduced by spectral filtering in range and discarding of the non-overlapping Doppler frequencies in azimuth. On the other hand, this filtering leads to increase of the decorrelation of strongly scattering pixels, due to the reduced resolution (decorrelated phase from neighbourhood contribute to this dominant reflection).

This method can be used as complementary to the PSI method, as it has been (with a modified approach) implemented in the StaMPS software (Hooper, 2008), increasing the number of processed pixels. More detailed description of the original Small Baselines Subset (SBAS) method can be found in (Berardino et al., 2002). Also other approaches exist that were designed for specific purposes, such as for monitoring of rock slides that doesn't show so stable reflection to be detected as PS (Lauknes et al., 2008) or an analysis of a very short temporal baseline to apply in wetlands with a fast water level variance (Wdowinski et al., 2008).

2.6.2.3 Problems and Limitations

The multitemporal InSAR methods in general can unveil subsidence of a mm scale per a very long time period. With these methods it is possible to remove many sources of unneeded noise due to atmospheric artifacts, DEM and orbital errors in a quality that is not possible using only two images formed by DInSAR. Using modern algorithms it is possible to achieve almost real estimation of land deformation trend.

Unfortunately it seems to be too sensitive to achieve a real trend in case of a fast subsidence that exceeds the pixel phase detection limits (half of carrier wavelength). This is related to phase unwrapping issues, mostly in cases of a sparsely sampled deformation areas. Phase unwrapping algorithms cannot reconstruct the wrapped phase properly if the phase of neighboring pixels differ for more than π . In many cases, the affected area has MT-InSAR points detected in a large distance. In such case a fast deformation cannot be estimated correctly, however it could be evaluated if a high spatial sampling of these stable points is achieved.

Another problem can be a relativity in deformation mapping. Every deformation is measured as relative to some reference point that should be stable in the whole time series. If the reference point is also affected by deformation, its phase change in time is transferred as an error value into all detected pixels of interest (e.g. PS points).

Also, in an atmospheric phase screen (APS) estimation principle there is a possibility that also a part of deformation can be accidentally removed. The APS is formed under assumption of a large-scale phase difference signal that is spatially correlated, but not correlated in time (atmospheric change happens uniquely in each interferogram). If a deformation will occur only in one interferogram or in some time it will largely deviate

from its temporal trend behaviour, it can be misinterpreted as an atmospheric artefact (or another spatially correlated error). In opposite way, atmospheric effects that are (by chance) temporally correlated can be misregarded as a deformation - this is a problem in specific places like coast areas or areas with the same seasonal atmospheric conditions.

To properly estimate APS, minimally 3-4 PS/km² should be detected.

2.6.2.4 Coherence Matrix

Coherence matrix (CM) is an instrument that describes the behaviour of a chosen reference pixel in all the images time series. Every line of the matrix shows the coherence between the pixel in the master image and the same pixel in all the other images, usually sort by time. The information taken from the matrix is used with advantage to weight the images potentials to create proper interferograms or to compute a more precise velocity of deformations evolution etc. For example it improves the PSI technique results by carefully weighting each image contribution by the means of the sample covariance matrix. Its usage results in overcoming some of the PSI technique limitations, i.e. that the pixel reflectivity must remain the same in *all* the images to be detected as a PS pixel.

According to (Ferretti et al., 2000), the actual CM technique works as a PSI post-processor. After the PSI processing of series of SAR images coregistered on a common master image, a Maximum Likelihood algorithm estimates the fine elevation and a line-of-sight deformation velocity from the given complex observations and their covariance matrix. If used within the scope of this thesis, this technique could enhance the MT-InSAR results. It is planned to be implemented and tested in a future work.

2.6.3 StaMPS Processing Techniques

Stanford Method for Persistent Scatterers (StaMPS) is an interesting approach for a multitemporal InSAR processing where (Hooper, 2006) modifies the original PSI technique by own ideas and adds a method for Small Baselines processing, to achieve an instrument capable for multitemporal monitoring of non-urban areas. The technique is also available free of charge as an open-source (although its scripts use various toolboxes of Matlab®). It uses ROI_PAC for focusing raw SAR data and Doris for forming differential interferograms. Nowadays, various projects exist that incorporate other original ideas to improve the StaMPS processing.

In comparison with the original PSI technique that uses only an amplitude dispersion index to choose PS pixels, the StaMPS implements a PS selection by the pixel phase stability in time. Thus also more lower but stable scattering pixels can be detected which has advantages in the areas without artificial objects. In usual PSI techniques also the phase differences of detected pixels are investigated as deviations from the main temporal model that is supposed to properly describe the deformation trend. StaMPS estimates the deformation rate without any a priori information.

Because of its flexible design, much less interferograms can be formed to achieve reliable results than in similar methods. Here, 12 interferograms should be sufficient while in a very optimal case also a stack of only 4 interferograms can be evaluated.

2.6.3.1 Forming of Differential Interferograms

Although StaMPS uses Doris for DInSAR processing, also some differences from the classical approach exist. To avoid high geometrical decorrelation, StaMPS uses a coregistration algorithm that applies an amplitude based method to estimate offsets in position between pairs of images with a good correlation. For PS processing, also combinations of very high baselines can be formed. Within such combinations, a large decorrelation will cause a failure in a conventional coregistration method that uses an amplitude cross-correlation between two images. So, the principle of the new coregistration method is to estimate coregistration parameters only for small baselines combinations and then a relation to the master image is computed.

With this approach, combinations of large B_{perp} are really formed properly. Even that Doris is (since version 4.01) capable to coregister also using a DEM which makes master-slave coregistration possible even for long baselines, a (slight) coherence increase can be expected in the StaMPS coregistration approach for large B_{perp} .

2.6.3.2 Selection of Persistent Scatterers

The process of the StaMPS method of Persistent Scatterers (PS) is similar to other persistent scatterers techniques. The principle is to find pixels with a high phase stability. It means to search for points that are (almost) not affected by noise. Each differential interferogram pixel phase φ includes contributions due to a deformation φ_{defo} , atmosphere φ_{atmo} , topography residual φ_{DEM} , orbital errors φ_{orb} and noise (decorrelation) φ_{noise} . The noise is mostly due to the fact that every pixel contains more physical scatterers that have their own different phase contributions.

The mentioned phase contribution have their specific characteristics. The error φ_{DEM} caused by DEM inaccuracies, together with changes in look angle, is directly related to the perpendicular baseline - it can be estimated relatively easily and in a dm accuracy. All other contributions are varying in spatial dimensions, except for the noise (note that under this assumption, very local deformation can be lost - however this phase spatial variance threshold can be set in StaMPS).

The strategy of StaMPS in investigating the phase stability is to find such pixels where the $\varphi_{\text{noise}} \simeq 0$. For each investigated persistent scatterer candidate (PSC) pixel a small spatial radius (let's say, up to 100 m) will be formed. All the pixels within this radius are assumed to be biased by the same amount of $\varphi_{\text{defo}} + \varphi_{\text{atmo}} + \varphi_{\text{orb}}$, so, a difference between any of the pixels and the PSC will cause a removal of these parts and only a value of φ_{noise} can be read. If this term approaches zero (if its phase is stable) within all the interferograms in a stack, this PSC will be selected as a PS. Also a check for side-lobes will be performed afterwards.

Compared to the amplitude-based PS detection only in other conventional methods, StaMPS detects usually a higher amount of stable PS points in natural terrain. Using oversampled data, even several times more points are detected (Sousa, 2009), without a loss of quality due to side-lobes.

2.6.3.3 Phase Unwrapping Solution

After selection of persistent scatterers, a procedure of 3D phase unwrapping can take a place. There are two different original methods implemented here. The latest method, described in (Hooper, 2009), uses optimisation routines of Snaphu that help to solve problems of phase jumps.

In general, the phase unwrapping again can be successful only if the phase difference between the pixel's neighbours in any dimension will not exceed π . Sometimes it does because of $\varphi_{defo} + \varphi_{atmo} + \varphi_{orb}$ term. In these cases the interferograms are first filtered for long wavelength changes that are estimated as φ_{long} , then they are unwrapped and afterwards the long term φ_{long} is added back.

After a correct phase unwrapping, errors of PS pixels are removed. It is assumed that terms of $\varphi_{atmo} + \varphi_{orb}$ are not correlated temporally while φ_{defo} is. They correlate only spatially, varying in each interferogram. So this spatially correlated error term can be estimated by a high pass temporal and a low pass spatial filtering for each interferogram. Obviously, the most precise evaluation of the errors can be done for the master image since it will be present in every formed interferogram.

2.6.3.4 Small Baselines Processing

The Small Baselines (SB) principle is in fact similar to the PSI approach. All images are coregistered to one common master but only images that form short baselines B_{perp} , B_{temp} , B_{Dop} with the master are combined into interferograms. This way the decorrelation of all pixels will be much lower than in the PS case, more stable pixels can be detected, especially in non-urban areas. These interferograms are also spatially filtered before searching for phase stable pixels (note that this may on the other hand degrade present dominant scatterers). After processing, that is same as in PSI case, the pixel values are recomputed to a common reference time and space.

2.7 Summary

In this chapter, general issues concerning Synthetic Aperture Radar Interferometry were described - theoretical concepts of SAR as well as an overview of actual SAR satellite missions.

Practical limits of a differential InSAR were pointed out in Section 2.5. The deformation detectability depends on the SAR wavelength and resolutions. Most of described decorrelation sources are dependent on the geometrical configuration of the SAR satellite when taking

our acquisitions, i.e. perpendicular and temporal baselines that should be both minimized to increase the final coherence. This is all limited mostly technically, by SAR mission limits - see Tab. 2.2. The temporal decorrelation effects are often caused in vegetated areas that are temporally very variable. If it is not possible to use a higher resolution data or SAR of a lower carrier frequency, a shorter temporal baseline or acquisitions between the same season with a less vegetation activity (autumn, winter), the phase information of ground movement will be lost in the resolution cell.

A large progress has been done in the field of corrections for atmospheric noise. Atmospheric effects cause delays of the radar wave. Differences of these delays (mostly due to variable water vapour) will have an impact on the InSAR phase measurements. The phase measurements are sensitive also for heavy rain (mostly X-band SAR). Even that the rain can cause a Rayleigh scattering to all directions, it will propagate mostly as a wave dispersion, so again a phase delay will be caused. Because of such character, the places of rain or clouds or a higher water vapour will be observed in the final interferometry phase image as a fake deformation in the direction from the satellite (like a subsidence). The atmospheric effects are well described in (Li, 2005).

Many of the limits and obstacles of a differential InSAR technique can be overcome by using multitemporal interferometry methods. They are able to estimate other errors, such as phase residuals by orbit or DEM errors or atmospheric retardations that can sometimes totally cover the area of deformation. They can estimate in many cases a precise deformation rate for selected points. Also combinations exceeding DInSAR limits (large baselines) can be used within these techniques. They can identify very slow deformation rates, theoretically better than a mm/year precision, of particular physical objects.

Several studies find a status of MT-InSAR being able to substitute terrain work for measuring deformations. However this optimistic scenario is possible only in case of not too fast deformations and sufficient sampling of both available SAR data and stable scatterers on site.

The original form of PSI or its similar derivatives are based on a fitting of phase measurements to some a priori known temporal model (for example a linear trend assumption). This is problematic in the case of mining subsidence because the deformation areas advance together with the exploitation movement. In this case, StaMPS seems to be more suitable since it doesn't require any a priori model.

A whole comparison between approaches of DePSI and StaMPS can be found in the work of (Sousa, 2009). Both of the techniques have their pros and cons. It seems that StaMPS is more suitable for non-urban areas and deformations that are fast and variable in time. On the other hand, due to the assumption of a spatial smoothness, it can miss deformations that are very local, within a singular anomalous pixel, which would be detected if processed by DePSI. Anyway, generally results from both techniques show very similar estimations that fit well with the on-site measurements.

"And who knows (there is no saying with certainty), perhaps the only goal on earth to which mankind is striving lies in this incessant process of attaining, in other words, in life itself, and not in the thing to be attained, which must always be expressed as a formula, as positive as twice two makes four..."

FYODOR M. DOSTOYEVSKY, NOTES FROM UNDERGROUND

Chapter 3

Monitoring of Subsidence in Northern Moravia

Several missions of radar interferometry in the field of monitoring of subsidence in undermined Northern Moravia can be identified. First of all, generally, the subsiding locations should be detected and a rate of deformation should be estimated. If these estimations will fit with available levelling measurements, the InSAR might fully substitute future levelling missions that are economically very demanding.

A temporal process of the subsidence can be generalized according to (Bláha et al., 2009): *"the affection of coal exploitation on the ground surface is estimated to 3-5 years... The effects on the surface depend on used mining technology... A general trend is that there is no subsidence during the year of exploiting itself. First year after exploitation, around 60% of estimated subsidence will occur - a second year it is expected to be 30% and the third year the remaining 10%."* Using radar interferometry, this assumption can be well investigated.

In official processes, areas that are affected by subsidence are estimated with a forecasted rate using a computational model. InSAR can be used to evaluate the model reliability. Unfortunately, I wasn't able to achieve proper official data about expected subsidence from the OKD Corp. mining company for a comparison.

Also, according to (Jiráňková, 2006), it seems that right before the subsidence occurs, the area over the exploited space is first slightly uplifted, due to geomechanical processes. This uplift should be also detected by InSAR, thanks to its high sensitivity; however usage of X-band data is recommended for such purpose.

3.1 Area of Interest

It can be said that a mining industry (together with a heavy industry) shaped the history of the Moravian-Silesian Region of Czech Republic, mainly in its geographical and sociological aspects. Salt springs were exploited in history since 13th century in Orlová and Fryštát (part of Karviná today), the black coal was found in the middle of 18th century in Ostrava, then in other parts of the region as well.

Nowadays the Ostrava-Karviná coalfield (further as OKR, “Ostravsko-karvinský revír”) represents the main area of coal mining in the Czech Republic since 90% of Czech coal stock is deposited here. Since the beginning of 21st century OKR is the only area in Czech Republic where this high quality and economically very important raw material is exploited.

On the other hand, the mining necessarily forms the whole undermined relief. Many civil structures were damaged or demolished during the 200 years mining history including historical objects, tramlines or other transportation networks. Subsidence in mine-affected areas reached a groundwater level and large areas including inhabited houses were flooded. The whole area is unstable even today. The post mining subsidence can be present on the mining site several years after an end of exploitation.

Statistical data in this section were gathered from annual reports of OKD, Corp. [14], (Martinec et al., 2004) and (Dopita et al., 1997). A situation map of all actual mines together with closed mines can be seen in Fig. 3.4.3 (note that Frenštát mine isn't included in this map - this mine located to the south is in a non-active conservation regime).

3.1.1 Exploitation of Black Coal in OKR

A black coal is exploited since the end of 18th century in the Ostrava-Karviná coalfield. The coalfield is a part of Upper Silesia Coal Basin of which a majority lies in neighbouring Poland. In the Czech part the territory is around 1550 km² large while the mines in OKR covered 320 km² in total. In the whole area around 92 coal seams are exploitable, their height generally ranges between 0.8 – 1.6 m in Ostrava region and 1.2 – 6 m (up to 15 m) in Karviná region. The full deposit is estimated around 20.6·10⁹ tons in a depth less than 2 km while in the western part, due to Variscan orogeny in the Carboniferous period, the coal is deposited steeply down to around 3 km depth. Mining is performed in a depth down to 1.2 km.

During 20th century the annual coal production was exceeding 10·10⁶ tons/y, during 1970-1989 (socialistic regime) even two times more within 17 mines. Today the yearly production is back to be around 10·10⁶ tons/y. Since 1990s mines in Ostrava (and Petřvald) are closed and the exploitation continues in the east and to the south. A large reserve is expected also in the mountain area of Low Beskydy, here the mining isn't performed. Today 4 mines operate in 8 sites actively in the whole regions of Karviná and Paskov covering a total area of around 130 km². With the current speed and expected deposit, the mining in current sites is expected not to end before 2030. Future exploitation is planned to continue to lower depths, down to around 1.4 km.

Coarsely 50% of the annual production is exported to European countries, other 50% of the annual coal production is needed in Czech energetics, heavy industry (coke), or chemical industry (anthracite). The OKR area is the only source of black coal in the Czech Republic, nowadays all active mines belong to OKD, Corp. company.

3.1.2 Effects of Undermining in OKR

During cca 200 years of black coal mining activity, around $1.6 \cdot 10^9$ tons of black coal and probably some $0.65 \cdot 10^9$ tons of tailing rock was exploited from the underground, together with perhaps some 3 km^3 of saline mine water that was pumped out from boreholes (Martinec et al., 2004). No filling (or percentually very small portion) was performed after the mining in the abandoned underground structures. Such amount of retrieved material will cause a comparable ground subsidence in a generally shallower depth but larger affected areas.



Figure 3.1.1 – Effects of mine subsidence - tramline to Karviná and damaged housing. Photo: Archive VŠB-TUO, 1954.

The subsidence height differs according to the amount of exploited material - maximal subsidence is measured in Karviná district, numerous places subside faster than 6 m per 10 years. A church of St. Peter of Alcantara in this district subsided for 37 metres since 1854 after exploitation of 27 coal seams with total thickness of 50 m from ČSA and Darkov mines (Grmela et al., 2002). The whole road network in Karviná surroundings is affected by subsidence as well as building structures. Many affected buildings had to be supported by specific constructions, such as a concrete underlay of church of Virgin Mary in Orlová in 1960s. More than 20 multi-storey houses had to be demolished in Doubrava in 1970s as well as a Mettenclouit Castle in Orlová. Tramlines and a railway in Orlová were dissolved.

In Ostrava area the subsidence was much lower, maximally around 1 m in the period of 1985-1994 was modelled by appropriate methods. Still during the whole mining period there are areas of up to 20 metres of subsidence. A Silesian-Ostrava Castle has subsided for 16 m and had to be reconstructed in 2004.

The exploited tailing rock was used by the building industry or for a terrain reclamation - but almost a half of this tailing rock has been concentrated in tailing piles where they are a source of an air and ground pollution due to running chemical reactions. Early piles were formed in Ostrava, now they are a typical landscape feature. For example, Ema tailing pile of around $4 \cdot 10^6 \text{ m}^3$ volume is a third highest point in Ostrava of 315 m above sea level. Since 1950s the tailing dumps are formed flat.

A presence of methane gases (with an emission to air of several hundred 10^6 m^3 per year) is still a danger in both mines and ground objects. A concentrated methane can cause explosions. This happened numerous times in the history, today the gases are extracted controllably.

A geologically specific issue in OKR is an occurrence of detrit, a lower Badenian basal clastics containing fossil seawater. The area filled by detrit is around 270 km^2 in the S, N and E part of OKR, detrit is in the depth between 50-284 m (or more). Several accidents of detrit break-out into mine area happened in the past. Following change of a hydrostatic tension can also influence the ground stability.

There is also some seismic activity that can be experienced on the ground but this doesn't have any significant effect on terrain changes. An extreme local seismic activity can be caused by a detrit break-out or methane explosion in mines and can exhibit an amount of 3^{rd} degree of Richter scale. Most of the thousands of detected seismic events per year in Karviná district are negligible.

Creation of underground open spaces and other alterations in the rock deposit can cause changes also in the flow of groundwater. These changes can cause damages in unexpected places, out from the subsidence troughs. Also due to a higher looseness of the ground rocks and unfilled spaces, effects of floods can have a higher magnitude. A typical example is a road near to the Žofie Mine in Orlová that started to subside since large floods in 1997 and has declined for 1.8 m within 2 years (Grmela et al., 2001). Also landslides occur for similar reasons.

After mine closure and termination of water pumping, the groundwater fills the rock cavities and forces out gas. In Ostrava, methane emissions were detected even 3 years after mine closure.

Prevention and Reclamation of Land

After mine closure, reclamation works should cover up the effects of mining activities by shaping and hardening terrain, greening, etc. Changes in the relief of the rehabilitated area shouldn't emerge any further. Such an area is used for agriculture, forestry or for another purpose. A Heřmanice pond is a protected natural territory now, Landek hill is a national reservation.

The area affected by subsidence is forecasted computationally using a Budryk-Knothe method. Such models are used also by local authorities. Several zones are defined within the region that are taken into account when requesting a permission for construction within these zones or other purposes [14].

3.1.3 Formation of Subsidence Trough

Subsidence troughs over OKR mines cause a considerable morphology, creation of non-outflow areas even directly in settled sites. Mainly Karviná area morphology is affected by this anthropogenic influence. Most of the area lies in some of the mine subsidence troughs, with the highest peaks at places of shaft safety pillars.

The whole process of subsidence trough formation can be read from Fig. 3.1.2. According to (Jiráňková, 2006), a subsidence trough is forming dependently on the overburden material, geological settings and a volume of exploited material from a certain depth.

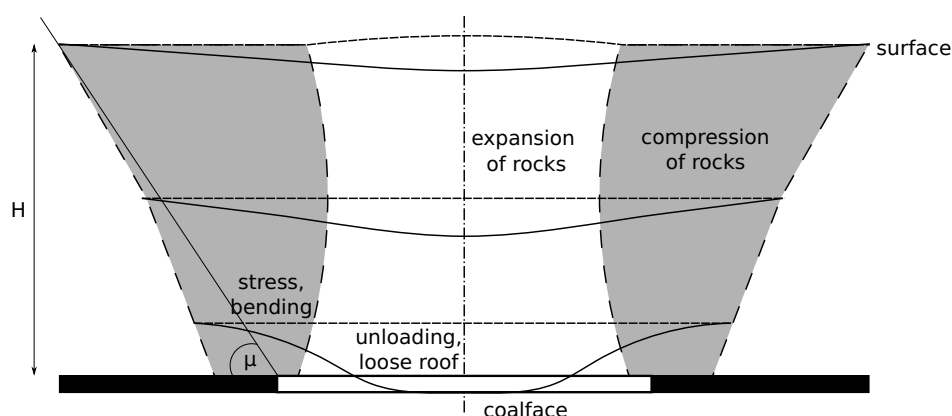


Figure 3.1.2 – Formation of subsidence trough over undermined area; simplified from (Jiráňková, 2006)

A subsidence trough extends the area directly over the mining site to a large extent dependently on a mining depth and a boundary angle of influence μ . In the area out of the mining site projection the maximal subsidence can reach up to 25% of the whole subsidence trough. If the exploited deposit lies more or less horizontally, a uniform vertical direction of subsidence is expected. In the OKR, most of the deposit lies in steep angles. Its exploitation would cause land movements also with a horizontal component which is also a significant part causing an instability of objects built within the subsidence trough.

After an area is exploited, all protection mechanisms removed, the free space starts to be filled by an overburden material. The material above gets loosened so the subsidence on the surface will not reach the total mass of retrieved material (especially if the deposit is deep enough). The amount of subsidence can be computed by numerical models, a Budryk-Knothe model is used for official estimations. An evaluation of a model by Schenk and Knothe using precise levelling was performed in (Jiráňková, 2006). In this publication also an effect of expansion was confirmed - it seems that right before the phase of subsidence, the area directly over an exploited coalface can first be slightly uplifted because of an expansion of rocks due to the pressure of surrounding compressed rocks (see Fig. 3.1.2).

While in Ostrava district the black coal was exploited from coal beds of a smaller thickness (around 1 m), in the Karviná region where much larger deposits are present, mining of deposits typically of 1-6 m thickness is performed mostly using a larger scale long-wall method with a controlled caving. An average depth for exploitation today is around -930 m below surface (i.e. around -700 m below sea level). The overburden in OKR

Carboniferous deposits is formed mostly by Lower Baden strata (mudstones, siltstones) and West Carpathian nappies with relatively plastic rocks (Martinec et al., 2004). The whole OKR area is geologically complicated with numerous tectonic faults in various depths (Dopita et al., 1997).

3.2 Available Datasets

3.2.1 SAR datasets

All SAR data that I use within this thesis were achieved within ESA Category-1 project ID C1P.4578. I have achieved and investigated in total 12 SAR acquisitions of ERS-1, 123 of ERS-2, 45 of Envisat, all from one track in each ascending and descending passes. Moreover, 7 acquisitions of two tracks of ascending Alos Palsar were investigated. Except for raw files of Alos Palsar from track 625, all data has been acquired as a single look complex (SLC) data. Images fully cover the area affected by black coal mining in Moravian-Silesian Region, Alos Palsar covers the area only partially but with a higher resolution.

3.2.1.1 ERS Acquisitions

I have acquired 135 ERS-1/ERS-2 of descending track 494 in total. From this amount of data, 12 acquisitions are from ERS-1. There are 6 tandem (ERS-1+ERS-2) pairs of 1 day temporal baseline available between 1995-1996.

From this set, however, only 49 images of a period 1995-2000 could be used for a proper MT-InSAR processing (while even this number had to be reduced). The reason is a high and variable deflexion of ERS-2 satellite due to a total failure of gyroscopes in 13 January 2001. On the figures shown in this section, the acquisitions out of the scope for a proper MT-InSAR combination (w.r.t. a selected master chosen to represent optimal configuration for MT-InSAR processing) are shaded in gray.

As since 2001 the ERS-2 satellite is piloting using only one active gyroscope of the original number of three, its course is not so stable anymore, which impacts on too unsteady sensing view angle characterized by the Doppler centroid frequency number. The maximal Doppler centroid baseline still applicable for the PSI processing is assumed to be about 700 Hz but the difference in the newer ERS-2 data achieve even more than 10 kHz (which corresponds with a squint angle around 2°).



For ascending track, only acquisitions before 2001 were ordered - it was only 8 acquisitions of track 415, one of the images is from ERS-1. Their configuration for MT-InSAR processing is depicted in Fig. 3.2.2. Their usage for MT-InSAR will be challenging due to a small number of acquisitions and still with relatively high baselines dispersion.

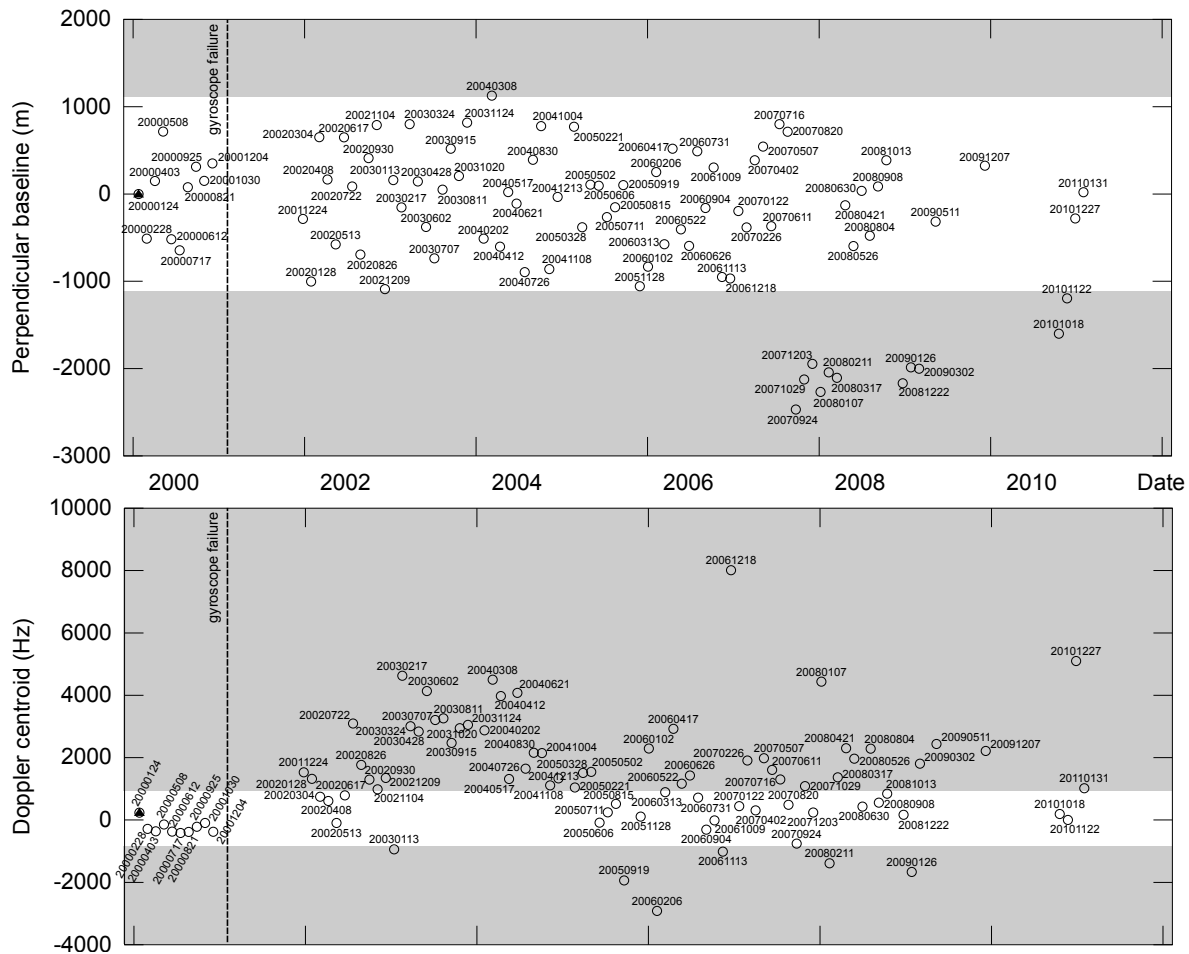


Figure 3.2.3 – Descending ERS-2 acquisitions (track 494) after a total failure of gyroscopes in January 2001

3.2.1.2 Envisat Acquisitions

For the descending track 494 (of the same extent as ERS), 17 Envisat acquisitions were achieved, see Fig. 3.2.4, while in its ascending mode (Fig. 3.2.5) there are more, 28 images, of track 415. Large temporal gaps observed in the data stack of descending Envisat acquisitions indicate possible MT-InSAR processing problems due to temporal decorrelation.

Since October 2010, Envisat acquisitions of this area of interest are not suitable for interferometric combinations anymore (Miranda, 2010).

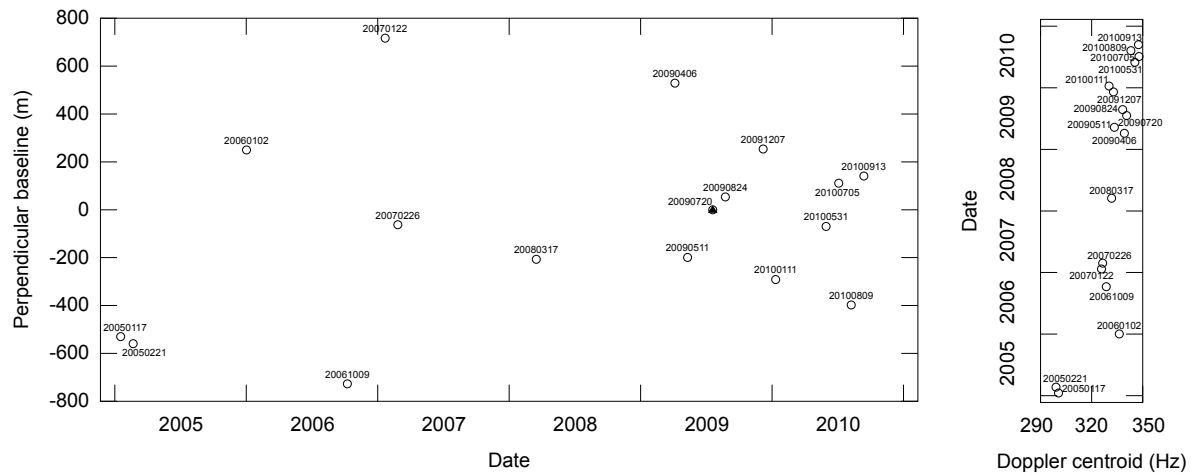


Figure 3.2.4 – Descending Envisat acquisitions (track 494)

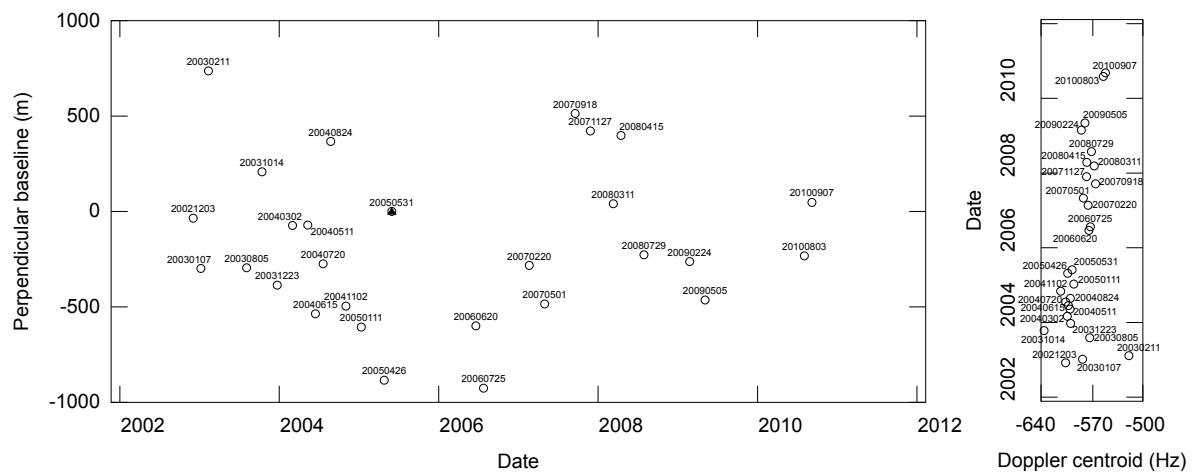


Figure 3.2.5 – Ascending Envisat acquisitions (track 415)

3.2.1.3 Alos Palsar Acquisitions

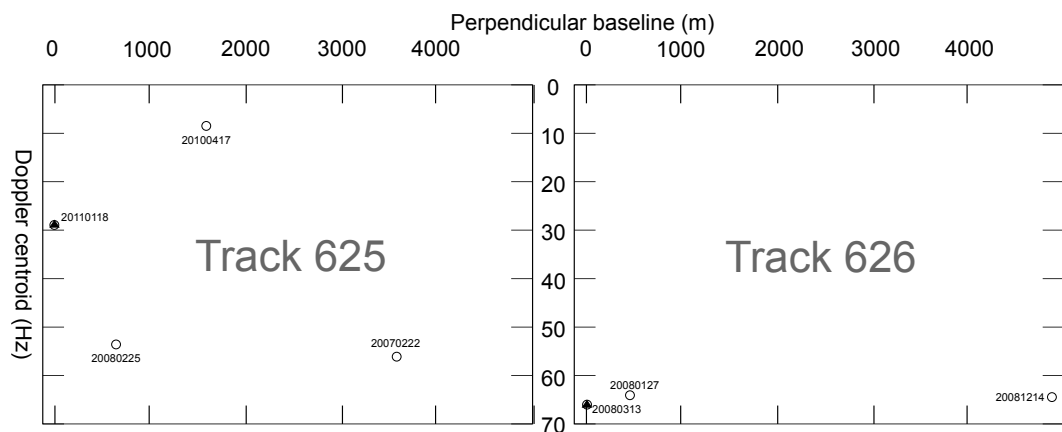


Figure 3.2.6 – Ascending Alos acquisitions

I have acquired in total 7 Alos Palsar acquisitions of Fine Beam Single polarization (FBS) from two tracks. First of all, track 626 was investigated, achieving very positive results as will be shown. For this track, already focused data were retrieved of level 1.1. Because of a specific focusing technique that was used the data show very stable Doppler centroid - this could be achieved by computation of Doppler centroid frequency separately for each pixel. available software tools are not ready yet for processing such data - the track 626 acquisitions were properly processed by GAMMA® while for the track 625 only raw data were ordered and focused by ROI_PAC.

Note the high perpendicular baseline of an outlying acquisition in both of the tracks in Fig. 3.2.6. Although the critical $B_{\text{perp},\text{crit}} \simeq 13 \text{ km}$ for Alos Palsar FBS acquisitions, as it was also shown in Section 2.5.4.2, some geometrical decorrelation problems (and also temporal in the case of track 625) still can be expected using these outliers.

With this small amount of acquisitions that include too large temporal and also geometrical baselines it doesn't seem feasible to use single track MT-InSAR methods. Future acquisitions are planned but due to JAXA observations strategy the acquisitions over the area of interest will be temporally always distributed very sparsely, in up to 3 acquisitions per a track per year. Also, several planned acquisitions over the area were cancelled, without stating any detailed reasons. Actually, it is possible to combine the FBS data with FBD (dual polarization fine beam data) - then even 6 acquisitions can be used during one year, however the resolution will get two times coarsened to the resolution of FBD which is around 20 m in the slant range.

3.2.2 Levelling Datasets

Levelling data of the subsidence site were achieved from various sources. Unfortunately, the origin of some of them is not clear - these couldn't be used for reference purposes. Two levelling missions were taken by VŠB-TUO for locations of Mine Lazy and Holkovice surroundings, the levelling methodology was well described and should provide reliable results.

Levelling near Lazy Mine The levelling is performed since September 1998 within 40 levelling points selected in a line with a distance of 50 meters, in the area of Karviná Mine, section Lazy (further only as Lazy Mine). Since April 2009, the measurements continue in one month periodicity using a precise electronic levelling instrument Leica NA 3003. Levelling parameters are set to achieve a measurement precision of first millimetres within the levelling line. The levelling results reveal a large subsidence in this site in the line profile plot in Fig. 3.2.7.

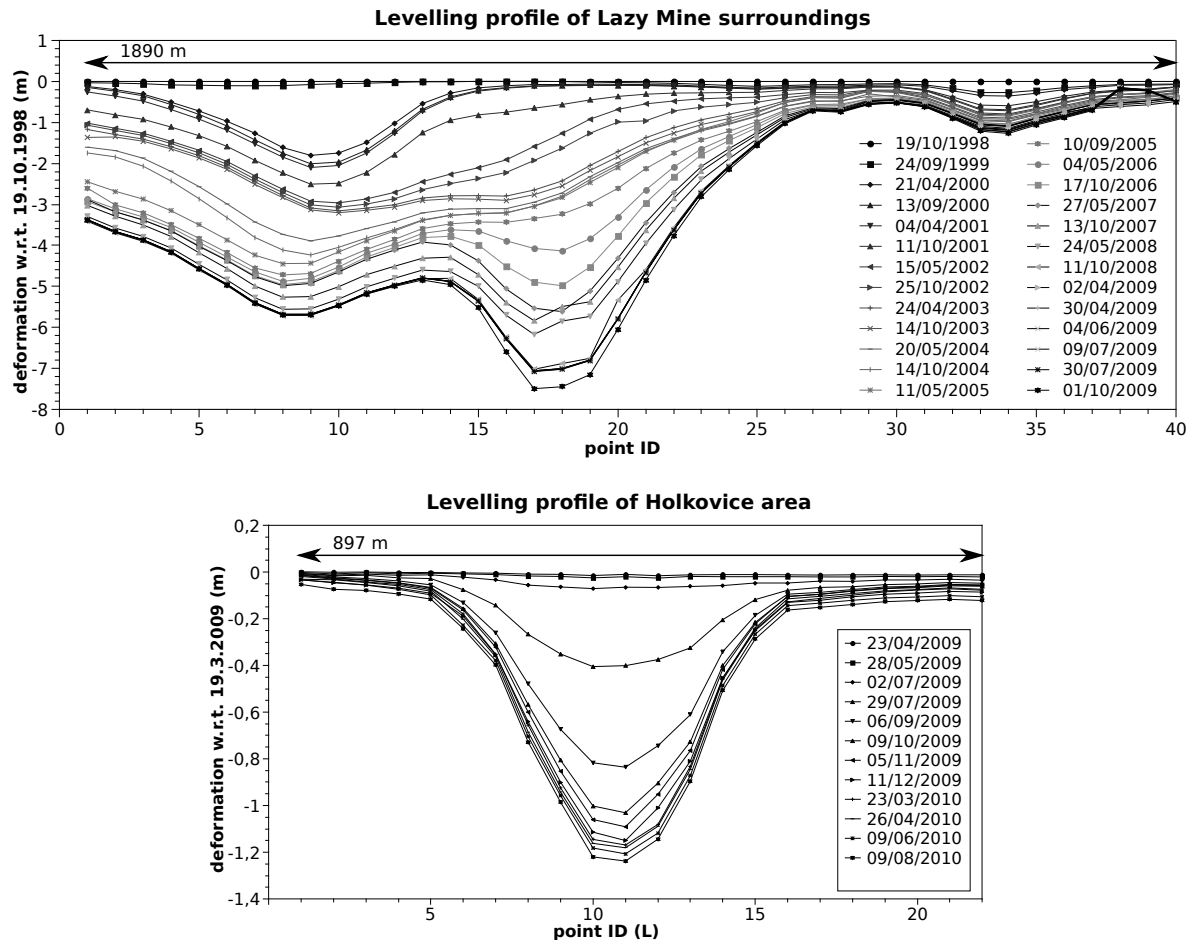


Figure 3.2.7 – Profile plots of levelling results of (a) Lazy Mine area and (b) Holkovice

Levelling in Holkovice This levelling is performed with similar parameters as in the Lazy Mine case. The location is affected by a subsidence of ČSM Mine. Also here the measurements are performed each month since 2009 (with more archived measurements available).

There are two levelling profiles that form a cross following subsiding roads on the site. The shape and location is figured together with the InSAR processing results in Section 3.4.2.3. A subsidence plot of an E-W (horizontal) profile is shown in Fig. 3.2.7.

3.3 InSAR Processing Issues

3.3.1 Differential InSAR Processing

3.3.1.1 Key for Interpreting Differential Interferograms

Because of a high deformation rate that often causes phase jumps in the interferograms and due to large decorrelation errors, the phase unwrapping procedure was not applied successfully. For the monitoring purposes, however, the wrapped phase fringes are enough

for a proper (however manual) interpretation of subsidence. Within this thesis, all shown differential interferograms will be wrapped.

To read differential interferograms properly, fringes should be count. One fringe represented by a full colour gradient depicts a phase change of 2π rad in the satellite line of sight (LOS), caused by propagation of the radar beam to the observed location and back to the satellite. This phase change can be interpreted as a terrain change in the LOS of a half cycle, i.e. $\lambda/2$, within the line represented by the whole fringe. For ERS or Envisat one fringe will mean a terrain change of 2.8 cm (their wavelength is $\lambda = 5.6$ cm). The direction of the change can be interpreted using the key in Fig. 3.3.1. If the phase values direction is to the positive, higher values, it means that the radar beam has travelled further in the second acquisition and it will mean a receding movement as a subsidence. In opposite case it will be interpreted as an uplift.

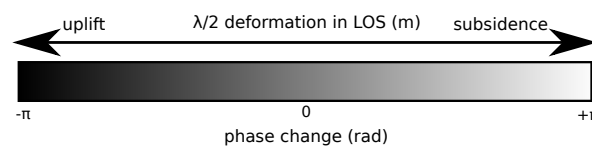


Figure 3.3.1 – Gray colour scale used for wrapped interferograms

Unfortunately, in most cases the area is decorrelated mostly due to a presence of vegetation. Then this interpretation is often impossible without filtering. Also atmospheric effects or DEM errors can cause a misinterpretation.

3.3.1.2 Effects of Limiting Factors

The main limiting factor in DInSAR processing was the temporal decorrelation. Both ERS and Envisat have the revisit time of 35 days, with exceptions of tandem missions between ERS-1 and ERS-2 which allowed to achieve acquisitions with only 1 day difference. In figures of this section I demonstrate effects of main decorrelation factors of temporal (Fig. 3.3.2) and perpendicular (Fig. 3.3.3) baselines together with an effect of year period (Fig. 3.3.4a) using coherence maps from the interferograms, with a greyscale spectrum ranging from black (theoretical zero coherence) to white (100% coherence).

To minimize influence of another error, both other parameters were chosen with an appropriate threshold. I couldn't fulfill this condition for Doppler centroid baseline error that I don't include here. However, the effect of linear decorrelation should be similar, with a stronger decorrelation from around 700 Hz for ERS/Envisat. For the demonstration purposes I have chosen an industrial zone in Ostrava. Several metallic buildings preserve high and stable reflectivity in the NW part. The neighbourhood area is composed by rural areas, inhabited zones, a river and a forest which causes main decorrelation (situated in the middle to E). There are both railway and a main road in this selected cutout. The situation can be read from the ortophotomap provided in Fig. 3.3.4b.

To minimize influence of another error, both other parameters were chosen with an appropriate threshold. For example when investigating B_{temp} influence in Fig. 3.3.2, maximal values of other parameters of interest were $B_{perp} = 85$ m and $B_{Dop} = 75$ Hz. The exception

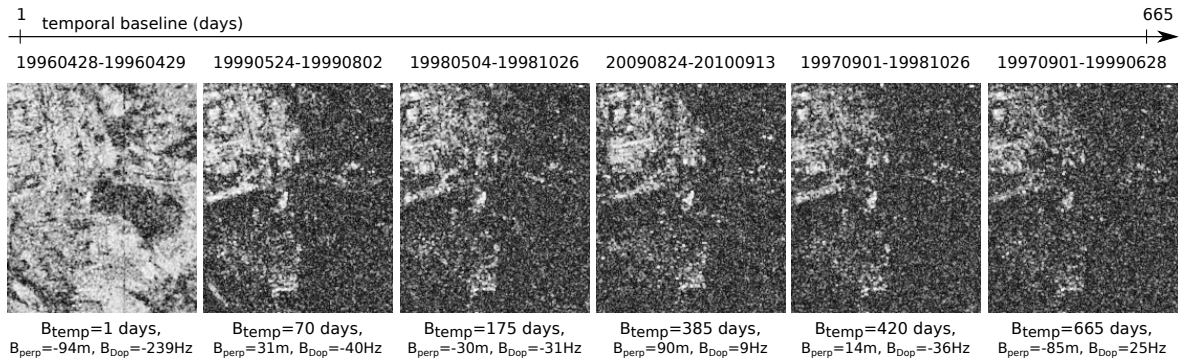


Figure 3.3.2 – Decorrelating effect of temporal baseline in ERS and Envisat

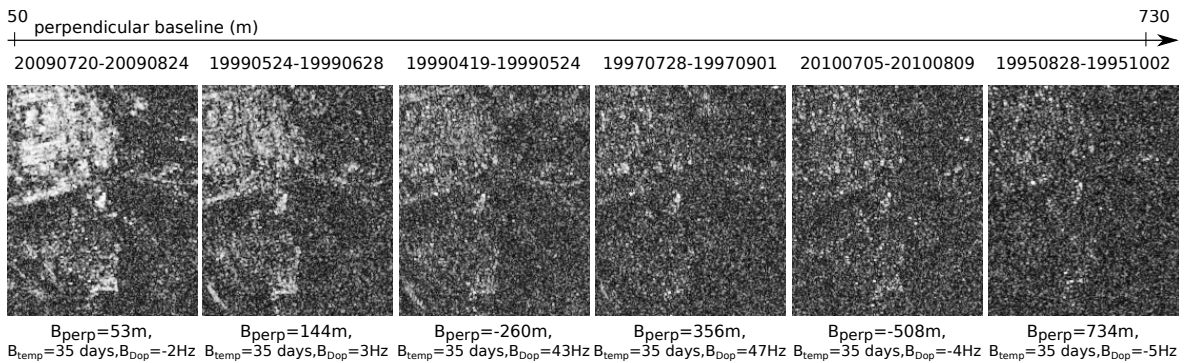


Figure 3.3.3 – Decorrelating effect of perpendicular baseline in ERS and Envisat

is the tandem pair where both other parameters are higher ($B_{perp} = 116$ m, $B_{Dop} = 253$ Hz) but these don't seem to have a significant influence - the tandem combinations have an outstanding high coherence. Areas covered by a dense vegetation, such as forests, or water filled areas are however decorrelated also within only this 1 day.

It can be observed that with one of the baseline terms increasing, the decorrelation drops down in the non-urban area. Urbanized areas usually have a stable response in time. Because of SAR images spectrum filtering and advanced coregistration techniques in available InSAR processing tools the effect of look angle change due to Doppler centroid variances and larger B_{perp} is diminished.

Seasons of the year cause a characteristic coherence decrease in vegetated areas. In Fig. 3.3.4a I show typical coherence maps from the whole dataset that display the seasonal effects. The decrease is most significant when combining images from two different seasons, for example between a winter time and a time when the vegetation is growing.

An advantage of achieving a high coherence with even longer temporal baseline is in the case of Alos Palsar data (Fig. 3.3.4b). The L-band penetrates through vegetation canopy (but the forest on the figure stays decorrelated however) because of both longer wavelengths and because of around 3 times higher resolution.

Note that it is possible to combine such ERS-2 images even after the gyroscopes failure if the B_{Dop} is not too large, let's say, better than $B_A/2$, i.e. $B_{Dop} < 700$ Hz. But, unfortunately these interferograms cannot be processed by MT-InSAR properly.

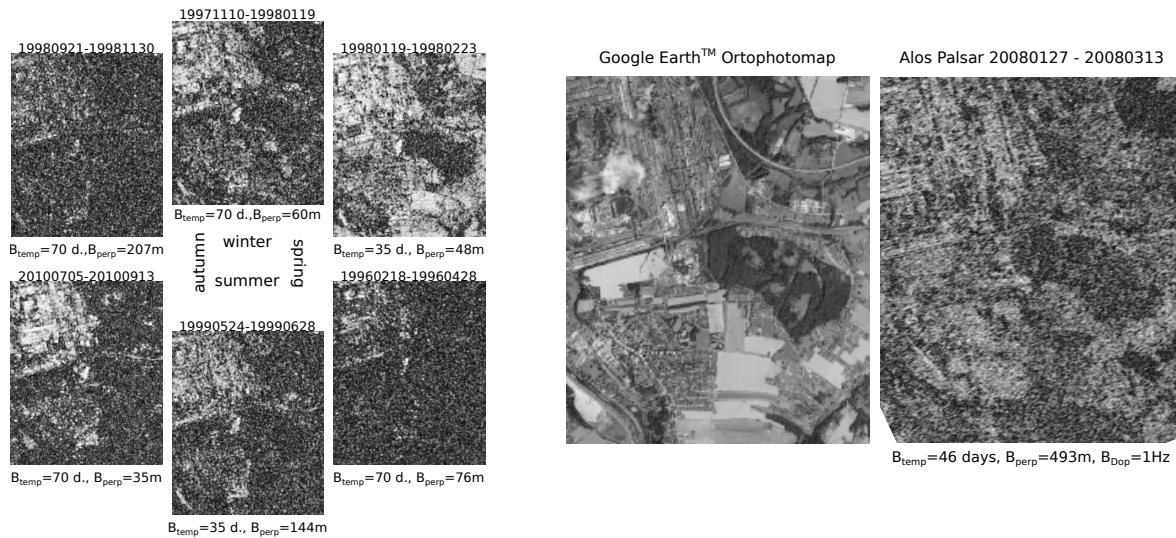


Figure 3.3.4 – ERS/Envisat interferogram coherence with regards to the seasons of the year (a), ortophotomap (by Google EarthTM) of the area of interest selected for this section compared to Alos Palsar coherence of 46 days interferogram (b).

3.3.1.3 Advanced Phase Filtering

In most cases the interferometric phase should be filtered to increase an interpretation ability. Such a filtered interferogram can be used for visualisation purposes but it loses its precise phase measurements that could be otherwise used for an MT-InSAR processing.

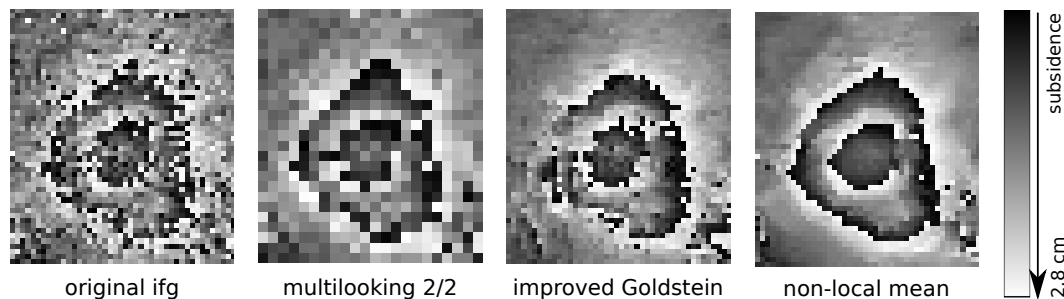


Figure 3.3.5 – Example of phase filtering of subsiding area

In most cases a simple multilooking gives a sufficiently better overview at the expense of a resolution decrease. Areas of my region of interest are affected by decorrelation strongly and in some cases I need to understand very local deformations. In these cases I use two advanced filtering techniques when the DInSAR interpretation is needed. First is an adapted Goldstein filtering by (Baran et al., 2003) that use a coherence image for weighting a reliability of phase measurements. Second is a non-local mean filtering method (NL-MEAN) proposed by (Deledalle et al., 2010) that tries to reconstruct the phase affected by noise for homogeneous areas (using the intensity image of interferogram). Both these methods are strong, even relatively aggressive in the terms of changing phase measurements, but seem as very valuable tools for interpretation purposes. I have partially modified the NL-MEAN scripts for a usage of already formed differential interferogram as an input instead of using original SAR images as was originally intended.

An example of phase filtering using these techniques is demonstrated in Fig. 3.3.5. Here, a local deformation was detected in the Havířov-Dolní Suchá inhabited area from ERS-2 interferogram of dates 23 Feb 1998 - 30 March 1998. The original interferogram was multilooked 1/5 to achieve a square like dimensions. The area is of 1.7 km² and the deformation was detected as about 6 cm in the satellite LOS. This pattern was found also in other interferograms close in time.

3.3.1.4 Atmosphere Filtering

One possibility to filter atmospheric effects is demonstrated on Fig. 3.3.6. Here the atmospheric phase screen (APS) was modeled in StaMPS for ERS-2 acquisition of 29 April 1996. In this day, a precipitation of around 5.8 mm is reported, there were storms during this day.

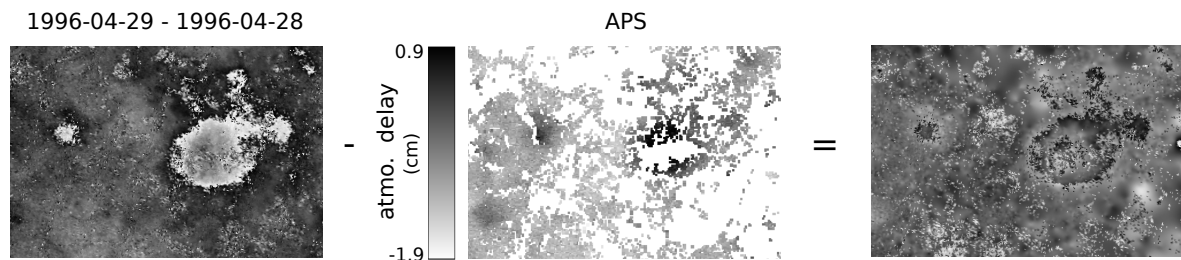


Figure 3.3.6 – Removal of atmospheric phase screen from differential interferogram

The APS was created as a product of PS processing of 28 interferograms combined for this date selected as a master. I have interpolated the PS pixels grid to match dimensions of 2/10 multilooked original interferogram¹, phase-wrapped and removed this APS from an interferogram formed by a combination with 28 April 1996. Because this combination is a tandem pair, I don't expect a large detected subsidence. The effect shown in Fig. 3.3.6 propagated into every other interferogram pair in the same scale. This is obviously an error term, most probably caused by an atmospheric artefact in the master date. Removing the error term and supposing no other noise, the result should be a flat homogeneous image. It can be observed that the most of the error term was removed by the computed APS, still some portion of the artefact remains - this is mostly due to the actual PS pixels density, but also due to inaccuracies of APS estimation.

This attempt has several disadvantages. First of all, a whole MT-InSAR processing should be performed with this particular acquisition selected as a master. Second, if there is some detectable change that occurred only in this date, it will be removed together with the atmospheric effect. Also, if there are no stable points used for MT-InSAR or if they are in a very sparse distribution, the atmospheric screen cannot be estimated at all.

¹for a sparse grid interpolation I used a freely available `inpaint_nans` tool for Matlab [11] by John D'Errico

3.3.1.5 Analysis of DEM Models for Topography Removal

At least three DEM models of a sufficient quality are available for the topography removal of the area of interest. I have inspected applicability of global models of SRTM and Aster GDEM, with regards to the national geodetic model of ZABAGED. A deeper investigation of the models can be found in (Guth, 2010).

Table 3.1 – General parameters of available DEMs

DEM model	coverage	technology	actual date	resolution	$\sigma_{vertical}$
SRTM	-56°/60° lat.	C-band InSAR	Feb 2000	90x90 m	10 m
Aster GDEM	-83°/83° lat.	stereo multispect.	2000-now	30x30 m	15 m
ZABAGED	Czech Rep.	geodetic meas.	2008	<10x10 m	2 m

A small area around Doubrava was selected to investigate a precision of SRTM and Aster GDEM by comparing these global models with an accurate ZABAGED model. I tried to find a known stable area from these DEMs. I have coregistered all three DEMs and coarsened their resolution to match that of SRTM DEM (around 90x90 m) and investigated their differences. Both global models deviated around $\pm 15\text{m}$ in the area regarded as stable with a standard deviation of $\sigma_{S,A} = 5.9\text{m}$. This could be expected due to characteristics of both DEMs. The version of ZABAGED, that I achieved, was updated in 2008 by geodetical measurements (still it can contain old, but precise data). Differences between the global models showed that SRTM matches ZABAGED better - the differential standard deviation was $\sigma_{S,Z} = 4\text{m}$, while differences to Aster GDEM had $\sigma_{A,Z} = 7.6\text{m}$. Both models show maximal errors in areas covered by a forest. But a general trend of topography was better mapped in SRTM, while Aster GDEM showed several erroneous artefacts and more variable height differences.

There was a need of a precise topography removal of Alos Palsar combination that is more discussed in Section 4.7.1.5. Here the pixel resolution was around 10x10 m, with a $B_{perp} = 493\text{m}$ the $H_{amb} = 114\text{m}/2\pi$. Doubrava area has a low topography and with such a high H_{amb} , even small DEM accuracy can be tolerated. The differences between both global DEMs propagate into phase observations of up to 2.4 rad differences as a local maximum (but the standard deviation from the mean difference is much smaller, around $\sigma = 0.35\text{ rad}$). This is caused probably due to Aster GDEM's lower vertical accuracy, mostly in highly vegetated areas where its optics doesn't penetrate to the ground. On the other hand, Aster GDEM provides a more detailed elevation model than SRTM that might be useful in some cases.

Fig. 3.3.7 shows results of topography removal using all three DEMs, from a place where some higher difference was found. Aster GDEM has tendencies to overestimate height differences as it was also in this case that can be also misinterpreted as a slow deformation - for example an area in the lower part of the interferogram area, the field, shows some slight "change" caused by Aster GDEM removal. In this place the difference between ZABAGED and Aster GDEM height values was 18 m. No such significant differences were found between ZABAGED and SRTM, even on other stable places.

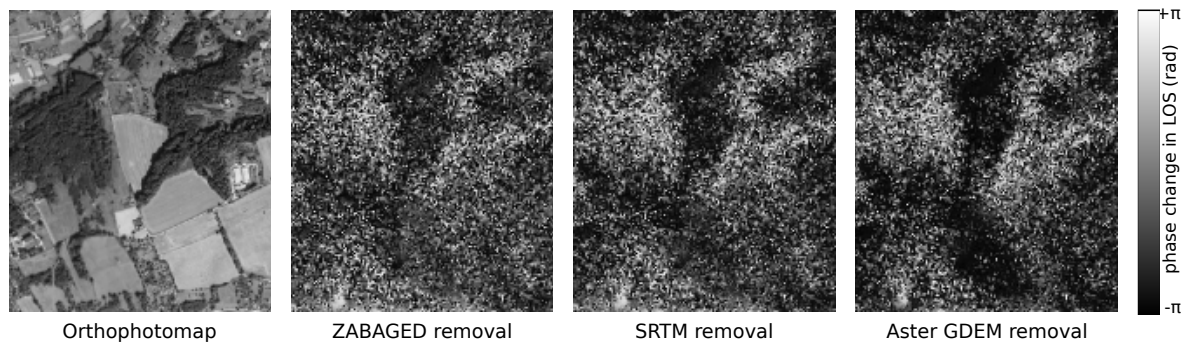


Figure 3.3.7 – Topography removal in Alos Palsar 46 days interferogram by chosen DEM models. Background image by Google EarthTM.

Conclusions Some more confident results were achieved differencing ZABAGED and SRTM models, Aster GDEM is regarded as not so reliable and will not be used for topography removal in DInSAR. SRTM model showed an appropriate precision - the error deviation of $\sigma_{S,Z} = 4\text{ m}$ is according to the official SRTM dataset parameters and should be used for DInSAR. Higher topography errors in vegetated areas can be expected when using SRTM in case of L- or X-band DInSAR processing - the non-US SRTM model was created only from C-band data processing so it reflects differently from vegetation canopies than other bands. However in usual cases the accuracy of SRTM should be adequate for DInSAR usage. The advantage of SRTM against more accurate ZABAGED is its free of charge disposition.

As an additional finding, in places known to subside (note that in non-urbanized areas), some changes were detected also in the DEMs. However because of high error terms that are present in areas even without subsidence, they cannot be evaluated properly to subsidence monitoring purposes. Another situation will be when comparing datasets that were created using the same (or very similar) technique - this can be investigated for example between SRTM and TanDEM-X models that should be available in following years. Such change detection within more than 10 years from DEMs can be used to add another reliable overview to investigations of subsidence in the area.

3.3.1.6 Geocoding

Using such features as precise orbits and a DEM coregistration it is possible to geocode pixels in radar coordinates to some coordinate system commonly used in GIS, in a sub-pixel level precision. For the visualisation purposes in this thesis I used only WGS-84 coordinates of corner pixels of an interferogram raster image to geocode the whole raster. This way detected fringes will not be deformed largely by a change of coordinate system. On the other hand, this attempt will include errors but because there are not large elevation changes in the area of interest, these coordinate errors will not be significant, still they can range a difference of several pixels.

3.3.2 General Notes for MT-InSAR Processing

3.3.2.1 DePSI Processing Attempt

I have tested Delft Persistent Scatterers Interferometry Toolbox (DePSI) to estimate the deformation rate from 21 images of ERS-2 of 1999-2001. Unfortunately in the area that is mostly vegetated, there was a too low amount of suitable PSC points found on the low amplitude dispersion basis. After some experimenting with DePSI parameters a fine number of detected PS formed a network to estimate APS together with orbit errors but they were affected by large errors and a very low ensemble coherence. Estimations were found unreliable, areas known to subside were estimated more or less as stable while only a few points were detected in the subsidence basin area.

It is possible that problems were caused by an improper temporal model that was set based on a real subsidence expected in the basin that was too large to be detected by PS processing (decimetres per year). Also some errors while forming interferograms themselves should be addressed.

Some more information about the processing can be found in (Lazecký et al., 2010). Since for this area the StaMPS processing showed some higher suitability and since it was investigated for example in (Sousa, 2009) that the results of StaMPS match these from DePSI, only the StaMPS processing was evaluated in further work. In addition, StaMPS is publicly available.

Note that in general, DePSI project achieves very good results even for a high subsidence rate in mining area. In Gardanne, France, subsidence of a range from few centimetres up to some decimetres in few months was underestimated to be maximally 2 cm/year by ERS data used in DePSI, but still the locations were detected properly by (Samiei-Esfahany, 2008).

3.3.2.2 StaMPS Processing and Evaluation

Because of its flexible phase-stability based PS detection, StaMPS method is successful in MT-InSAR processing of areas that don't include man-made objects, especially when input interferograms have appropriate shorter baselines and if they are oversampled before actual StaMPS processing. To discuss issues that should be expected for StaMPS processing, I would like to mention a comparison work of (Sousa, 2009) first where many practical aspects are investigated and described.

In general, if I assume perfectly coregistered images (StaMPS includes a procedure to improve coregistration as was already discussed in Section 2.6.3) to one common master, that should be carefully chosen to minimize effective baselines, and a proper selection of phase stable points, the most problems in processing are connected with a proper phase unwrapping. Because of the rule of sampling known as a Nyquist criterium that in the end describes the fact that the sampling rate should have more than two times higher frequency than the sample length, in this case where every sample/pixel is described by a value from a 2π interval, only deformation in the pixel of less than half of this interval (i.e. a reliable interval of π which means a deformation of $\lambda/4$) can be certainly evaluated and unwrapped.

For ERS/Envisat this would mean a maximal detectable change in one pixel of 1.4 cm/35 days. In fact, even such change can cause unwrapping problems (Colesanti et al., 2006).

Fortunately, StaMPS includes techniques to cope with the phase jumps using `snaphu` (Chen et al., 2001) within a statistical cost phase unwrapping solution (Hooper, 2009). Still in practice there are often phase unwrapping errors that are usually connected to some source of noise contribution. A manual optimisation of phase unwrapping results can be done by simply dropping interferograms that are strongly affected by decorrelation (even that only in phase stable pixels).

Practical notes for StaMPS processing The actual version of StaMPS 3.2 processes data in 8 steps for PSI processing. The data input is a pre-selection of PS candidates using an amplitude dispersion index (set quite large since this selection will be further filtered) by an `mt_prep` utility. It is a good idea to check the interferograms that were formed beforehand. If there is some totally decorrelated it will cause a detection of much less PS points or a total drop of PSC points selection to zero.

More detailed information about the processing itself can be found in the StaMPS Manual (Hooper et al., 2010).

Step 1 The first step only prepares the processing itself, reading input data and setting proper input parameters.

Step 2 In the second step a phase noise of PSCs is estimated based on various parameters. From a selected area range around each PSC a spatial correlation is investigated and each PSC will get a phase noise value. Here the defaults are set reasonably for usage of ERS/Envisat data but if some very local deformation is to be monitored, the parameters should be experimented with to investigate a smaller area or to tolerate a higher deviation.

Step 3 In the third step a PS selection is performed using the estimated noise. Noisy pixels would cause processing problems and their contribution cannot be smoothed using low-noise (stable phase) pixels if they are distributed in space too densely. Here the noisy pixels can be dropped if their density exceeds some chosen threshold. Again, the default parameters are set according to experience and can be left unchanged in usual cases.

Step 4 In the fourth step PS points are weeded. Pixels affected by side-lobe effects, too noisy pixels in general and pixels which noise deviates significantly (w.r.t. noise deviation of other pixels) are dropped. This step is crucial for the final count of selected PS pixels. For this step I usually select a lower time smoothing window because the expected deformations vary fast, according to mining progression in the area. Also a weed standard deviation can be set larger since the deformation is expected to be too large causing high deviations in data.

Step 5 The fifth step doesn't need to be operated at all. Here spatially uncorrelated look angle error terms (SULA) caused by DEM errors are estimated and removed. Also, if the processing was performed in separated patches (to overcome memory issues processing large amounts of data), the final filtered data are merged from these patches.

Step 6 In the sixth step a phase unwrapping is performed. Here two different methods can be selected for unwrapping noted as 3D and 3D_QUICK. In general, the 3D should result in more accurate results, with a better treatment of phase jumps, however it is more sensitive to PS quality. Before unwrapping the phase can be prefiltered by an adaptive Goldstein filter (and a SCLA error term if available). Here parameters should be changed to fit more the expected behaviour of the site (i.e. temporal and spatial variability).

After this step one may use a `ps_calc_std_ifg` to calculate a noise standard deviation for each interferogram and if it is too large (say >70% of scene is regarded as a noise), such interferograms should be dropped from the processing. If restarted from the step 3, more phase stable pixels can be chosen.

Step 7 In the seventh step a SCLA (spatially-correlated look angle error) and AOE (atmospheric and orbit errors) is estimated. Note that only well unwrapped interferograms should be used as an input - this interferograms selection can be set here. It should be also noted that the SCLA error is proportionally larger in interferograms with increasing B_{perp} .

After performing this step it is very recommended to run a Step 6 as a second iteration - here the SCLA and AOE will be removed from interferograms helping to solve a phase unwrapping more properly. If more of the interferograms are unwrapped well, they can be propagated to the SCLA+AOE reestimation of Step 7. Also the `scla_deramp` function can be activated - then a phase trend ramp that wasn't removed in DInSAR processing is estimated for every interferogram.

Step 8 In the final (optional) step the results are smoothed, outliers are filtered in series of low-pass filters, in space and in time.

Small Baselines and Merged Processing For small baselines processing and also for processing of final data after merging PS+SB results together, the same steps are performed. One more parameter exists for interferogram dropping purposes - it is possible to drop only selected (noisy) SB interferograms or all these ones that include an acquisition already dropped in PS processing.

Fine Tuning of Unwrapped Phase My approach in phase unwrapping was to prefilter the phase using an adaptive Goldstein with a large alpha parameter (inspired from the modification from (Baran et al., 2003)) and a smaller unwrapping window for both time and space to include also local and variable deformations. Then I chose interferograms that seemed properly unwrapped for SCLA computation together with computation of phase ramps. After reunwraping with these error terms filtered I repeated the step 7

using interferograms that were more smoothly unwrapped. I always had to check the interferograms subset if some obvious error term didn't propagate as a deformation (this can happen if an error is accidentally correlated with a B_{perp} in more than one interferogram).

I continued with these iterations until the SCLA didn't improve phase unwrapping results anymore. Then I removed interferograms with large deviations from the whole processing and processed the 3D unwrapping (with a more strict parameters) again to exclude the outlier effects.

It should be noted that practically for the initial SCLA only interferograms with a $B_{\text{perp}} < 200\text{m}$ could achieve reasonable estimations. Acquisitions including too large atmospheric effects should be also removed from the initial SCLA computation. Yet there must be some minimal count of let's say 4-5 well unwrapped interferograms for a proper SCLA.

3.3.3 Actual StaMPS Processing Approaches

I have processed all available data of ERS and Envisat satellites using StaMPS PSI+SB, found out practical processing limitations, fine-tuned the results and selected a proper configuration to be used for final InSAR overview of deformations in my area of interest. General information about each processing approach and their basic comparison is presented in Tab. 3.2. Baselines configurations of each set are plotted in Section 3.2. Final network of interferograms used in SB processing together with plots of mean velocities per year (normalized to values of -12;+4 mm/y) is shown in Fig. 3.3.8. All these approaches were created using oversampled data, steps 1-5 of StaMPS processing chain were performed with the same parameters.

All deformation values were spatially referenced w.r.t. an area corresponding to a cluster of main buildings of VŠB-TU Ostrava. Here the undermining effects are not expected - the location should be stable, a precise height is measured continually by a GPS station installed permanently on one of the buildings roof. I have chosen the whole area of interest for processing, i.e. an area of around 35x35 km including all mines of Ostrava-Karviná district together with the outlying Staříč and Paskov mines. The subsidence is non-linear in time and with many subsidence troughs throughout the scene which challenges current StaMPS processing. No a-priori information was applied for the processing.

Table 3.2 – Performed StaMPS processing approaches of ERS/Envisat data

Satellite pass	Time period master	PS (SB) ifgs used/formed	Pixels count total (PS/SB)	PS (SB) range velocity mm/y	PS (SB) stats $\bar{\sigma}_{noise}$ / \bar{B}_{perp}	Master weather
ERS asc	07/95-08/00 27/07/99	4/7 (7/8)	13114 (24607/7233)	-14.7; 11.4 (-15.1; 9.8)	26°/142 m (18°/199 m)	overcast
ERS desc	08/95-06/99 28/07/97	18/20 (72/83)	97083 (76592/34090)	-18.3; 6.5 (-15.8; 4.8)	49°/292 m (47°/198 m)	scat. clouds, light rain
ERS desc	10/95-12/00 29/04/96	25/48 (253/253)	(not merged) (71008/27948)	-10; 3.9 (-11.3; 4.3)	48°/262 m (62°/189 m)	storm, rain 5 mm/d
Envisat asc	12/02-09/10 31/05/05	(22/27) (69/74)	88009 (68946/33681)	-6.7; 2.7 (-10; 5.2)	51°/347 m (45°/215 m)	mostly cloudy
Envisat desc	01/05-09/10 20/07/09	13/16 (32/35)	(not merged) (47545/33772)	-8.8; 4.2 (-19.6; 11.7)	42°/321 m (39°/198 m)	partly cloudy

The parameters of an average standard deviation (see Tab. 3.2) of interferograms phase noise can be used as a reliability factor of an unwrapping and error estimation. High values around $\bar{\sigma}_{noise} = 50^\circ$ show large deviations. A small value in the case of ERS ascending processing means quite a proper fit of the estimations with all 4 (7) interferograms in PSI (SB) processing. But because of too low number of acquisitions, existing phase jumps were probably not modelled reliably.

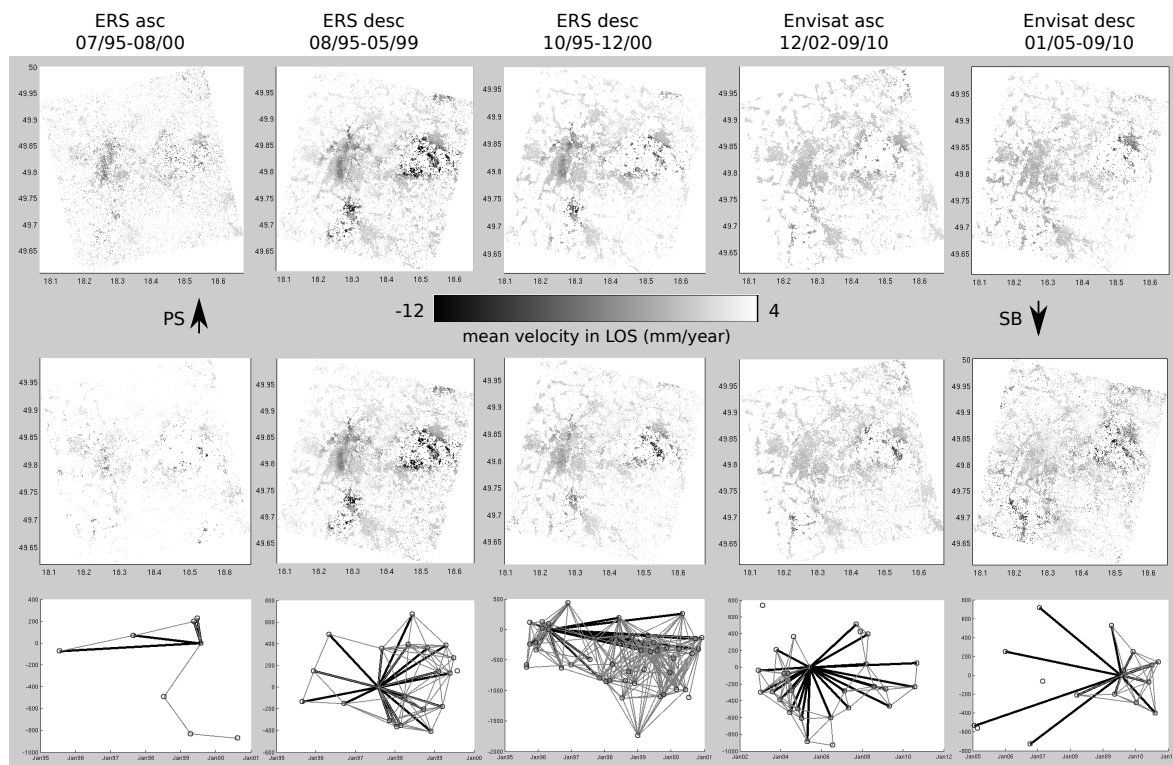


Figure 3.3.8 – Small baseline configurations of StaMPS processing approaches

3.3.3.1 Processing notes

ERS ascending processing (07/1995-08/2000) This processing attempt was very challenging. For the similar time period as in the previously described ERS descending mode where 49 images were available, in this case only 8 acquisitions were available. Here I didn't expect any reliable results - the region suffers from so fast subsidence that it simply cannot be estimated from PSI of 7 C-band interferograms. Still some moving terrain might be detected and used to check the subsiding locations found in the ERS descending case.

In this processing the PS/SB network is really very sparse (much less pixels show a proper phase stability in the area). They are affected by large phase unwrapping errors, as expected. The SCLA errors were wrongly estimated probably because of the low amount of input data - some errors propagated into SCLA and caused a detection of a false deformation. This error would propagate into second iteration of phase unwrapping if left in the estimation. To achieve a proper SCLA estimation one should use only well unwrapped interferograms and this almost couldn't be achieved here. After experimenting I realized that with this low amount of input data (that have too long temporal and in two cases also perpendicular baselines) any attempt for SCLA estimation ends in a misdetection of the deformation.

So in the end I had to drop both interferograms of $B_{\text{perp}} > 800\text{ m}$ from the whole processing. Then the 3D algorithm didn't use these problematic interferograms. I have rerun the phase unwrapping process without using previous estimation of SCLA (I used only estimated phase ramps) and repeated the same steps with the same parameters but without these two interferograms. Because the SCLA cannot be properly estimated, the unwrapping process still yields high errors. Only interferograms with small B_{perp} can be quite properly unwrapped. So for the final PS result I have dropped also an interferogram of $B_{\text{perp}} = 493\text{ m}$ leaving only 4 interferograms with $B_{\text{perp}} < 230\text{ m}$.

In SB processing also the dropped acquisitions were used since they could be connected in smaller baselines configuration (the network can be seen on Fig. 3.3.8). Here the SCLA was estimated better so also the interferogram dropped from PS processing (of $B_{\text{perp}} = 493\text{ m}$) could be properly unwrapped and used here. One may experiment with using this SCLA also for PSI processing, this can be done also after merging both PS+SB solutions.

I have to conclude that in this case only very small baseline interferograms could be used. In the SB processing, however, too many pixels were removed. The pixel count can be enlarged using pixels with a larger standard deviation of their phase distribution. Since I don't consider this set of 8 images to be able to properly describe the deformation in my AOI, I didn't continue to improve the results here.

In the final result the locations of the main subsidence were really detected and confirm the detected subsidence areas found in ERS descending data.

ERS descending processing (08/1995-06/1999) In the ERS case, the largest amount of data is available, 49 images of the track 494 ranging April 1995 - December 2000. Later acquisitions couldn't be used for a high Doppler centroid variability (see Fig. 3.2.1). In the first processing attempt of all these images, all detected PS points were considered noisy by StaMPS filtering algorithm and were removed.

I have chosen only a subset of interferograms based on quite strict parameters of $B_{\text{perp}} < 650 \text{ m}$, $B_{\text{DC}} < 150 \text{ Hz}$ - the subset consists of 20 interferograms only from ERS-2 that are ranging August 1995 - June 1999. For the processing, I have chosen an appropriate master image of 28 July 1997 - the configuration depicted in Fig. 3.2.1 is related to this image.

This date is a week after an end of catastrophic 150-years floods in the region. In this image some large scale temporally uncorrelated (i.e. only occurring in this image) artefacts can be detected that might be related to the flood after-effects. Since this day scattering clouds were detected, these artefacts can be related to atmospheric effects. However the APS was estimated as too large. The range of $(-4.1; 6.3) \text{ rad}$ can also mean large scale terrain changes observable only during this date ranging $(-1.8; 2.8) \text{ cm}$ in LOS. The APS of 28 July 1997 is shown in Fig. 3.3.9a, against the APS for 29 April 1996 master (see further). One may investigate this deeper to find a usage of the APS for the flood effects determination.

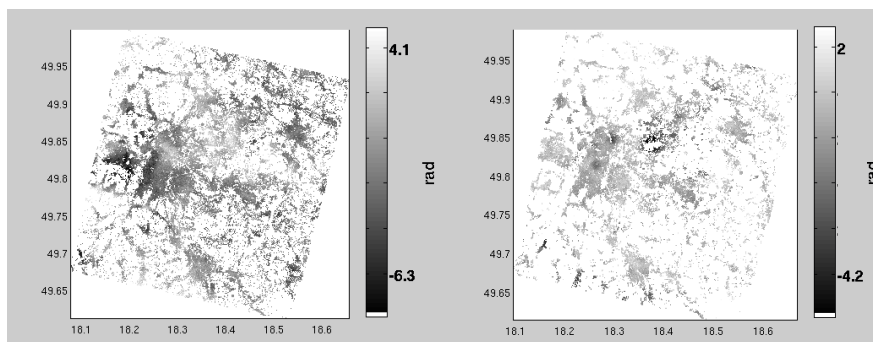


Figure 3.3.9 – Atmospheric phase screen of StaMPS processing master image: (a) 28/07/1997 and (b) 29/04/1996

Note that with this strict selection (even that theoretically also much more images can be used for such MT-InSAR processing) the highest number of phase stable pixels were picked and the deformation rates are estimated in the highest rate comparing to other processing, even that the resulting rates still seem to be underestimated.

From an incremental plot of deformations with around 1 year difference in Fig. 3.3.10 it can be concluded that the estimated subsidence seems to change in time - since 1998 the deformation gets lower. This seems to be a computation error. As can be seen from the dataset baselines plot in Fig. 3.3.8, for 1995-1997 only 6 interferograms were available while within 1998-1999 even 12 interferograms were used for PSI (from the set of 14, two had to be removed for improper unwrapping). It seems that for 1995-1997 where the temporal baselines were larger, more phase jumps were supposed by the unwrapping algorithm.

Comparing the mean velocities computed for these two periods in Fig. 3.3.11, one can observe changes in locations with a maximal rate of subsidence. This can be also an estimation error but can be related to the real subsidence changes in the terrain - this is to be investigated also by comparison with levelling data.

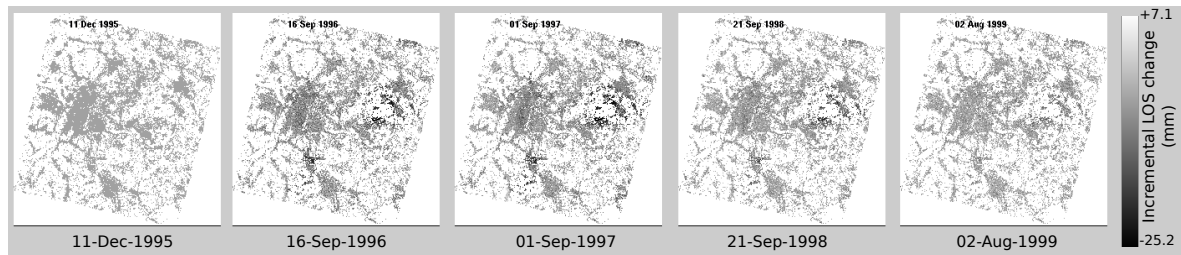


Figure 3.3.10 – Incremental deformation estimations between selected acquisition times of ERS descending

In the end the 18 selected interferograms estimated over 76 500 pixels in PS processing and more than 34 000 pixels in SB mode. Many of the SB points do not overlap with the points detected as PS, so after merging, 97 000 pixels were evaluated by StaMPS clearly showing subsidence areas that correspond with locations of (even closed) mines of rate up to 3 cm/year of mean subsidence velocity in the ERS line of sight (which inclines of around 21° from vertical).

ERS descending processing (10/1995-12/2000) To qualify the previous ERS processing, I have maintained a similar processing with a larger set of data and a different master image. For a different master I have chosen an acquisition taken at 29 April 1996. In this date the ERS-2 formed a “tandem” configuration with ERS-1 that took an acquisition previous day. I have used this tandem pair in advantage for a precise geocoding and for assessing a correct APS estimation (Fig. 3.3.6). However using this acquisition, many formed interferograms had to be dropped due to large baselines.

From 48 formed I have chosen only 25 interferograms for PS processing that show some higher overall coherence and a noise standard deviation less than some 50° . Note that visually an interferogram can seem very decorrelated but it still contains an extractable data of selected phase stable points, even that the backscatter of a pixel will differ due to scattering variability of objects when observed from too different positions (Doppler centroid difference and B_{perp} effects) or that will move in time.

I have formed 253 interferograms suitable for the SB processing. Even that many of them show a large noise standard deviation, I haven’t dropped any to achieve as highest temporal sampling as possible. Only a suitable subset was used for SCLA estimation.

A comparison with the previous attempt is shown by selected subsets in Fig. 3.3.11. Even that the number of phase stable pixels is significantly lower, the results of 1995-1997 are very similar - probably because a higher temporal sampling of SB processing, it shows a more proper phase unwrapping result (it can be proved that the effect visible in the top-left image, i.e. SB of previous processing with 28 July 1997 as a master, is in fact an APS residual of that master image). More difference is visible in the case of the 1998-1999 subsets. The subsidence locations are found the same but the estimated rate differs significantly - the results must be compared with levelling.

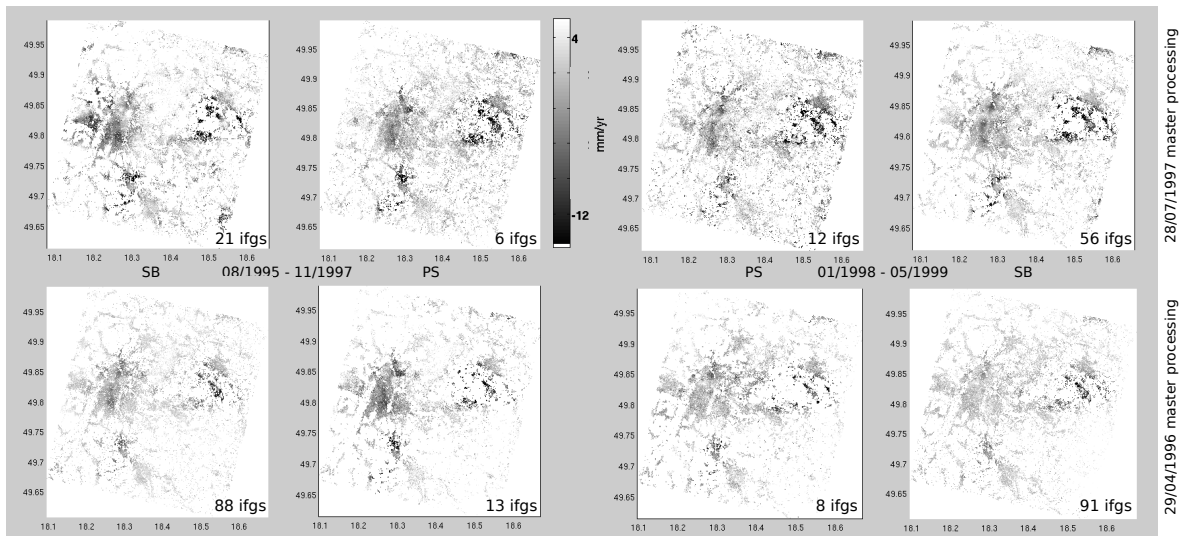


Figure 3.3.11 – Comparison of mean LOS velocity results of two attempts of ERS processing

Envisat ascending processing (12/2002-09/2010) From this period, 27 promising interferograms for PS processing with relatively short baselines and relatively regular temporal sampling were formed from oversampled data. An acquisition of 31 May 2005 was chosen as a master, for the achieved images configuration overview see Fig. 3.2.5 or an interferogram network in Fig. 3.3.8. During this date there was a strong rain of about 22.3 mm/day. It was a second day of raining, storms and drizzle. The rain in a summer day can be dangerous for using in the processing here since the ascending pass is achieving an image during the evening when the water may be evaporated more into the air due to evening temperature changes. Because the StaMPS algorithm assess the master APS quite confidently and there is a fair amount of available data, I chose this acquisition anyway as a master of the PS stack.

After around 10 iterations of phase unwrapping and recomputation of SCLA I have been forced to drop 5 interferograms that couldn't be unwrapped reliably. Two of these interferograms had a $B_{perp} > 700$ m, the other 3 were taken in a winter time so I suppose the problems were caused by a presence of a snow cover.

For SB processing, 75 interferograms were formed in total. For SCLA estimation I have selected only 29 interferograms with a $B_{perp} < 200$ m. After the final SCLA computation I have rewrapped all the SB interferograms using 3D unwrapping method.

Envisat descending processing (01/2005-09/2010) Acquisitions of this track show very long temporal gaps in the period 01/2005-04/2009 and large B_{perp} deviations (see Fig. 3.2.4 or Fig. 3.3.8). Using all these 17 (oversampled) images, 58 885 individual pixels were detected in total by both PSI and SB processing. For PSI processing, 3 interferograms were dropped due to large deviations of unwrapped phase, all of these were formed with winter time acquisitions supposing also a reflection from a snow cover.

During processing I have realized large unwrapping errors and probably wrongly estimated SCLA. This wasn't obviously caused only by poor temporal sampling and large B_{perp} . These

errors can be related to the weather conditions during acquisitions². A relation between the weather factors, B_{perp} and estimated noise error standard deviation is plotted in Fig. 3.3.12. However, for more confident conclusions about such dependency, a larger dataset should be used.

Date	B_{perp} (m)	Humidity	Weather conditions	σ_{noise} (°)
17/01/2005	530	60%	clear	53
21/02/2005	559	70%	mostly cloudy	63
02/01/2006	250	100%	light snow	57
09/10/2006	727	65%	clear	65
22/01/2007	717	65%	clear	64
26/02/2007	63	100%	overcast, light rain	55
17/03/2008	207	80%	mostly cloudy, rain?	34
06/04/2009	529	73%	scattered clouds	44
11/05/2009	199	68%	clear	32
20/07/2009	0	64%	partly cloudy	45
24/08/2009	54	68%	partly cloudy	30
07/12/2009	254	100%	overcast, rain?	34
11/01/2010	291	93%	overcast, snow?	61
31/05/2010	70	90%	rain showers	34
05/07/2010	111	78%	cloudy, rain?	30
09/08/2010	397	78%	scattered clouds	40

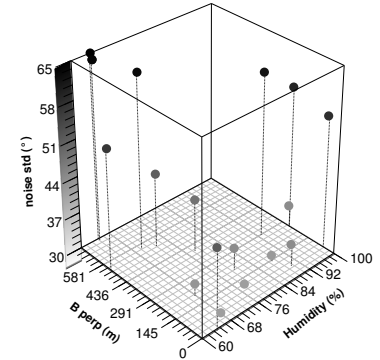


Figure 3.3.12 – Observed relation between B_{perp} and weather conditions (air humidity) factors on noise standard deviation σ_{noise}

The phase unwrapping was most sensitive for B_{perp} conditions, the weather problem was a secondary factor - if a proper set of interferogram is used, the atmospheric delay errors can be properly removed by SCLA error estimations. Within the configuration of these acquisitions confident results weren't achieved. I have performed several iterations of the unwrapping process, together with the SCLA modelling, using stronger filtering options. This way however, local deformations got lost in smoothing.

A more proper attempt would be to use only acquisitions of 2009-2010 since they are better sampled temporally and were taken from a closer satellite position. Still the weather wasn't optimal in such case (4/9 acquisition were probably affected by precipitation). Such processing was performed using SB - here I have used 32 interferograms formed from acquisitions 2008-2010 only (because of small B_{perp} of several combinations, also the acquisition of 2008 was used). Here some unwrapped noise can be found, but most of it was removed by SCLA, without a need of reweeding PS points.

²Data about weather conditions were achieved from Ostrava Mošnov airport data collected by Weather Underground [18]

3.3.3.2 StaMPS Application in a Subregion

There are several issues that should be noted for the whole area of interest. The area is mostly rural, subsidence is both spatially and temporally variable and can achieve a very high rate of decimetres per year in many places. The subsidence locations will be compared with levelling results later on. However it can be seen that the StaMPS processing technique most probably underestimates the deformation rate due to large phase unwrapping errors.

The processing described in the previous section was applied for the whole undermined region. It shows an overview of subsiding places. Here I could figure out which data yields the highest coherence and so it will be possible to use this stack for a more optimized processing in a selected subregion.

Parameter	default	optimized	Parameter	default	optimized
max_topo_error	5	10	unwrap_time_win	730	365
clap_win	32	16	unwrap_gold_alpha	0.8	5
weed_standard_dev	1.0	1.5	unwrap_grid_size	200	100

Table 3.3 – Changing parameters of StaMPS processing optimizing results for local areas

Table 3.3 shows parameters that were changed to optimize the MT-InSAR results. I have selected only interferograms that show a high overall coherence, removed these including unwanted weather conditions (snow cover, obviously strong atmospheric effects), cropped them to a smaller area of interest and reprocessed by StaMPS. Maybe even stronger changes in parameters may take place, this is a topic to further investigation.

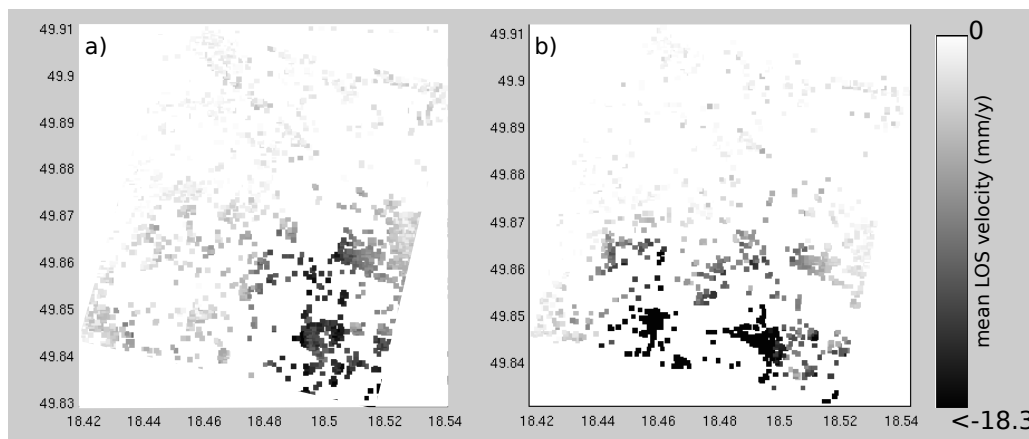


Figure 3.3.13 – Mean LOS deformation velocities in Doubrava area from ERS (1995-2000): a crop from general OKR processing (a), and reprocessing using optimized parameters for a local area (b)

This was performed in Doubrava surroundings where there was a need for a landslide monitoring of a place nearby a fast subsidence. The processing and final results of the subregion will be described in Section 4.7.2. Hereby in Fig. 3.3.13 I present only a comparison of mean velocity results from a general processing and the one optimized for a smaller area.

Note that the number of selected pixels remains similar, even that I expected a strong increase of them. In the case of using optimized parameters, subsidence rate values were estimated much higher (more phase jumps were detected).

For general comparison in Fig. 3.3.13 I provide a colormap stretching to (-18.3; 0) mm/year that fits the subsidence w.r.t. the same reference point in the general parameters case, but it must be taken into account that within the “optimized” parameters the maximal subsidence velocity was estimated even at the rate of -39.5 mm/year. In the Fig. 3.3.13b case the maximal subsidence is detected in southern area, however it was evaluated as a more or less stable area in the case of whole OKR processing of Fig. 3.3.13a. This needs to be confirmed, for example by levelling. It must be also taken into account that the phase unwrapping may not be performed reliably in the corner parts of a scene. Here the middle of the scene was the target of investigations which is estimated in both cases similarly.

3.3.4 Comparison with Levelling Data

3.3.4.1 Data Preparation

To compare MT-InSAR estimations with levelling data the character of the unwrapped phase values must be considered. MT-InSAR estimations are in fact always related to some reference time (same as levelling measurements) but also to some spatial reference point. I have obtained levelling data that were already recomputed to absolute height values. Similarly to (Hanssen, 2001) I have related heights of levelling points to one selected to form levelling double difference values. For MT-InSAR data that are valid for the satellite LOS direction, I have recomputed these to the metric units in vertical direction by taking into account look angle θ_{look} :

$$\Delta H_{vert} = \Delta \varphi_{LOS} \cdot \cos \theta_{look} \cdot \frac{\lambda}{4\pi} \quad (3.3.1)$$

In addition, I have cropped and recomputed all available MT-InSAR processing attempts using only highly coherent interferograms without snow or too strong APS to achieve more dense phase-stable pixels network in the chosen subarea. For a spatial reference point I have selected a phase-stable pixel that was in the smallest distance from the reference point selected for computation of levelling double differences. This way the MT-InSAR results could have been compared with the levelling data.

Because the PS points are obviously not the same points as used for the levelling, I have used a mean value of deformation from all PS points that were located in a 50 m radius from the selected levelling point. Height change values were recomputed w.r.t. first overlapping MT-InSAR date (levelling height was interpolated from one previous and one next measurement in a proper ratio).

3.3.4.2 Selected Results

Within the Fig. 3.3.14 I demonstrate usual results of the MT-InSAR processing. In a case of any larger deformation the phase unwrapping results wrongly. In fact I haven't found any real fitting pair of a PS and levelling point in the investigated data. This is however related to the fact that the levelling points measure high deformation rates that are not possible to properly estimate using C-band MT-InSAR.

The interferograms of ERS in descending pass have a good temporal sampling, deformations can be estimated more properly. Still the deviation is too high to be used operationally.

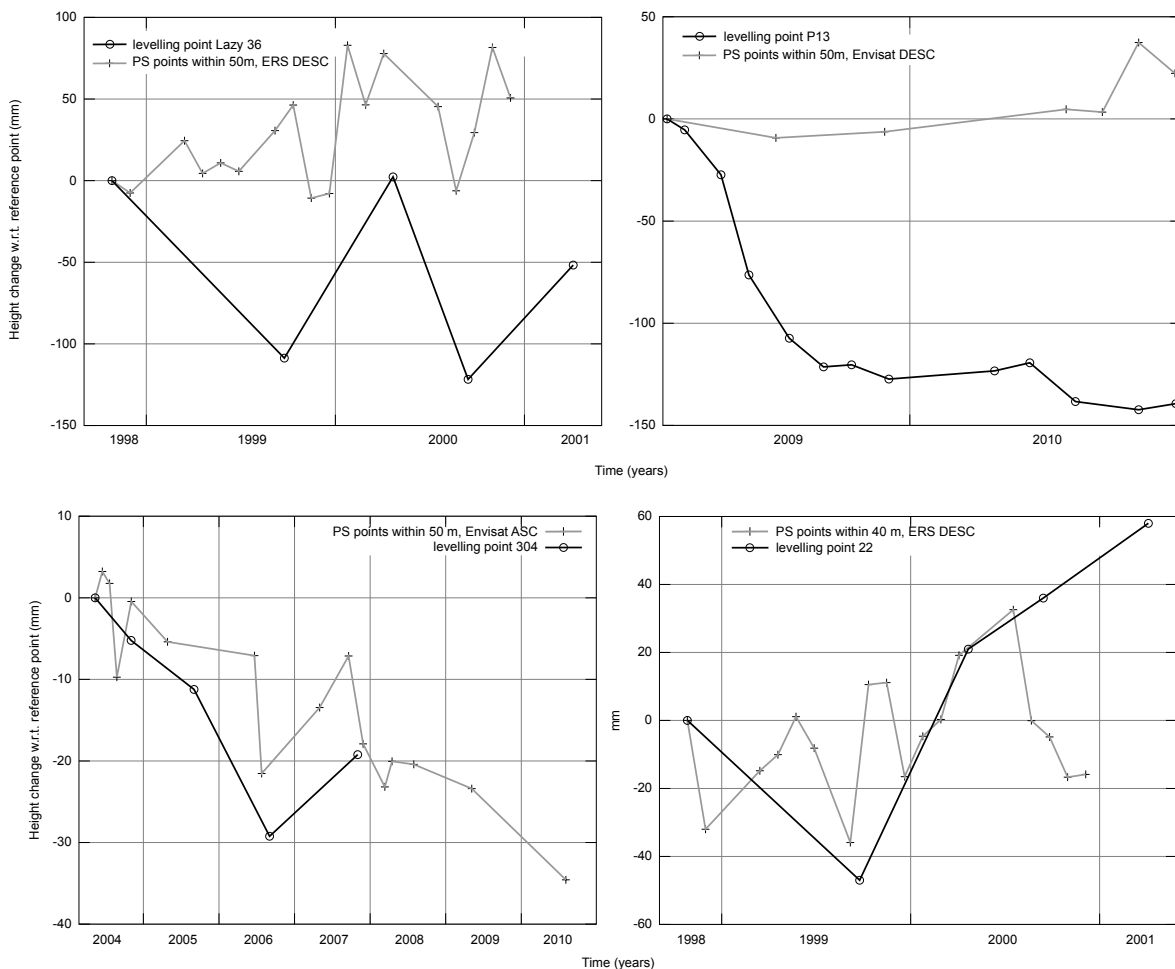


Figure 3.3.14 – Selected results from levelling comparison

3.3.4.3 Conclusions

Unfortunately there are too many error factors that incorporate into the final MT-InSAR processing results. Even with the most optimistic scenario, i.e. that all the errors were removed properly, the main remaining problem is the phase unwrapping in the places of a fast subsidence.

With a subsidence of a rate higher than $\lambda/4 \cdot \cos \theta_{look}$ per a resolution cell and the acquisition frequency, i.e. 1.3 cm/35 days for ERS/Envisat, the subsidence rate estimations will be affected by phase unwrapping jumps that have to be modelled computationally and the real velocity are most likely to be wrongly estimated. Even this value is very optimistic, in reality much smaller deformation can be unwrapped really properly from noise-free data. The most reliable phase change for unwrapping should be 0.6 rad according to (Colesanti et al., 2003), i.e. 0.27 cm/35 days for ERS/Envisat (in the line of sight).

In the MT-InSAR processing itself not all of the interferograms could be used. Largely decorrelated interferograms or interferograms including snow had to be removed from processing - this indicates even higher sensitivity for the subsidence rate in the phase unwrapping.

The principle of processing using StaMPS is that it manages to unwrap phase values to estimate a deformation rate without fitting to any a-priori known model. However in the locations of too large subsidence the estimation failed. Note that as a reference point for double-differences computation of MT-InSAR, also a point in an unstable area was chosen. Therefore the error may double. But even by choosing a relatively stable point the results didn't fit with the absolute levelling measurements.

Even that the timeline results would be very appreciated for an application in monitoring of subsidence, in this case they seem too unreliable. I will assume this to be connected with a high rate of subsidence and will use the timelines only in cases where a lower subsidence is expected, for example monitoring effects after mine closure.

3.3.5 Discussion

The character of investigated area is in general not very suited for common InSAR processing. It is mostly covered by vegetation and there are mostly natural scatterers within the subsidence basin itself. The overall decorrelation is significant in most of the C-band interferograms and the area needs to be processed by MT-InSAR or an advanced filtering to achieve some suitable results. Using an advanced processing of StaMPS that is well suited for an observation of natural objects changes I have detected very similar deformations in the whole undermined area using different datasets. Computation of their rates seems underestimated, however this will be investigated further. The whole subsidence basin is bordered by points of a mean subsidence velocity ranging within 3.5 cm/year (in the LOS direction). In the area of interest, much faster subsidence of up to a meter/year is expected. This is undetectable using C-band InSAR only - such a high change will often cause a phase instability of affected (local) area and even if detected as in a stable pixel, the phase cannot be unwrapped correctly without some a-priori known temporal model.

It was observed that atmospheric effects cause problems with phase unwrapping. These effects and SCLA in general can be estimated with a proper number of highly coherent interferograms. These error estimations were not reliable in the Envisat descending case. This dataset has too large temporal gaps and B_{perp} as well (see Fig. 3.2.4). In the case of processing of descending ERS acquisitions there is a large number of more appropriate acquisitions. I have performed two StaMPS processing attempts using different master images of ERS. Thanks to an existing tandem pair of a 29 April 1996 master case it was

proven that StaMPS estimates the APS quite properly. In the second case an extreme APS was estimated probably well of an image from 28 July 1997. It should be profitable to rebuild the whole InSAR data stack again with the corrected master image to achieve a larger amount of detected PS points. Another idea for a further work can be an investigation of the APS from 28 July 1997 to determine short time deformations that might have been caused by the large flood that occurred a week before.

3.4 Final InSAR Overview of Regional Subsidence

3.4.1 Overview of OKR Subsidence Basin

The progression of the subsidence in the area can be clearly read from the differential interferograms. Fig. 3.4.1 shows differences within 10 years. First interferogram is from ERS-2 taken with small baselines in proper dates when the vegetation didn't cause high decorrelation. The second interferogram is from Alos Palsar. Due to different wavelengths, temporal baselines and look angles these interferograms cannot be compared directly. Anyway the changes of subsidence activity in the locations of mines impact is visible. The Alos Palsar interferogram seems smoother due to better penetration abilities of the L-band. Both interferograms were filtered using modified Goldstein filter (Baran et al., 2003).

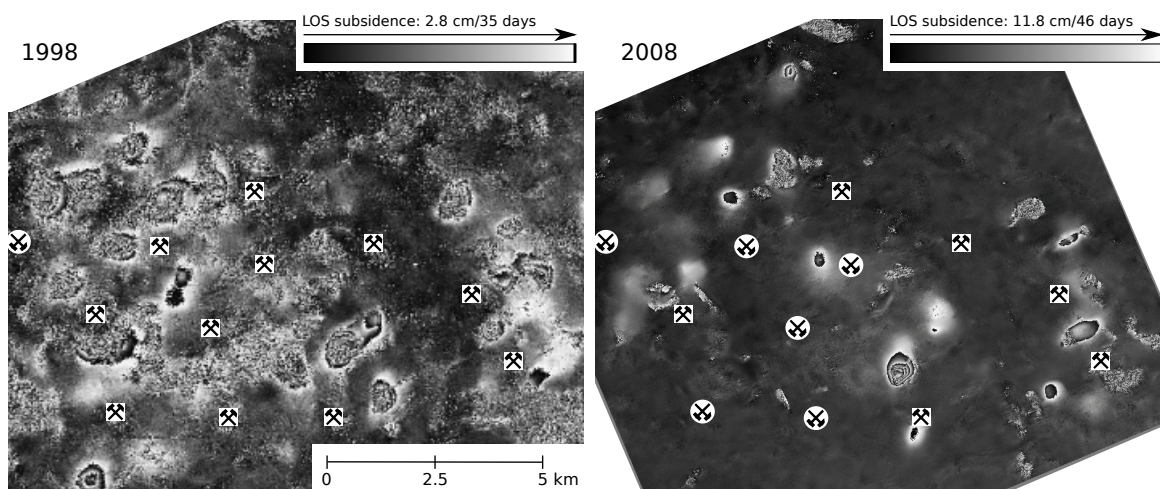


Figure 3.4.1 – Subsidence basin of Karviná district detected from (a) ERS data between 23/02/1998 and 30/03/1998 (35 days), and from (b) Alos Palsar data between 27/01/2008 and 13/03/2008(46 days)

Another example is shown in Fig. 3.4.2. Even though the long temporal baseline, it was possible to achieve an interpretable overview of the whole subsiding area in the Karviná surroundings from Alos Palsar of almost 3 years delay. The Fig. 3.4.2 shows a changing area that is not clearly distinguishable from decorrelated parts, however coordinates of the subsidence borders can be achieved.

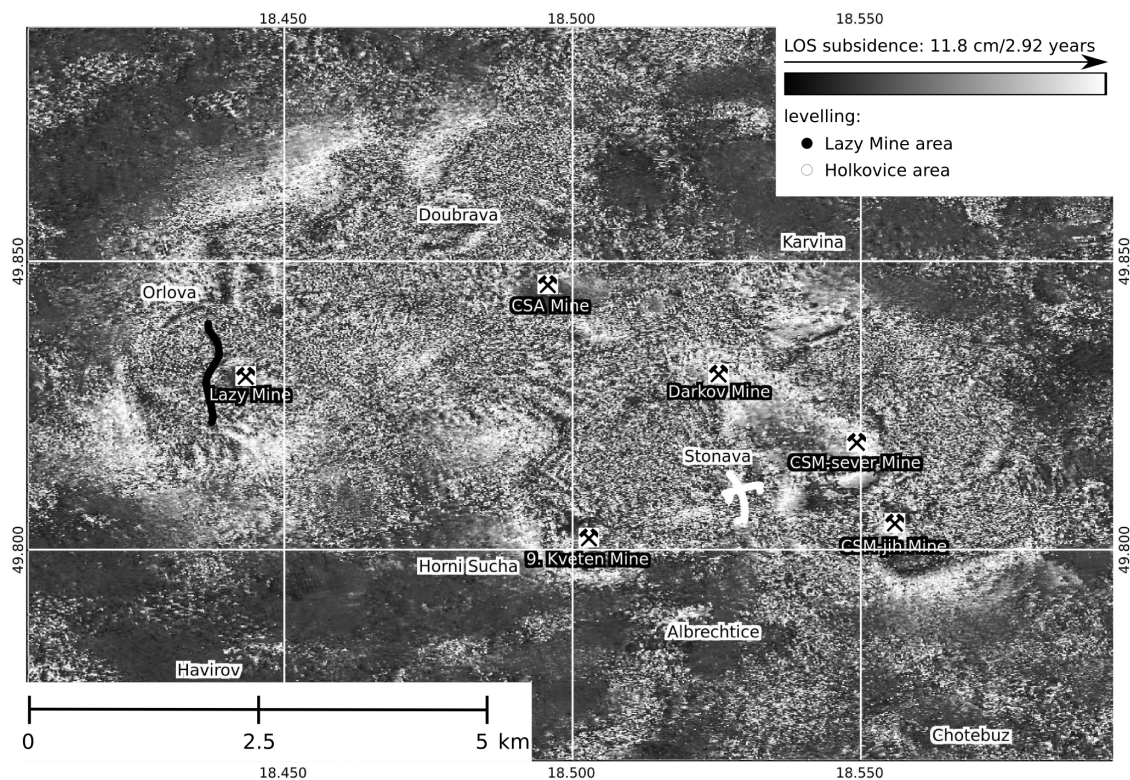


Figure 3.4.2 – Extents of the whole subsidence area of Karviná district as retrieved from Alos Palsar: 25/02/2008 and 27/01/2011. Presently active mines are parts of: Karviná Mine (Lazy Mine and ČSA Mine), Darkov Mine (Darkov Mine and 9. Květen Mine) and ČSM Mine. There are also locations of current levelling missions depicted.

In the Karviná district, the relatively high rate of large scale subsidence can be interpreted clearly from the DInSAR fringes. For the subsidence detection in Ostrava district the situation is different. A subsidence is visible as fringes only on several interferograms with appropriately long temporal baseline. Because of a slower rate of subsidence, the MT-InSAR techniques can be used with an advantage of monitoring urbanized area with a large number of PS pixels. Such monitoring results performed by ERS acquisitions from 1995-1999, i.e. a period of successive closing of mines in Ostrava, was put into a map in Fig. 3.4.3.

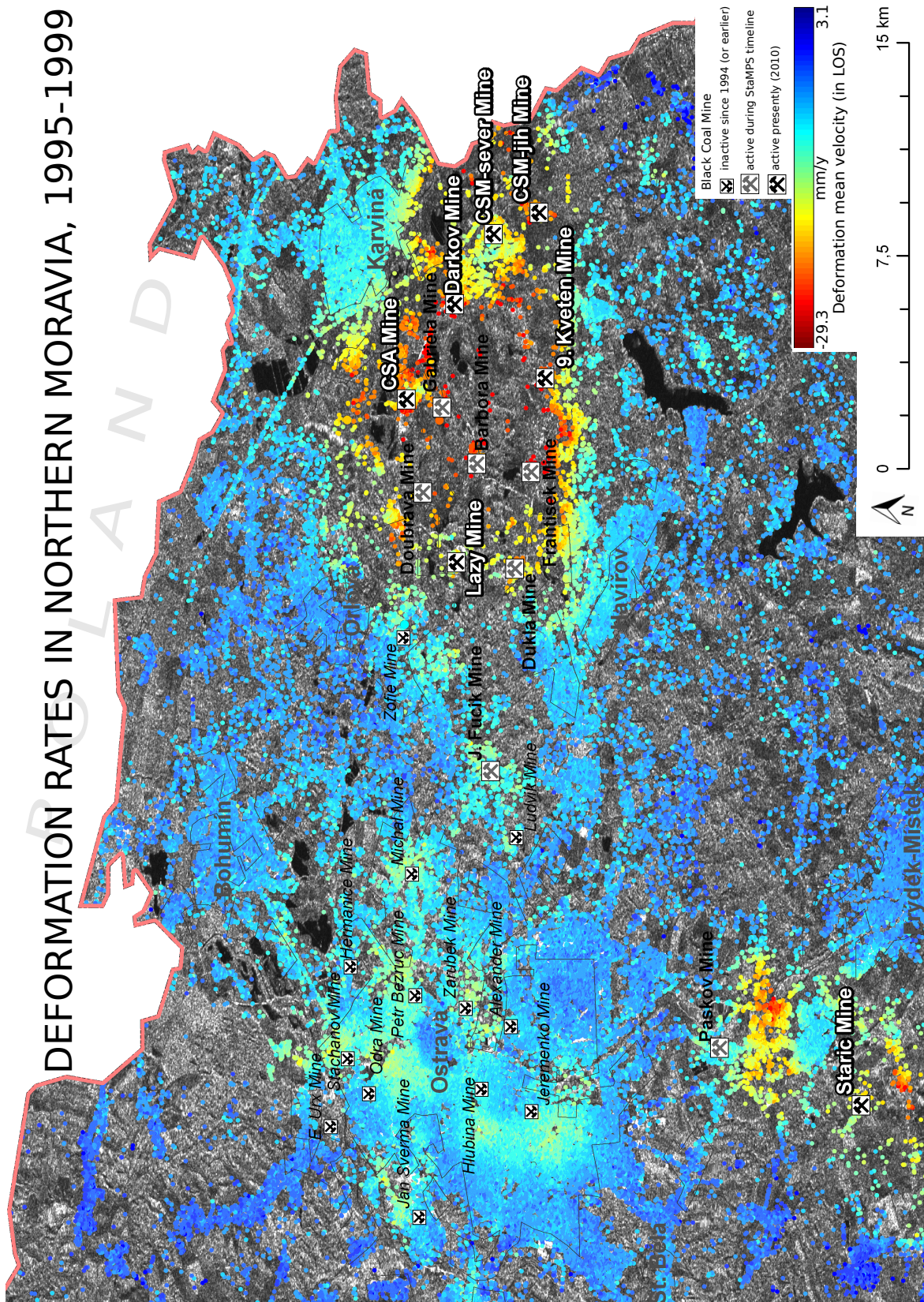


Figure 3.4.3 – The whole region of interest investigated by multitemporal InSAR processing of ERS acquisitions, 1995-1999. Mines marked as presently active merged and changed their names to: Karviná Mine (Lazy Mine and ČSA Mine), Darkov Mine (Darkov Mine and 9. Květen Mine) and ČSM Mine.

3.4.2 Overview of Selected Sites

3.4.2.1 Decay of Mining Activity in Ostrava City

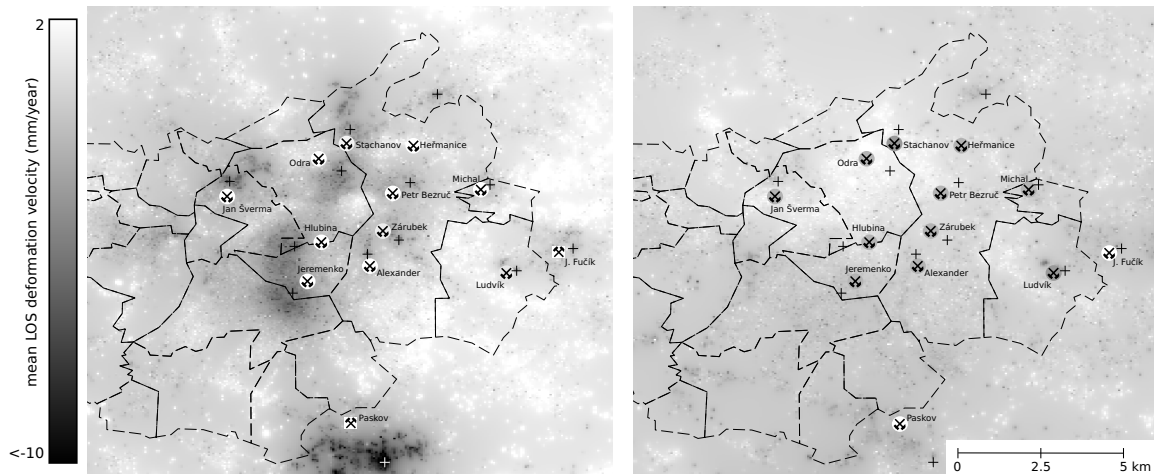


Figure 3.4.4 – Investigation of Ostrava area by MT-InSAR of (a) ERS descending dataset of 08/1995-06/1999 and (b) Envisat ascending subset of 12/2002-09/2010, interpolated by IDW method.

Since 1998 all mines of Ostrava city are inactive. A subsidence is accounted to exist in the city - the post-mining effects can remain several years after the mine closure. Here the multitemporal InSAR processing of ERS data revealed a slow decay subsidence that couldn't be detected using any other technique. The subsidence is very slow, often not producing fringes in DInSAR images. Detected subsiding areas fit well with locations of mines - this can be also read from the Fig. 3.4.3.

Urban areas such as the Ostrava city are the most suitable targets for InSAR. The coherence is preserved high in most of the city area. The phase stable pixels have an outstanding density. Because there is not too high rate of subsidence it is also often possible to reliably estimate the subsidence velocities by MT-InSAR. Actually the MT-InSAR is very valuable in this case - I can provide also differential interferograms where a subsidence is interpreted showing some deformations during 1990s but no deformations can be interpreted from interferograms even with a longer temporal baseline of 2000s. But combining interferograms by MT-InSAR also some (very slow) deformations in the newer set can be extracted - see Fig. 3.4.4. From the Envisat processing approaches it can be concluded that since 2003 (or even sooner) the area is mostly stable. In several locations, some rest subsidence was found, however. Note that for a fine determination of the real stability of an urban area, a more accurate X-band processing is advisable.

I have performed a temporal analysis that reveals the subsidence after mine closures. In Ostrava, mines were successively closed during the whole 1990s. A comparison with the levelling in a non-urban area in Sec. 3.3.4 shown wrong MT-InSAR results. In the city area with much lower expected subsidence rate, the MT-InSAR should be capable of more confident results. Unfortunately, no reference data were acquired to perform some comparison of the reliability of results presented in Fig. 3.4.5 with a levelling or GPS data.

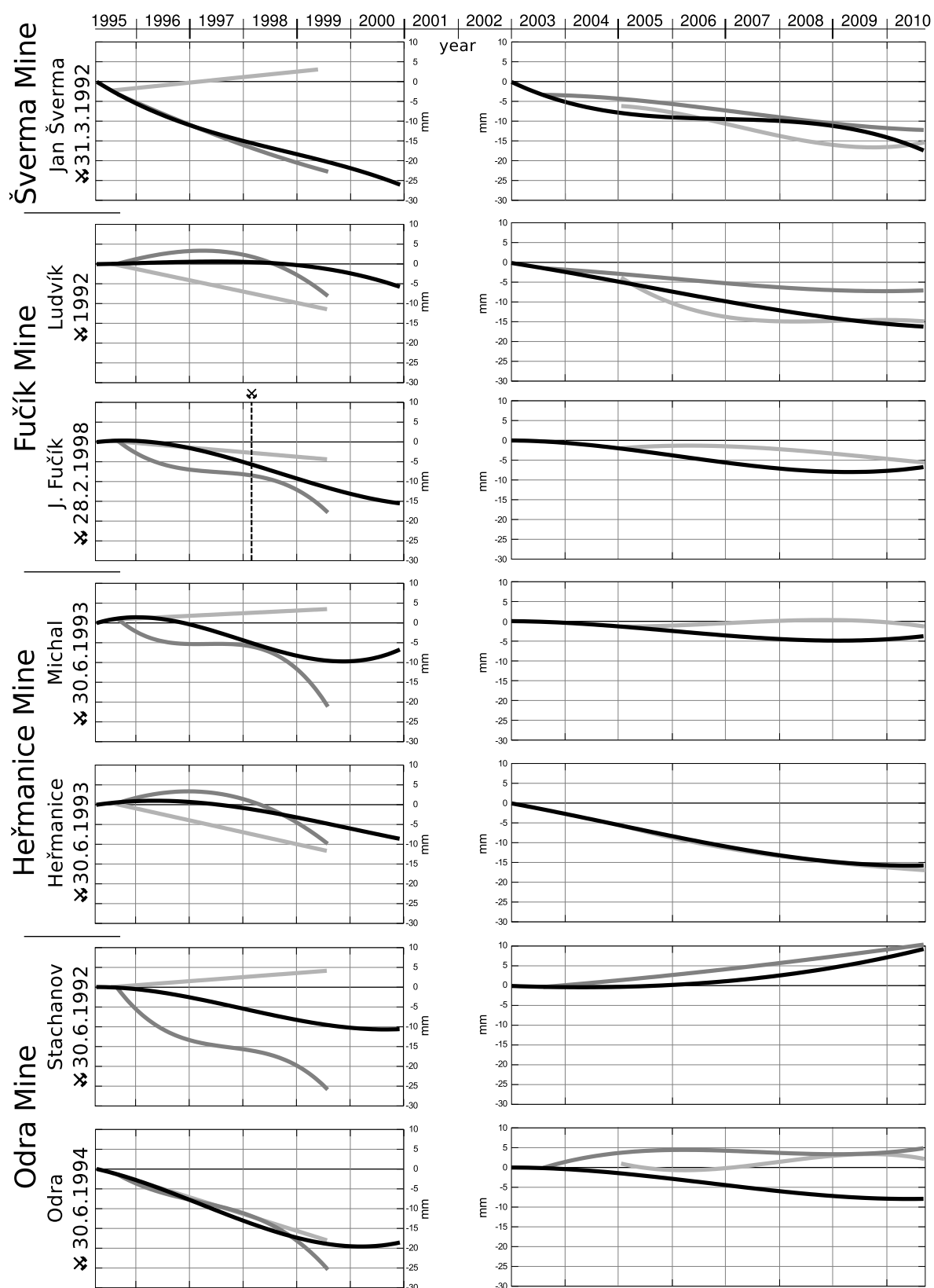
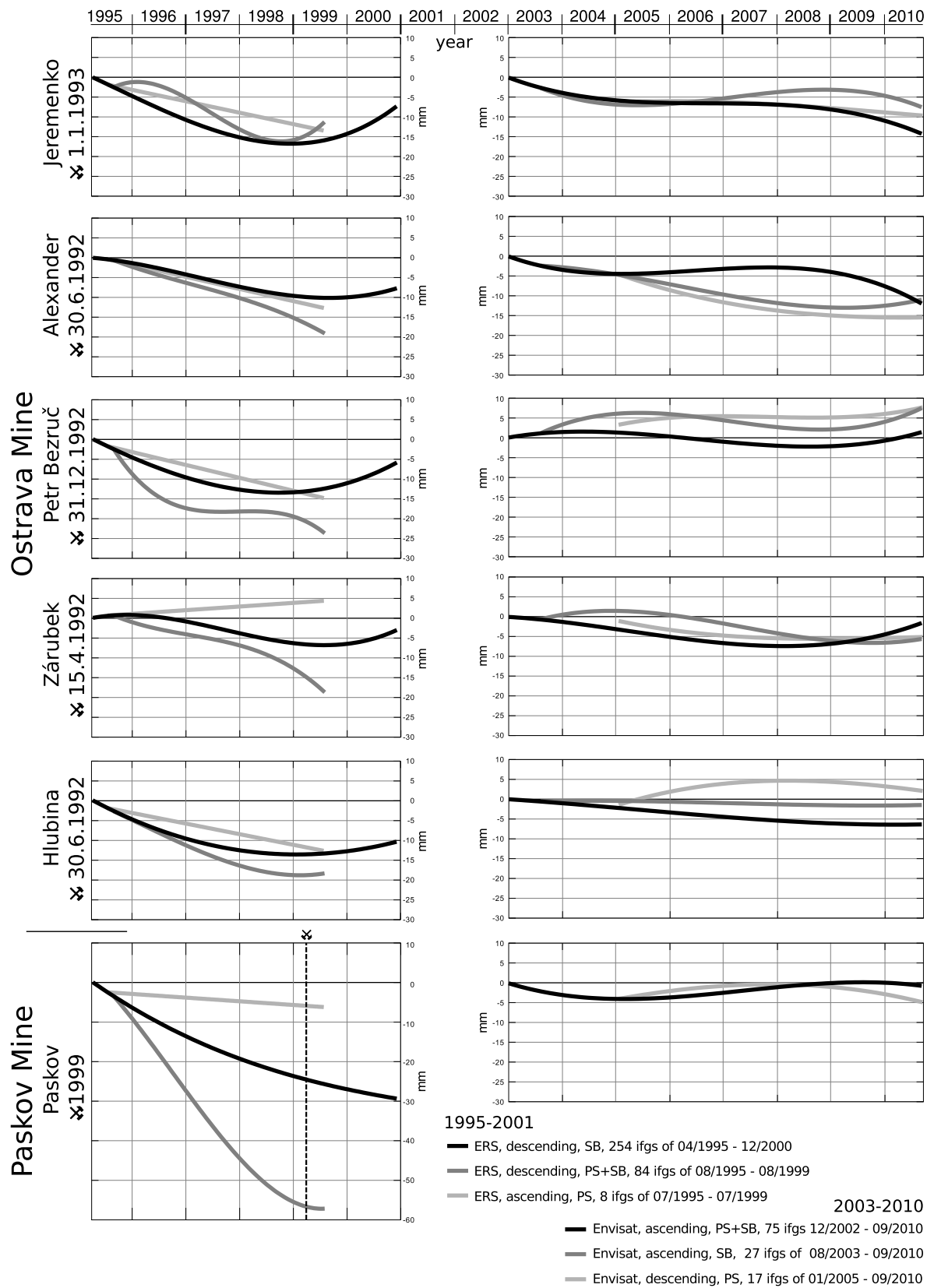


Figure 3.4.5 – Subsidence activity nearby Ostrava mines from MT-InSAR analysis of 1995-2000 (ERS) and 2003-2010 (Envisat) - double-sided figure



To create these graphs, locations were selected in the mines neighbourhood that show some subsidence in the 1995-2000 time series. Around these locations (that are depicted in Fig. 3.4.4 as crosshairs), all pixels within a 150 m radius were chosen, their estimated deformations relatively to a reference value in a (probably) stable areal of VŠB-TUO were recomputed to the first date, a mean value of all these points being fit by a 3-degree polynomial (1-d for ERS ascending case) and an interval difference of fit functions that do not start from the first date in the series was compensated.

Note that ERS ascending data analysis cannot be regarded as confident here since in fact only 4 interferograms within 4 years were used. A dataset named “Envisat, ascending, SB” was created with a more strictly chosen subset (no winter data, very small baselines, less atmospheric influence in slave images), analysis was performed only for Ostrava area. Because of unwrapping problems at the edges of chosen area of interest, I have decided not to include points from this dataset that are located in the Ostrava city borders.

According to the processing results, several locations are affected by subsidence even after more than 15 years after mine closure. As I have mentioned, the subsidence movement should be first confirmed by onsite measurements before concluding about real deformations in these areas.

3.4.2.2 Area of Lazy Mine

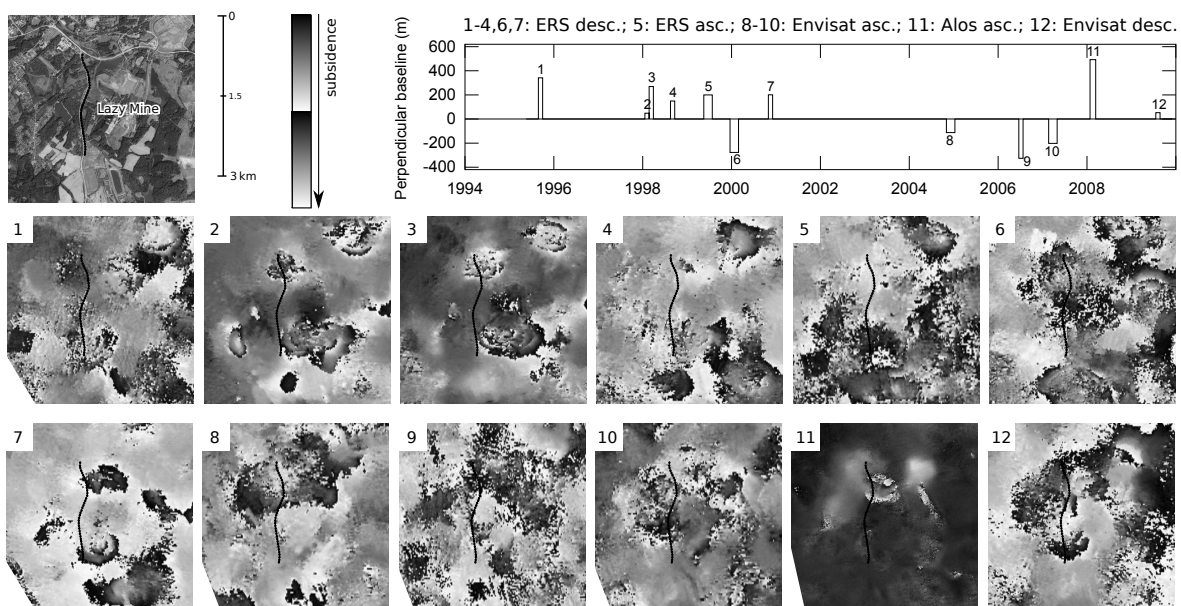


Figure 3.4.6 – DInSAR results of Lazy Mine surroundings, filtered by NL-MEAN algorithm. Background image by Google EarthTM.

A work of (Mulková, 2007) monitors landscape changes in the Lazy Mine surroundings from aerial photography since 1940s. During intensified mining it was found from photos between 1971-1995 that the landscape changed significantly from an inhabited area to a shrubbery, forest, agricultural areas. About 92 houses forming inhabited colonies were demolished due to damages caused by subsidence. Through the years of 1995-2003 the

most of the area was recultivated, subsidence effects are expected much smaller or none at all at these places.

In the same thesis a comparison between digital models of ZABAGED (2003) and a DEM made from contour lines from a national map SM 1:5000 (1951) took place to find height changes in Lazy Mine mining site between 1951-2003 in a range of 16-30 m. If I uncorrectly assume a linear subsidence trend, I should count with a subsidence rate of around 300-580 mm/year. In current ERS/Envisat limits, this will not be possible to estimate by MT-InSAR. This is one of reasons to proceed with a strategy of processing a local area with a (more stable) reference point set already inside a subsidence basin. Still the expected variance can be some 280 mm/year in the area - this would reach the whole 2π phase change even if sampled through the year fully by ERS/Envisat. It will not be possible to properly unwrap such a phase change.

A selected set of differential interferograms where a subsidence may be interpreted from is shown in Fig. 3.4.6. These interferograms were in many cases strongly affected by decorrelation. I have performed an appropriately strong filtering using NL-MEAN algorithm. This way noisy area were overridden (even that not completely) by an intensity weighted local mean replacement. However more detailed fringes disappeared together with the noise. From this figure only subsidence borders can be interpreted.

The area around Lazy Mine is not strongly urbanized. This showed problems in MT-InSAR processing. The processing described in Sec. 3.3.3 used only very stable scatterers that correspond with built structures. A subsidence of these structures was detected and estimated to rates of cca 1 cm/year. There were no points detected directly on the road Lazecká that was monitored by levelling missions. According to these measurements, Lazecká road has sunk up to 7 metres between years 1999-2009. Such subsidence probably cannot be estimated properly using C-band data MT-InSAR.

Still I have tried to process the crop of the area by MT-InSAR using highly overall coherent interferograms only. I have used more relaxed parameters for PS detection so there was a relatively dense initial network of less stable pixels formed of the site. A comparison of final selected points of both attempts is visible in Fig. 3.4.7. In the Fig. 3.4.7b case a smaller area was fully reprocessed - a south-west border of this area ends in the figured place. A phase unwrapping of border area is often wrong, probably because the investigated pixels are not surrounded by other pixels to form a centralized unwrapping network. This can be seen here as too different velocity estimations of similar locations from both approaches. In fact there is a difference within all the processed locations. This may be another unwrapping problem of one (or both) of the approaches, wrong estimated and removed error screens or this doesn't have to be any error at all since in both cases different interferograms subsets were used, with different reference spatial points set.

Because technically the real rate of subsidence is too high, as is expected, it is practically impossible to properly estimate it from C-band data. Thus the MT-InSAR succeeded in both cases. In both cases it detected a subsidence in the area. In the former processing (3.4.7a), more reliable pixels were used that are not affected by surrounding distributed scatterers at all. They represent mostly a strong reflection from buildings.

For a monitoring of subsidence in this site I have to recommend using SAR data of a higher resolution - so pixels may be formed by less contributing scatterers. Using L-band

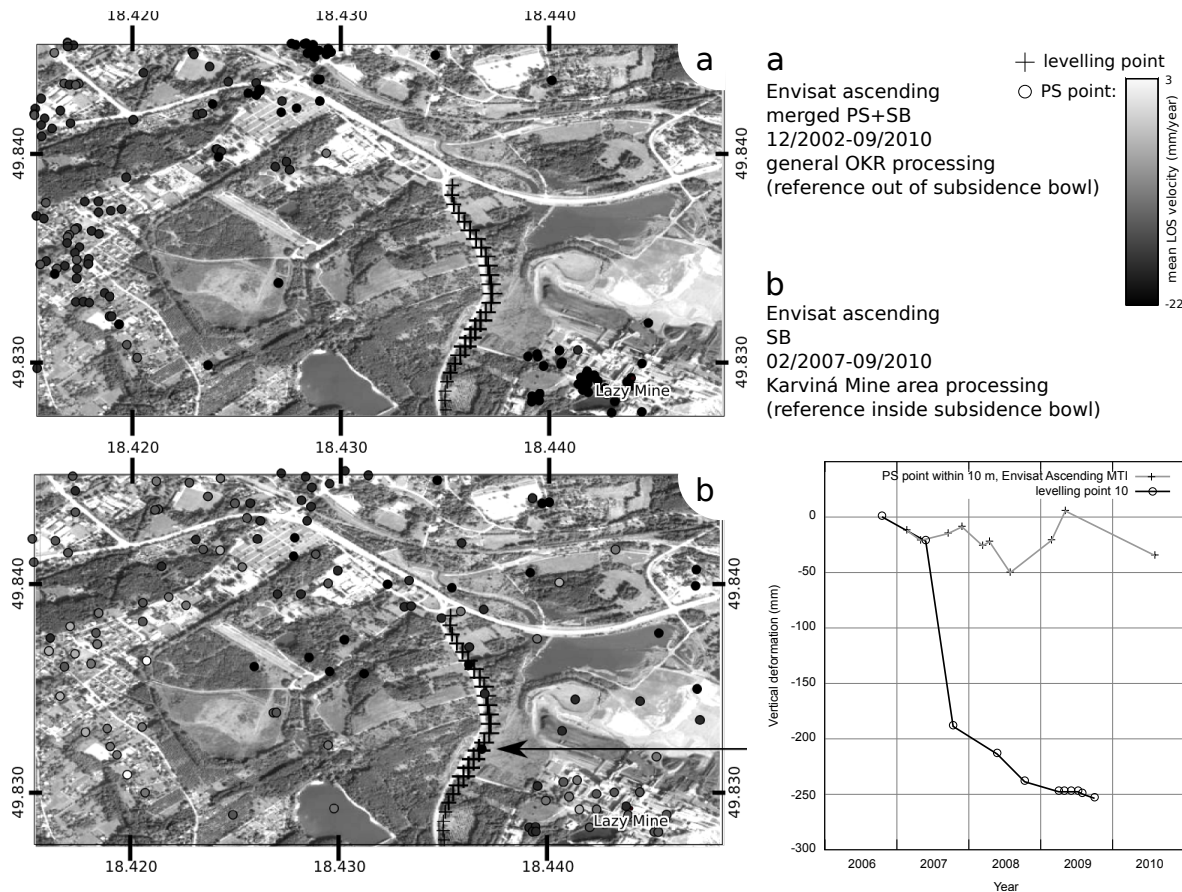


Figure 3.4.7 – Two MT-InSAR processing attempts using Envisat ascending data: a) crop of a full OKR processing (2005-2010), b) reprocessing of Karviná Mine area subset (2007-2010). Values for a graph comparing subsidence trend between a levelling point and a closeby PS point from MT-InSAR(b) were referenced to another pseudo-common point on the Lazecká road. Background image by Google EarthTM.

data would be also beneficial, unfortunately the revisit time of Alos Palsar is too long to properly monitor such high subsidence using MT-InSAR from actually existing data. And also L-band data are often decorrelated here because of a high ratio of deciduous forest on the site which cause problems mostly when combining winter and spring data as it is usual for Alos Palsar.

3.4.2.3 Area of Holkovice

This area is influenced by a mining of ČSM Mine since 1996, according to (Jiráňková, 2006). Mining was performed in two coal beds in a depth of 700-880 m. In both coal beds a height of the deposit can achieve even more than 4 m. Supposing an area where both coal beds were exploited, a total amount of exploited material height can exceed 8 m. Referencing geomechanical concepts, rocks in a layer directly over the exploited area will get impaired and leave some amount of an unfilled space within them. In such a mining depth and current rocks conditions it is expected that these spaces will correspond with around 25% of total exploited material. Rock layers above will lay down and fill all the gaps almost completely,

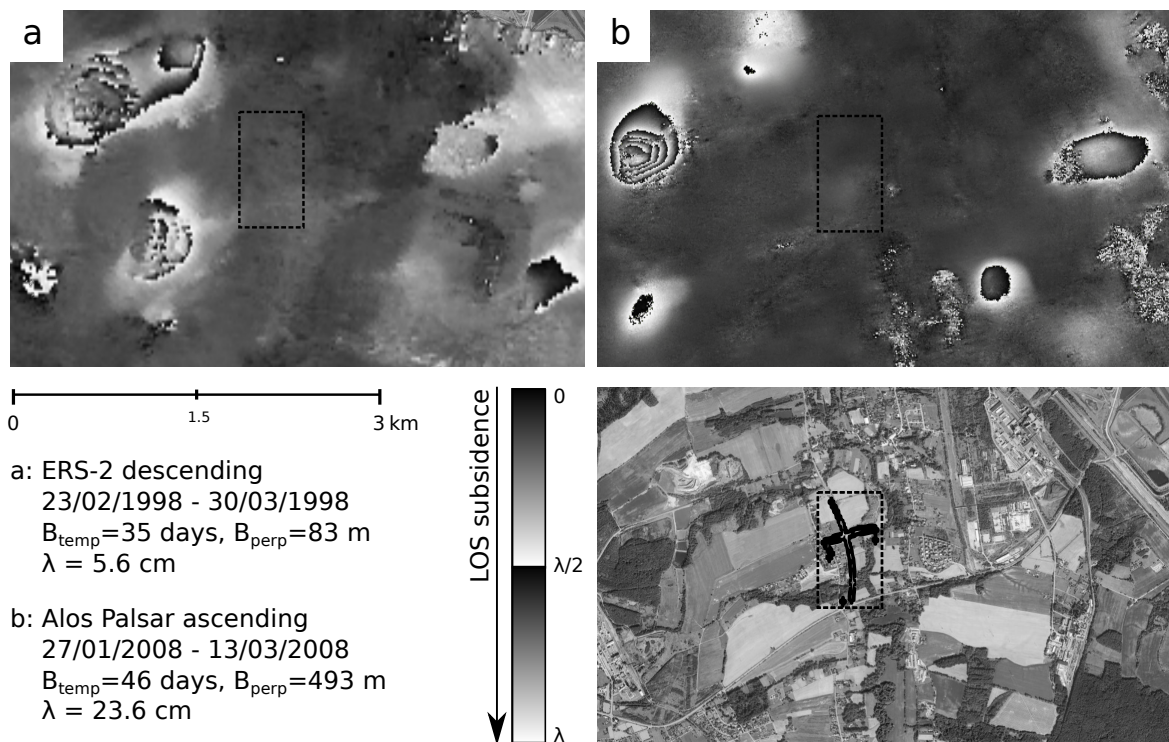


Figure 3.4.8 – DInSAR results around Holkovice area, differences within 10 years. Background image by Google EarthTM.

therefore the final expected total subsidence (that will be formed within several years after exploiting) is around 75% of total retrieved material, in this case up to around 6 m.

An advance of subsidence in this site in a 10 years range as processed from ERS-2 and Alos Palsar data is demonstrated in Fig. 3.4.8. Changes around the levelled subsiding site can be distinguished from these interferograms. The subsidence rate in the levelled area doesn't seem significant from these particular interferograms. On the other hand temporal changes of surrounding subsidence troughs are clearly visible. The actual rate of subsidence of the trough to the W seems to be very high. Interpreting fringes in the Alos Palsar case from 2008, the subsidence trough can descend in the rate of around 70 cm/46 days. The ERS-2 interferogram from 1998 shows much shallower subsidence but it may be out of ERS-2 detectability range as well.

Unfortunately the area is strongly decorrelated in most of interferograms. An example of a filtering effect is seen in Fig. 3.4.9 together with an attempt to inspect the subsidence progression using interferograms. Note that visible square artefacts are caused by a filtering window patching. Phase ramp was cycled to visually match homogeneous areas.

During 2009 the largest subsidence was measured. Some change that was detected within a 35 days in a summer time from Envisat (descending) is shown here in Fig. 3.4.9 - the original interferogram image is heavily decorrelated, the filtered result cannot be reliably interpreted. Still it reveals some deformation directly in the area of levelled site.

In Fig. 3.4.10 I provide an MT-InSAR results, interpolated into a grid of the same extent as in Fig. 3.4.8, using an inverse distance weighting (IDW) method. The values

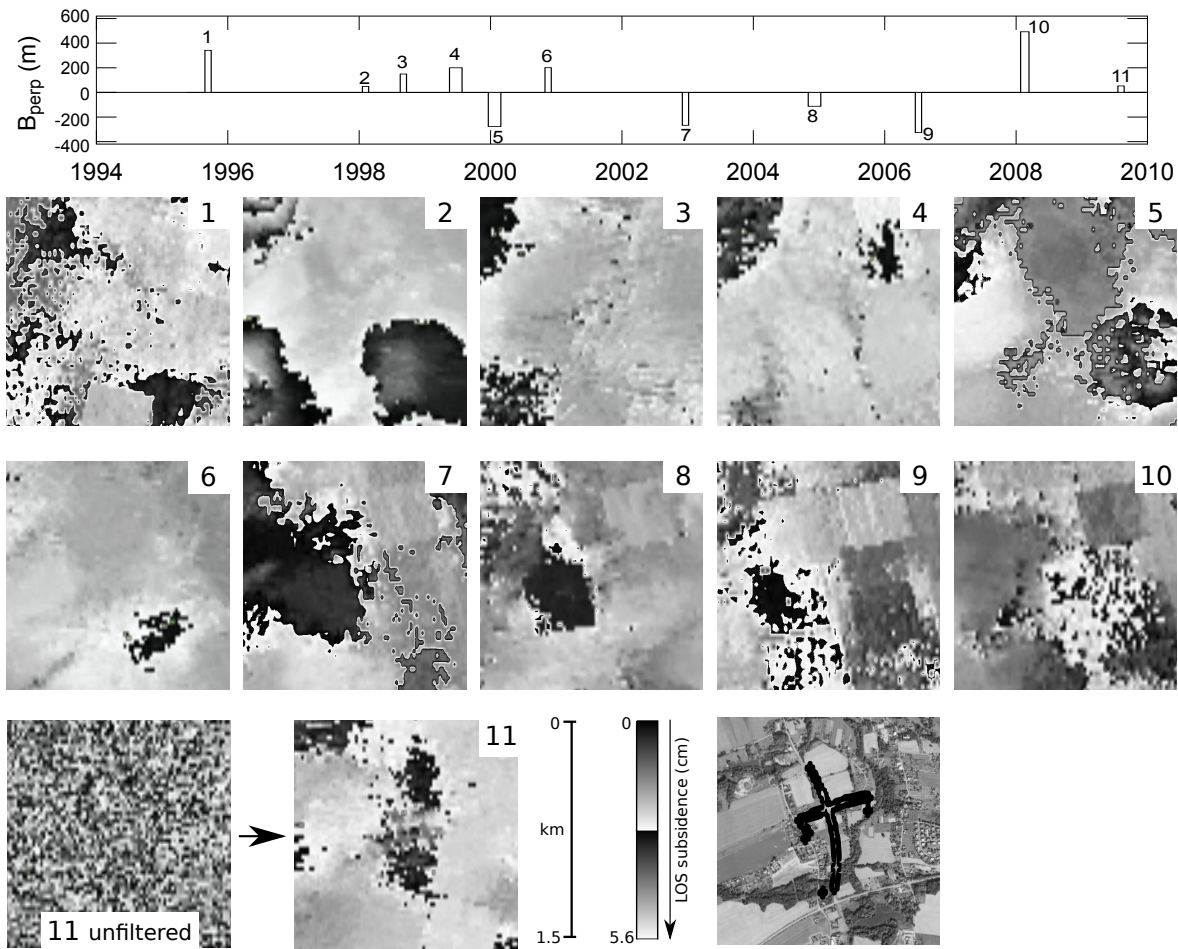


Figure 3.4.9 – DInSAR to observe subsidence progression of levelled Holkovice site. Background image by Google EarthTM.

are recomputed with a reference of a common location (points within a 50 m distance) assumed as relatively stable. Upper part of the figure, i.e. Fig. 3.4.10a,b shows probably more appropriate results - this is a part of the whole OKR processing where only pixels with a high stability were chosen. When applying more relaxed parameters (but for selected coherent interferograms), more pixels were used in the area out of urbanized zone. However this result in Fig. 3.4.10c,d differs significantly from the whole OKR processing above. Comparing to interferograms in Fig. 3.4.8, the detected subsidence troughs projected into these MT-InSAR results - these places were regarded as phase-unstable in the more strict OKR processing and removed, while in the latter case of reprocessing they are used but their rate is most probably underestimated. Thanks to much larger number of detected PS/SB points after reprocessing, it was possible to reconstruct also some subsidence area south from the levelled roads. Unfortunately I have no data to compare this finding with - it cannot be declined that this detected subsidence is not only a result from incorrect phase unwrapping/SCLA estimations. Also, the levelling data simply shows too large subsidence that cannot be matched by any of the ERS/Envisat processing strategies.

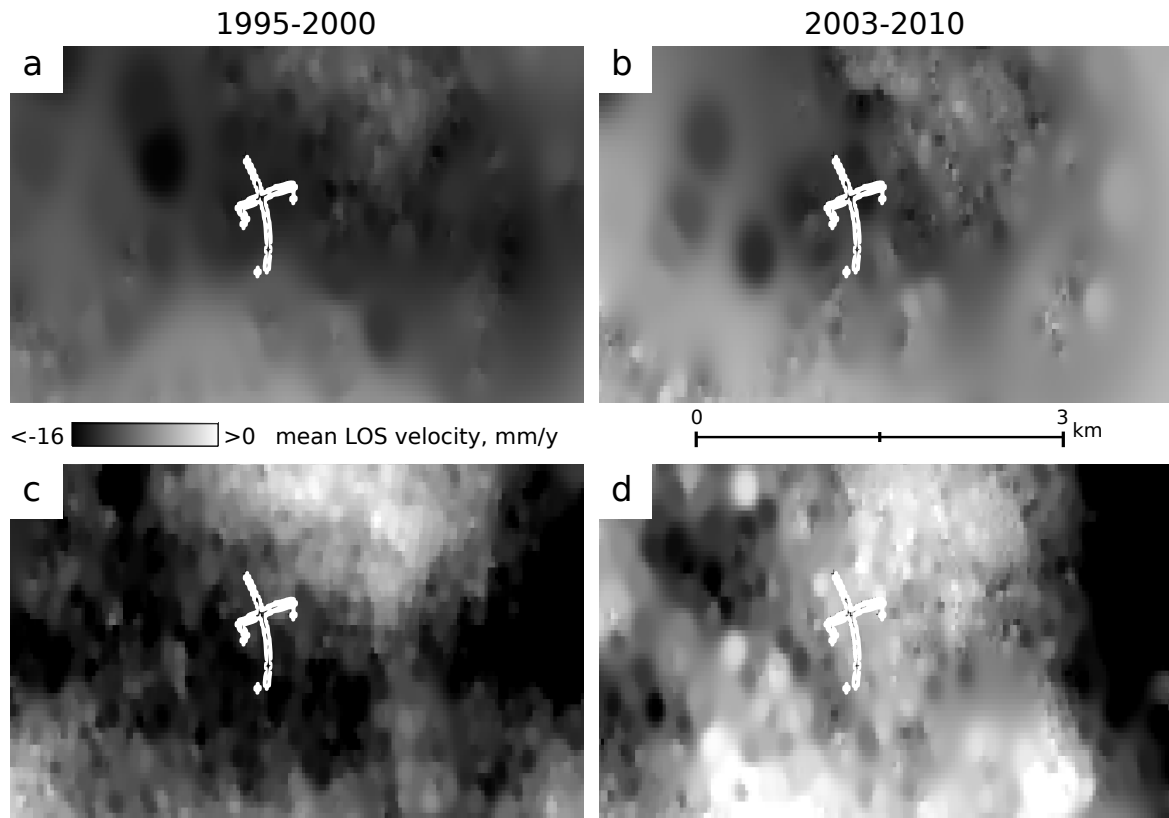


Figure 3.4.10 – MT-InSAR processing of Holkovice area. a,c) ERS-2 desc. SB processing of 04/1995-12/2000, b,d) Envisat asc. PS+SB processing of 08/2003-09/2010, a,b) original processing of OKR, c,d) local area reprocessing.

3.5 Summary

It must be taken into account that the area is affected by strong deformations that often exceed detection limits of C-band phase measurements. Alos Palsar confirmed its suitability but there is a lack of data from this sensor. The scene is decorrelated in large areas, mainly within C-band data. In DInSAR, a strong spatial filtering seems to be the only possibility to extract some information from the interferograms.

MT-InSAR of C-band achieved quite a sparse network of stable points with a high ambiguity of unwrapped phase due probably to such a high rate of deformation. Only several pixels overlapped with levelled locations - their comparison didn't show an appropriate fit. Due to high sensitivity for a deformation it is almost impossible to properly estimate such a high subsidence rate using MT-InSAR techniques applied on C-band data in a pixel network that is as sparse as in this vegetated area. Pixels that are found on the subsidence trough borders (where the subsidence is much slower) may be estimated more properly revealing actual extents of the trough. However again there is a problem of relatively low density of stable points in the area. When relaxing StaMPS processing parameters to find more pixels, these less stable pixels usually don't seem to follow a subsidence trend of its surroundings and cannot be properly unwrapped at all.

In general, subsiding places are found using MT-InSAR but the unwrapping errors and often also SCLA estimations lead to strongly speculative results. Theoretically relating the unwrapped values to some reference point closeby can give more reliable results - first of all the unwrapping errors do not enlarge with an increasing distance to the reference point. Processing of a smaller area bordering a subsidence trough without using generally low coherent interferograms estimated much faster rate of subsidence than when processing overall OKR area. Still the unwrapping process can succeed only if SCLA+APS errors are properly estimated and removed - if only coherent interferograms that are known not to be affected significantly by atmospheric variations are used, the probability of a proper unwrapping increases.

Speaking about phase unwrapping, it seems that the StaMPS algorithms result wrongly in the bounds of the dataset. Because a three dimensional phase unwrapping is used, the improper values are estimated in both spatial borders of a scene but also in temporal bounds of the dataset. Some deviation is usually detected in the last dates - this can be regarded in graphs of Fig. 3.4.5 that show a subsidence and then often an uplift in time which is not really probable.

Chapter 4

Detection of Landslide in Doubrava

4.1 Introduction

In the Northern Moravia region, the subsidence is not the only field where the satellite InSAR technique can find its suitable application. A phenomena of landslides is also active in the region. Mostly in periods of flood activity or after a heavy raining the landslides can cause large damages in the urbanized areas situated in the surroundings of some hill. This is the case of the Doubrava city. The photo in Fig. 4.1.1 was taken directly after floods in May 2010, in a distance of a few km from the hill that is to be investigated.



Figure 4.1.1 – Damages caused by landslide after floods in 2010. Photo by RNDr. Pavel Bláha, CSc., GEOTest Corp.

In the Doubrava-Ujala area with extents plotted in Fig. 4.7.6, two phenomenas are affecting the terrain profile. A subsidence due to the underground black coal mining in the south-eastern part and the landslide of the hill in the center of the crop. Both subjects are

specific and both are challenging actual InSAR capabilities. It is proved in (Bláha et al., 2009) that the activity of Karviná Mine: ČSA implies an activity of the landslide. The surroundings are covered mostly by grassland and a mixed forest with a higher ratio of deciduous trees. Only several buildings in the neighbourhood will provide some higher phase stability to perform a proper MT-InSAR.

Results of an InSAR application described in previous Chapter 3 give an overview to the terrain movements in the whole Northern Moravia, which this hill is a part of. However only a few differential interferograms has showed some sufficient coherence. They will be presented in Section 4.7. To allow a multitemporal processing of this area of interest, a corner reflector was designed, three reflectors were constructed and installed on site. Their usage didn't show convenient results in fact but the experience gathered can be applied in some following project.

4.2 Area of Interest

The object of interest is a hill situated in Doubrava city, Czech Republic, with a height of 282 m over sea level peaking around 70 m over its surroundings with a slope steepness up to about 30 m per 100 m (in average the slope steep angle is smaller, of about 10°). The hill is known to be sliding mostly due to the groundwater activity – the landslide developed after every strong water activity, some higher activity is observed after a catastrophic precipitation in July 1997 when the landslide caused major damages to several populated houses. After this a deep drainage was performed. According to the levelling, the bottom part of the slope has uplifted then for cca 4 cm, since 2005 it is slowly descending again, an average measured subsidence is 8 cm during 2005-2008. These and following data are taken from (Bláha et al., 2009) that investigates relations between a slope stability and undermining discourse using modern geophysical methods: geoacoustic, geoelectrical and seismic measurements, also using precise inclinometry, tape extensometry and levelling.

The hill is located close to the subsidence trough of OKR black coal mining area, the Karviná Mine: Doubrava (ČSA) was active in this area, already since 19th century. In the 20th century, 5000 tons per day in average of black coal in up to 6.5 m thick deposits were exploited from the range of 10-1000 m under the ground, only barrier pillars containing approximately 8 milion tons of black coal were left after the mine closure in 2007. Since then, the pillars are being exploited from neighboring Karviná Mine: Jan Karel (ČSA) causing a very fast subsidence in so-called Ujala area, exceeding 1 metre per year. Populated houses in Ujala area were bought and demolished by the OKD, a.s. mining company. The >3 m deep subsidence trough is now filled by a swelling lake. The hill is situated at the edge of the subsidence trough and its geophysical properties respond to the surrounding mining activity. Therefore it can be expected that the landslide activity of the hill will raise. Several occupied houses are situated on the hill, a road leads at the bottom of the hill. More monitoring of the hill activity is therefore needed.

4.3 InSAR for Landslide Monitoring

The use of InSAR to measure ground movement along slopes is not as common as other applications, such as measuring crustal deformation due to earthquakes and volcanoes or measuring subsidence. There are issues associated with using InSAR that are accentuated when it is applied to measuring slope movement. An application for landslide monitoring was investigated in (Colesanti et al., 2006), following text is according to their findings.

Due to the radar principles and satellite track characteristics, the sensitivity of a SAR system to the actual slope movement monitoring depends on the geometrical relation of the slope and the overflying satellite, as well as spatial and temporal resolutions of the area affected by landslide. For the current polar-orbiting SAR satellites, the look direction (except at high latitudes) is generally either east or west, for either ascending or descending orbits respectively. These SAR systems are, therefore, sensitive to movement along slopes facing either east or west, and insensitive to movements in either a north or south direction. In this direction a landslide should be monitored using combinations of both ascending and descending tracks.

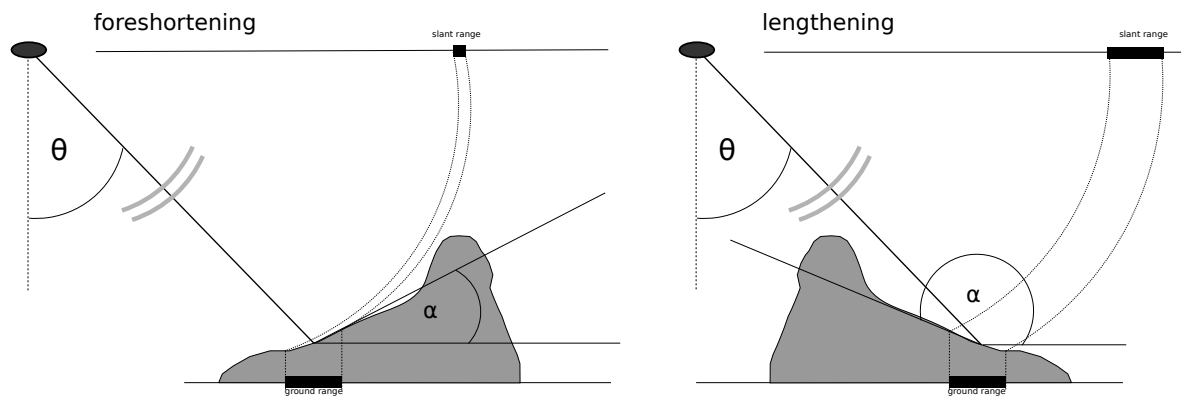


Figure 4.3.1 – Influence of look direction to the hill slope: foreshortening (a) and lengthening (b)

The geometric distortion effects, as described in Section 2.2.2.3, affect the applicability of InSAR. It can be observed in general that the slopes facing the sensor will be displayed shorter while the reverse side will get lengthened. A steeper topography (or a more narrow look angle) will enforce this shortening effect. Let's define angles θ as the SAR look angle w.r.t. direction to nadir and α as the local terrain slope towards the satellite line of sight, as depicted in Fig. 4.3.1. Then if:

- $0 < \alpha < \theta$, the slope will be imaged with a lower resolution. This is due to a foreshortening effect - the radar beam will be scattered back from objects which range distance from the satellite is closer, independently on their actual ground distance. Therefore their scattering contributions will be summed up. The slope will get compressed into fewer image pixels with a higher intensity,
- $\alpha \approx \theta$, the slope will be imaged in a unique range pixel, regardless of its actual areal extension (Colesanti et al., 2006) since the whole slope lies within the same range distance to the satellite,

- $\theta < \alpha < (90^\circ - \theta)$, the slope will be inverted. The top of the slope will backscatter earlier than the bottom. This effect is called as a layover,
- $(90^\circ - \theta) < \alpha \leq (90^\circ + \theta)$ (or $-\alpha \geq 90^\circ - \theta$), this area and the area immediately behind is not illuminated at all and will lie in a shadow zone,
- $\alpha > 90^\circ + \theta$ (or $-\alpha < 90^\circ - \theta$), this slope is facing away from the satellite line of sight. This configuration is optimal for the slope monitoring since the slant range distance of the objects will be larger than their horizontal (ground) range. The resolution of the illuminated area is increased, the back slope will be lengthened in the image. However, the threat of a shadow still persists.

Apart from the slope orientation dependency and general limitations that were already discussed in Section 2.5, the InSAR is even more limited for the landslide monitoring usage. The deformation is measured towards the satellite line of sight where even a very small deformation can be detected. Since this direction is much more to vertical than horizontal, also the terrain deformation rate can be retrieved in a high precision in the vertical direction only - large horizontal movements will cause a decorrelation since the scatterers position will change providing coregistration misfits.

Three basic phases of the landslide area can be recognized - some slow pre-failing movements can be observed within more plastic geological materials, the InSAR may be able to detect this fine movement. The slide itself then occurs very quickly without any possibility to capture its progress using spaceborne InSAR - maybe some ground-based SAR systems could be used that would beam the slope frequently. This sliding phase will be visible in an interferogram as a decorrelated area; then it can be possible to detect its extent but no quantitative representation of the terrain changes is possible. However the InSAR can be valuable monitoring the post-failure movements. After a slide, the slope stability gets degraded and the landslide can be reactivated. Some subsequent movements occur at a low speed, brought by seasonal water pressure changes or other reasons and may continue being active over long time periods, even some tens of years.

For this post-failure monitoring, multitemporal techniques can be used. However, in the absence of some stable scatterers like rock outcrops or man-made structures, there is actually a very small chance for proper MT-InSAR application that would overcome some of the differential InSAR limitations.

4.3.1 Needs for Corner Reflectors

Since the area of interest is mostly covered by vegetation, the most recommended data is L-band that penetrates through the vegetation canopy well. The landslide is a local phenomena, therefore images should be of a higher spatial resolution. Even for this reason, the only active L-band Alos Palsar is preferred against ERS/Envisat images, that afford images of a slant resolution around 7x7 m, see Tab. 2.2. Unfortunately, only a few images exist of the area from Alos Palsar sensor, disallowing MT-InSAR processing.

Previous differential InSAR results from Envisat ASAR images are totally depreciated by temporal decorrelation and therefore the monitoring doesn't seem possible this way. The

problem of temporal decorrelation caused mainly due to scattering changes of vegetation can be mitigated through the MT-InSAR processing of phase-stable targets, such as buildings, other anthropogenic infrastructure, rock or gravel outcrops, or radar reflectors - artificial objects designed to reflect the received radar wave in the exactly same direction.

With an idea to use MT-InSAR technique in the landsliding terrain that doesn't contain sufficient amount of proper candidates of persistent scatterers, three corner reflectors were constructed and installed on the site in 2010. In addition, to achieve as confident results as possible, a GPS receiver was also active closeby during the Envisat acquisitions to perform zenith wet delay estimations. According to the corner reflector experiment as described in (Hanssen, 2001), where the achieved results of MT-InSAR processing were fit with the levelling measurements in some 1.6 mm for Envisat (after sub-pixel correction), it is expected that even a very slow creeping landslide should be detectable using this attempt. For the landslide monitoring, it was expected to achieve some 10 Envisat acquisitions during 2010 that would be challenging to process by MT-InSAR and also some own modifications of the technique were awaited.

The corner reflectors are designed to be as smallest as possible with keeping their proper functionality even if used for other SARs as well. Additionally, a special mounting mechanism was designed to mount the CR directly on hydrogeological drills used to evaluate groundwater properties by GEOTest, Corp. with a possibility of setting of the view angle to allow using the same CRs also for other satellites in following projects.

4.4 Design of Corner Reflector

A proper reflection of the designed corner reflector should be of the same/parallel direction to the incoming radar beam and with a minimized loss of the beam power. This is achieved by

- usage of a proper material/technology that would reflect the beam without a power loss,
- a proper CR geometry that would reflect the beam back in the exactly same direction.

Several types of CR designs exist and are used mostly for radar calibration purposes, as GPCs for precise geocoding or as an artificial persistent scatterer. Passive reflectors come in several variations including flat panels (mirror-type), dihedrals (two perpendicular panels) or trihedrals in combination with a metal material or a dielectric (D'Agostino et al., 1999).

4.4.1 Radar Cross Section

When an object is illuminated by an electromagnetic wave, it scatters the incident energy in all directions. For the particular interest in a monostatic radar echo (i.e. a return of the wave in the same direction) the fraction of the intercepted power and the power returned to the radar, called radar cross section (RCS), can be used to describe the backscattering properties of the object.

The RCS is affected by both the object properties (geometry or electrical properties) and the wave properties (wavelength, polarization). The typical values can range from some 10 000 m² (metal objects, ships) to near-zero, like 0.0001 m² for insects. All this response can have its part in the final detection. For better practical usage, lowering the range of used values without losing the detected information, values of RCS (σ) are commonly recomputed to decibels, related to the squared meters:

$$\sigma_{\text{dB}[\text{m}^2]} = 10 \cdot \log_{10} \sigma_{\text{m}^2}$$

As described in (Skolnik, 1990), if the radius of an object retro-reflecting area A is some 10x larger than the signal wavelength, the return has a pure specular character from the object and the RCS can be approximated using geometric optics. If a precise RCS computation is needed, for situations where

$$\frac{\sqrt{A}}{\lambda} < 10 \quad (4.4.1)$$

, a physical optics computation method described for example in (Sarabandi et al., 1996) should be used instead. This approach accounts for the creeping-wave contributions (Rayleigh distortions) that are significant in such ratio.

In this thesis, only a geometrical optics solution will be used. The common used equation for RCS σ of an object backscattering within the whole area A is

$$\sigma = \frac{4\pi}{\lambda^2} A^2 \quad (4.4.2)$$

A ... effective retro-reflecting area of the target,

λ ... SAR wavelength.

For the trihedral corner reflectors the situation is different since the triple rebound should be taken into account. The square plates trihedral CR has the ability of a self-reflectance, meaning that the radiation scattered back to the radar direction is always from one of the CR plates, without external contributions. This is not the case of cut-sided triangular trihedral CR since also a part of the signal will be rebounded from the ground. The RCS for a square plate CR is computed as a sum of a reflection from all three plates with their retro-reflecting areas of A_1 , A_2 , A_3 . Each of these areas is a backscattering area of each plate that was illuminated after a double rebound from the other plates. When the corner reflector is oriented properly to achieve the radar beam center to its boresight, these areas are accordant $A_1 = A_2 = A_3$ and the maximum RCS can be then computed, based on Eq. (4.4.2), as:

$$\sigma_{\text{max}} = \sigma_1 + \sigma_2 + \sigma_3 = 3\sigma = 3 \cdot \frac{4\pi A^2}{\lambda^2} = 12 \cdot \frac{\pi \cdot a^4}{\lambda^2} \quad (4.4.3)$$

This is also according to (Curlander et al., 1991). To achieve the strongest reflectance of a radar beam from the designed CR, it should be oriented with its axis of symmetry pointing directly to the antenna. This is called a boresight configuration. The axis of symmetry for hereby designed corner reflector is depicted in Fig. 4.4.3, in this case $\alpha_H = 45^\circ$, $\alpha_V = \arctan \frac{\sqrt{2}}{2} = 35.26^\circ$. The relations to the incident angles different from the boresight direction can be found explained for example in (Sarabandi et al., 1996), a very simple approximation from (Richards, 2009) is to multiply the boresight RCS by $\cos^2(\Delta\alpha)$, however this will be valid only in for very limited small deviation $\Delta\alpha$ from boresight.

Note that the computed value of RCS will be different than the RCS measured by satellite SAR system even in boresight. This is caused by other RCS contributions that distort the electromagnetic wave during its way, and other factors.

4.4.1.1 Material of a Corner Reflector

To achieve a strong reflection of the radar beam from the corner reflector, every its plane should be flat and smooth to prevent unwanted scattering from a rough surface. The reflection also depends on the chosen material that may more or less absorb the electromagnetic energy. Metal objects have a high conductivity, they do not absorb the energy, they reflect most of it.

For non-metal objects the material permeability and permittivity should be taken into account, a relevance to the reflector material is depicted in Chapter 5 of (Richards, 2009). However for the metallic material, aluminum, that is used within this corner reflector, this material loss will be regarded as insignificant.

4.4.1.2 Geometry of Corner Reflector

Trihedral corner reflectors offer a fairly broad range of aspect angles with a large RCS. The triple rebound in trihedrals is achieved when the beam directs on their effective retro-reflecting area. This is projected on each plate as a pentagonal area sharing the same point of origin as depicted in Fig. 4.4.3. Different geometries are designed for trihedrals to achieve the highest RCS with the smallest amount of material outside of the effective area. Even that an optimal geometry is then within a trihedral corner reflector with sides of a pentagonal shape, for practical construction the triangle shaped sides reflectors are often used since they can be more compact and easy to construct.

However these triangle shaped trihedrals have several disadvantages (Sarabandi et al., 1996). Their effective area is small in relation to their size - in the optimal conditions of a maximum RCS, only two-thirds of each panel is lit. Their two side triangle planes allow the third reflection to come from the ground. A minimum interaction with the ground can be expected with a square panel geometry and the illuminated area is also larger (see Fig. 4.4.1) - in the boresight direction the square panel trihedral CR will be self-illuminated.

On the other side the tolerance from the boresight gets lower for the square panels. As stated in (Richards, 2009), a 23° cone angle around boresight is regarded as effective with a half RCS loss (for C-band), while in the (cut) triangle sides CR, the RCS drops two times over a more broad cone of 40° . This ensures about a squared CR tolerance of a proper

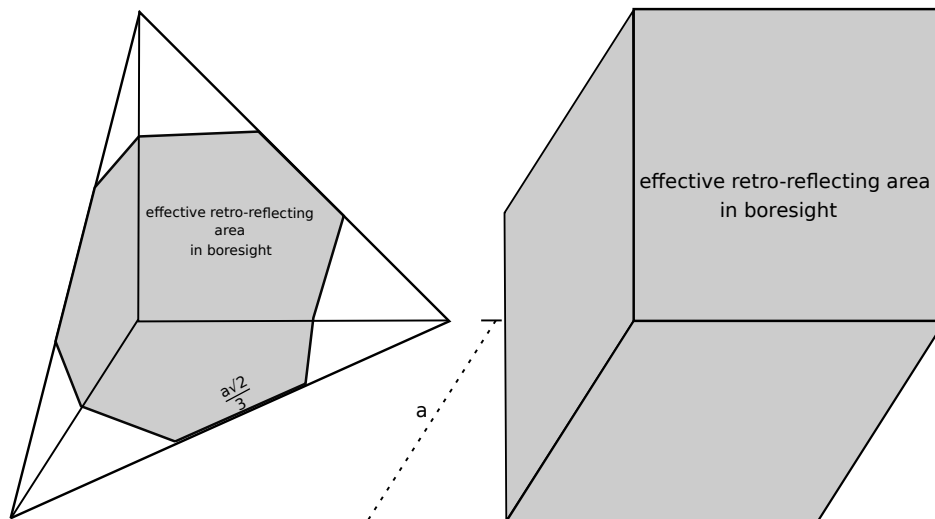


Figure 4.4.1 – Retro-reflecting area of basic corner reflectors plate shapes

orientation in some 11.5° from the actual boresight which is in practice achievable quite easily. Other literature (Norris et al., 2004; Villasenor et al., 1993) recommends to achieve an orientation precision of up to 3° from the boresight.

4.4.1.3 Proper Perpendicularity

To achieve a triple rebound back to the same direction as the incoming ray, all three plates should be exactly perpendicular to each other - according to geometrical optics, any deviation will cause a total change of the rebound direction. However, in reality, the scattered wave from each panel has some finite beamwidth (Sarabandi et al., 1996) that makes the wave propagate in multiple directions. So then, the signal gets only distorted regarding to the corner angle imperfection. The limiting factors can be computed using the physical optics.

If the faces of a CR do not meet at exactly 90° , then the beam which would have been reflected back to the transmitter is divided into several beams, none of which, in general, are directed exactly towards the transmitter. As a result, there will be a reduction in signal received at the transmitter. Results of the error magnitude computation are summarized in (Bonkowski et al., 1953). It is reported that the RCS of square corner reflectors are twice as sensitive to errors in the corner angles than that of triangular corner reflectors. For the bore sight direction of incident beam in the square trihedral CR design, the backscatter is reduced to one half of the backscatter maximum RCS if any of the side plates, where furthest from the common point of origin, deviates for $\Delta = 0.4\lambda$ - and this equals to three errors within all three plates that would be $\Delta = 0.24\lambda$. Note that these errors are independent on the size of the corner reflector. This half RCS decrease in Envisat radar imagery corresponds to a maximum deviation of $\Delta = 0.24\lambda = 1.3\text{cm}$ on all the plate side ends.

This can be also a problem related to a resistivity of the CR end points to a strong wind, however without a serious effect and, when correctly orientated, the most of the reflection is close to the CR origin anyway, that is resistant to a plate bending.

4.4.2 Final Corner Reflector Design

Several requisitions are put for the corner reflector design. The corner reflector has to be

- economically affordable,
- suitable for various SAR systems usage (but mainly devoted to Envisat ASAR acquisitions),
- mountable on the hydrologic drills,
- prepared for frequent redeployment.

With regards to accessible sources and information, a relatively small trihedral corner reflector of square sides from aluminum plates was designed. The corner reflectors will be installed in vegetated areas without any strong reflectance that would coincide with the CR backscatter. To detect the corner reflector on the SAR image, at least 12 dB difference amongst surrounding pixels should be ensured (Ugsang et al., 2001). A strong backscatter is not necessary for the interferometrical purposes since the phase stability of a resolution cell (that would be filled by the CR backscatter at whole) can be used to find the CR cell and use as a persistent scatterer. However the CRs will be used in a strategy of redeploying them on the exact same position each time of acquisition. This attempt should preserve the quality of CRs stored in a safe dry place, but the remounting will cause the phase instabilities due to mounting inaccuracies.

The squared plates instead of commonly used triangular shaped plates were chosen to achieve a higher RCS. The extra material affords CRs to have a larger retro-reflecting area than of triangular shaped plates with the same side length - see Fig. 4.4.1. The whole plate will be used for the backscatter while in the case of triangular CR only 2/3 of each plate area would be used.

To find an appropriate CR side length, the RCS was computed for various side lengths and combinations with different radar wavelengths to find an optimal and universal length. In a project using Radarsat-1 to detect various corner reflectors as described in (Norris et al., 2004) the smallest trihedral CR with a base length of 45 cm was detected, however its $\sigma_0 = -3.17\text{dB}$. In the case of CR with a length of 75 cm, the backscatter strength was $\sigma_0 = 8.38\text{dB}$. The vegetation can achieve a various RCS dependent on the season (if the backscatter is achieved through the foliage from a tree trunk, it can have a relatively strong double rebound causing RCS of several dBs), so practically this 75 cm corner reflector can be a real minimum for this corner reflector design when used in C-band data. However, with a squared plates geometry it can achieve even stronger response. Theoretical values of square trihedral RCS valid in the boresight beaming direction were computed by geometrical optics solution - Eq. (4.4.3) - and are introduced in Tab. 4.1.

The appropriate side length for CR was chosen to be 80 cm for usage with wavelength of 5.6 cm, the lit area as figured in Fig. 4.4.1 can be computed as $A = a^2 = 0.64\text{m}^2$, therefore $\sqrt{A}/\lambda = 14.3 > 10$ which is large enough for RCS computation using geometrical optics solution, as explained in Section 4.4.1: Eq. (4.4.1). However for the values marked by asterisk in Tab. 4.1 L-band the situation would be different (for $\lambda = 26.3\text{cm}$ the ratio

Table 4.1 – Boresight Radar cross section of a squared trihedral corner reflector with various configurations

Side length	0.4 m	0.6 m	0.8 m	1.0 m	1.2 m
$\sigma_{dB[m^2]}(\lambda = 3.1\text{cm})$	30.0	37.1	42.1	45.9	49.1
$\sigma_{dB[m^2]}(\lambda = 5.6\text{cm})$	24.9*	31.9	36.9	40.8	44.0
$\sigma_{dB[m^2]}(\lambda = 23.6\text{cm})$	12.4*	19.4*	24.4*	28.3*	31.5*

* computed by inappropriate solution

$\sqrt{A}/\lambda = 3.04$). A usability of this CR for L-band SAR wasn't investigated even that it can be valuable for our area of interest for application of Alos Palsar data.

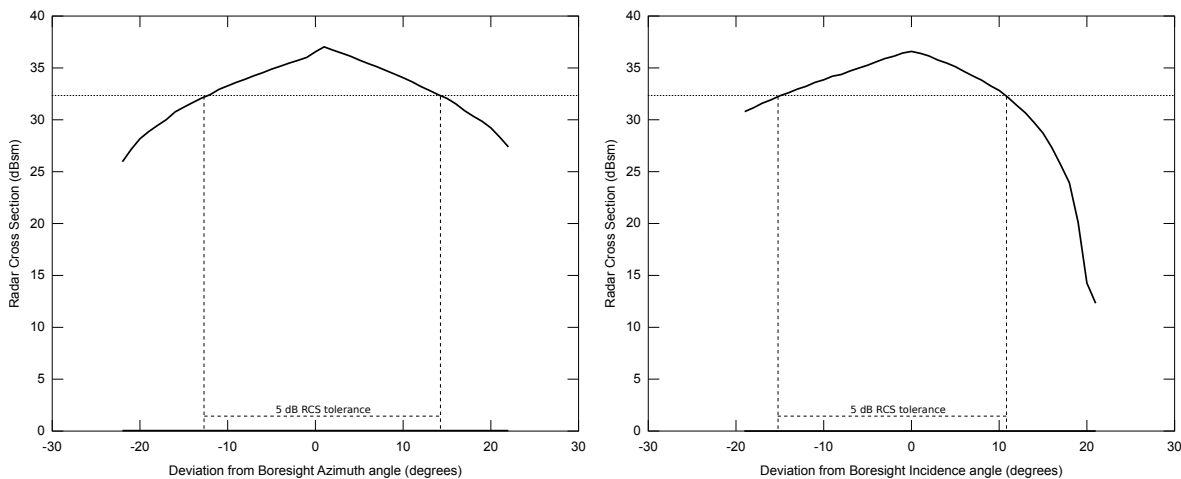


Figure 4.4.2 – Dependency of horizontal (a) and vertical (b) angle deviations for computed RCS of a trihedral corner reflector of square sides $a = 0.8\text{m}$ using wavelength of $\lambda = 0.056\text{m}$.

The sensitivity for an angle deviation for various types of corner reflectors is described for example in (Sarabandi et al., 1996). I have applied the set of equations presented in Appendix B of this publication, after an adaptation to the square-side trihedral CR, to estimate the orientation sensitivity for the chosen CR design (its parameters will be introduced further). Even though the mathematical imperfections, the presented trend should be reliable - see Fig. 4.4.2. The area marked as a 5 dB tolerance represents angle deviation borders where if exceeded, the RCS $[m^2]$ will get lowered two times for this CR configuration. According to this estimation, the proper CR orientation is regarded to be in a tolerance of $\pm 12^\circ$ in either horizontal or vertical direction.

From the photo in Fig. 4.4.3(b) the designed system for mounting on the hydrological drills can be observed. This bottom construction is attached to the reflector from the back side so the connection doesn't lower the RCS of the corner reflector. The pipe can be laid over the drill tube and there can be adjusted using attached bolts for the correct horizontal position and azimuth orientation. The CR bottom can then be flexibly tilted for a high range of angles.

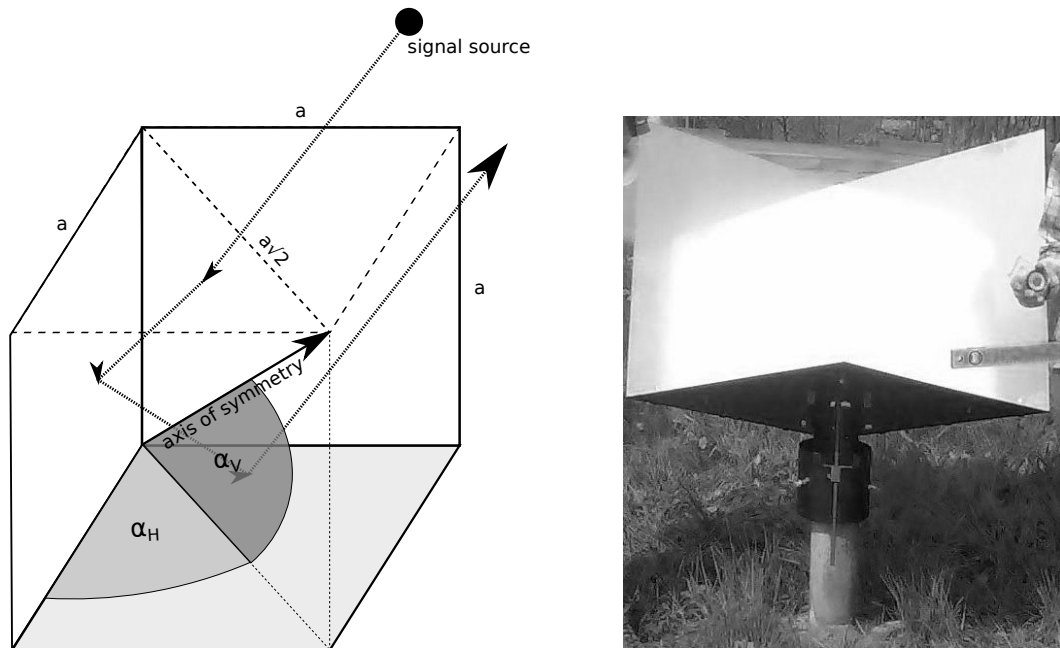


Figure 4.4.3 – Design of the corner reflector (a) and its deployment in terrain (b)

Practical Notes

For practical reasons, if the corner reflector has to be installed in a terrain for a longer time period, its plates should contain holes to avoid problems due to a rain accumulation and lower the wind impact. As stated in (Parizzi et al., 2006), even 60% ratio of fill/vacuum in plates can preserve a good RCS, where the holes can reach a diameter of 1 cm for any current SAR system. This wasn't performed in this case since the corner reflectors are to be deployed in a different strategy - by a redeployment for each satellite overflight.

To detect an object in the SAR intensity image, its reflectivity should be at least 12 dB higher than the background targets (Ugsang et al., 2001). This is ensured by a proper design to achieve adequate reflectivity (as a parameter called radar cross section - RCS), a correct orientation to the radar sight and of course by a deployment in appropriate area, distant from strong scatterers as house structures and with no multipath contribution.

4.5 Orientation of Corner Reflector

To achieve an appropriate backscatter from the corner reflector, it must be accurately oriented to the satellite line of sight. The precision of corner reflector orientation is recommended to be about 2-3 degrees in both horizontal and vertical direction for C-band SAR satellites and a regular trihedral CR design in (Villasenor et al., 1993). The corner reflector elevation difference of 2.4° had no significant impact on CR visibility in (Norris et al., 2004). However, as can be read in Section 4.4.2, even some 12° difference can be tolerated for the precise orientation to achieve still a strong corner reflector RCS.

The sun-synchronous orbit of SAR satellites is characteristic for illumination of a specific area in the same local mean solar time, with the same illumination angle, although slight differences of satellite position in different time exist. Therefore, once properly oriented, the position of CRs can remain the same during more acquisitions without losing their optimal reflectance.

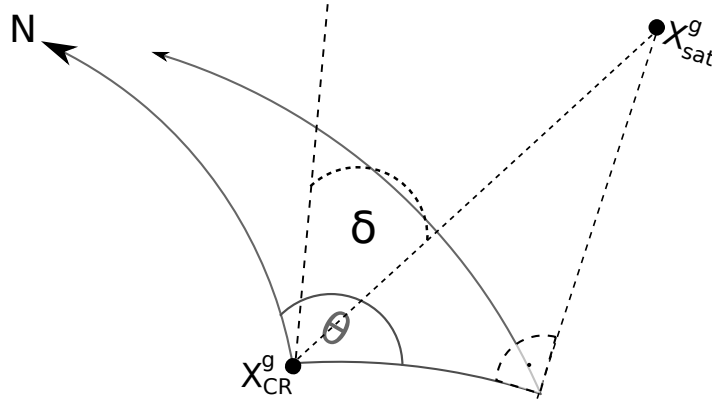


Figure 4.5.1 – Orientation of a corner reflector to the satellite line of sight

To properly orientate a corner reflector (CR), two parameters need to be obtained, as they are depicted in Fig. 4.5.1 - a tilt angle of the CR φ and the azimuth θ , i.e. an angle w.r.t. geographic North. The tilt angle of the corner reflector has to be adjusted relatively to the SAR's incidence angle δ , i.e. the angle w.r.t. the local vertical. This is affected mostly by the satellite looking angle, so it varies within the acquired swath width - see Tab. 2.2. The corner reflector maximum reflection is at its axis-of-symmetry, that is in this case in $\alpha_H = 45^\circ$ from side planes and $\alpha_V = \arctan(a/a\sqrt{2}) = \arctan(\sqrt{2}/2)$ from the horizontal plane (Fig. 4.4.3). Therefore the CR tilt angle φ can be computed simply as:

$$\varphi = 90^\circ - \alpha_V - \delta = 54.73^\circ - \delta \quad (4.5.1)$$

Several methods to compute both azimuth and incidence angle were evaluated and described since they can be used in different conditions, in terms of available data required to compute these angles. Their results for application in HP-3 location (see Tab. 4.3) are compared in Section 4.5.1. To increase the readability of this thesis, I have put the described computation methods into an Appendix. The scenarios can be described from the least precise to the most reliable approximation:

- only coordinates of resulting image extent/footprint are known. See Section A.1.4,
- only information about satellite direction (and inclination) is available. See Section A.1.3,
- orbital data are available but no previous acquisition. See Section A.1.1,
- orbital data are available together with an acquisition of the same settings. See Section A.1.2.

4.5.1 Comparison of Methods

Using the appropriate equations as described in Appendix A, the azimuth angle θ and incidence angle δ were computed for HP-3 location. The result together with these other attempts is provided in Tab. 4.2. For the azimuth values, also a squint angle correction ($+2.5^\circ$) has been performed.

Table 4.2 – Results of different methods to obtain azimuth angle θ and incidence angle δ .

Satellite Inclination (using orbits)	Image Footprints	Local Reference Frame (using orbits)	Existing acquisition (20 July 2009)	Comparison with 31 May 2010
$\theta = 105.7^\circ$	$\theta = 104.3^\circ$	$\theta = 105.9^\circ$	$\theta = 106.1^\circ$	$\theta = 106.1^\circ$
-	$\delta = 21.18^\circ$	$\delta = 21.89^\circ$	$\delta = 21.85^\circ$	$\delta = 21.85^\circ$

Provided computations in the Tab. 4.2 were compared with the data read from achieved acquisition of 31 May 2010, using method described in Section A.1.2.¹

Discussion

If the values of azimuth θ and incidence angle δ computed from 31 May 2010 are taken as a reference, it is observable that all the methods can fit the requirement of orientation accuracy up to 3° . The azimuth angle estimation deviates up to 0.25° , apart from the method using image footprints, as expected, that deviates maximally, in $\Delta\theta = 1.8^\circ$. The method using Image footprints therefore is not recommended for precise corner reflectors orientation. The incidence angle differs minimally.

Please note that the methods were described for different source data available. The results of accuracy will differ based on the data quality. It is possible to use different input data combinations with these methods - for example it may be practically of concern to use a satellite track inclination angle for computation of coordinates in Local Reference Frame method instead of precise orbit data. The difference in the satellite direction would be significant only if there were some satellite maneuvers during investigated time period.

4.5.2 Applied Computations for Current Experiment

The previously mentioned computations were investigated after the experiment runtime. For computation of azimuth orientation of corner reflectors, the image footprints were used since they are provided with adequate accuracy, as compared with the already available data. However, because of lack of knowledge of geodesy, I have wrongly presumed a possibility of using a non-geodetic attempt (considering the Earth surface as a flat plane) in computation of azimuth that would be precise for points in a distance of more than 280 km, i.e. a corner reflector and a nadir image of satellite. To obtain the azimuth angle θ for point B aiming

¹Computation parameters were: $t_0 = 9:10:46.99$, $t_{CR} = 9:10:52.34$, therefore $\lambda_{sat} = 22.241^\circ$, $\phi_{sat} = 49.245^\circ$.

to point A as seen on Fig. A.1.4, that was presumed to be the same as for every point within the swath, I have used a simplified Eq. (4.5.2) below:

$$\theta = \pi - \beta = \pi - \left(\frac{\pi}{2} - \alpha \right) = \frac{\pi}{2} + \arctan(\tan(\alpha)) = \frac{\pi}{2} + \arctan\left(\frac{|\lambda_B - \lambda_A|}{|\phi_B - \phi_A|}\right) \quad (4.5.2)$$

Then, the azimuth was computed as $\theta = 98.076^\circ$. This is distinct from more precise computations of around 4° which already decreases a proper CR reflectance significantly and is over a recommended tolerance. Also, the squint angle wasn't accounted for, therefore it deviates from computations demonstrated in Tab. 4.2 even of 6.2° . Theoretically this still can provide a sufficient response.

To determine the incidence angle, an incidence angle tie point grid from an older available dataset from 20 July 2009 was used - for the HP-3 location, the incidence angle $\delta = 21.85^\circ$.

4.6 Corner Reflectors Experiment

4.6.1 Corner Reflectors Deployment

The corner reflectors will be mounted in three stations. Two of them, HP-3 and HV-2 are situated directly on the sliding hill, the third one, V-100, is in the relatively stable area of Doubrava city center. Their WGS-84 coordinates are listed in Tab. 4.3. The height over WGS-84 ellipsoid was acquired from ZABAGED updated in 2008.

Table 4.3 – WGS-84 coordinates of corner reflectors mounting points

Id	longitude ($\lambda, ^\circ$)	latitude ($\phi, ^\circ$)	height (m)
HP-3	18.48667	49.87590	230
HV-2	18.48718	49.87317	223
V-100	18.48206	49.87590	226

Two CRs were deployed on top of drills on the observed hill slope, with the third as a reference point in the Doubrava city center. Because the drills are situated on an unsecured area that is visible from a nearby road, the CRs couldn't be installed permanently during the whole year. In every acquisition day the CRs were mounted on place and were carried away afterwards. It wasn't practically possible to orientate the CRs identically in every installation. That's why we have to count with a lower precision of the interferometrically estimated landslide velocity.

The setting of CRs rotation was done by utilizing electronic compass within GPS with north direction set to True North of WGS-84 ellipsoid definition, the vertical direction was set by tilting of corner reflector basement from horizontal spirit level tool. The computed angles of azimuth and vertical angle were discussed in Section 4.5.2. From the beginning there was probably around 6.5 degrees deviation from the correct satellite line of sight direction, not including possible errors of practical installation.

During the experiment, it was believed that the corner reflector has a very wide look angle range, even 10 degrees deviation should be acceptable, as mentioned in the article [2] and as was investigated with a result of Fig. 4.4.2. However, in several scientific papers only a deviation of up to 3 degrees was afforded. It must be taken into account that the distance between CR and satellite can be around 900 km, thus the needs for accuracy.

The corner reflectors in principle have the ability to show a strong response so the measured phase within the resolution cell containing CR is dominant and not affected by surrounding objects.

4.6.2 Evaluation of Experiment

4.6.2.1 Acquisitions of 2010

Only five Envisat ASAR acquisitions of Doubrava surroundings could be planned for the year 2010 instead of an expected number of 10 acquisitions. On 22 October 2010 Envisat has changed its orbit descending of 17.4 km. There is no inclination drift control anymore, the perpendicular baselines can reach values even 20 km, while the limit for InSAR is around 1 km. Only areas in $38 \pm 5^\circ$ degrees of latitude are covered by InSAR available acquisitions (Miranda, 2010). Acquisitions were planned in advance for the year 2010 within an ESA CAT-1 project. Because of conflict with projects of higher priorities, the acquisitions of 15 February and 22 March couldn't be ordered and the acquisition of 26 April had to be achieved in HH polarization mode while other executed acquisitions at 31 May, 5 July, 9 August and 13 September had to be ordered in polarization VV. In the end, only 5 acquisitions were ordered that will include installed corner reflectors. Normally it is not eligible to combine images with different polarization interferometrically since the physical objects reflect such waves in different ways, based mostly on different geometrical orientation. But in the case of corner reflectors this is theoretically of no concern because the reflectors would presumably reflect waves of both types of polarization identically².

The hill is facing to the east. Even that problems of foreshortening can be expected, the descending track was chosen to observe the corner reflectors. In fact, to use ascending data for these purposes, we would have to use L-band satellite data or cut down many of the surrounding trees since the planned positions of the CRs are located behind a forest, w.r.t. ascending track line of sight.

4.6.2.2 Detection of Corner Reflectors

In order to evaluate the corner reflectors behaviour in the Envisat ASAR IMS data, these acquisitions had to be pre-processed. The images were coregistered into a stack on a pixel level. The IMS files are processed without antenna pattern correction, only external parameters are included within the image file. Because the measured physical quantities are usually distorted by the sensing instrument and the transmission channel, the data must be calibrated with regard to the antenna pattern gain, transmitted chirp power, factor

²as discussed and confirmed by Prof. Eric Pottier

needed for digitization, to geometric attenuation and for the look angle (Maître et al., 2008). Therefore, the intensity values were radiometrically calibrated³ using ESA provided auxiliary files and converted to dB[m²] in order to make the images comparable between each other – to achieve a pixel radar reflectivity σ_0 . To confirm the proposed comparison methodology, another strong reflector has been found in the scene that corresponds to a house with a metal roof. This reflector's σ_0 values in all acquisitions get about 35dB±2.5 dB and its position was the same in the whole stack of coregistered images.

The CRs reflections were found using the known WGS-84 coordinates. As a reference ASAR product, 7 May 2010 acquisition was chosen. In this date the reference CR wasn't installed on the place. This reference amplitude image has been reprojected using range-Doppler terrain correction algorithm to match with the SRTM DEM coordinates in WGS-84 system. Using only available precise orbit files leads to coregistration errors. This was firstly tested, achieving a deviation of 15" in longitude and 1.5" in latitude, which corresponds with an error of 308 m (w.r.t. national S-JTSK coordinate system). After the terrain correction, the CRs were coarsely identified, together with their radar coordinates. In the Tab. 4.4, each CR is depicted as a pin as identified in the reference image. The value of intensity in dB is a value of the most reflecting point in the located pin neighbourhood, supposed to be the peak of CR reflectivity in each image. Locations of the CRs in the area of interest is presented in Fig. 4.7.6 or Fig. 4.6.1.

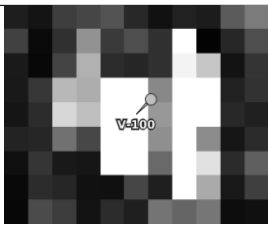
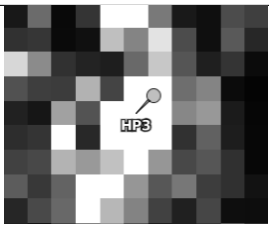

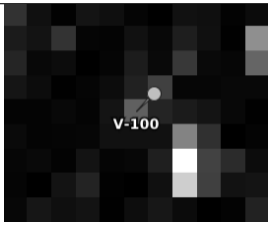
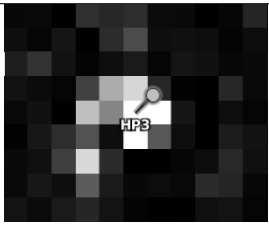
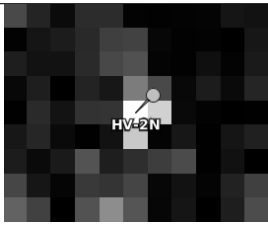
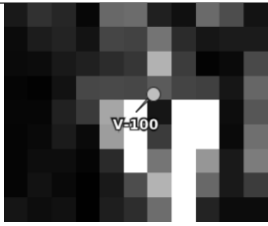
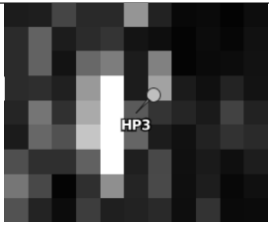
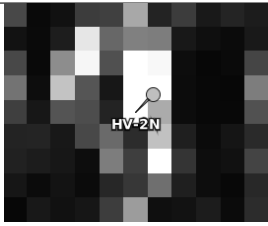
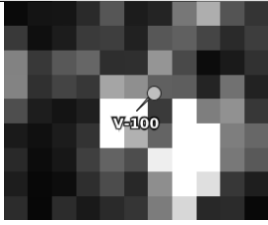
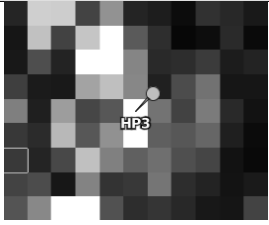
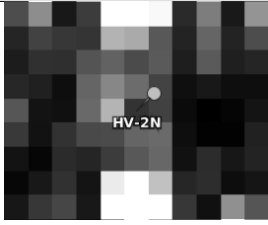

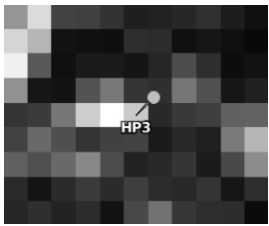
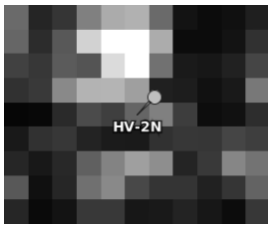
In the presented overview of CRs and their behaviour in the radiometrically calibrated images we can observe a very different reflectivity and mislocation. Even that theoretical reflectance of the CRs is more than 36 dB, in the SAR images the CRs exhibit reflectance of only 2-10 dB. The CRs couldn't be localized correctly because of the slope foreshortening. The reference V-100 position is nearby a tree (within the 25 m tolerance of an Envisat resolution cell) that probably causes a double rebound. Also the reflectivity is lowering during the time. This might be also due to the material abrasion.

Corner reflectors were investigated also using an attempt of a Multi-Image Reflectivity Map (MIRM). After the image intensity calibration, the intensity images are combined to achieve a MIRM image. With this approach I expected the varying intensity mostly from the vegetation to average into a lower value while the stable (even that not too intense) reflectivity of corner reflectors would be better distinguishable. That wasn't the case here. The CRs are installed on the slope borders - nearly on the top (HP-3) and on the bottom (HV-2). Because of the foreshortening of the slope, their signals are mixed together with the foreshortened slope signal. A weak signal can be regarded from the location nearby V-100. This could be verified.

I have computed a MIRM of older images of 2008 and 2009 (from the corresponding seasons to achieve a similar image) and this I have subtracted from the MIRM of 2010 images that include the corner reflectors. In this result, a CR installed on V-100 location could be with some probability distinguished. However, the other CRs couldn't be identified. A MIRM subtraction is depicted in Fig. 4.6.1. In this figure, note also other changes that got distinguishable in the area. The lake that originated from the mine activity on the eastern part and some reflectivity increase in time in the west part of the hill - this change is visible also as an increase of several meters in newer Aster GDEM amongst the 2000 SRTM.

³Capabilities of Nest were applied here.

Table 4.4 – Identification of corner reflectors in the SAR reflectivity images

Date	V-100	HP-3	HV-2
26 April 2010	 8.49 dB	 10.80 dB	 2.89 dB
31 May 2010	 (not installed)	 9.32 dB	 4.55 dB
5 July 2010	 4.14 dB	 2.42 dB	 2.74 dB
9 August 2010	 2.97 dB	 1.17 dB	 2.41 dB
13 September 2010	 -2.69 dB	 -0.44 dB	 1.43 dB

I have investigated the CR locations also by coherence. If the CR was stable, it would yield a high coherency in interferograms formed from images that both include the CRs. Since we know they are not very stable, they can on the other hand lower the coherency of their location. Anyway their sudden presence should be detectable in coherence of interferograms formed by one image before CR mounting and second image with the

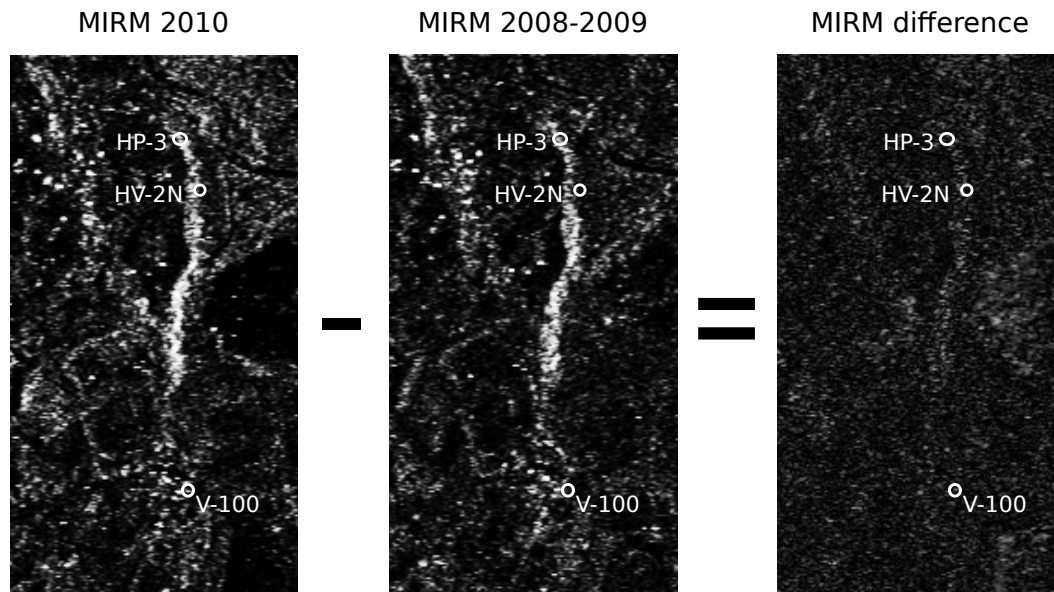


Figure 4.6.1 – Multi-Image reflectivity map of SAR images of 2010 that include CRs (a), of 2008-2009 without CRs (b), and their difference (c).

installed CR. Unfortunately, the signal from CRs is not dominant enough and is suppressed by its neighbouring area of coherence window estimation.

4.6.3 Summary

Due to practical imperfections, the corner reflectors experiment couldn't be evaluated properly. The optimistic opinions about a high orientation tolerance were not confirmed. Since the reflectivity of CRs should be comparable after the radiometric calibration, and it is regarded to be at least very similar in all of the cases, they are not in this case - I have to admit that these corner reflector measurements are not usable for the purpose of MT-InSAR. The CRs should be stably mounted and surrounding phase contributions should be low enough to not interfere with the signal of CRs.

Because of the depicted problems with the corner reflectors in the acquisitions, the usage of original StaMPS software (Hooper, 2008) to detect and determine the deformation velocity of the area of interest failed to pick the pixels containing the corner reflectors as persistent scatterers. Because of the CRs pixel mislocation thus also a strong phase change due to CRs manipulation when remounting on the site, the pixels weren't used. No manual computations were applied since the CRs lack proper phase stability to provide terrain deformation measurements.

There would be a possibility to achieve some useful results if the SAR data were acquired in their RAW formats and then focus them on another Doppler centroid frequency that would correspond with an orientation angle of the corner reflectors. However because the phase will be unstable anyway due to the multiple remounting strategy, this analysis wasn't performed. Therefore this project mostly failed due to the stated reasons. The corner reflectors still can be used in another future mission, in that case they would be installed permanently.

4.7 Results of InSAR Processing

4.7.1 Differential InSAR Processing

From all the available C-band data, all possibly convenient combinations (with limitations of $B_{perp} < 900$ m, $B_{temp} < 491$ days) within the same sensors were used to create differential interferograms using the Doris InSAR processor (Kampes et al., 2003). For the topography phase removal, the SRTM3 data was used.

Unfortunately, most of the images contain a large amount of disturbing signals, affecting the interferograms with a strong decorrelation, mostly caused by vegetation. Only a few (around 10) generated differential interferograms can predicate the terrain deformation by visual interpretation. These successful interferograms have as shortest temporal baseline as was possible and are usually of autumn or winter seasons when the vegetation cannot cause so high decorrelation effect.

Different approaches were undertaken to filter out the noisy areas that prevented to acquire the terrain deformation induced phase values. Hereby, I present and evaluate only several interferograms that have the highest competence to describe the landslide activity. To enhance the resulting interferograms and detect the landslide, the non-local mean filtering⁴ was used (Deledalle et al., 2010) as an advanced smoothing filter.

The Fig. 4.7.6 shows the actual final results that can be compared with more of information about the landslide that is explained in (Bláha et al., 2009). Following text will describe these results.

4.7.1.1 Geometrical Distortions in DInSAR Images

The geometrical distortions are one of the most important obstacles for a proper landslide evaluation. According to the relations between the observed slope and current SAR configurations as explained in Section 4.3, the optimal configuration for the slope monitoring can be estimated.

The landslide occurs with the highest activity on the eastern part of the hill (Bláha et al., 2009) where the steepness is up to around 35 m/90 m, i.e. the slope angle $\alpha \simeq 21^\circ$. According to Fig. 4.7.1, it can be seen that the slope is facing directly the line of sight of ERS/Envisat satellites in their descending phase. The incidence angle at the slope is in the case of ERS/Envisat around $\theta_{inc} = 21.8^\circ$. Because this slope angle is approaching $\alpha \approx \theta_{inc}$, the foreshortening effect is regarded to cause difficulties when using data from the descending track.

This was really observed in the resulting interferograms - see Fig. 4.7.2. The slope representation is compressed in the descending track of ERS-2, while it could be better monitored by Envisat and Alos in their ascending tracks (ignoring the forest barrier).

⁴The original script supposes to use two original SAR images that it will combine interferometrically, and filter. The filtered phase is difficult to process further by DInSAR. Thus a modification was performed where as the master SAR image, a differential interferogram was used, while its magnitude substituted the slave SAR image. This approach was also approved by the author of the filtering method.

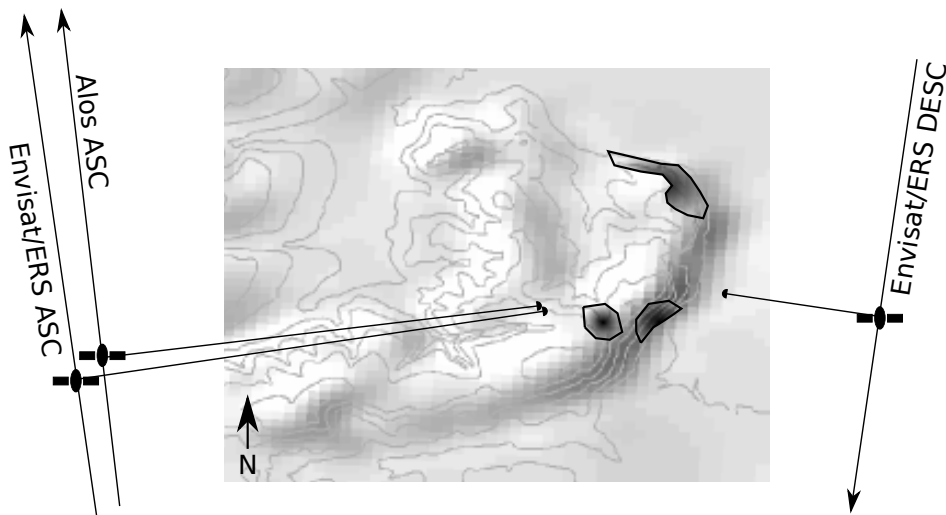


Figure 4.7.1 – Viewing directions of SAR satellites during observing the Doubrava-Ujala slope

The foreshortening effect caused a compression of pixels representing the slope, coarsening the resolution. However this is not a fatal distortion, in comparison with a shadow effect that will most probably not affect the observations in this site (no slope angle of the hill reaches the critical value of $90^\circ - \theta_{inc}$).

4.7.1.2 Interferograms of Descending Track

Unfortunately, most of the interferograms from the ERS/Envisat descending track are affected by a loss of coherence such significantly that it is usually not possible to interpret these on the slope itself.

A detailed interpretation of one chosen interferogram with a high overall coherence will be investigated in following section. Here, in Fig. 4.7.3, I would like to shortly present several interferograms that contain some artefacts directly under the sliding hill, that can correspond with the findings from (Bláha et al., 2009).

Note that only ERS results are presented since there was no optimal Envisat configuration found that would result in a highly coherent interferogram of the area. It would be very favourable to achieve an overview of the time during floods in July 1997. Unfortunately, interferograms that include an image from 28 July 1997 or formed by images before and after this date, are all decorrelated in this area.

It can be observed that there are some terrain changes right below the hill. The artefacts depict a subsidence which borders reach the hill. This subsidence is most probably related to the mining activity of the Karviná Mine: ČSA.

4.7.1.3 Interferogram of ERS-2, 23 February – 30 March 1998

The selected interferogram of ERS-2 dating 23 February – 30 March 1998 has a proper configuration for deformation monitoring. The perpendicular baseline is not large, $B_{\text{perp}} = 83$ m, acquisitions taken in delay of $B_{\text{temp}} = 35$ days. Both dates were investigated for weather

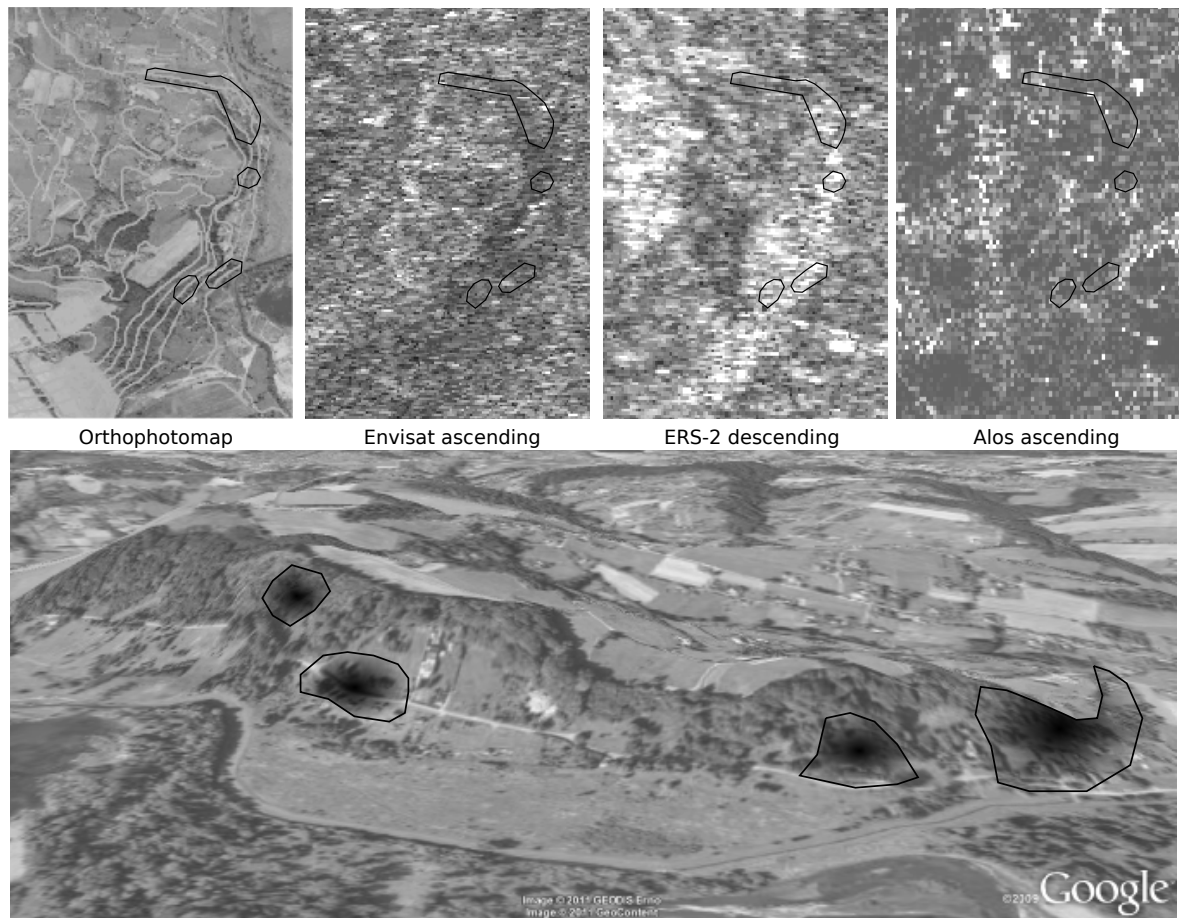


Figure 4.7.2 – Intensity images of constructed interferograms. Foreshortening effect can be observed in the descending track of ERS-2. Below, a 3D situation is figured to demonstrate the vegetation cover of the observed hill (background image by Google EarthTM).

conditions using CHMI data of Ostrava-Mošnov station. In both selected dates the weather trend is very similar – a week before acquisition there was a snow, then the temperature raised to range 0-15°C, it was raining but during the acquisition it was clear, with a snow most likely melted away, temperature >10°C and a mild wind of around 9 km/h. Within these conditions, especially with no main factors for the temporal decorrelation as is a presence of the (wet) snow cover and a movement of tree leaves or grass, the site preserves a high pixel coherence. It is possible that the leaves weren't grown fully yet since the whole month it was raining with a few sunny days in the end of March. In comparison with other interferograms from the ERS/Envisat descending track data, this interferogram shows clear homogeneous areas of the same phase shift. A heterogeneous area is detected in the place of the investigated slope which can depict a landslide.

Interpretation of Possible Deformation Artefact

The interferogram, as can be seen in Fig. 4.7.6, shows some phase gradients that can be interpreted as deformation movements. These gradients nearly fit to the locations known for the landslide activity. The phase shift shows a movement of the land mass closer to the

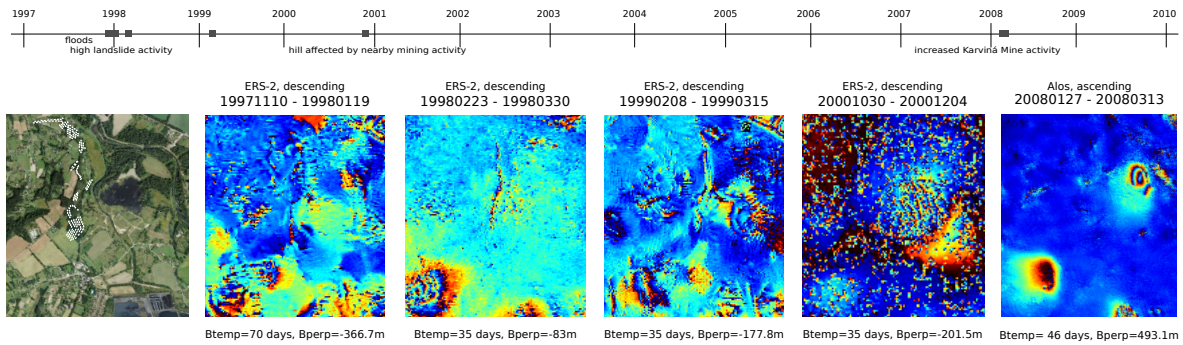


Figure 4.7.3 – Selected interferograms showing the landslide activity. Background image by Google EarthTM.

satellite line of sight - this can be expected on the bottom of the slope, see Fig. 4.7.4. On the other hand, as explained in Section 4.7.1.1 and figured in Fig. 4.7.2, the area is due to ERS-2 observing direction affected by a geometrical distortion - a foreshortening effect. The interferogram was filtered using a technique of NL-MEAN that tries to reconstruct shapes in interferogram based on its intensity values - and the intensity is due to the foreshortening high within the whole slope. In fact the trend is same also in the original interferogram, while the filtering lets the phase changes propagate more widely, into neighbouring pixels. Note that I investigate the original interferogram in following paragraphs.

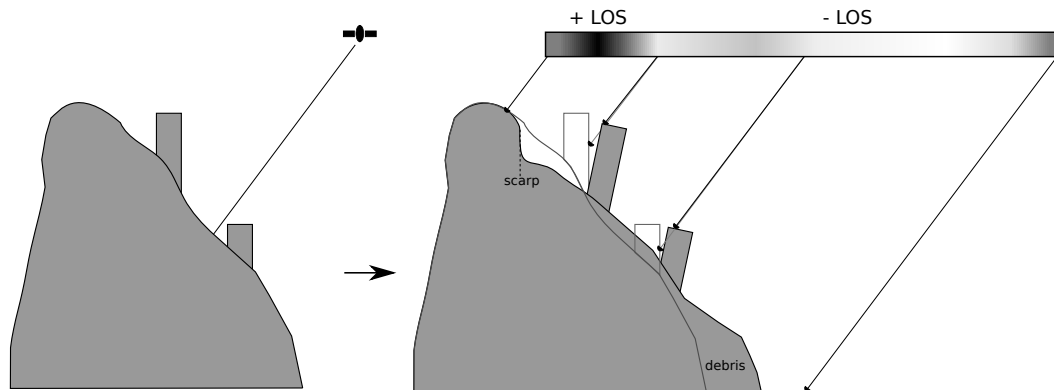


Figure 4.7.4 – Expected phase change caused by a landslide as observed in descending track

I will interpret the foreshortening effect similarly to the effect of multilooking. The resolution is coarsened, meaning that objects in a larger area will contribute a phase change together into one resolution cell. Local deformations will be lost in the interferogram evaluation. But deformations of a larger scale will not be affected by small discrepancies. The main problem here is that this detected landslide is relatively too local. The affected slope is represented by a number of pixels that is not sufficient to securely interpret the phase changes as a terrain movement. So, what else can this phase trend mean, if not a deformation?

First of all, the area is covered by a deciduous forest. A strong temporal decorrelation due to the movement of tree branches or leaves is expected here. Since the acquisitions are from a period of beginning of spring, the leaves may not be large in that time and the radar beam may penetrate to the branches, trunks and the ground. Even if there already were

leaves, a decorrelation shouldn't cause such a trend - it would behave more like a speckle phase noise.

However the movement of the trees (or their parts) in some common direction could cause such a phase trend. A wind blowing in direction from the hill in the moment of this morning acquisition can cause such an effect as well as a bending of trees under a snow cover in the first acquisition - unfortunately I do not have any proper data about a snow cover in this time and place. On the other hand, if there was really a landslide during this period of time, the trees could bend also in correspondence to the landslide direction, the phase change would have the same trend as showed in Fig. 4.7.4.

Second idea to interpret such phase changes was a possibility of a DEM induced error. The interferogram has indeed a relatively small perpendicular baseline parameter causing a $H_{amb} \simeq 90\text{m}/2\pi$. The detected phase shift can be around 2π , i.e. the DEM error would have must to be around 90 m in this area (a DEM error of 90 m within a distance of 100 m), which is highly improbable if not impossible. But, because the slope nearly faces the satellite line of sight, it will be illuminated in a local incidence angle approaching $\theta_{inc}^{local} > 0$. If this will be taken into account, the perpendicular baseline should be recomputed as (Hanssen, 2001)

$$B_{perp}^{local} = B \cdot \cos(\theta_{inc}^{local} - \alpha) \quad (4.7.1)$$

, where B is a geometrical baseline (distance between sensors) and the angle α is a baseline orientation.

Then, the local $B_{perp}^{local} \simeq 95\text{m}$ if $\theta_{inc}^{local} = 2^\circ$ and the height ambiguity using these local parameters in Eq. (2.5.4) is $H_{amb}^{local} \simeq 8\text{m}/2\pi$. Such a H_{amb} can really approach accuracy of used DEM (SRTM) especially in this part of a slope within 100 m where there is really a steep height change (up to 30 m) that could be misfitted in the 90 m spatial resolution of SRTM and propagate as a topography residual in the differential interferogram.

A possibility of such DEM induced error was however declined. As it was stated earlier, there is a grassland area of a higher coherence on the hill (in Fig. 4.7.6 this is on the southern part, directly behind the landslide zone) that is still facing in a very similar direction with the same elevation change. The height ambiguity might be less precise here since it is not facing the satellite directly but the difference is negligible⁵. This area is somehow out of the landslide danger zone. The phase is almost homogeneous. If the investigated phase trend was topography related, some phase residuals would be seen here as well. They were not.

Conclusion According to mentioned findings, the phase shift can be really interpreted as the landslide activity, but because of the coarse resolution it is not really reliable to estimate the landslide rate. There is maximally 1 fringe, i.e. phase change of 2π which corresponds with the wavelength λ . So, the detected deformation in the ERS-2 LOS can be as up to cca

⁵according to local incidence angle computation using a Terrain correction algorithm in Nest the difference of local incidence angles of landslide area and neighbouring stable zone is in arc minutes

$\lambda/2 = 2.8$ cm interpreted as a LOS uplift (landslide facing the satellite LOS) in the direction from the top of the slope to its bottom, as can be regarded in Fig. 4.7.6.

There is no known reliable information about the landslide activity during this period of time to compare with, but the “movement” was detected in the locations that are known for landslide danger. The interferogram is unique for the weather conditions and optimal geometrical configuration but still it must be taken into account that the most of the radar reflection showing a possible movement (towards the satellite) is from a forested area. So the interpretation of a landslide activity might be wrong.

4.7.1.4 Interferograms of Envisat Ascending Track

In the case of ascending track, different outputs were achieved from Envisat data. Here the slope is observed from more feasible angle, the whole slope length is sampled by more pixels. However because of the dense vegetation canopy on the slope, and due to other factors, the area is too decorrelated in all interferograms to be interpreted.

4.7.1.5 Interferogram of Alos Palsar, 27 January 2008 - 13 March 2008

This interferogram has $B_{temp} = 46$ days and $B_{perp} = 493$ m. Acquisitions were taken in the ascending mode, thus in the evening of cca 22:04 local time (+1 GMT). During this evening time the weather conditions are known to get stable compared to the day time when there was a temperature of 0-6°C and 2-8°C during the acquisitions and a rain of around 3 mm/day in both cases. Because of the low temperature, the water didn't vapourize so much to influence the phase measurements significantly as can be regarded as a problem in summer time ascending interferograms.

The use of a longer wavelength (23.6 cm) has two main advantages. First, it penetrates through the vegetation much easier and second, it can detect a higher phase change within a pixel. Because of this, the fast terrain changes due to the subsidence caused by Karviná Mine: Jan Karel (ČSA) activities since 2007 are visible (eastern part of Fig. 4.7.6c). The detected subsidence of these activities can be estimated as around 28 cm per 46 days within the subsidence trough of a radius around 200 m. The subsidence trough borders are about 150 m from the hill. The geophysical influence of the subsidence trough on the landslide is investigated in (Bláha et al., 2009).

Because the area is fully vegetated, even in L-band data some noise can be observed. This noise has been filtered using NL-MEAN algorithm (Deledalle et al., 2010) since it has an ability to reconstruct shaped artefacts and average phase values of textured areas such as a forest. An example of effect of the NL-MEAN filter is shown in Fig. 4.7.5. Here, the change patterns on the hill fit with the expectations of the landslide locations were detected. See also Fig. 4.7.6 for reference.

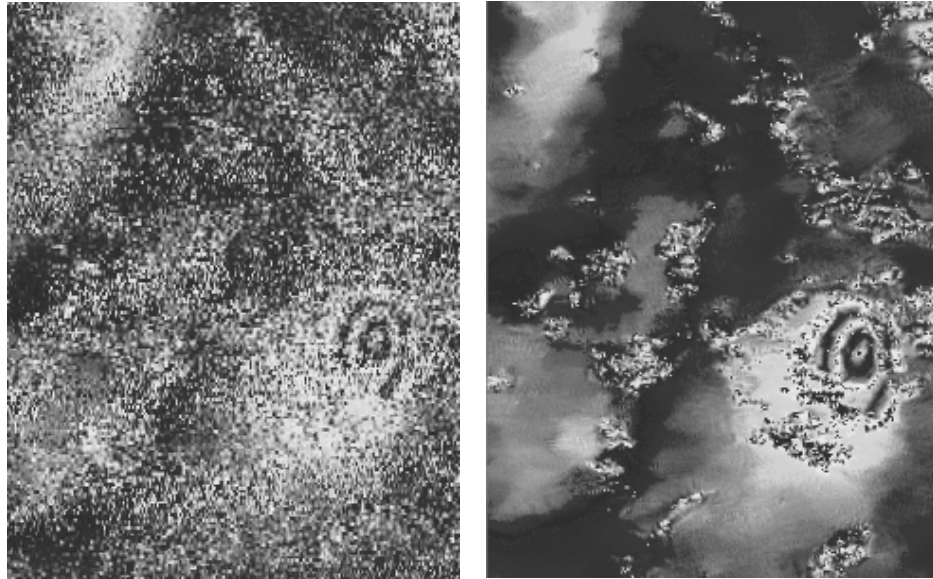


Figure 4.7.5 – Effect of non-local mean filtering for Alos Palsar interferogram: a) original phase image, b) modified NL-MEAN filtered phase image

Practical Note - Interpretation of a Topography Artefact

In the final interferogram, a strange phase artefact corresponding to the outline of the investigated hill has been found, in the interferogram with already subtracted topography. This can be seen as a “mark over the hill” in Fig. 4.7.5. The error source was identified and corrected, as explained in the end of this paragraph. Following text contains possibilities to interpret this artefact (with a hope to help an interpreter in a similar situation).

First, a possibility of DEM error is checked. As it is seen from Fig. 3.3.7, usage of DEMs with various height accuracy can influence the topography removal phase of forming the interferogram. A perpendicular baseline of $B_{\text{perp}} = 493 \text{ m}$ between acquiring satellite positions causes the interferogram not to be strongly sensitive to the topography. The hill observed for landslides differs from the stable surroundings by phase values lifted by around $+\pi/3$. This behaves like a DEM error to be investigated. The $H_{\text{amb}} = 114,3 \text{ m}/2\pi$ for this particular interferogram, as computed by Eq. (2.5.4). With this value of height ambiguity, the detected $+\pi/3$ corresponds to an elevation gradient of -19 m in the satellite LOS, in a distance of around 300 m . The minimal relative height accuracy of SRTM can be around $10 \text{ m}/90 \text{ m}$ and for Aster GDEM it is cca $15 \text{ m}/30 \text{ m}$. So, in a very unfortunate case it would be possible to have this “mark” be caused by a DEM error. On the other hand the DEMs can have such large spatial errors maybe in cases of tropical forests but not in this case. A DEM error would behave very locally, on a part of the hill maybe, as demonstrated in Fig. 3.3.7. Anyway, I have investigated the area of the hill for the DEM differences and found no significant change - there are indeed differences but they are not significant. Even after comparison of interferograms with both different DEMs subtracted, no important difference over the whole hill was observed.

Another possibility of the “mark” interpretation is a deformation. If the $+\pi/3$ is a propagation of an error to the terrain deformation, such a phase change would correspond

to $\lambda/6 = 3,93$ cm within the radius of around 500 m. This can be related to a terrain uplift of the whole hill or a subsidence of the whole surroundings. In fact this is improbable.

It has to be mentioned that in case of a high change in soil moisture, such uplift can really occur - according to (Barrett et al., 2009), an increase in soil moisture can cause a detectable soil expansion of several centimetres. During both days of acquisitions it was raining. On the other hand, it should be raining much heavier to cause such a high expansion of a soil over the whole hill - and especially an uplift of area under the hill would be rather expected for the reason of holding the water content. Moreover, the L-band is highly sensitive for the moisture content which means the coherence would drop rapidly with the moisture changes - but in this interferogram the coherence was very high over the area.

Similar case can happen with a change of a snow cover that in fact also leads to the loss of coherence - it doesn't have to, necessarily, in very special cases. However this hypothesis can be verified e.g. by exploitation of optical images that could show a snow cover in the area. This was investigated from Envisat MERIS data from the morning times of each following days. None of these images showed a snow cover in the area of interest.

The most probable reason of the artefact was a tropospheric delay changes. In (Ballatore, 2006) the vertical tropospheric stratification induced tropospheric phase changes were found to bring about 2.9 fringes within 1200 m in a whole interferogram stack. Supposing a linear distribution, the phase change would be $\pi/3$ in the case of topography height difference $\Delta H = 69$ m. The height change in the case of the hill (where such phase change of $\pi/3$ occurs) is $\Delta H \simeq 50$ m thus it is comparable with the former results. Even that it is stated in (Remy et al., 2003) application that in the height less than 500 m over the sea level the stratification changes were not significant, investigations of (Hanssen, 2001) show that the atmospheric refractivity varies stronger especially at lower altitudes. Unfortunately, there are no precise meteorological data of the hill available that could be used in the technique mentioned in 2.5.5.1 to verify the possibility of having the tropospheric stratification as a source of this phase change.

I have tried to remove the "mark" by an assumption of the tropospheric delay that is related linearly to the elevation changes - even that (Remy et al., 2003) proves that this delay doesn't behave linearly at all, this assumption can be used for small elevation changes in a local area. An attempt was performed here also - the phase change of $\Delta\varphi_{tropo}$ estimated for a given height difference $\Delta H = H_{top} - H_{ref}$ has been subtracted from every other height difference $\Delta H_x = H_x - H_{ref}$. This way local phase differences in the area of hill surroundings has been really suppressed but still it seemed to be a very local correction only - the "mark" didn't vanish at the whole no matter what value of $\Delta\varphi_{tropo}$ was attempted.

Conclusion Now, when probable scenarios of interpreting this mark were found (I include this here so one may find ideas and references of interpreting and removal of similar problems), a real source of error will be explained. Because there were problems of processing the input data in Doris due to actual Doppler focusing strategy of the Alos Palsar SLC data, I have processed data within one borrowed session of GAMMA®, converted the GAMMA® outputs and used them in Doris to subtract topography using a DEM. Probably due to problems in conversion, the geographical extent of the interferogram was identified wrongly and the DEM was shifted. The shift was large, about 600 m, but it wasn't detected due to a regular

topography of the area and relatively small height ambiguity. Once detected and after Doris version 4.01 with proper abilities was available, it helped to estimate the interferogram timing error, shifted the DEM and remove it properly. The result is visible in the final Fig. 4.7.6c.

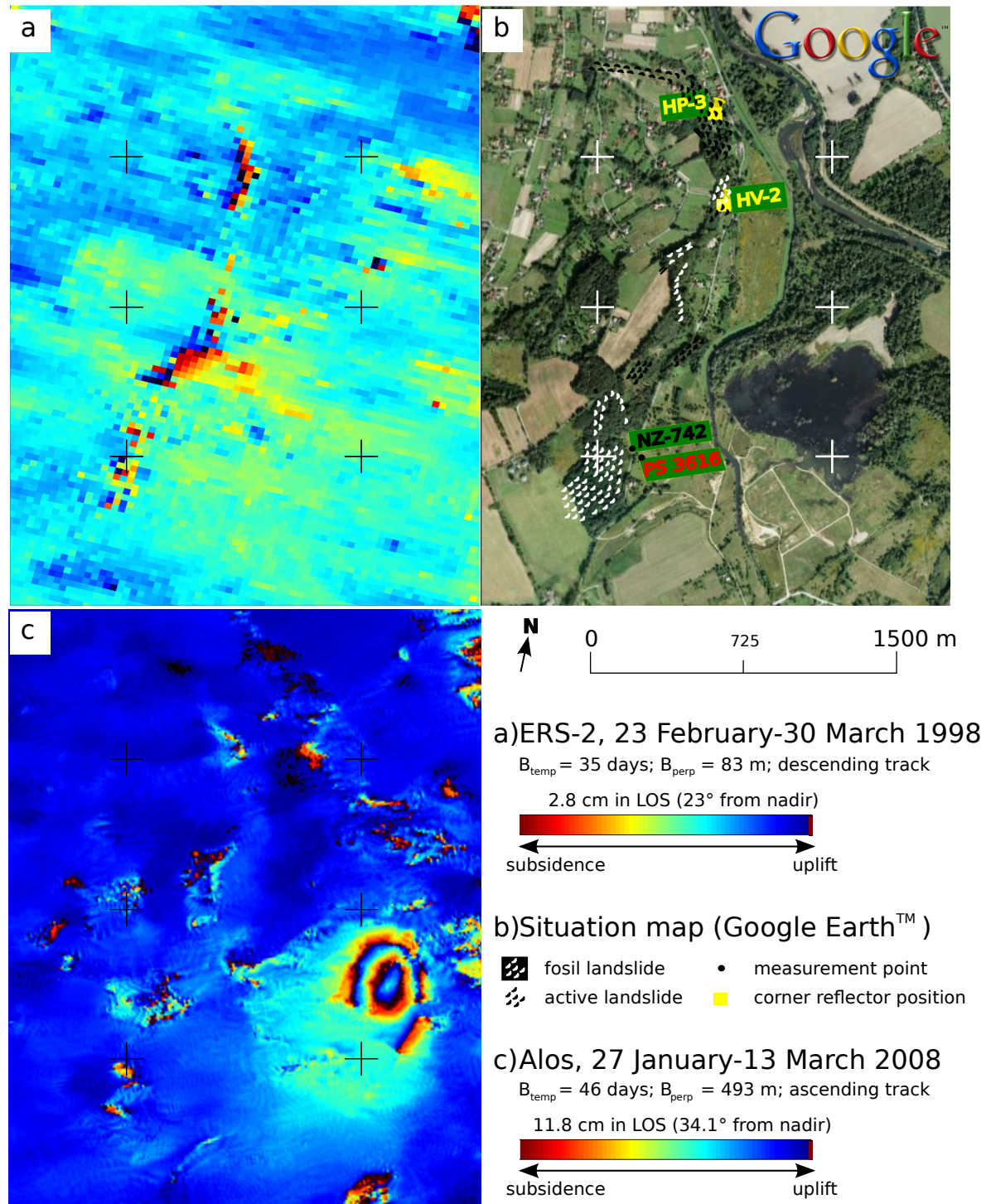


Figure 4.7.6 – Situation map and differential interferograms of landslide in Doubrava-Ujala: a) ERS-2 interferogram from 1998, b) Situation map over Google Earth™ background, c) Alos Palsar interferogram from 2008

4.7.2 MT-InSAR Processing

4.7.2.1 Envisat Descending Processing

The primary objective was to detect corner reflectors during 2010 and evaluate them using MT-InSAR. As was explained, the corner reflectors experiment failed. In the MT-InSAR processing of Envisat data from 2010, pixels representing locations of CRs were not found as phase-stable. Even a pixel of CR at position of V-100 (that was identified in MIRM - see Fig. 4.6.1) was affected by low coherence. Using more relaxed parameters for pixel weeding it was possible to use this pixel in processing, however its interpretation wouldn't help to raise the experiment to a valid state.

The area is handicapped by a strong decorrelation mostly due to the vegetation cover of forests and rural areas suspected to suffer by subsidence; there was also a strong atmospheric moisture during most of the acquisitions of 2010. During 31 May 2010 and 5 July 2010 acquisitions it was raining, all 2010 acquisitions were affected by clouds. The idea was to use values of zenith wet delay (ZWD) from measurements on site together with ZWD values computed from fixed GPS stations in the region. Unfortunately, the distance between the GPS stations is too long (more than 20 km) to provide a reasonable image of ZWD variabilities. Therefore only atmospheric phase screen (APS) computed by StaMPS could be used to filter the error sources due to water vapour. The APS component is highly correlated in space but with no or random temporal correlation, contrary to the terrain deformation behaviour monitored during a longer time period. Therefore it is possible to estimate the APS using a spatial low-pass/temporal high-pass filters algorithm supposing a sufficient amount of SAR images in the MT-InSAR processing.

So, in the end the area of interest was processed using the whole available Envisat dataset (see Sec. 3.2.1.2), neglecting the CR experiment and trying to detect at least some stable pixels on the hill. There are 17 Envisat ASAR VV acquisitions on disposal that fit the recommended minimum of 15 images for Permanent®/Persistent Scatterers method (PSI) but with a non-optimal geometrical and temporal settings, that worsen the quality of final deformation estimation.

Reading the stack configuration figured already in Fig. 3.2.4, the Doppler centroid values differ less than 42 Hz from the image selected as a master which is a very small deviation - the recommended maximal B_{Dop} for precise MT-InSAR processing is 500 Hz (Ketelaar, 2009). On the other hand, the range of B_{perp} is large, almost ± 800 m causing look angle errors and there are also large temporal gaps between images causing phase jumps in areas affected by a strong subsidence on the site. Small Baselines (SB) method seems to achieve more confident results than in the case of PS, still the output is affected by large phase unwrapping errors and wrong estimations of APS and other noise screens. Also, SB results are more affected by spatially correlated errors than the PS.

Unfortunately, in the area of Doubrava hill, no proper phase stable pixels were evaluated. This is because of the vegetated area mostly composed by a deciduous forest. The direction of the hill cause a foreshortening effect in the descending case. This seems not to be a disadvantage - first I supposed a physical multilooking effect that may increase the phase stability by averaging scattering contribution of trees to some value that may not change highly during time. This wasn't confirmed, C-band data simply are not suited for monitoring

in forested areas and the foreshortened area doesn't seem to yield pixels of a spatially stable phase.

4.7.2.2 Monitoring of Deformation Preceding Demolitions

In a middle part of the Doubrava hill a landslide caused large damages that resulted in a need of demolition of several inhabited houses. This situation can be seen on Fig. 4.7.7. Hereby an ortophotomap from 2006 shows the buildings that were demolished one year later. The MT-InSAR processing of ERS (1995-2000) found some stable points corresponding to a location of these buildings. A graph of a deformation trend related to a reference point in a stable area 0.5 km further is provided. The right image shows an actual situation from 2009.

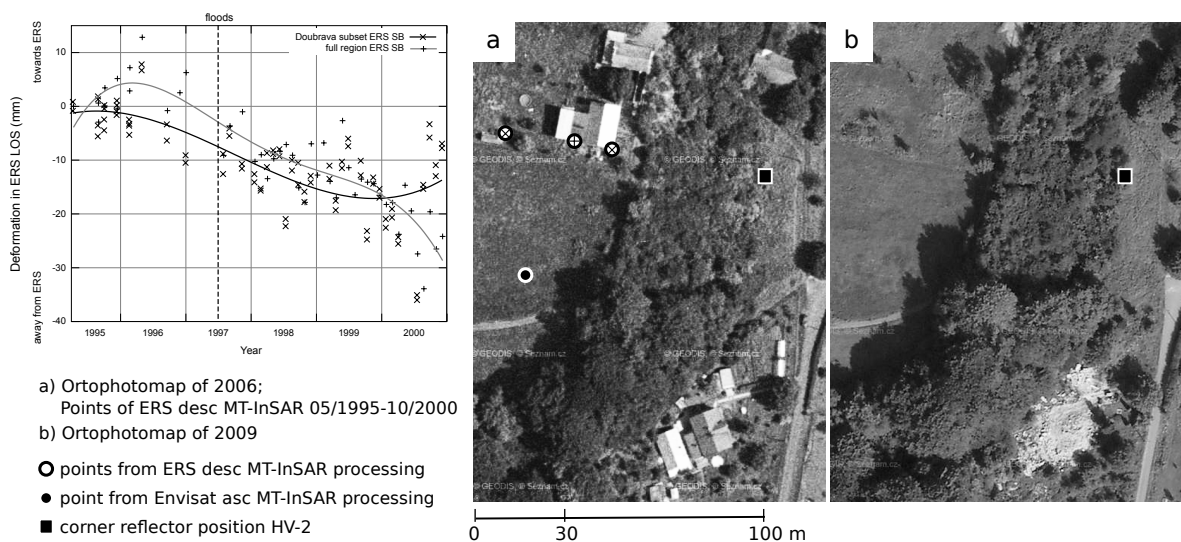


Figure 4.7.7 – Progression in the surroundings of HV-2 location. Background image by GEODIS BRNO, Ltd.

As could be expected due to the demolition of buildings somewhere during 2006-2009, no MT-InSAR points were found analysing dataset that includes images from this period. That's why I have reprocessed the Envisat datasets using data only of a period up to the beginning of 2006. In the descending case such dataset included only 4 SAR images. Therefore I used only Envisat ascending data for the final MT-InSAR processing. The hill is inclining specifically so that the slope almost copies the line of sight of the ascending pass. The spatial sampling of the slope is higher and a resolution is therefore even better than monitoring the flat ground. The buildings on the top of the hill should be clearly visible and should allow a PS investigation but the buildings on the hill slope will most probably be shadowed by surrounding trees. In the actual processing the pixels containing buildings on the top of the hill, however, were not selected as phase stable. Their evaluation would be possible by a processing with greatly relaxed parameters. These pixels, however, would be affected by strong errors.

Thus I used only ERS processing to form a possible deformation trend. From two different processing attempts of ERS I achieved 3 points on the top of the hill. Both show a

similar trend of the area. It seems that a higher change occurred during 2000. The phase was unwrapped differently in both processing attempts but the deviation of the points got visibly higher. This may have been caused by some greater change but it may as well be only an error in processing.

4.8 Summary

InSAR investigations of landslide in Doubrava were partially successful. On several DInSAR images (mostly from the period of winter and beginning of spring) the landslide is interpretable even that it is occurring in a forested area that complicates a common DInSAR usage. In such areas the sensitivity of InSAR on various factors have to be taken into account. Factors were described. Even that the slope orientation towards the descending track line of sight can cause geometrical distortions, it was shown that in this case the results from this track detected probably a landslide activity. Ascending track C-band acquisitions encounter a problem of penetrating the forest canopy. Alos Palsar data are regarded as the most suitable to monitor high-rate subsidence. For the landslide monitoring application its high resolution and great penetration abilities resulted in a better interpretability of landslide movement. To enhance the results, several approaches were described. However, due to lack of proper data, only some were successfully applied. For DInSAR, a freely available non-local mean algorithm showed its high filtering potential.

The MT-InSAR techniques failed to detect stable points located on the hill, probably because of a strong loss of coherence mostly due to large phase variations caused by numerous scatterers within a resolution cell in vegetated areas. An experiment to use remountable corner reflectors for MT-InSAR has failed, probably due to wrong orientation on site. An attempt to use only highly coherent interferograms and less stable pixels as well managed to evaluate some deformation of buildings on top of the hill, starting around 10 years before they had to be demolished (Fig. 4.7.7). The reliability of the deformation results is a subject of speculations. In this place the density of stable points is some 15 points/km² which should be dense enough to provide proper estimations.

"Deus quer, o homem sonha e a obra nasce.
Deus quis que a terra fosse toda uma,
Que o mar unisse, já não separasse."

(God wants, people dream and so the work of art is born.
God wanted the Earth to be as one,
that the sea unites and never separates.)

FERNANDO PESSOA, O INFANTE

Chapter 5

Final Summary

Summarizing facts that were presented in this thesis I have to remind the thesis aim again. I haven't designed any new processing method, neither I have succeeded in any significant improvement of existing methods (not mentioning series of scripts to perform an analysis over an MT-InSAR subset, several modifications of StaMPS scripts, or a slight modification of NL-MEAN filtering algorithm to apply in interferograms). This work still may be found useful since I focused on depicting problems that can discredit a proper usage of InSAR for a continuous monitoring in OKR area, a non-densely urbanized undermined region with subsidence rates exceeding phase detection limits of most of current available SAR satellites.

To use techniques of InSAR for a continuous monitoring of deformations in OKR area, several limitations and conclusions must be considered.

5.1 Discussion

5.1.1 General Limitations

Not every interferogram can yield a proper overview of a subsiding area as would be expected. This is related to actual satellite configuration of acquisitions or reflections overlaying the deformation itself - like caused by movements of a vegetation cover or weather conditions. The radar signal passes through the clouds but they would cause its phase delay. The radar signal would be also reflected by a snow yielding often highly coherent images of changes in the snow cover.

Subsidence troughs are situated mostly out of urban areas where they cause a relatively deep subsidence. Longer wavelength SAR should be used that will be able to capture such subsidence and penetrate to the vegetation. Alos Palsar data seem to be appropriate here. On the other hand, for needs to detect a very small subsidence years after a mine closure, shorter wavelength data should be chosen due to a higher sensitivity for such change.

It can be concluded from MT-InSAR processing of ERS/Envisat C-band data using StaMPS approach after a comparison with levelling that it can be effectively used when investigating a subsidence practically around a velocity up to first centimetres per year. A higher velocity will cause underestimations of the deformation or, in very unfavourable conditions of a low amount of stable reflecting objects in the subsiding area, it can even estimate an improper direction (an uplift can be interpreted instead of a subsidence).

Generally, MT-InSAR has a strong advantage in monitoring of a continuous deformation through a long time. Existing StaMPS algorithms may correct most of the errors (phase changes not induced by a physical deformation). However these errors can contain also real deformation parts in specific cases - for example if the algorithms will find a correlation between the deformation and B_{perp} or if the deformation happened only during one date in the data stack without a temporal continuation of its effects, and is spatially large enough to be misinterpreted as an atmospheric effect. The whole processing should be carefully operated with an approximate knowledge of the described area, even that the algorithms are actually capable of an automatic processing.

5.1.2 Can MT-InSAR fully Replace Levelling?

From the demonstrated results it seems that multitemporal InSAR usually underestimates the real rate of subsidence when this is too high. If the subsidence is too large with a high local variability, it even leads to not incorporating affected locations in the MT-InSAR processing (pixels are regarded as without proper phase stability).

For a computation of vertical part of the deformation, I have ignored its horizontal part at all. A more feasible solution would be to compute the vertical part by combining both ascending and descending MT-InSAR results, interpolating their spatial distribution to achieve overlapped areas - from these areas, deformation parts of any direction can be extracted then. However, I didn't find this solution important due to a strong subsidence in my AOI that wouldn't be estimated accurately neither by this solution.

Due to phase unwrapping problems, MT-InSAR may fully replace levelling only in the case of very slow deformations of up to several centimetres per year when using C-band SAR data, or up to first decimetres per year using more proper L-band SAR data. However the only available L-band Alos Palsar has too large temporal gaps between existing datasets and there is only a small amount of archived data of my AOI, therefore this couldn't have been tested here yet.

Of course various MT-InSAR methods from different institutions will present different results as can be read e.g. in (Raucoules et al., 2009); within this thesis only StaMPS processing was fully investigated as a method that can achieve good results in non-urban areas without a-priori data (which is a general condition to replace levelling). Even despite

of its advanced phase unwrapping techniques the deformations are strongly underestimated - after a phase jump (that is common in this area) the phase can be interpreted in both vertical directions - as subsidence but also accidentally as an uplift, as is demonstrated in a comparison with levelling in Fig. 3.3.14. However I haven't found any technique that can be really used reliably in this area of interest to replace levelling.

I have to recommend using the InSAR techniques as only complementary to levelling or precise GPS measurements. However there is a strong potential (using more proper data and/or some adapted MT-InSAR algorithms) that may replace the levelling appropriately in the future.

Phase Unwrapping Limits The MT-InSAR in general should be used in appropriately smaller areas where a relative deformation will not exceed current data sensitivity limits. In other words, subsidence rates can be probably well estimated in case they do not exceed $\lambda/4 \cdot \cos \theta_{look}$ per a resolution cell and the acquisition frequency, i.e. 1.3 cm/35 days per pixel for ERS/Envisat. In fact, current algorithms seem capable of overcoming problems of phase jumps - they attempt to find a general trend in data and figure out a number of corresponding phase cycles that the deformation caused. Their solutions however are still affected by a large ambiguity and practically they often fail in cases of a fast subsidence. According to (Colesanti et al., 2003), the unwrapping process will be *really* reliable in case of changes between neighbouring cells up to 0.6 rad which for ERS/Envisat means a maximal change of less than 3 mm/35 days per pixel. Using advanced phase unwrapping algorithms, also a larger deformation should be estimated appropriately. However its success depends on the actual coherence of the area to be unwrapped.

Mentioned limiting values for phase unwrapping are related to surrounding pixels. The subsidence trough may reach large deformations but it may be very shallow, developing into a large affected area. If this area includes a sufficiently dense network of highly coherent pixels, so the phase difference between them doesn't exceed mentioned limits, it would be possible to unwrap such area properly. This is also related to a maximal steepness of the deformation with regards to the spatial data resolution - an Eq. (2.5.1) can be used for an enumeration of this SAR data limit. The phase will decorrelate at all if the physical deformation exceeds current phase gradient limit, i.e. maximally 2.9 mm/m in LOS for ERS/Envisat (Hanssen, 2001), which after multiplying with pixel spacing of two pixels corresponds with a deformation up to ~4.6 cm in LOS between neighboring pixels.

5.2 Results and Findings

I have evaluated possibilities of InSAR for monitoring subsidence in OKR. Here the differential interferometry is proven to be a strong instrument for a precise ranging of subsidence trough extents, for an identification of unstable areas.

It was however found less reliable trying to estimate a real rate of subsidence from C-band data (ERS, Envisat). First of all it is largely affected by a decorrelation and secondly, the subsidence in OKR often exceeds ERS/Envisat data limits - in an extreme case, from Alos Palsar (L-band) interferogram a subsidence of around 70 cm/46 days was estimated in

an area that was possible to evaluate from Envisat only by MT-InSAR processing (since the area was spatially decorrelated) and here it yielded an improper estimation of less than a centimetre within these 46 days.

From MT-InSAR only, effects of decay subsidence after closure of mines in Ostrava during 1990s could be detected. Some subsidence was found even from Envisat of 2003-2010 dates in the surroundings of the former mines. Some spatially large subsidence was detected at a railway in the neighbourhood of Heřmanice Mine (closed in 1993) which may subside in the rate of around 3 mm/year. This would mean that even if it is expected that the subsidence is fading up to some 5 years after a mine closure, in fact the undermined area may still be affected in a much longer temporal extent, maybe more than 15 years, yet in much lower rate.

An application in landslide monitoring did show some results even though the experiment with corner reflectors failed (a non-precise method was used to compute the orientation angles) - some deformation was detected in locations known for a landslide activity and a subsidence was detected directly below the sliding hill as well, both from differential InSAR. Some deformations on the hill were detected by the MT-InSAR processing of ERS data, also on a location known for landsliding - because of a low amount of phase-stable pixels in the hill area, the phase may not have been properly unwrapped, so the reliability of estimation of the deformation rate is however questionable.

5.2.1 Comparison with other works

Various works monitoring subsidence of mining areas using InSAR techniques were already investigated in Section 1.2. Hereby I try to compare my findings with works that examine areas of similar conditions, i.e. relatively steep local subsidence in mostly non-urban areas, in continental weather conditions.

Such similar area is in Upper Silesia in Poland and was investigated by differential InSAR. Same problems were detected as in my case. As shortest interval between acquisitions as possible was recommended with a total loss of coherence in ERS/Envisat already after 70 days interval. Only man-made structures remained coherent over long time scales, a *"careful data selection according to meteorological data"* is proposed in (Perski et al., 2003). If fringes were successfully detected, then *"fringe pattern strongly relates on the position, shape and length of the mining front, the rate of mining advance and technique applied for the roof control and the geological structure of rock mass and the presence of abandoned underground workings"* (Perski, 2000). The advantages of a high temporal sampling as well as spatial resolution of TerraSAR-X managed to properly evaluate the subsidence in (Krawczyk et al., 2008). Alos Palsar was found suitable against other existing SAR data for monitoring deep subsidence in (Ng et al., 2008).

More problematical is the use of ERS/Envisat in MT-InSAR techniques. In non-urban areas with similar subsidence conditions, results are usually underestimated or no stable points are detected at all. MT-InSAR applied to subsiding cities in rate of a maximally a few cm/y often fit with levelling or GPS measurements very well, in any of published works. A comparison between StaMPS and GAMMA small baselines processing using ERS/Envisat with similar conditions as here has shown a better fit with in-situ data in the case of GAMMA

processing in (Dehghani et al., 2009b). On the other hand, a PSI implementation in GAMMA was already used to monitor subsidence in OKR - results published in (Wegmuller et al., 2004) detected no PS pixels at all in the subsidence affected area, only points in the far borders of Karviná district were evaluated of a rate up to about 1 cm/year - this result is similar to my processing using StaMPS with a difference that here StaMPS detected and evaluated a significantly higher number of PS/SB pixels in the affected area.

It seems that MT-InSAR can be used for monitoring of subsidence in Karviná district only in combination with other SAR data - this is a plan for future work. Data from Alos Palsar were processed by MT-InSAR in (Nitti et al., 2009) for monitoring of an abandoned salt mining site in Poland. There were 12 acquisitions available during 3 years. Results corresponded with ERS/Envisat processing, however the low amount of acquisitions showed more outliers in presumably stable areas, these were regarded as a noise. More acquisitions with a higher temporal sampling of TerraSAR-X (15 acquisition between March-July 2009) were applied in MT-InSAR by (Liu et al., 2010) - a rate of up to around 5 cm/year was detected in a strongly subsiding urbanized area in China.

5.2.2 Suitability of InSAR for Subsidence Monitoring

Depending on the target area to be monitored - expected rate of deformation, land cover properties etc., different InSAR methods and SAR datasets should be selected. Multitemporal InSAR methods are very valuable for monitoring in large temporal extents and are capable to correct most of unwanted phase contributions. If the deformation rate doesn't exceed current limits that are mostly related to capabilities of each SAR system, the deformation can be accurately enumerated if a sufficient number of stable points are detected in the area. Other conditions for an appropriate application are of course a proper temporal sampling of available acquisitions and physical conditions during taking acquisitions (geometrical configuration of satellite, weather).

For the monitoring in OKR area, ERS/Envisat MT-InSAR showed a proper application while monitoring a **decay subsidence** after closure of mines in Ostrava. On the other hand, deformation rates of non-urbanized areas that are known to subside fast (Karviná district) were usually strongly underestimated, as could have been expected.

In densely vegetated terrain, other unsuitable areas or wet weather during acquisitions, a strongly filtered differential interferogram is often the only possibility to extract some information about terrain deformations. A strong filtering however may impair existing interferometrical fringes and a real rate of subsidence cannot be evaluated. Using L-band data that better penetrate through vegetation and can detect larger subsidence as well, only some fine filtering is often enough to be applied. Due to a low amount of existing L-band data of OKR, MT-InSAR techniques couldn't be applied. Still the usage of L-band data is found appropriate to monitor the main subsidence **during mining activities** while ERS/Envisat may be used to evaluate the subsidence trough borders where also MT-InSAR can be applied.

Because of many erroneous factors that may affect the processing of ERS/Envisat data by MT-InSAR, the accuracy of estimated deformation rates cannot reach theoretical accuracy of a sub-millimetre order. This is indeed not important for monitoring of much faster subsidence

in OKR. On the other hand, to evaluate the possible uplift in the *beginning of mining activities* that precedes the process of subsidence, or to monitor (slower) deformations of **objects in urbanized areas**, higher frequency data of X-band should be used for MT-InSAR processing.

Only data from ERS, Envisat and Alos Palsar were tested within this work. The results conform with expectations, however many of new expectations are formed based on the results. It is expected that the planned mission of Sentinel-1 will be suitable enough for any of the areas of InSAR application due to a frequent revisit time and high resolution of the SAR. But decorrelating factors such as a dense vegetation may still corrupt its final results.

Also, only StaMPS techniques in combination with Doris (differential) InSAR processor were successfully applied within this work for MT-InSAR processing of available C-band data. These techniques showed appropriate results in their numerous applications by other authors, yet processing using some different tool with different approaches may form more suitable results in the (non-urban) areas of a steep subsidence. Several examples were already given in Section 1.2.

5.3 A Proposal for a Systematic Monitoring of Terrain Changes in Moravian-Silesian Region using InSAR

Synthetic aperture radar interferometry include specific problems that often disallow its proper usage for monitoring of deformations in such area as the Moravian-Silesian Region is. Still it was proven that with the right attitude and approach of an InSAR operator it is possible to identify subsiding locations, to extract a valuable information about the progress, size and shape of subsidence troughs in time and space, in some cases the rate of subsidence can be also precisely evaluated. The technique can be very valuable to conclude about a continuance of terrain deformations after an end of a mine activity.

I would like to propose a scheme for a systematic monitoring of an undermined area in Moravian-Silesian Region here for a future use.

Data Sets The most proper data for evaluation of a fast subsidence in the AOI is Alos Palsar. Its unique ability to penetrate through vegetation thanks to used L-band frequency preserves a high correlation in most of the area where C-band data simply fails. I propose to focus the future InSAR monitoring on using these data. This also includes a need to order an acquisition planning in advance for all possible future acquisitions. If using both single and dual polarization data (dual polarized data are of a half spatial resolution as single polarized) this leads to a maximum 6 acquisitions per year of one area which would allow also a proper MT-InSAR processing.

After a Sentinel mission will be launched it will be possible to process also these C-band images of about 5x higher spatial resolution and almost 3x more frequent revisit time than in the case of ERS and Envisat. These data might be interesting also because of expected favourable policy for non-commercial purposes but its use will be still problematical in the non-urban areas where MT-InSAR processing may still underestimate high subsidence rates.

For a precise monitoring of effects after mine closure in urban areas, X-band data such as TerraSAR-X or Cosmo-SkyMed can be investigated. On the other hand, it will most likely not reveal any deformation signal in vegetated areas. They should be used only where the more coarse C-band data processing will not satisfy the precision requirements - for example in case of monitoring deformations of such structures as highways over an undermined area.

Data Storage and Processing The results achieved from InSAR processing have to be converted into a GIS, data should be stored in some form of a geodatabase, for example in the fashion described in (Lazecký, 2008). The storage of DInSAR results is almost straightforward - from the final DInSAR wrapped phase data, raster files should be formed, appropriately filtered and geocoded once for the whole area of interest. A phase unwrapping procedure can be applied additionally only where the interferogram parts are not decorrelated strongly. It is not necessary to store corresponding unfiltered complex binary files as well since they can be reconstructed from source data - instead of this, parameters that were used to form such interferograms should be stored.

Results of MT-InSAR processing can be stored as a point vector data, referenced to a stable area. However the MT-InSAR processing showed not very reliable results when performed over the whole OKR area. Unfortunately the MT-InSAR suffered from too large ambiguities in the results of such strongly deformed AOI while more details of current deformations were preserved when processing with a closer focus on each site, preferring interferograms of a higher coherence over the site. Thus subsiding sites should be selected and for each site a smaller crop should be reprocessed by an InSAR operator using parameters matching the needs of the current task.

An appropriate solution for this is to process the whole area in patches that are small enough, from fairly coherent interferograms, refer these patches to a very stable point (preferably to one of which his close neighbourhood is already monitored by levelling or GPS) and when combining the patches together, relate these patch reference points to some common reference by a precise unwrapping or (better) using the insitu measurements. Using a geodetical approach it would be possible to even recompute the deformation rates to absolute values in some common height coordinate system - in such case, however, the best scenario would be to omit the horizontal part of the signal since we are interested in subsidence only.

From such formed GIS it would be possible to extract information about deformations and its progress of any selected area in the OKR within almost any selected date. With combination with data from other sources (GPS, levelling, LIDAR, current and future mining plans and subsidence models) it will be possible to extend the whole knowledge about the subsidence in OKR, together with more appropriate future predictions. This is needed mostly for purposes of building on the undermined area, to better characterize hazard zones and estimate the time when the subsidence trough gets stabilized after a mine closure in the area.

5.4 Ideas for a Future Work

Weighting a-priori Information to Enhance StaMPS Results From the comparisons with levelling that are assumed to provide correct information it seems that StaMPS attempts to find some general trend of the movement in time from which the deformation can however deviate. If there is some deformation jump that exceeds SAR sensitivity limits, it is often regarded as a deviation from the general trend and StaMPS tends to estimate further values to the opposite direction to decrease the effect of this deviation. Such principle is understandable - an error would not propagate further. If some a priori information about the subsidence in the area are used, at least very coarse ones, the unwrapping algorithms would be able to extract a more appropriate general trend. A significant enhancement for the InSAR usability in the areas of large subsidence would be a usage of a-priori information from levelling or GPS measurements that would be used as a reference to unwrap surrounding pixels. Some similar attempt was applied by (Dehghani et al., 2009a). However this would be again a hard estimation of a subsidence exceeding physical limits of used C-band data.

Strongly filtered Interferograms as Input to StaMPS Techniques of MT-InSAR can extract a very precise information about a deformation advancement. However in the case of my AOI the deformation rate was strongly underestimated and a PS density was usually low. Differential interferograms got visually readable only after a strong filtering. In this way a precise information is lost. However if such precise information is not expected to be reachable as is this case, the filtered DInSAR images might be used as an input for StaMPS to achieve a higher number of detected points and significantly decrease the influence of surrounding distributed scatterers. An improved Goldstein filtering by (Baran et al., 2003) may be a proper filtering since it preserves most of highly coherent phase.

Usage of Intensity Information of Radar Signal Delay What should be inspected in the case of a large deformation is the other information that can be derived from the SAR data. Unfortunately, this wasn't investigated yet within writing this thesis but it should be possible to coarsely estimate a deformation using intensity images - at least for a high resolution data, this can be practically helpful. An attempt of using magnitude image to coarsely estimate a too large deformation movement was mentioned already in (Yun et al., 2007).

Extended use of Atmospheric Delay Estimations by StaMPS A proper revealing of deformation by InSAR can be done by reducing interferograms from all unwanted contributions. A problem still persists in the field of atmospheric contribution even that several solutions were described. A significant improvement in both DInSAR and MT-InSAR can be seen when using interferograms with removed atmospheric effects. An idea of a processing improvement is to use atmospheric phase screens that can be estimated using StaMPS, even that this would mean a reprocessing the whole data stack for each date selected as a master. Such APS can then be interpolated for the whole scene, wrapped and removed from the phase terms of the input SAR image of current date. This attempt is computationally very demanding and is based on a correctness of APS estimations. Its

effect wasn't tested yet but it should influence DInSAR deformation interpretability as well as it might increase phase stability for PS selection in MT-InSAR.

Monitoring of other Phenomenas using InSAR It was shown that InSAR can be used more widely, not only for monitoring of subsidence. I want to mention only two ideas that may be investigated more in the future for the OKR region - a possible effect of a slight uplift before the subsidence due to geomechanical processes in the ground rocks and effects of floods in the region. The slight uplift is expected to be minimal and should be investigated using X-band data with a high temporal frequency on places where the mining activities are to begin. The flood danger is persistent in the OKR region and floods that actually happened in 1997 and other years were already monitored by remote sensing and even an attempt to use InSAR was performed. Some deeper investigation however can provide more information about flood affected areas as well as post-flood effects of groundwater in the undermined region.

5.5 Final Words

As discussed within this chapter or this thesis in general, methods of InSAR have several unique advantages that allow us to monitor subsidence or landslides remotely. These methods promise accurate estimations of terrain deformation rates and extents. However data are limited by numerous unwanted factors, known as sources of phase decorrelation. Phase decorrelates in wet or vegetated areas, by too steep slope of monitored deformation or other factors discussed within this thesis. The investigated area of OKR is challenging current InSAR techniques - it is highly vegetated, subsidence in the area is very steep and the weather is very variable as well.

Even that often decorrelated, interferometrically processed C-band data of ERS/Envisat located subsidence troughs in OKR. Several available L-band data of Alos Palsar demonstrated a high suitability of such data for subsidence monitoring in OKR. Using MT-InSAR processing of ERS/Envisat, very slow deformations many years after closure of mines in Ostrava were found.

Despite stated processing problems, InSAR proved its usability for a continuous monitoring of terrain deformations in the undermined area of interest. Its unique ability to detect very shallow deformations and provide a whole overview of the subsiding terrain can be used together with other data (levelling, subsidence models etc.) to form a complete GIS concerning deformations of OKR. InSAR can be used to monitor real influence of mines on the terrain development or for another tasks. Using more appropriate SAR data in the future processing, many of evaluated problems can be surpassed.

To properly achieve thesis objectives I have worked on several subtopics:

- achieving a proper knowledge of current InSAR advantages and limits - I have achieved and put together information from various publications, I have computed various limits for modern SAR satellites,

- a proper image processing of differential interferograms - I have found various existing possibilities to improve DInSAR images and used them for evaluations of terrain deformations in OKR,
- a proper application of StaMPS for monitoring of OKR - I have demonstrated needs of a careful selection of input interferograms, suggested proper processing parameters of StaMPS and discussed current ERS/Envisat limits found in StaMPS processing. I have performed several StaMPS applications achieving an overview of deformations in the whole OKR area,
- a comparison with levelling data - I have performed a double difference for available levelling data to compare them with a vertical part of MT-InSAR unwrapped phase estimations from ERS and Envisat, and found out large differences in areas of a steep deformations exceeding SAR limits,
- an evaluation of corner reflector experiment - together with a team, I have designed a corner reflector and performed an experiment to increase a number of phase-stable points on the sliding hill in Doubrava-Ujala. The experiment failed but reasons of the failure were found, described and will be evaded in similar future experiments,
- a methodology for a continuous monitoring of terrain changes in OKR - I have proposed a methodology combining InSAR results into a GIS, together with other data of interest, I have proposed a set of SAR data that is needed for a proper monitoring of OKR.

Vyhodnocení

V disertační práci byly popsány a vyhodnoceny možnosti, ale i omezení metody družicové radarové interferometrie (InSAR) pro monitorování terénních deformací - především se zaměřením na poklesy a sesuvy v podmínkách Moravskoslezského kraje, v poddolovaném území Ostravsko-karvinského revíru (OKR). Byly představeny výsledky ze zpracování radarových dat družic ERS/Envisat a Alos Palsar, pracujících ve frekvenčních pásmech C, respektive L. Byly prozkoumány možnosti překonání některých omezení a problémů zpracování dat v daném území.

Ve zkoumaném území se projevují rychlé poklesy, které mohou přesáhnout míru 1 m/rok v poměrně malé ploše (o průměru stovek metrů). Takové poklesy není možno korektně vyhodnotit pomocí družic ERS či Envisat, použití jejich dat je proto omezeno pouze na detekci těchto poklesů, například pro zjištění hranic poklesové kotliny. Tato data se však jeví velmi vhodná pro sledování doznívajících poklesů po ukončení hornické činnosti, nejlépe pomocí vícesnímkových technik InSAR. Použitím těchto dat v technikách implementovaných do algoritmů StaMPS je možné přesně vyhodnotit poklesy o rychlosti prvních centimetrů za rok (teoretická spodní hranice se udává až méně než 1 milimetr za rok). Tak byly zjištěny velmi malé lokální zbytkové poklesy na území Ostravy až více než 15 let po ukončení těžby tamějších dolů. Ze srovnání výsledků zpracování StaMPS s dostupnými nivelačními daty vyplynuly významné nepřesnosti - ty byly způsobeny především právě detekčními omezeními radaru z ERS/Envisat. Nivelační data se týkala vždy silně klesajícího území.

Zpracování dat z družice Alos Palsar technikou diferenciální InSAR prokázalo nesporné výhody radaru o vyšším rozlišení a nižší frekvenci (pásmo L) pro monitorování hlubokých poklesů a pro použití v územích pokrytých středně hustou vegetací. Bohužel z důvodu nedostatku takových dat z Alos Palsar pro sledované území nebylo možné vyhodnotit terénní deformace vícesnímkovými technikami InSAR - použití těchto dat pro OKR je však silně doporučeno, data je nutné předem naplánovat.

Zjištěná fakta uvedená v disertační práci vedou k několika závěrům a doporučením týkajícím se využití technik InSAR pro sledování terénních deformací v poddolovaném území:

- použití dat pořízených radarem o frekvenci pásem C či X pro zjišťování terénních deformací je možné jedině mimo plochy porostlé vegetací nebo je-li vegetace v nehybném stavu (například v zimním období po rostání sněhu). Data z pásma L dekorelují až v případech hustě zalesněného území,
- atmosférické vlivy výrazně ovlivňují radarový signál, a to především u X a C frekvenčních pásem. Tento vliv je možno odstranit použitím některé z existujících metod, ovšem

pouze za dispozice dalších dat, což může být: vyšší počet radarových dat pro vícenímkové zpracování (alespoň 10 snímků, doporučuje se však vyšší počet) nebo data z dostatečně husté sítě GPS stanic ve zkoumaném území, která by vyprodukovala přesný atmosférický model. Jiné známé metody bohužel nedosahují dostatečného rozlišení, které je potřeba pro použití v území s lokálními deformacemi (v OKR),

- data pro použití k monitorování poklesů je nutno vybírat na základě očekávané míry poklesů s přihlédnutím na časové a prostorové rozlišení dat a detekční schopnosti jednotlivých radarových zařízení. Každé zařízení má svá specifika - v případě podmínek OKR se jeví nejvhodnější použití L-pásmových dat Alos Palsar pro jednorázové zjištění změn mezi dvěma pořízeními, avšak vzhledem k nadměrným časovým odstupům je pro průběžné sledování poklesů doporučeno použít časově frekventovanější data z méně vhodných frekvenčních pásem. Nutnost pravidelných nivelačních měření pro přesné zhodnocení míry poklesů použitím InSAR neodpadá,
- pro sledování sesuvu je nutné vzít v úvahu orientaci sesouvajícího se svahu vůči střednímu směru pohledu družice a rovněž očekávanou rychlost sesuvu. Systémy SAR mají nejvyšší detekční schopnost pro deformace ve směru svého pohledu - pro monitorování sesuvu je tak často vhodné použít snímky získané s vyšším úhlem pohledu od vertikály než jaké jsou standardně dodávány. Sesuvy bývají často na velmi lokální úrovni a často se projevují pomalým sesouváním, který je vhodné monitorovat. Proto je doporučeno použít data o dostatečně vysokém rozlišení,
- v případě nedostatku dominantně odražejících stabilních bodů na sledovaném území je možné trvale instalovat umělé koutové odražeče za předpokladu jejich přesné a správné orientace.

"The length of my life depends on how fast I am moving
relative to the people who want to talk about such a concept."

JOHN D. BARROW COMMENTING ON A TIME DILATION IN "THE WORLD
WITHIN THE WORLD"

Bibliography

- Alvarez, L. J. *Envisat-1 Mission CFI Software Mission Conventions Document*. 2.0. ESA, GMV. 1997, p. 55. URL: http://eop-cfi.esa.int/CFI/ENV_CFI_DOCS/mcd2.0.pdf.
- Arnaud, A., N. Adam, R. F. Hanssen, J. Inglada, J. Duro, J. Closa, and M. Eineder. "ASAR ERS interferometric phase continuity". In: *IEEE International Geoscience and Remote Sensing Symposium, IGARSS'03*. Toulouse: IEEE International, 2003, p. 3.
- Attema, E., P. Bargellini, P. Edwards, G. Levrini, S. Lokas, L. Moeller, B. Rosich-Tell, P. Secchi, R. Torres, M. Davidson, and P. Snoeij. "Sentinel-1: The Radar Mission for GMES Operational Land and Sea Services". In: *ESA Bulletin* 131 (2007), p. 8.
- Baby, H.B., P. Gole, and J. Lavergnat. "A model for the tropospheric excess path length of radio waves from surface meteorological measurements". In: *Radio science* 23.6 (1988), pp. 1023–1038. ISSN: 0048-6604.
- Ballatore, P. "Synthetic Aperture Radar Interferometry: Separation of atmospheric artifacts from effects due to the topography and the terrain displacements". In: *Earth, Planets, and Space* 58.8 (2006), pp. 927–935. ISSN: 1343-8832.
- Baran, I., M. P. Stewart, B. M. Kampes, Z. Perski, and P. Lilly. "A Modification to the Goldstein Radar Interferogram Filter". In: *IEEE International Geoscience and Remote Sensing Symposium, IGARSS'03*. Vol. 41. 9. Toulouse: IEEE International, 2003, pp. 2114–2118.
- Barrett, B. W., E. Dwyer, and P. Whelan. "Soil Moisture Retrieval from Active Spaceborne Microwave Observations: An Evaluation of Current Techniques". In: *Remote Sensing* 1 (2009), pp. 210–242. ISSN: 2072-4292. DOI: 10.3390/rs1030210.
- Berardino, P., G. Fornaro, R. Lanari, and E. Sansosti. "A new algorithm for surface deformation monitoring based on small baseline differential SAR interferograms". In: *Geoscience and Remote Sensing, IEEE Transactions on* 40.11 (2002), pp. 2375–2383. ISSN: 0196-2892.
- Bevis, M., S. Businger, T. A. Herring, C. Rocken, R.A. Anthes, and R.H. Ware. "GPS meteorology – remote-sensing of atmospheric water-vapour using the global positioning system". In: *Journal of Geophysical Research-Atmospheres* 97.D14 (1992), pp. 15787–15801.
- Bláha, P., R. Duras, P. Konečný, and H. Doleželová. *Antropogenní změny z poddolování a svahové deformace*. Tech. rep. Final report of project ČGS 2549/2006. Ostrava: GEOtest Brno, 2009, p. 186.
- Bonkowski, R. R., C. R. Lubitz, and C. E. Schensted. *Studies in Radar Cross-Sections-VI. Cross-sections of corner reflectors and other multiple scatterers at microwave frequencies*. Tech. rep. University of Michigan. Radiation Laboratory, 1953.
- Carbognin, L. *Overview of the activity of the UNESCO-IHP working group IV project M-3.5 (C) on land subsidence*. Tech. rep. UNESCO, 2003.

- Chen, C.W. and H.A. Zebker. "Two-dimensional phase unwrapping with use of statistical models for cost functions in nonlinear optimization". In: *JOSA A* 18.2 (2001), pp. 338–351. ISSN: 1520-8532.
- Colesanti, C. and J. Wasowski. "Investigating landslides with space-borne Synthetic Aperture Radar (SAR) interferometry". In: *Engineering geology* 88.3-4 (2006), p. 27. ISSN: 0013-7952. DOI: 10.1016/j.enggeo.2006.09.013.
- Colesanti, C., A. Ferretti, C. Prati, and F. Rocca. "Monitoring landslides and tectonic motions with the Permanent Scatterers Technique". In: *Engineering Geology* 68.1-2 (2003), pp. 3–14. ISSN: 0013-7952.
- Covello, F., F. Battazza, A. Coletta, M. L. Battagliere, V. Bellifemine, and L. Candela. "One-day interferometry results with the cosmo-skymed constellation". In: *IEEE International Geoscience and Remote Sensing Symposium, IGARSS'10*. Honolulu: IEEE International, 2010, pp. 4397–4400. ISBN: 978-1-4244-9564-1.
- Cumming, I.G. and F.H. Wong. *Digital Signal Processing of Synthetic Aperture Radar Data: Algorithms and Implementation*. Artech House, 2004. ISBN: 1580530583.
- Curlander, J.C. and R.N. McDonough. *Synthetic aperture radar - Systems and signal processing*. New York: John Wiley & Sons, Inc., 1991, p. 396.
- D'Agostino, F., C. Gennarelli, and G. Riccio. "PO Evaluation of the field backscattered by a trihedral corner with a resistive face". In: *Microwave and Optical Technology Letters* 21.3 (1999), pp. 173–177.
- Dehghani, M., A. Hooper, R. Hanssen, and M.J.V. Zouj. "Hybrid Conventional and Persistent Scatterer SAR Interferometry for Land Subsidence Monitoring in Southwest Tehran, Iran". In: *Fringe Workshop*. Frascati: ESA, 2009. ISBN: 978-92-9221-241-4.
- Dehghani, M., V. Zoej, M. Javad, E. Iman, M. Ali, and S. Sassa. "InSAR monitoring of progressive land subsidence in Neyshabour, northeast Iran". In: *Geophysical Journal International* 178.1 (2009), pp. 47–56. ISSN: 1365-246X. DOI: 10.1111/j.1365-246X.2009.04135.x.
- Delacourt, C., P. Briole, and JA Achache. "Tropospheric corrections of SAR interferograms with strong topography. Application to Etna". In: *Geophysical Research Letters* 25.15 (1998), pp. 2849–2852. ISSN: 0094-8276.
- Deledalle, Ch. A., F. Tupin, and L. Denis. "A non-local approach for SAR and interferometric SAR denoising". In: *IEEE International Geoscience and Remote Sensing Symposium, IGARSS'10*. Honolulu: IEEE International, 2010. ISBN: 978-1-4244-9564-1.
- Doin, M.P., C. Lasserre, G. Peltzer, O. Cavalié, and C. Doubre. "Corrections of stratified tropospheric delays in SAR interferometry: Validation with global atmospheric models". In: *Journal of Applied Geophysics* 69.1 (2009), pp. 35–50. ISSN: 0926-9851.
- Dopita, M., J. Aust, et al. *Geologie české části hornoslezské pánve (Geology of the Czech part of the Upper Silesian Basin)*. Geological Map of Paleozoic of the Czech part of the Upper Silesian Basin 1:100 000 included. Ministry of Environment of the Czech Republic, Prague, 1997, p. 280. ISBN: 80-7121-011-5.
- Duesmann, B., I. Barat, N. Miranda, B. Rosich, M. Pinol, and D. Kuijper. *ERS-2 and ENVISAT orbit control Current and future strategy*. Nov. 2007. URL: http://earth.esa.int/fringe07/participants/717/pres_717.pdf.
- ESA. *EnviSat ASAR Product Handbook*. 2.2. ESA. 2007. URL: http://envisat.esa.int/pub/ESA_DOC/ENVISAT/ASAR/asar.ProductHandbook.2_2.pdf.

- *ERS-2 InSAR restored to life*. 2008, p. 16. URL: <http://earth.esa.int/object/doc.cfm?fobjectid=5864>.
- Ferretti, A., C. Prati, and F. Rocca. "Nonlinear subsidence rate estimation using permanent scatterers in differential SAR interferometry". In: *IEEE Transactions on Geoscience and Remote Sensing* 38.5 (2000), pp. 2202–2212.
- Fiedler, H., E. Boerner, J. Mittermayer, and G. Krieger. "Total zero Doppler Steering—a new method for minimizing the Doppler centroid". In: *IEEE Geoscience and Remote Sensing Letters* 2.2 (2005), pp. 141–145. ISSN: 1545-598X.
- Franceschetti, G. and R. Lanari. *Synthetic aperture radar processing*. CRC, 1999. ISBN: 0849378990.
- Gabriel, A.K., R.M. Goldstein, and H.A. Zebker. "Mapping small elevation changes over large areas: Differential radar interferometry". In: *Journal of Geophysical Research* 94.B7 (1989), pp. 9183–9191. ISSN: 0148-0227.
- Ge, L., Ch. Rizos, S. Han, and H. Zebker. "Mining Subsidence Monitoring using the combined InSAR and GPS Approach". In: *10th FIG International Symposium on Deformation Measurements*. Vol. 10. Orange 2001.
- Gray, A. L., K. E. Mattar, and G. Sofko. "Influence of Ionospheric Electron Density Fluctuations on Satellite Radar Interferometry". In: *Geophysical Research Letters* 27.10 (2000), pp. 1451–1454.
- Grmela, A., J. Müllerová, and P. Janas. "Analysis of Reasons of Road Failure in Orlová". In: *Geologia a životné prostredie*. Bratislava: UK Bratislava, 2001, pp. 49–53. ISBN: 80-88974-25-9.
- Grmela, A. and N. Rapantová. "Protection of Groundwater resources quality and quantity in mining areas". In: *Deposit and Geoenvironmental Models for Resource Exploitation and Environmental Security* (2002), pp. 358–397.
- Guang, L., G. Huadong, F. Jinghui, G. Xiaofang, Z. Perski, and Y. Huanyin. "Mining area subsidence monitoring using multi-band SAR data". In: *Joint Urban Remote Sensing Event 2009*. IEEE International. Shanghai: IEEE International, 2009, pp. 1–6. ISBN: 978-1-4244-3461-9.
- Guth, P. "Geomorphometric comparison of Aster GDEM and SRTM". In: *ISPRS Technical Commission IV & AutoCartio & ASPRS/CaGIS 2010 Fall Specialty Conference*. Orlando, Florida 2010. URL: <http://www.asprs.org/publications/proceedings/orlando2010/files/GUTH.PDF>.
- Hanssen, R. F. *Radar interferometry: data interpretation and error analysis*. Dordrecht: Kluwer Academic Publishers, 2001, p. 328. ISBN: 0-7923-6945-9.
- Hlaváčová, I. "Interferometric stacks in partially coherent areas". PhD thesis. Prague: ČVUT Praha, 2008, p. 170. URL: http://www.insar.cz/pgs/hlavacova_disertace.pdf.
- "Satellite orbit errors and their influence on interferograms". MA thesis. ČVUT Praha, 2005. URL: <http://insar.cz/diplomka.pdf>.
- Hoen, W. and H.A. Zebker. "Penetration depths inferred from interferometric volume decorrelation observed over the Greenland ice sheet". In: *Geoscience and Remote Sensing, IEEE Transactions on* 38.6 (2000), pp. 2571–2583. ISSN: 0196-2892.
- Hooper, A. "A multi-temporal InSAR method incorporating both persistent scatterer and small baseline approaches". In: *Geophysical Research Letters* 35 (2008). ISSN: 0094-8276. DOI: 10.1029/2008GL034654.

- Hooper, A. "A statistical-cost approach to unwrapping the phase of InSAR time series". In: *Proceedings of ESA FRINGE Workshop, Frascati, Italy, November 30–December 4, 2009*. 2009.
- "Persistent Scatterer Radar Interferometry for Crustal Deformation Studies and Modeling of Volcanic Deformation". PhD thesis. Stanford University, 2006.
- Hooper, A., H. Zebker, P. Segall, and B. Kampes. "A new method for measuring deformation on volcanoes and other natural terrains using InSAR persistent scatterers". In: *Geophys. Res. Lett.* 31.23 (2004), pp. 1–5.
- Hooper, A., K. Spaans, D. Bekaert, M. C. Cuence, M. Arikan, and A. Oyen. *StaMPS/MTI Manual*. TU Delft. Netherlands 2010.
- Jiráňková, E. "Časoprostorové vytváření poklesové kotliny v závislosti na charakteru horského masivu". PhD thesis. Ostrava: VSB-TUO, 2006. URL: <http://hdl.handle.net/10084/76752>.
- Kampes, B. M. "Displacements Parameter Estimation using Permanent Scatterer Interferometry". PhD thesis. Delft University of Technology, 2005.
- Kampes, B. M., R. F. Hanssen, and Z. Perski. *Doris User's manual and technical documentation*. 2008, p. 166. URL: http://enterprise.lr.tudelft.nl/doris/software/doris_v4.02.pdf.
- "Radar interferometry with public domain tools". In: *Fringe Workshop*. Frascati: ESA, 2003, p. 6.
- Karney, Charles F. F. *Geodesics on an ellipsoid of revolution*. Feb. 2011. URL: <http://arxiv.org/abs/1102.1215>.
- Ketelaar, V. B. H. *Satellite Radar Interferometry: Subsidence Monitoring Techniques*. 1st. Remote Sensing and Digital Image Processing. Dordrecht: Springer, 2009, p. 270. ISBN: 978-1-402-094-272.
- Komac, M. and K. Oštir. "PSInSAR and DInSAR methodology comparison and their applicability in the field of surface deformations: a case of NW Slovenia primer SZ dela Slovenije". In: *Geologija* 50.1 (2007). URL: <http://www.dlib.si/v2/Details.aspx?URN=URN:NBN:SI:DOC-NI00MBEI>.
- Krawczyk, A., Z. Perski, P. Marinković, and R. F. Hanssen. "Evaluation of TerraSAR-X InSAR for the measurements of mining subsidence". In: *3rd TerraSAR-X Science Team Meeting*. DLR. Oberpfaffenhofen 2008, p. 8.
- Krieger, G., A. Moreira, H. Fiedler, I. Hajnsek, M. Werner, M. Younis, and M. Zink. "TanDEM-X: A satellite formation for high-resolution SAR interferometry". In: *Geoscience and Remote Sensing, IEEE Transactions on* 45.11 (2007), pp. 3317–3341. ISSN: 0196-2892.
- Lauknes, T. R., P. Shanker, H. A. Zebker, and Y. Larsen. "A combined small baseline and persistent scatterer InSAR method for resolving land deformation in natural terrain". In: *33rd International Geological Congress, IGC33*. Oslo 2008.
- Lazecký, M. "Datový sklad pro Dopravoprojekt, s.r.o. (Data warehouse for Dopravoprojekt, s.r.o.)" MA thesis. Ostrava: VSB-TUO, 2008.
- Lazecký, M., E. Jiráňková, and D. Böhmová. "Usage of InSAR techniques to detect and monitor terrain subsidence due to the mining activities". In: *GeoScience Engineering LVI.4* (2010), pp. 32–49. ISSN: 1802-5420. URL: <http://gse.vsb.cz/2010/LVI-2010-4-32-49.pdf>.

- Lee, H., S.-J. Cho, N.-H. Sung, and J.-H. Kim. "Development of a Ground-based Synthetic Aperture Radar System for Highly Repeatable Measurements". In: *IEICE Tech. Rep.* 107.277 (2007), pp. 1–5.
- Li, F. and R.M. Goldstein. "Studies of Multi-baseline Spaceborne Interferometric Synthetic Aperture Radar". In: *International Geoscience and Remote Sensing Symposium*. Ann Arbor 1987, pp. 1545–1550.
- Li, Z. "Correction of atmospheric water vapour effects on repeat-pass SAR interferometry using GPS, MODIS and MERIS Data". PhD thesis. University College London, 2005.
- Li, Z., E.J. Fielding, P. Cross, and J.P. Muller. "Interferometric Synthetic Aperture Radar Atmospheric Correction: GPS Topography-Dependent Furbulence Model". In: *Journal of Geophysical Research* 111.B02404 (2006). DOI: 10.1029/2005JB003711.
- "Interferometric synthetic aperture radar atmospheric correction: Medium resolution imaging spectrometer and advanced synthetic aperture radar integration". In: *Geophysical Research Letters* 33.6 (2006), p. L06816. ISSN: 0094-8276.
- Li, Z., T. Li, S. Zhang, S. Zhang, J. Liu, and Y. Xia. "Study on GPS Station's Zenith Delay to Mitigate the InSAR Atmosphere Effect Reduction of Atmospheric Water Vapour Effects on Envisat ASAR Interferograms Using MERIS near IR Measurements". In: *International Society for Photogrammetry and Remote Sensing Congress*. Beijing 2008. ISBN: 1684-1750.
- Liu, G., H. Jia, R. Zhang, M. Cen, and T. Zhang. "Subsidence Detection by PSInSAR Based on High Resolution TerraSAR-X Images". In: *Progress In Electromagnetics Research Symposium Proceedings*. Xi'an 2010.
- Maître, H. et al. *Processing of Synthetic Aperture Radar Images*. Paris: Ecole Nationale Supérieure des Télécommunications, 2008, p. 408. ISBN: 9-781848210240.
- Manunta, M. "New Advances in Multi-Temporal Differential SAR Interferometry for Full Resolution Data Analysis". PhD thesis. University of Cagliari, 2009.
- Martinec, P. and B. Schejbalová. "History and environmental impact of mining in the Ostrava - Karviná coal field (Upper Silesian coal basin, Czech Republic)". In: *Geologica Belgica*. Proceedings of the 5th European Coal Conference 7.3-4 (2004), pp. 215–224.
- Massonnet, D. and F. Adragna. "A full-scale validation of Radar Interferometry with ERS-1: the Landers earthquake". In: *Earth Observation Quarterly* 41 (1993).
- Meyer, F. and J. Nicoll. "The Impact of the Ionosphere on Interferometric SAR Processing". In: *IEEE International Geoscience and Remote Sensing Symposium, IGARSS'08*. Boston 2008.
- Miranda, N. *Impact of the Envisat Mission Extension on SAR data*. ESA. 2010. URL: <http://earth.esa.int/download/envisat/Impact-of-Envisat-Mission-Ext-SAR-data-aug10.pdf>.
- Mulková, M. "Využití konvenčních metod DPZ při sledování antropogenních změn krajiny v poddolovaných oblastech". PhD thesis. Brno: Masarykova Univerzita v Brně, 2007.
- Ng, AH, H. Chang, L. Ge, C. Rizos, and M. Omura. "Radar interferometry for ground subsidence monitoring using ALOS PALSAR data". In: *Proceedings of The XXI Congress, The International Society for Photogrammetry and Remote Sensing*. Citeseer. 2008.
- Nitti, DO, LD Vitis, F. Bovenga, R. Nutricato, A. Refice, and J. Wasowski. "Multi-temporal L-band SAR interferometry confirms C-band spatial patterns of subsidence in the ancient Wieliczka Salt Mine (UNESCO Heritage Site, Poland)". In: *Fringe Workshop*. Frascati 2009.

- Norris, J., P. Vachon, D. Schlingmeier, R. English, and L. Gallop. *Expendable Trihedral Corner Reflectors for Target Enhancement and Position Control in RADARSAT-1 Fine Beam Mode SAR Imagery: Results from an Exercise Narwhal Pre-Trial Deployment*. Defence R & D Canada-Ottawa, 2004, p. 44.
- Osmanoglu, B., T. H. Dixon, S. Wdowinski, E. Cabral-Cano, and Y. Jiang. "Mexico City subsidence observed with persistent scatterer InSAR". In: *International Journal of Applied Earth Observation and Geoinformation* 13.1 (2011), pp. 1–12. ISSN: 0303-2434. DOI: 10.1016/j.jag.2010.05.009.
- Parizzi, A., D. Perissin, C. Prati, and F. Rocca. "Artificial Scatterers for SAR Interferometry". In: *2005 Dragon Symposium*. Vol. 611. 2006.
- Perski, Z. "The Interpretation of ERS-1 and ERS-2 InSAR Data for The Mining Subsidence Monitoring in Upper Silesian Coal Basin, Poland, Iaprs, Vol". In: *International Archives of Photogrammetry and Remote Sensing XXXIII.B7* (2000).
- Perski, Z., R. F. Hanssen, and P. Marinković. "Deformation of the margin of Sudety mountains (Southern Poland), studied by persistent scatterers interferometry". In: *Fringe Workshop*. Frascati: ESA, 2007, p. 4.
- Perski, Z. and D. Jura. "Identification and measurement of mining subsidence with SAR interferometry". In: *11th International Symposium on Deformation Measurements*. Santorini 2003, pp. 165–171.
- Perski, Z., T. Wojciechowski, and A. Borkowski. "Persistent Scatterer SAR Interferometry Applications on Landslides in Carpathians (Southern Poland)". In: *Fringe Workshop*. Frascati: ESA, 2009, p. 5. ISBN: 978-92-9221-241-4.
- Pipia, L., X. Fabregas, A. Aguasca, C. Lopez-Martinez, S. Duque, J.J. Mallorqui, and J. Marturia. "Polarimetric differential SAR interferometry: First results with ground-based measurements". In: *Geoscience and Remote Sensing Letters, IEEE* 6.1 (2009), pp. 167–171. ISSN: 1545-598X.
- Puysegur, B., M. Rémi, and J.-P. Avouac. "Tropospheric phase delay in interferometric synthetic aperture radar estimated from meteorological model and multispectral imagery". In: *Journal of Geophysical Research* 112.B05419 (2007), p. 12. DOI: 10.1029/2006JB004352.
- Raucoules, D., B. Bourguin, M. de Michele, G. Le Cozannet, L. Closset, C. Bremmer, H. Veldkamp, D. Tragheim, L. Bateson, M. Crosetto, M. Agudo, and M. Engdahl. "Validation and intercomparison of Persistent Scatterers Interferometry: PSIC4 project results". In: *Journal of Applied Geophysics* 68.3 (2009), pp. 335–347. ISSN: 0926-9851. DOI: DOI:10.1016/j.jappgeo.2009.02.003. URL: <http://www.sciencedirect.com/science/article/B6VFC-4VNKG76-3/2/6d1b673c69e05c30ce0b5ebc0d9d254c>.
- Remy, D., S. Bonvalot, P. Briole, and M. Murakami. "Accurate measurements of tropospheric effects in volcanic areas from SAR interferometry data: application to Sakurajima volcano (Japan)". In: *Earth and Planetary Science Letters* 213.3-4 (2003), pp. 299–310. ISSN: 0012-821X.
- Richards, J.A. *Remote Sensing with Imaging Radar*. Springer Verlag, 2009. ISBN: 3642020194.
- Rosen, PA, S. Hensley, G. Peltzer, and M. Simons. "Updated repeat orbit interferometry package released". In: *Eos Transactions AGU* 85.5 (2004), p. 47. DOI: 10.1029/2004E0050004.
- Samiei-Esfahany, S. "Improving Persistent Scatterer Interferometry Results for Deformation Monitoring". MA thesis. Delft University of Technology, 2008.

- Sandwell, D., R. Mellors, X. Tong, M. Wei, and P. Wessel. *GMTSAR: An InSAR Processing System Based on Generic Mapping Tools*. 2010. URL: <http://topex.ucsd.edu/gmtsar/tar/GMTSAR.pdf>.
- Sarabandi, K. and T.C. Chiu. "Optimum corner reflectors for calibration of imaging radars". In: *Antennas and Propagation, IEEE Transactions on* 44.10 (1996), pp. 1348–1361. ISSN: 0018-926X.
- Seeber, G. *Satellite geodesy*. Walter De Gruyter Inc, 2003. ISBN: 3110175495.
- Skolnik, M.I. *Radar handbook*. Vol. 2. McGraw-Hill Newyork, 1990, p. 846.
- Solheim, F. S., J. Vivekanandan, R.H. Ware, and C. Rocken. "Propagation Delays Induced in GPS Signals by Dry Air, Water vapor, Hydrometeors and Other Particulates". In: *Journal of Geophysical Research* 104 (1999), pp. 9663–9670.
- Song, X., D. Li, and M. Liao. "Reproduction of InSAR Atmospheric Signal Using GPS Data Based on Topography-Dependent and Turbulent Mixing Model". In: *Dragon 1 Programme Final Results 2004-2007*. Beijing 2008.
- Sousa, J. J. M. "Potential of integrating PSI methodologies in the detection of surface deformation". PhD thesis. University of Porto, 2009, p. 216.
- Ugsang, D. M., K. Honda, and G. Saito. "Assessment of Small Passive Corner Reflectors for Geometric Correction of RADARSAT Fine Mode SAR Data". In: *22nd Asian Conference on Remote Sensing*. Singapore 2001, p. 6.
- Villasenor, J. H., D. Fatland, and L. D. Hinzman. "Change detection on alaska's north slope using repeat-pass ERS-1 SAR images". In: *IEEE Transactions on Geoscience and Remote Sensing*. Vol. 31. 1. 1993, pp. 227–236.
- Wang, X., G. Wang, Y. Guan, Q. Chen, and L. Gao. "Small satellite constellation for disaster monitoring in China". In: *IEEE International Geoscience and Remote Sensing Symposium, IGARSS'05*. Vol. 1. IEEE. Seoul: IEEE International, 2005, p. 3. ISBN: 0780390504.
- Wdowinski, S., S.H. Hong, S.W. Kim, and J.S. Won. "Small Temporal Baseline Subset (STBAS): A New InSAR Technique for Multi-Temporal Monitoring Wetland's Water Level Changes". In: *IEEE International Geoscience and Remote Sensing Symposium, IGARSS'08*. Vol. 3. Boston: IEEE International, 2008, pp. 550–553. ISBN: 978-1-4244-2807-6.
- Wegmuller, U., C. Werner, T. Strozzi, and A. Wiesmann. "Monitoring mining induced surface deformation". In: *Geoscience and Remote Sensing Symposium, 2004. IGARSS'04. Proceedings. 2004 IEEE International*. Vol. 3. IEEE. 2004, pp. 1933–1935.
- Werner, C., Z. Lu, A. Wiesmann, U. Wegmuller, and T. Tazio. "SAR Interferometric Point Target Analysis for Long-Term Deformation Mapping". In: *AGU Fall Meeting Abstracts*. Vol. 1. 2003, p. 02.
- Xia, Y., H. Kaufmann, X. F. Ge, and X. D. Yang. "CR-Based TerraSAR-X Interferometry for Landslide Monitoring". In: *3rd TerraSAR-X Science Team Meeting*. DLR. Oberpfaffenhofen 2008. URL: http://sss.terrasar-x.dlr.de/papers_sci_meet_3/paper/LAN0284_xia.pdf.
- Yun, S.-H., H. Zebker, P. Segall, A. Hooper, and M. Poland. "Interferogram Formation in the Presence of Complex and Large Deformation". In: *Geophys. Res. Lett.* 34 (2007). DOI: 10.1029/2007GL029745.
- Zhang, T., Q. Zeng, Y. Li, and Y. Xiang. "Study on Relation between InSAR Coherence and Soil Moisture". In: *International Society for Photogrammetry and Remote Sensing Congress*. Beijing 2008. ISBN: 1682-1750.

Website References

1. Alos Palsar Obs. Strategy: http://www.eorc.jaxa.jp/ALOS/en/obs/palsar_strat.htm
2. Corner Reflector: <http://www.microwaves101.com/encyclopedia/cornerreflector.cfm>
3. DLR Earth Observation Site: <http://www.eoweb.de>
4. Doris Delft: <http://doris.tudelft.nl>
5. Earth Observation Link - Stand Alone: <http://eoli.esa.int>
6. Envisat: <http://www.nrsc.gov.in/envisat.html>
7. Envisat Nominal Attitude: <ftp://ftp.aviso.oceanobs.com/pub/ids/satellites/en1att.txt>
8. ESA Earth Observation Site: <http://eopi.esa.int>
9. GeographicLib Utilities: <http://geographiclib.sf.net>
10. IDIOT: <http://srv-43-200.bv.tu-berlin.de/idiot>
11. inpaint_nans: <http://www.mathworks.com/matlabcentral/fileexchange/4551>
12. Letter Designations of MW Bands: <http://www.jneuhaus.com/fccindex/letter.html>
13. NEST: <http://www.array.ca/nest>
14. OKD, a.s. Annual Reports: <http://www.okd.cz/en/about-us/annual-reports/>
15. Radar Tools (RAT): <http://radartools.berlios.de/>
16. SAR-Lupe: <http://en.wikipedia.org/wiki/SAR-Lupe>
17. TecSAR: <http://en.wikipedia.org/wiki/TecSAR>
18. Weather Underground: <http://www.wunderground.com>

About the Author

Milan Lazecký (1984, Moscow) has finished his studies of Geoinformatics for a master degree at VŠB-TU Ostrava in 2008. Within his diploma thesis he developed a full system for a storage of various geodata together with their metadata in a Microsoft SQL Server 2005 geodatabase, with a secured access through an intranet based on PHP and a visualisation using MapGuide OpenSource. The system was created to fit the needs of Dopravoprojekt, Ltd. company. The work was awarded by a 2nd place in a national student competition Gisáček 2008. It was never installed in the company environment.

During his study years he was involved in several projects concerning a regional development - he assisted an agency for regional development ARR, he co-organized an internationally sponsored project to support sport activities of “capoeira” in the region, he worked as a geoinformatics specialist in an ecological organization Vita, o. s. where he experienced aspects of ecological issues in the region more deeply. He is a member of Futra Orlová, a local movement supporting socially, psychologically or otherwise disadvantaged (young) people.

As a matter of fact, he decided to continue for a PhD directly after finishing the master degree - but he had chosen a totally unfamiliar topic, i.e. to investigate satellite radar interferometry application for monitoring subsidence in the region. To learn about this technology he spent 7 months at TU Delft, Netherlands in a group of InSAR specialists (for some reasons he also started to play a saxophone there). After returning to Ostrava he continued investigating InSAR mostly on his own. His presentation about InSAR abilities to monitor subsidence in undermined regions was awarded by a 2nd place in an international student competition Topical Issues of Subsoil Usage in Sankt Peterburg in 2010.

His interests stay to be connected in some degree with regional problems. He intends to participate in designing an information system of mine activity effects. His dream is to participate in improving the air quality in the region.

Main investigator of projects:

- ESA Cat-1 2009 - project 4578 - Surveillance of man-induced terrain changes using earth observation data. Still in active state.
- IGS 2009 – Evaluation of subsidence of undermined areas using radar interferometry.

- MSK 2010 – programme Mobility – Longtime monitoring of subsidence due to mining activities in Northern Moravia. A project to participate in a conference IGARSS 2010, presenting results of monitoring mine subsidence.
- SGS 2010 – Accurate assessment of relief changes in selected locations using radar interferometry, combined with GPS technology.

Training, professional development :

- 02/2009 - 09/2009: Erasmus study at TU Delft, Netherlands (7 months) - educating in a DEOS group of Prof. Ramon F. Hanssen,
- 28.6.2009 - 3.7.2009: ESA workshop: Advanced Training Course on Land Remote Sensing, Prague, CZ (assisting Prof. Ramon Hanssen in practical classes of InSAR),
- 25. - 27.11.2009: ESA workshop: NEST Toolbox Training Course, Frascati, Italy,
- 27.6. - 2.7.2010: ESA Tutorials (Biosphere, Atmosphere, Solid Earth), demonstrations of ESA EO Toolboxes - Beam, Nest, Beat etc. - Bergen, Norway,
- 2.8. - 13.8.2010: ESA Earth Observation Summer School - Frascati, Italy - remote sensing workshop, more information at <http://envisat.esa.int/envschool>,
- 02/2011 - 07/2011: Erasmus working internship at UTAD Vila Real, Portugal (6 months) - collaboration with Joaquim J. de Sousa PhD in InSAR processing.

Teaching experience of subjects (at VŠB-TU Ostrava):

- 2008 - 2009 - Basics of Geoinformatics
- 2009 - 2010 - Operating Systems, Algorithmization of Spatial Tasks, Data Processing of Remote Sensing, Basics of Geoinformatics
- 2010 - 2011 - Remote Sensing, Data processing of Remote Sensing

Leading of other diploma thesis :

- Bc. Andrea Tkáčiková - Usage of Radar Interferometry for Terrain Changes Evaluation after Floods in 1997
- Bc. Zdeněk Brokeš - Data Warehouse of Elevation Changes Measurements

List of Relevant Publications

(in Chronological Order)

Hanzlová, M., Lazecký, M., Rapant, P., Böhmová, D., and Jiráňková, E. "Radarová interferometrie při vyhodnocování poklesů vlivem poddolování (poster)", In: *17th Conference GIS ESRI in Czech Republic*, 23.- 24.10.2008, Prague.

Lazecký M. "Detection of land subsidence due to mining activities in Northern Moravia region using satellite radar interferometry". In: *Zeszyty Naukowe Politechniki Śląskiej, Serie Górnictwo* 287.1814 (2009), pp. 135-140, Gliwice. ISSN: 0372-9508.

Lazecký M. "InSAR used for subsidence monitoring of mining area OKR, Czech republic". In: *Fringe Workshop*. Frascati: ESA, 2009. CD-ROM, 3 pp. ISBN: 978-92-9221-241-4 ISSN: 1609-042X.

Lazecký M., Jiráňková E., Böhmová D. "Usage of InSAR techniques to detect and monitor terrain subsidence due to the mining activities". In: *GeoScience Engineering*, Vol. LVI.4 (2010), pp. 32-49. ISSN: 1802-5420. Online: <http://gse.vsb.cz/2010/LVI-2010-4-32-49.pdf>.

Lazecký M. "InSAR used for subsidence monitoring of mining area OKR, Czech republic". In: *Proceedings - Symposium GIS Ostrava 2010*, Ostrava, 2010, CD-ROM. 3 pp. ISBN: 978-80-248-2171-9.

Lazecký M. "Monitoring of subsidence of mining area in Northern Moravia by radar interferometry techniques". In: *Proceedings of Topical Issues of Subsoil Usage*, Sankt Peterburg, 2010, pp. 77-79. ISBN: 978-5-94211-447-3.

Bláha, P., Černý, V., Duras, R., Fousek, J., Horský, O., Lazecký, M., Oprchal, J., Tábořík, P., Peshawa, A., Aziz, B.Q. "Geoelectrical Surveys for the Feasibility Study of the Bawanur Dam Site". In: *Exploration Geophysics, Remote Sensing and Environment*. Vol. XVII.2 (2010), pp. 14-48 (35 p.), CD-ROM. ISSN: 1803-1447.

Lazecký M., Jiráňková E., Böhmová D. "Monitoring of fast subsidence in a mining area of Northern Moravia, Czech Republic". In: *Proceedings of ESA Living Planet Symposium 2010*, 28.6-2.7.2010, Bergen, Norway, CD-ROM. ISBN: 978-92-92221-250-6 ISSN: 1609-042X.

Lazecký M., Jiráňková E. "Longtime monitoring of mine subsidence in Northern Moravia, Czech Republic using different InSAR techniques". In: *Proceedings of the 2010 IGARSS*, 25-30th July 2010, Honolulu (USA), pp. 3331-3334. ISBN: 978-1-4244-9564-1.

Lazecký, M. "Družicové monitorování poklesů půdy – radarová interferometrie". In: *Proceedings of Těžba a úprava surovin III*, 15.12.2010, Ostrava: VŠB-TU Ostrava, 2010. ISBN: 978-80-248-2365-2.

Lazecký, M., Kačmařík, M. "Measurement of landslides in Doubrava using radar interferometry". In: *Proceedings of GIS Ostrava 2011*, 24.-26.1.2011, Ostrava: VŠB-TUO, 2011. ISBN: 978-80-248-2366-9.

Appendix A

Computation Methods to Properly Orientate a Corner Reflector

A.1 Computation Methods of Azimuth and Incidence Angle

A.1.1 Computation in Local Reference Frame

A framework to estimate both precise azimuth angle and looking direction is presented here. It is based on a conversion of parameters known in the global geometry frame to a local reference frame. It is possible to achieve precise coordinates of a corner reflector location and a position of satellite in the time of acquiring its location (in a perpendicular direction to the satellite track vector) using orbital data, in WGS-84. The problem is reduced to compute coordinates of this satellite position (using Eq. A.1.1) to a local reference frame with the corner reflector position used as a point of origin and one of the axis heading to the North, for advantage in azimuth reading, and z axis as a local vertical, to read the incidence angle. Situation is depicted in Fig. A.1.1.

To compute local coordinates of the satellite as vector $X_{sat}^L = (x_{sat}^L, y_{sat}^L, z_{sat}^L)$, the global geocentric vector $X_{sat}^g = (x_{sat}^g, y_{sat}^g, z_{sat}^g)$ has to be translated by $X_{CR}^g = (x_{CR}^g, y_{CR}^g, z_{CR}^g)$ and rotated by $D(\phi_{CR}, \lambda_{CR})$ to the local reference system of $X_{CR}^L = (0, 0, 0)$ as origin. This computation of X_{sat}^L is schematized in Eq. A.1.1:

$$X_{sat}^L = D(\phi_{CR}, \lambda_{CR}) \cdot (X_{sat}^g - X_{CR}^g) \quad (\text{A.1.1})$$

, where $D(\phi_{CR}, \lambda_{CR})$ is a rotation matrix as determined in (Seeber, 2003), p. 23:

$$D(\phi, \lambda) = \begin{bmatrix} -\sin \phi \cdot \cos \lambda & -\sin \phi \cdot \sin \lambda & \cos \phi \\ -\sin \lambda & \cos \lambda & 0 \\ \cos \phi \cdot \cos \lambda & \cos \phi \cdot \sin \lambda & \sin \phi \end{bmatrix}$$

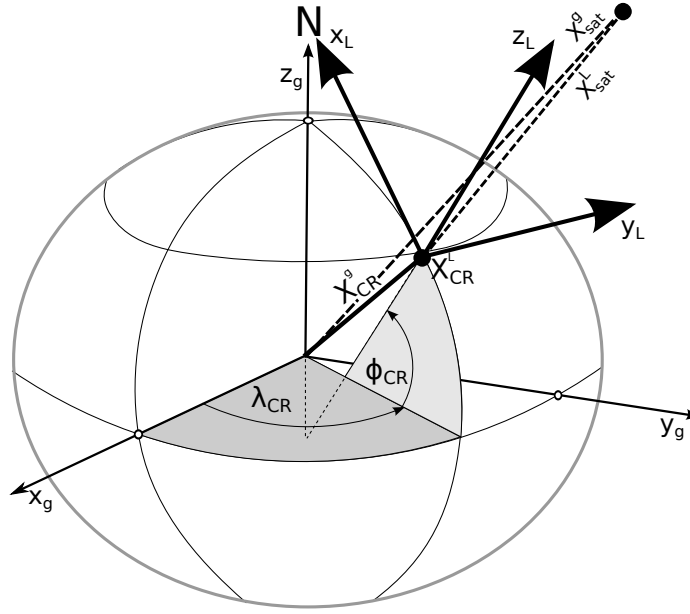


Figure A.1.1 – Geometrical relations between corner reflector and satellite position; adapted from (Seeber, 2003)

The azimuth θ and incidence angle δ can be computed then using equations Eq. A.1.2 and Eq. A.1.3:

$$\theta = \arctan \left(\frac{y_{sat}^L}{x_{sat}^L} \right) \quad (A.1.2)$$

$$\delta = \arctan \left(\frac{\sqrt{(x_{sat}^L)^2 + (y_{sat}^L)^2}}{z_{sat}^L} \right) \quad (A.1.3)$$

The CR location coordinates of latitude ϕ_{CR} , longitude λ_{CR} and a height over mean sea level h_{CR} of the global geocentric coordinate system WGS-84 are known, for computation of corresponding metric coordinates X_{CR}^g in a Cartesian geocentric coordinate system, a `CartConvert` utility [9] can be used (Karney, 2011). To achieve Cartesian geocentric coordinates of the satellite in the moment of acquiring CR response, a satellite orbit data can be applied, assuming the same track and acquisition properties for the future acquisition.

Computation of satellite position in Geocentric Coordinates

There are two basic ways on how to determine a satellite position during beaming of a point of interest (HP-3 in this case) from precise orbits. If the beam line containing this point is known precisely, the precise time of such line acquisition can be computed (see Eq. A.1.4) and used for example in `getorb` utility to obtain the satellite coordinates. However, if no

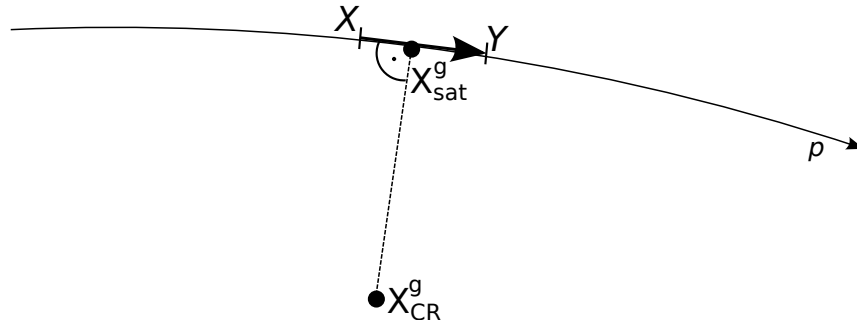


Figure A.1.2 – Computation of satellite position

existing radar image is available beforehand, this line of interest cannot be identified. Then, the satellite position can be computed on analytical geometry basis, as will be described in this section.

As can be observed from Figure A.1.2, the coordinates of X_{sat}^g are possible to compute using analytical geometry in 3D space. Let's suppose that the SAR images will be formed focused on zero-Doppler frequency. Then, the highest peak of CR reflectance that will be stored as an intensity value, is directed perpendicularly to the satellite flight vector. The problem is then reduced to search for the nearest point X_{sat}^g of line p to point X_{CR}^g . Using orbit data over the same swath (supposing similar conditions in future acquisition), the line $p=(X, \vec{u})$ representing flight track valid for the time during the scene acquisition will be written as:

$$p = (X, \vec{u}) : X = [x_1, x_2, x_3], \vec{u} = (u_1, u_2, u_3) = Y - X$$

, where both X and Y are locations of the satellite during the time period when acquiring the scene, in the geocentric coordinates.

In this case, Envisat in his descending phase is approaching the area of interest every 35 days around 09:11 GMT, for example on 20th July 2009. Using `getorb` utility and appropriate ODR file containing orbit data that include this epoch, the X and Y was determined and vector \vec{u} was computed. A 10 seconds period between both locations was used (the whole 100 km scene is acquired within less than 17 s). Note that the satellite position slightly differs each pass over the area.

By running `getorb ymd=20090720091050,20090720091100,10 ~/ODR` ,
 $X = [4\ 325\ 944.01; 1\ 774\ 113.76; 5\ 418\ 954.72]$ and
 $Y = [4\ 384\ 408.75; 1\ 776\ 010.84; 5\ 371\ 252.47]$.

The WGS-84 coordinates of the HP-3 location (see Tab. 4.3), here as X_{CR}^g coordinates, are converted to the geocentric coordinate system using:

`echo 49.873056 18.487222 242 | CartConvert`
The resulting $X_{CR}^g = [3\ 906\ 271.80; 1\ 306\ 051.63; 4\ 853\ 886.13]$.

Afterwards, to achieve the coordinates of satellite in the time of the nearest (perpendicular) position to the X_{CR}^g , a plane S is interladed through the point X_{CR}^g perpendicularly to the line p . Thus its directional vector is used as the plane S normal vector to form an equation of:

$$S : u_1x + u_2y + u_3z + d = 0; \text{ therefore } d = -(u_1x + u_2y + u_3z).$$

Parameter d can be computed by constituting X_{CR}^g coordinates instead of x, y, z .

Then, a simple computation of intersection X_{sat}^g between the plane S and line p is performed. The parametric equations of line p is:

$$\begin{aligned} x &= x_1 + u_1t \\ p : y &= x_2 + u_2t, t \in R \\ z &= x_3 + u_3t \end{aligned}$$

From equation S ,

$$x = -\frac{u_2y + u_3z + d}{u_1}$$

When substituting x, y, z from parametric equations of p to above mentioned equation, the parameter t can be computed as

$$t = -\frac{u_1x_1 + u_2x_2 + u_3x_3 + d}{u_1^2 + u_2^2 + u_3^2}$$

Afterwards, the X_{sat}^g coordinates are computed from already complete parametric equations of line p and can be used then in Eq. A.1.1 to obtain X_{sat}^L needed for azimuth angle θ and incidence angle δ estimation.

In this case, $X_{sat}^g = [4\ 341\ 655.74; 1\ 774\ 623.58; 5\ 406\ 135.29]$.

After computation of $D(\phi_{CR}, \lambda_{CR})$, the $X_{sat}^L = [-73\ 415.33; 306\ 333.74; 784\ 135.07]$.

Azimuth and incidence angle for HP-3 location

After computation of X_{sat}^L coordinates, the azimuth θ and incidence angle δ are computed using Eq. A.1.2 and Eq. A.1.3, respectively, to achieve $\theta = -76.523^\circ$ and $\delta = 21.887^\circ$. The azimuth angle should be directed from North to the satellite, therefore $\theta' = \theta + 180^\circ = 103.477^\circ$.

Discussion

This approach takes an advantage of analytical geometry computations within a Cartesian geocentric coordinate system. Because of precise orbit data usage, the satellite track vector over the area of interest is achieved with a maximal available precision. This local vector should be more reliable than compared to the general satellite inclination angle usage as described in Section A.1.3.

A.1.2 Computation based on Existing Acquisition

Because of the same illumination angle thanks to the sun-synchronous orbit of a SAR satellite, information of an incidence angle and a computation of azimuth valid for an existing image will be the same as in the future acquisition of the same frame and swath, with insignificant deviations.

After application of precise orbit data on such acquisition or even after terrain correction of the image, the point of interest should be detected and the incidence angle can be read simply using some of the specialized software.

The question of searching for a corner reflector azimuth is in fact known as a so-called inverse geodesic calculation. A geodesic is the shortest path between two points on an ellipsoid, a WGS-84 in this case, see Fig. 4.5.1. There are precise tools available for computation of such a problem. I have used a Geod utility from GeographicLib [9] which should provide a very accurate solution (Karney, 2011).

To use such software for calculation of azimuth, both WGS-84 locations of corner reflector X_{CR}^g and satellite position X_{sat}^g must be known. A precise satellite position in a specified time can be obtained from precise orbit data using `getorb` utility. A line of interest L_{CR} containing the CR location in the focused image should be determined to compute the exact time t_{CR} of acquiring L_{CR} , using Eq. A.1.4:

$$t_{CR} = t_0 + \frac{L_{CR}}{PRF} \quad (\text{A.1.4})$$

The pulse repetition frequency (PRF) is a parameter specific for each satellite, for Envisat ASAR, $PRF = 1652.416$ Hz (as can be read from the image header).

Azimuth and incidence angle for HP-3 location

For this method, an existing acquisition from 20th July 2009 has been used. A precise orbit data computed from DORIS tracking instrument using `dorvor_to_odr.m` Matlab script from [4] was applied. The corner reflector location in the image was approximated visually, as will be discussed further in Section 4.6.2.2.

The incidence angle was interpolated from incidence angles tie point grid from this existing Envisat image header using `Nest`. For the point of interest, the incidence angle is $\delta = 21.8488^\circ$.

The HP-3 location is most probably in the $L_{CR}=7329^{th}$ line of current radar image. Because the first line was acquired, according to the image information after precise orbits timing correction, on 20th July 2009 in $t_0=9:10:56.66$, it is possible to compute the time t_{CR} of acquisition of L_{CR} using Eq. A.1.4, thus $t_{CR}=9:11:01.57$.

Using precise orbit data and getorb as their processor:

```
getorb ymd=20090720091100.86 ~/ODR
```

, the position of the satellite $X_{sat}^g = [\lambda_{sat}, \phi_{sat}]$ during the line L_{CR} acquisition was computed as $\lambda_{sat}=22.2396^\circ$, $\phi_{sat}=49.2448^\circ$. Then, the azimuth angle θ could be computed using the inverse geodesic calculation by Geod utility:

```
echo 49.87590 18.48667 49.2447511 22.2395892 | Geod -i
```

In the end, the azimuth angle was computed as $\theta = 103.06^\circ$.

Discussion

A quality of this method depends on the satellite track stability, precision of the orbit data and a correct identification of the location of interest in the image. Since proper utilities exist, getorb and Geod, this method is performed easily and accurately. The difference between computation from image without precise orbits timing correction and after this correction was evaluated. Without such correction, the azimuth was $\theta_{badTiming} = 102.408^\circ$, the timing error when not using precise orbit data then caused an azimuth error of $\Delta\theta = 0.65^\circ$.

A.1.3 Azimuth Computation using Satellite Inclination Angle

Since the satellite track doesn't change in the sun-synchronous orbit mode, the information about the orbit inclination from the reference plane (equator, see Fig. A.1.3) should be enough parameter to find the azimuth to the satellite.

Dr. Xia (Xia et al., 2008) presents Equation A.1.5 to compute the azimuth angle of the radar sight line. The equation was taken from (Curlander et al., 1991) as the azimuth angle dependency on the inclination of the satellite orbital plane ι and the geodetic latitude of the corner reflector ϕ_{CR} .

$$\theta' = \arcsin \left(\frac{\cos(\iota)}{\cos(\phi_{CR})} \right) \quad (\text{A.1.5})$$

Equation A.1.5 was used at least in two projects of the authors. However, as it is stated in (Xia et al., 2008), this approximation *"is strictly valid only for nadir pointing instruments and the location of the installed corner reflectors should be not too far from the equator (latitude < 60°). A more accurate approach to derive the azimuth angle θ is to use the location algorithm to determine the*

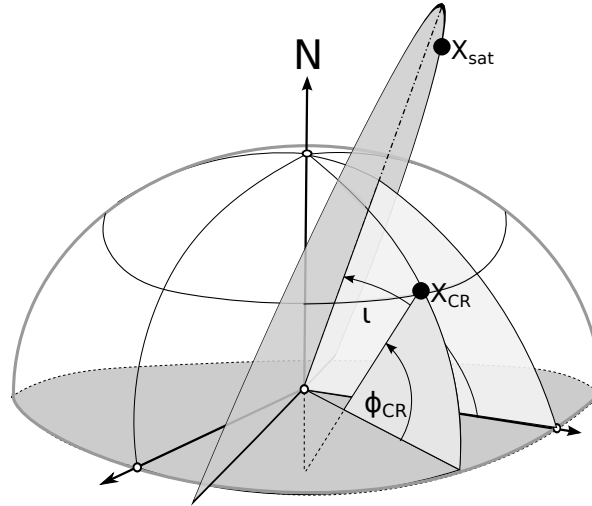


Figure A.1.3 – Satellite inclination angle

geocentric location of the satellite." Anyway, presented results show a strong radar response of TerraSAR-X.

By the Eq. A.1.5, an azimuth to the satellite direction is computed. However, this formulation simplifies the problem by locating the satellite at the CR position and the perpendicular look direction is not taken into account. Therefore, this equation was slightly edited by shifting the goniometrical function for $\frac{\pi}{2}$ and providing latitude of the satellite ϕ_{sat} during the pass over CR position :

$$\theta = \arccos\left(\frac{\cos(l)}{\cos(\phi_{sat})}\right) \quad (\text{A.1.6})$$

Azimuth for HP-3 location

The azimuth angle was computed by Eq. A.1.6 using parameters $l = 98.549^\circ \pm 0.009^\circ$, i.e. a general Envisat inclination valid until October 2010 (Duesmann et al., 2007) and $\phi_{sat} = 49.2448^\circ$ that was computed using precise orbit data as described in Section A.1.2. The resulting azimuth $\theta = 103.16^\circ$.

By using former Eq. A.1.5 (and correcting the result by rotating of 90°) in the way as it was proposed in (Xia et al., 2008), with coordinates of HP-3 (see Tab. 4.3), the resulting $\theta = 103.337^\circ$.

Discussion

The solution of the azimuth computation was strongly simplified within the former method that was not adapted for perpendicular angle look direction of SAR. However, since the distance between the satellite and the point of interest doesn't introduce a large difference in the azimuth in our latitude, also this former Eq. A.1.5 could be used. The difference in azimuth between using ϕ_{CR} and ϕ_{sat} latitude was $\Delta\theta = 0.17^\circ$.

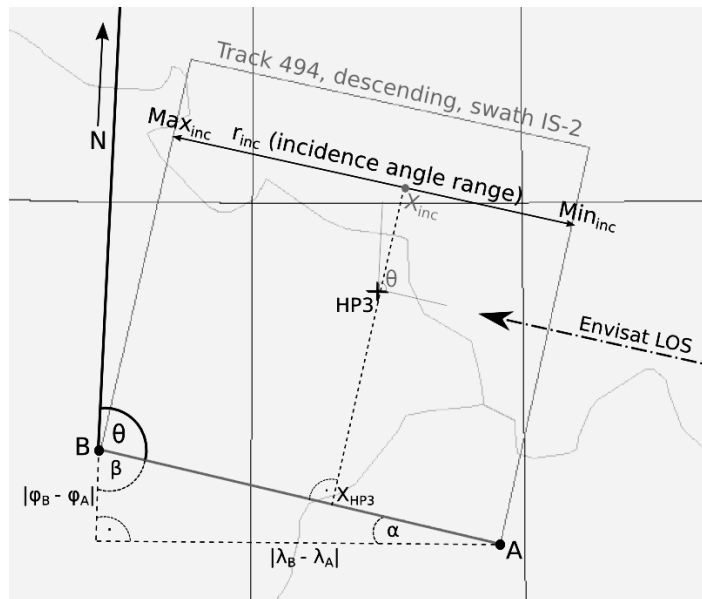


Figure A.1.4 – Computation of azimuth angle and incidence angle for point HP-3 illuminated by Envisat from descending track 494, in swath IS-2.

The information about satellite track inclination is usually provided as only a general satellite parameter. However the satellite position deviations from the central track are tolerable, therefore it can be used to compute CR orientation parameters. One may also use the inclination information in some other method, such as in Section A.1.1.

A.1.4 Azimuth Computation using Image Footprints

This method is recommended to use only for preliminary estimations or if no other input data is available. The basic assumption is that the image footprints, extents of SAR images as provided by an ordering/planning tools such as Eoli-Sa [5], are precise enough to achieve a direction of satellite line of sight for corner reflectors usage. The CR centerline angle can deviate up to ± 3 degrees in both vertical and horizontal direction. Even that a reduced accuracy is expected, it should be still possible to compute a reliable direction of corner reflector centerline without a need of orbital data from previous acquisitions.

The geometrical situation is depicted on Fig.A.1.4 together with Eoli-Sa illustration of required image extents.

Both northern and southern extent borders are parallel, every line of the image is so. This assumption was used to compute the azimuth angle θ valid for any point within the swath. Since the coordinates of extent corners are known, it is possible to compute θ using an inverse geodesic calculation (Karney, 2011) - a specialized utility Geod [9] can be used.

Azimuth for HP-3 location

This method ignores precise coordinates of a corner reflector location, it will assume the same azimuth for every point within the imaged swath. The coordinates of the bottom extent line

of 31th May 2010 acquisition are defined from Eoli-Sa catalog as A: $\lambda_A = 18.86^\circ$, $\phi_A = 49.04^\circ$, B: $\lambda_B = 17.4^\circ$, $\phi_B = 49.25^\circ$. When applying the computation using Geod utility:

```
echo 49.25 17.4 49.04 18.86 | Geod -i
```

, the result is: $\theta = 101.814^\circ$. When using upper extent coordinates, the result is very similar: $\theta = 101.783^\circ$, difference $\Delta = 0.03^\circ$ which can be affordable.

Discussion

This method is obviously less accurate since only a coarse estimation of final image extent is used as a data input. Still it can be valuable if a precise footprint is provided. It may be possible to increase the accuracy slightly by for example shifting coordinates of the processed line using analytical geometry, but the maximal difference between azimuth of first and last line as computed in previous paragraph is regarded as very small. On the other hand, the satellite position is located over a location much further - in this example, the nadir of Envisat scanning IS-2 swath is more than 230 km away from the swath. With such a distance the error can raise even higher, not speaking about even further swaths.

A.1.5 Incidence Angle Computation using Image Footprints

The incidence angle variation within a swath is linearly distributed, thus it is possible to compute the incidence angle valid for any point within the swath in a simple principle depicted in Fig. A.1.4. The incidence angle δ can be computed as a fraction x_{inc} of swath incidence angle range $r_{inc} = (Min_{inc} - Max_{inc})$. The analytical geometry can help by using southern or northern extent line. Supposing to use once more the same points A, B as seen on Fig. A.1.4:

$$\frac{r_{inc}}{x_{inc}} = \frac{|AB|}{|AX_{HP3}|} \rightarrow x_{inc} = \frac{r_{inc} \cdot |AX_{HP3}|}{|AB|}$$

, then the final incidence angle is $\delta = x_{inc} + Min_{inc}$, therefore:

$$\delta = \frac{r_{inc} \cdot |AX_{HP3}|}{|AB|} + Min_{inc} \quad (A.1.7)$$

Coordinates of A, B are known. To compute coordinates of a point X_{HP3} which is a perpendicular image of a point HP-3 in the line $p(A, \overline{AB})$, a problem of intersection between line p and line s that is perpendicular to p and contain point HP-3 has to be solved. The normal vector of line s equals direction vector of line p . Therefore:

$$\begin{aligned}
 \vec{u} &= (u_1, u_2) = (\lambda_A - \lambda_B, \phi_A - \phi_B) \\
 p(A, \vec{n}), \vec{n} &= (u_2, -u_1); s(HP3, \vec{u}) \\
 p : u_2x - u_1y + c_p &= 0; c_p = u_1\phi_A - u_2\lambda_A \\
 s : u_1x + u_2y + c_s &= 0; c_s = -u_2\phi_{HP3} - u_1\lambda_{HP3} \\
 X_{HP3}(\lambda_X, \phi_X) : \phi_X &= \frac{u_1c_p - u_2c_s}{u_1^2 + u_2^2}, \lambda_X = \frac{u_1\phi_X - c_p}{u_2}
 \end{aligned} \tag{A.1.8}$$

After defining coordinates of X_{HP3} , the $|AX_{HP3}| = \sqrt{(\lambda_X - \lambda_A)^2 + (\phi_X - \phi_A)^2}$. Range of Min_{inc}, Max_{inc} can be obtained from data header or general information of the instrument. In the case of Envisat, the incidence angles range from the nearest slant range to the far slant range between 18.7° and 26.2° in the IS2 swath (from [6] and confirmed by investigation of existing data header).

This way, using the same footprint coordinates as in Section A.1.4, the incidence angle for HP-3 was estimated as $\delta = 21.179^\circ$.

Discussion

The incidence angle variation is linearly distributed within the swath, therefore the resulting value of local incidence angle should be precise enough for corner reflector orientation, using this method.

A.2 Correction of Azimuth for a Squint Angle

The assumption of perpendicular looking direction to the satellite track during acquisition is simplified for physical phenomena. As it was described in Section 2.2.2, each point is in fact illuminated from many hundreds different angles and then, using procedure called SAR focusing, only one look direction will be achieved, often based on an average Doppler frequency caused by satellite movements. In the optimal case, this Doppler centroid frequency is $f_{DC} = 0\text{Hz}$ that indeed corresponds with the perpendicular look direction. However, this is not the case of most acquisitions. The non-zero Doppler centroid is caused by a deviation from the perpendicular look angle called a squint angle ψ . This situation is depicted in Fig. A.2.1. Squint can occur inadvertently as a result of satellite platform yaw or because of the rotation of the Earth during imaging (Richards, 2009). Contemporary satellites are able of (almost) non-squint angle acquisitions by yaw and pitch steering (Fiedler et al., 2005) - in these cases the yaw angle should be also accounted for CR orientation purposes.

The Eq. A.2.1 as taken from (Cumming et al., 2004), p.140 (based on approximated geometry - without regard on the Earth curvature):

$$f_{DC} = \frac{2v_{sat} \cdot \sin \psi}{\lambda} \rightarrow \psi = \arcsin \frac{f_{DC} \cdot \lambda}{2v_{sat}} \tag{A.2.1}$$

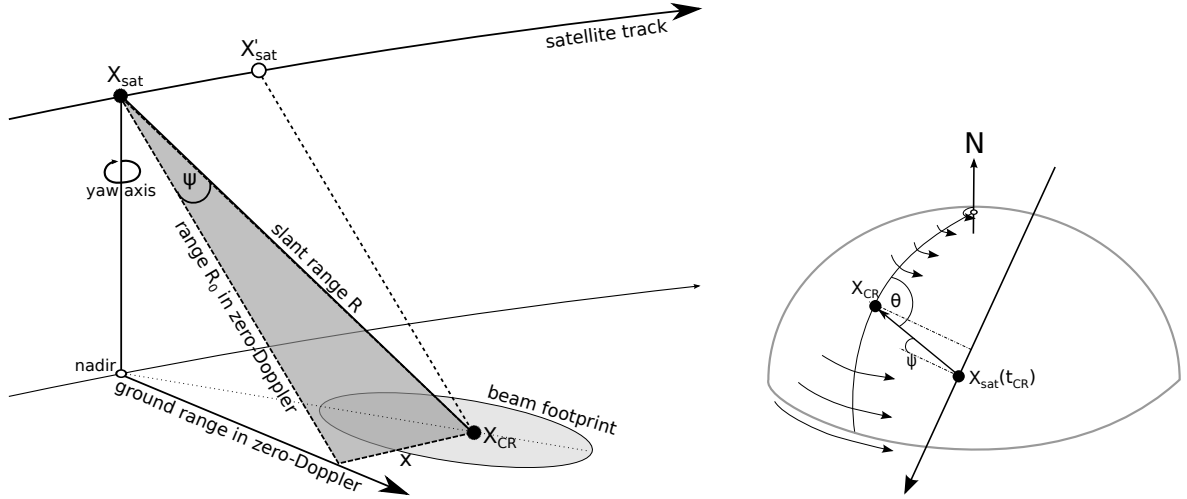


Figure A.2.1 – Squint angle; adapted from (Cumming et al., 2004)

, where v_{sat} is the satellite velocity, λ is the sensor wavelength, f_{DC} a Doppler centroid frequency and finally ψ is the squint angle.

Then, to correct the azimuth angle θ , this angle should be subtracted:

$$\theta' = \theta - \psi \quad (\text{A.2.2})$$

If we are to deal with the yaw steering satellites, such as the Envisat, this squint angle as computed from the SAR image f_{DC} parameter is just a (small) deviation from the yaw corrected angle ψ_{yaw} . In this case, the total squint angle ψ_{total} as a deviation from the satellite track should contain both components of ψ and ψ_{yaw} :

$$\psi_{total} = \psi + \psi_{yaw}$$

Correction for Envisat SAR images

Envisat is one of the satellites that offer a yaw steering mode in order to minimize the squint angle. A more detailed description of the look angle deviation problem due to the Earth rotation velocity can be found for example in (Cumming et al., 2004).

The yaw steering strategy of Envisat follows Eq. A.2.3 as provided in (Alvarez, 1997), Tab. 16:

$$\psi_{yaw} = c_z \cos(U_{lat}) \cdot \left(1 - \frac{[c_z \cos(U_{lat})]^2}{3} \right) \quad (\text{A.2.3})$$

, where U_{lat} is the satellite osculating true latitude in the True of Date coordinate system and c_z is a coefficient of AOCS rotation amplitude in yaw characterised by Horblin and Duesmann in [7] as $c_z = 3.9130^\circ$.

The True of Date coordinate system is a reference to the satellite orbital track beginning to ascend from position over equator ($U_{lat} = 0^\circ$) to the North pole ($U_{lat} = 90^\circ$) and then descending to the South pole position ($U_{lat} = 270^\circ$).

Correction for HP-3 location

The CRs will be arranged for Envisat approaching in its descending phase. Therefore the U_{lat} to compute the yaw angle ψ_{yaw} will be estimated as $U_{lat} = 90^\circ + (90^\circ - \phi_{sat})$, where ϕ_{sat} is the latitude of the satellite in time of acquiring the HP-3 location, read from orbit files as around $\phi_{sat} = 49.24^\circ$ (see Section A.1.2). Then $\psi_{yaw} = -2.55^\circ$.

The average frequency of Doppler centroid on which the last Envisat ASAR images have been focused, is around $f_{DC} = 325\text{Hz} \pm 25\text{Hz}$. Other parameters can be read from the instrument documentation (ESA, 2007): $v = 7450\text{m/s}$, $\lambda = 0.056\text{m}$. The squint angle for $f_{DC} = 325\text{Hz}$ is $\psi = 0.07^\circ$.

So, the final azimuth should be corrected for the total squint angle:

$$\theta' = \theta - \psi_{total} = \theta - (\psi + \psi_{yaw}) = \theta + 2.5^\circ$$

Discussion

Contemporary SAR satellites are able to correct for the squint angle by steering its yaw. This way, the SAR images can be focused on a stable near-zero Doppler centroid frequency. Otherwise the object movement in relation to the satellite velocity vector would cause large Doppler centroid frequency deviations of several kHz, peaking in the area of equator where the Earth rotates with the highest velocity - this is the main complication for example of Radarsat-1 data - see (Cumming et al., 2004), page 501. Or of ERS-2 that works without functional gyroscopes.

During the ascending mode, the yaw is steered to the point slightly more ahead, while for the descending mode it compensates the velocity of approaching objects on the Earth by steering slightly back. This yaw angle can range up to $\pm 3.92^\circ$ in the equator, while it becomes zero on the Earth poles. To direct the corner reflectors to the antenna boresight, this yaw angle should be accounted for as a deviation from the perpendicular direction to satellite track.